Effect of Loading History on Necking and Fracture

by

Yuanli Bai

B.S. Automotive Engineering, Tsinghua University, Beijing, China (2000)
M.S. Vehicle Engineering, Tsinghua University, Beijing, China (2003)

Submitted to the Department of Mechanical Engineering
in partial fulfillment of the requirements for the degree of

Doctor of Philosophy in Applied Mechanics

at the

MASSACHUSETTS INSTITUTE OF TECHNOLOGY

February 2008

© Massachusetts Institute of Technology 2008. All rights reserved.

Author .....
Department of Mechanical Engineering
November 30, 2007

Certified by .....
Tomasz Wierzbicki
Professor of Applied Mechanics
Thesis Supervisor

Accepted by .....
Lallit Anand
Chairman, Department Committee on Graduate Students

MASSACHUSETTS INSTITUTE OF TECHNOLOGY
APR 2 5 2008
LIBRARIES

ARCHIVES

Effect of Loading History on Necking and Fracture

by

Yuanli Bai

B.S. Automotive Engineering, Tsinghua University, Beijing, China (2000)

M.S. Vehicle Engineering, Tsinghua University, Beijing, China (2003)

Submitted to the Department of Mechanical Engineering
on November 30, 2007, in partial fulfillment of the
requirements for the degree of
Doctor of Philosophy in Applied Mechanics

Abstract

The effect of Lode angle parameter, or the third deviatoric stress invariant, on plasticity and fracture is studied using flat-grooved transverse plane strain specimens. A generalized asymmetric plasticity model for isotropic materials with both pressure and Lode angle dependence is developed. Calibration method of the plasticity model is discussed in detail. Test results on 2024-T351 aluminum alloy confirmed the proposed plasticity model. Similarly, a generalized asymmetric 3D empirical fracture locus with six free parameters is proposed. The proposed fracture locus, which depends on both stress triaxiality (or pressure) and the Lode angle parameter, is calibrated using two types of methods: classical specimens under uniaxial testing, and the newly designed butterfly specimens under biaxial testing. Experimental results on 2024-T351 aluminum alloy, 1045 steel, and A710 steel validated the proposed 3D fracture locus.

A concept of forming severity is introduced to study the loading history effect on metal forming limit diagram (FLD). Given the necking locus under proportional loading conditions, and using a non-linear accumulation rule of forming severity index, the proposed model well predicts the FLDs under different pre-loading conditions.

As an extension of the ductile fracture locus defined and calibrated under proportional loading conditions, a new damage accumulation rule considering the loading history effect is proposed. The new model uses the accumulated difference between directions of the back stress tensor and the current stress tensor to describe the non-proportionality of a load path. Several types of tests with complex loading histories were designed and performed to study the loading history effect on ductile fracture. Extensive experimental studies on 1045 steel confirmed the proposed ductile fracture model. The proposed model is successfully applied to predict fracture of crushed prismatic tubes undergoing strain reversal.

Thesis Supervisor: Tomasz Wierzbicki
Title: Professor of Applied Mechanics

Acknowledgments

First of all, I need to thank my advisor, Professor Tomasz Wierzbicki, for offering me great insight and advice through my four and a half years of study at MIT. I very much appreciated our daily discussions and his continuous guidance. The financial supports of this work through the MIT AHSS (Advanced High Strength Steel) Industry Consortium and the NSF/Sandia Alliance program are also gratefully acknowledged.

I received many constructive comments from the members of my Ph.D thesis committee, Professor Lallit Anand of the Department of Mechanical Engineering, Professor Ronald Ballinger of the Department of Nuclear Science and Engineering / Department of Materials Science and Engineering, and Professor Tony Atkins from the University of Reading, for which I am very grateful. Thanks are due to Professor R.M. Brannon of the University of Utah for providing me with valuable comments on Chapter 3. Comments received from Dr. Thomas Stoughton of GM on Chapter 6 are also greatly appreciated. Assistance of Dr. Nici Ames in conducting the torsional tests is gratefully acknowledged.

I have been very happy to work in the Impact and Crashworthiness Lab at MIT. I got a lot of help and I learned a lot from my colleagues: Dr. Yingbin Bao, Professor Dirk Mohr, Dr. Mulalo Doyoyo, Professor Chiara Bisagni, Dr. Xiaoqing Teng, Dr. Young-Woong Lee, Dr. Li Zheng, Dr. Liang Xue, Mr. Carey Walters, Mr. JongMin Shim, Mr. Min Huang, Ms. Allison Beese, Ms. Samar Malek, Mr. Cheok Wei Koh and Mr. Meng Luo. Special thanks are due to Dr. Yingbin Bao for helping me enter the field of ductile fracture mechanics. Also, I would like to thank Sheila McNary for her kind help in administrative matters. I get to know many friends during my stay at MIT. I can not list all of them, but I would like to thank them for their friendship. All of these assistance made my life at MIT smooth and enjoyable.

Finally, I would like to express my deepest thanks to my parents and my elder brother for their continuing support of my study from elementary school all the way to the Ph.D degree. My wife, Jingru Xu, gave up a good job in China, and stayed with me during the last two years. Her presence has been a constant source of strength and motivation in the final years of my Ph.D study at MIT.

THIS PAGE INTENTIONALLY LEFT BLANK

Contents

1 Introduction **25**

1.1 Ductile fracture mechanics 25

1.1.1 Brief background 25

1.1.2 Fracture locus calibration under monotonic loading 26

1.1.3 Loading history effect on fracture 27

1.2 Problem, approaches and objectives 28

1.3 Outline of the thesis 29

1.4 List of papers published, submitted or in preparation with reference to respective chapters 31

2 Derivation and application of stress triaxiality formula for plane strain fracture testing **33**

2.1 Introduction 34

2.1.1 Characterization of stress states 34

2.1.2 Ductile fracture models and calibration 36

2.2 Derivation of stress triaxiality formula for flat grooved plate plain strain specimens 39

2.3 Verification of analytical solution with finite element simulation 41

2.4 Results for 1045 steel 44

2.4.1 Fracture tests on smooth round bar and notched round bar specimens 44

2.4.2 Fracture tests on flat plane strain specimens with grooves 47

2.4.3 Fracture tests on tubular specimens in torsion 50

2.4.4 Summary of results of 1045 steel 52

2.5 Results for DH36 steel 55

2.6 Discussion and conclusion 56

3 A New Model of Metal Plasticity and Fracture with Pressure and Lode Dependence **59**

3.1 Introduction . . . 60
3.2 Characterization of the stress state . . . 61
3.3 A new form of metal plasticity . . . 64
3.3.1 Effect of hydrostatic pressure on yield . . . 65
3.3.2 Lode dependence . . . 66
3.3.3 The deviatoric associated flow rule . . . 69
3.4 Experimental calibration of 2024-T351 aluminum . . . 70
3.4.1 Smooth and notched round bars tensile tests . . . 71
3.4.2 Flat grooved plates tensile tests . . . 74
3.4.3 Cylindrical specimens upsetting tests . . . 75
3.5 The asymmetric 3D fracture locus . . . 77
3.6 Fracture locus calibration . . . 81
3.6.1 Fracture locus calibration using "classical" specimens . . . 81
3.6.2 Fracture locus calibration using butterfly specimens . . . 84
3.7 Damage evolution rule . . . 87
3.8 Discussion and conclusion . . . 88

4 Design of butterfly specimen **89**

4.1 Introduction . . . 90
4.2 Specimen design . . . 92
4.3 Methodology . . . 92
4.3.1 Testing . . . 92
4.3.2 Finite element simulation . . . 95
4.4 Analysis of the results . . . 99
4.5 Discussion and conclusion . . . 103

5 Application of Mohr-Coulomb Criterion to Ductile Fracture **105**

5.1 Introduction . . . 106
5.2 Characterization of the stress state . . . 108
5.3 Transformation of Mohr-Coulomb to the space of $(\bar{\epsilon}_f, \eta, \bar{\theta})$ . . . 111
5.3.1 Formulas for principal stresses in terms of σ_m, η and θ . . . 112
5.3.2 A new form of the Mohr-Coulomb model . . . 114
5.4 A limiting case: maximum shear stress criterion . . . 115

5.5 Representation of Mohr-Coulomb fracture criterion in 3D space of invariants 116
5.5.1 Pressure dependence . . . 117
5.5.2 Lode angle dependence . . . 118
5.6 Parametric study . . . 119
5.6.1 Effect of c_1 . . . 119
5.6.2 Effect of c_2 . . . 121
5.6.3 Effect of A . . . 121
5.6.4 Effect of strain hardening exponent n . . . 121
5.6.5 Effect of c_η . . . 123
5.6.6 Effect of c_θ^s . . . 124
5.6.7 Existence of a cutoff region . . . 124
5.7 Crack directions in the plane stress and uni-axial stress . . . 126
5.8 Experiment calibration and verification . . . 127
5.9 Damage evolution rule . . . 131
5.10 Discussion and conclusion . . . 132

6 Forming Severity Concept for Predicting Sheet Necking under Complex Loading Histories 135
6.1 Introduction . . . 136
6.2 Transformation of FLD to different spaces under plane stress . . . 137
6.2.1 Basic formulas for space transformation under plane stress . . . 137
6.2.2 Space of $(\bar{\varepsilon}_n, \alpha)$ . . . 139
6.2.3 Space of $(\bar{\varepsilon}_n, \eta)$ . . . 140
6.2.4 Space of $(\bar{\varepsilon}_n, \bar{\theta})$ . . . 142
6.2.5 Space of (σ_1, σ_2) . . . 142
6.2.6 Analytical representation of FLD under proportional loading . . . 143
6.3 A new model considering the loading history effect on sheet necking . . . 148
6.4 Model calibration . . . 152
6.5 Prediction of necking after initial prestraining . . . 153
6.6 Further application to steel sheets . . . 158
6.7 Discussion and conclusion . . . 159

7 Study on the Loading History Effect on Ductile Fracture 163
7.1 Introduction . . . 164
7.1.1 Ductile fractures under complex loading conditions . . . 164

7.1.2 Characterization of the stress state . . . 165
7.2 Constitutive modeling . . . 167
7.2.1 A plasticity model considering combined hardening rule . . . 167
7.2.2 A new form of ductile fracture model considering the loading history effect . . . 168
7.3 Damage accumulation process . . . 172
7.3.1 Damage accumulation under proportional loading . . . 172
7.3.2 Damage accumulation under non-proportional loading . . . 174
7.4 Fracture locus calibration on 1045 steel using "classical" specimens . . . 181
7.4.1 Calibration of plasticity model with combined hardening rule . . . 182
7.4.2 Fracture tests on unnotched/notched round bars and flat grooved specimens . . . 187
7.4.3 Fracture tests on tubular specimens . . . 189
7.4.4 Upsetting tests . . . 192
7.4.5 3D fracture locus of 1045 steel calibrated from classical specimens . . . 194
7.5 Fracture locus calibration using butterfly specimens under biaxial loading . . . 198
7.5.1 Fracture tests on butterfly specimens of 1045 steel . . . 198
7.5.2 3D fracture locus of 1045 steel calibrated from butterfly specimens . . . 205
7.5.3 Comparison of two 3D fracture loci of 1045 steel . . . 208
7.6 Calibration of the loading history effect on fracture on 1045 steel . . . 209
7.6.1 Two-stage-tension tests . . . 209
7.6.2 Compression followed by tension tests on notched round bars . . . 214
7.6.3 Torsion followed by tension tests on tubular specimens . . . 215
7.6.4 Parameter calibration . . . 219
7.7 Fracture validation tests on butterfly specimens with complicated loading histories . . . 221
7.7.1 Tests on butterfly specimens: complex loading of $+0^\circ \rightarrow +30^\circ$ . . . 221
7.7.2 Tests on butterfly specimens: reverse loading of $-90^\circ \rightarrow +90^\circ$ . . . 224
7.7.3 Tests on butterfly specimens: reverse loading of $-0^\circ \rightarrow +0^\circ$ . . . 225
7.8 Discussion and conclusion . . . 227

8 Application Example: Fracture of Prismatic Aluminum Tubes under Reverse Straining 229
8.1 Introduction . . . 229
8.2 Experimental program . . . 230

8.3 Analytical solution 234
8.4 Material model of plasticity and fracture 236
8.5 Finite element simulation 237
8.6 Discussion and conclusion 240

9 Conclusion and future studies **243**
9.1 Summary of main results 243
9.2 Suggestions for future studies 245

A Derivation of stress distribution inside the neck of a plane strain specimen **247**
A.1 Transverse plane strain specimens 247
A.2 Summary of three types of specimens: axisymmetry, plane strain and plane stress 251

Bibliography **253**

THIS PAGE INTENTIONALLY LEFT BLANK

List of Figures

1-1 Failures due to fracture in various structural systems 26

2-1 Three types of coordinate system in the space of principal stresses 35
2-2 A general 3D fracture locus newly postulated by Bai and Wierzbicki (2007a), see Chapter 3. 37
2-3 Necking in a round bar specimen 38
2-4 A sketch of a flat grooved plane strain specimen(left), and the cross-section of the specimen (right). 40
2-5 Verification and correction of Bridgman's formula of stress triaxiality in the center of a round notch bar, after Wierzbicki and Bao. 42
2-6 Finite element models of flat grooved specimens with different groove radii. . 42
2-7 Stress triaxiality v.s. equivalent strain in the center of flat grooved specimens from numerical simulations 43
2-8 Comparison of initial stress triaxialities from the analytical solution and numerical simulations 44
2-9 1045 steel round bar specimens with different notches 46
2-10 Force displacement response of 1045 steel smooth and notched round bar specimens 46
2-11 Stress v.s. plastic strain curve of 1045 steel used in numerical simulations . . 47
2-12 1045 steel plane strain flat specimens with different notches 48
2-13 Finite element model of flat grooved specimen, $t = 1.55mm, R = 3.97mm$. . . 48
2-14 Force displacement response of 1045 steel plane strain flat specimens with groove notch = 3.97mm 50
2-15 Dimension of torsional tubing specimens. 51
2-16 Two torsional tubing specimens after fracture. 51
2-17 The torque-rotation curves of tubes under torsional loading. 51

2-18 Comparison of the fracture loci of 1045 steel measured from two groups of classical specimen in the plane of equivalent strain to fracture and *initial* stress triaxiality, which clearly shows the effect of Lode angle of ductile fracture locus. 52
2-19 Fracture locus of steel 1045 from numerical simulations using *average* stress triaxiality 54
2-20 A comparison of fracture loci constructed on the basis of the *initial* stress triaxiality (direct method, solid line) and average triaxiality (inverse method, dash line) 54
2-21 Fracture locus of DH36 steel from experimental measurements using *initial* stress triaxiality 55
2-22 Fracture locus of DH36 steel from numerical simulations using *average* stress triaxiality 56
2-23 3D fracture loci of 1045 steel and DH36 steel, data from experimental measurements, assuming symmetric fracture locus ($\bar{\epsilon}_f^{(+)} = \bar{\epsilon}_f^{(-)}$). 57

3-1 Conceptual representation of the initial stress states on the plane of η and $\bar{\theta}$ 64
3-2 Three yield loci in the deviatoric stress plane 67
3-3 Examples of yield locus for plane stress condition. (Here, $c_\theta^t = 1$, and the effect of hydrostatic pressure is dis-activated, $c_\eta = 0$) 68
3-4 A postulated 3D yield surface 69
3-5 A group of smooth and notched round bar specimens 72
3-6 A comparison of force-displacement curves between experimental results and simulation results: smooth round bars, diameter = 9mm 72
3-7 A comparison of force-displacement curves between experimental results and simulation results: notched round bars, diameter =8mm, notch radius=4mm. 73
3-8 A group of flat grooved specimens 74
3-9 A comparison of force-displacement curves between experimental results and simulation results: flat grooved specimens, thickness = 2.11mm, groove radius=1.59mm. 75
3-10 Two groups of cylindrical specimens for upsetting tests 76
3-11 A comparison of force-displacement curves between experimental results and simulation results: cylindrical specimens, diameter=8 mm, height=6 mm. . 76
3-12 The fracture locus independent of ξ (or $\bar{\theta}$) postulated by Johnson and Cook (1985) (left), and a 3D symmetric fracture locus accounting for ξ postulated by Wierzbicki and Xue (Wierzbicki and Xue, 2005; Wierzbicki et al., 2005b)(right) 78

3-13 A new interpolation of Bao's data points of aluminum 2024-T351 (experimental data from Bao's tests (Bao, 2003)) 79
3-14 A newly postulated 3D asymmetric fracture locus 81
3-15 3D fracture locus of 2024-T351 aluminum (experimental data after Bao (2003); Wierzbicki et al. (2005b), see Table 5.1.) 83
3-16 A new type of butterfly shape specimen (A710 steel) 84
3-17 Fracture locus of A710 steel in the space of stress triaxiality and fracture strain (experimental data from Wierzbicki et al. (2005a), see Table 4.3.) . . . 85
3-18 Loading conditions of A710 steel in the plane of stress triaxiality η and the Lode angle parameter $\bar{\theta}$ (experimental data from Wierzbicki et al. (2005a), see Table 4.3.) 86
3-19 3D Fracture locus of A710 steel in the space of stress triaxiality, the Lode angle parameter and fracture strain (data points from Wierzbicki et al. (2005a), see Table 4.3.) 86

4-1 A newly designed specimen which has a gauge section with a double curvature profile. 91
4-2 Detailed geometry of the newly designed specimen 91
4-3 A universal biaxial testing device designed by Mohr and Doyoyo (2004). Specimen is positioned for 10° loading. 93
4-4 The experimental set-up. 93
4-5 All the specimens of A710 steel after fracture. 95
4-6 Crack initiation in 90° tension. 95
4-7 (a) Finite element discretization of butterfly specimen (A710 steel), (b) a close view of the central region of the specimen. 96
4-8 Calibrated stress-strain curve of A710 steel. 97
4-9 (a) Comparison of deformed butterfly specimens under +30° loading (A710 steel), (b) a close view of the central region of the specimen. 98
4-10 Comparison of force-displacement response for all eight cases (A710 steel). . 99
4-11 Evolution of the stress triaxiality parameter for all eight loading cases (A710 steel). 101
4-12 Evolution of the Lode angle parameter for all eight loading cases (A710 steel). 102
4-13 The fracture locus of A710 steel in the space of equivalent strain to fracture and stress triaxiality. 103

5-1 Different resolution quality of strain and stress parameters: the stress parameters have good resolutions in elastic region, and the strain parameters have good resolutions in plastic region. 107
5-2 Application of maximum shear stress failure criterion to ductile fracture for plane stress condition (Lee, 2005; Wierzbicki et al., 2005b). 108
5-3 Three types of coordinate system in the space of principal stresses 110
5-4 Geometry representation of principal stresses $(\sigma_1, \sigma_2, \sigma_3)$, deviatoric stresses (s_1, s_2, s_3), equivalent stress $(\bar{\sigma})$ and Lode angle (θ) on the deviatoric plane (π plane) 113
5-5 3D geometry representation of maximum shear fracture criterion ($A = 740MPa$, $n = 1/6$, $c_\eta = 0$, $c_\theta^{ax} = c_\theta^s = 1$, $c_1 = 0.0$, and $c_2 = 330MPa$). The curve on the surface represents the plane stress curve. 116
5-6 3D geometry representation of Mohr-Coulomb fracture model ($A = 740MPa$, $n = 1/6$, $c_\eta = 0$, $c_\theta^{ax} = c_\theta^s = 1$, $c_1 = 0.1$, and $c_2 = 330MPa$). 117
5-7 Mohr-Coulomb criterion in the space of equivalent strain to fracture and stress triaxiality (assuming $\bar{\theta} = 0$) 118
5-8 Mohr-Coulomb criterion on the space of equivalent strain to fracture and the Lode angle parameter (assuming $\eta = 0$) 119
5-9 Effect of c_1 on the new form of the Mohr-Coulomb criteria 120
5-10 Effect of c_2 on the new form of the Mohr-Coulomb criteria 120
5-11 Effect of A on the new form of the Mohr-Coulomb criteria 121
5-12 Effect of n on the new form of the Mohr-Coulomb criteria 122
5-13 A normalized plot to show the effect of n on the new form of the Mohr-Coulomb criteria 122
5-14 Effect of c_η on the new form of the Mohr-Coulomb criteria 123
5-15 Effect of c_θ^s on the new form of the Mohr-Coulomb criteria 124
5-16 A proposed shape of cutoff region of fracture one the plane of $(\eta, \bar{\theta})$ with $c_1 = 0.57$. 125
5-17 A physical interpretation of existence cutoff region using the concept of die-cone in friction. 126
5-18 According to Mohr-Coulomb fracture criterion, a crack direction locus is proposed for plane stress conditions. 127
5-19 Specimens used by Bao to calibrate the fracture locus for the wide range of stress triaxialtiy (Bao, 2003; Wierzbicki et al., 2005b) 128

5-20 3D geometric representation of Mohr-Coulomb fracture locus for 2024-T351 aluminum alloy 130
5-21 Mohr-Coulomb fracture locus for 2024-T351 on the plane of equivalent strain to fracture and stress triaxiality. 130

6-1 An example of forming limit diagram (FLD) of the transverse direction of aluminum alloy 6111-T4 (experimental data after Graf and Hosford (1994)) . 137
6-2 Transformation from FLD to the space of $(\bar{\varepsilon}_n, \alpha)$ for 6111-T4 aluminum. . . 140
6-3 Transformation from FLD to the space of $(\bar{\varepsilon}_n, \eta)$ for 6111-T4 aluminum. . . . 141
6-4 Transformation from FLD to the space of $(\bar{\varepsilon}_n, \bar{\theta})$ for 6111-T4 aluminum. . . . 141
6-5 Transformation from FLD to the space of (σ_1, σ_2) for 6111-T4 aluminum. . . 143
6-6 Two types of curve fitting of FLD in the space of $(\bar{\varepsilon}_n, \bar{\theta})$ 144
6-7 Power function curve fitting of FLD in the $(\bar{\varepsilon}_n, \bar{\theta})$ compared with the experimental results in the space of $(\varepsilon_1, \varepsilon_2)$ (transverse direction of 6111-T4 aluminum alloy, $\bar{\varepsilon}_n^{UA} = 0.340$, $\bar{\varepsilon}_n^{PE} = 0.197$, $\bar{\varepsilon}_n^{BA} = 0.485$, and $M = 1.35$). . . . 146
6-8 An example of the proposed power function curve fitting of FLD compared with analytical solution from Hill, Stören and Rice ($n = 0.244$ for analytical solution, and $\bar{\varepsilon}_n^{UA} = 0.488$, $\bar{\varepsilon}_n^{PE} = 0.2817$, $\bar{\varepsilon}_n^{BA} = 0.5773$, $M = 2$ for the power function). 147
6-9 Comparison of different weighting functions for the case of $c_g = 2$. 151
6-10 A sketch of transformation of model prediction for two-stage loading to the $(\varepsilon_1, \varepsilon_2)$ plane. 154
6-11 Comparison between model prediction (dashed curves) and experimental results (solid curves) on the plane of $(\varepsilon_1, \varepsilon_2)$ after different equi-bixial-prestraining. The FLD is for aluminum 6111-T4 in transverse direction. Path OAB is used for calibration. 154
6-12 Comparison between model prediction (dashed curves) and experimental results (solid curves) on the plane of $(\varepsilon_1, \varepsilon_2)$ after different uni-axial-prestraining. The FLD is for aluminum 6111-T4 in transverse direction. 155
6-13 Comparison between model prediction (dashed curves) and experimental results (solid curves) on the plane of $(\varepsilon_1, \varepsilon_2)$ after different plane strain prestraining. The FLD is for aluminum 6111-T4 in transverse direction. 156
6-14 Comparison between model prediction (dashed curves) and experimental results (solid curves) on the plane of $(\varepsilon_1, \varepsilon_2)$ after different uni-axial-prestraining in rolling direction. The FLD is for aluminum 6111-T4 in transverse direction. 157

6-15 Comparison between model prediction (dashed curves) and experimental results (solid curves) on the plane of $(\varepsilon_1, \varepsilon_2)$ under both proportional loading and with different prestraining. The FLD is for aluminum-killed sheet steel. 158
6-16 Comparison of model predictions with different values of c_g for the aluminum-killed steel sheet 160

7-1 Three types of coordinate system in the space of principal stresses 166
7-2 Three possibilities of damage accumulation under monotonic loading postulated by Bonora (1997). 173
7-3 An arbitrary loading path in the plane of stress triaxiality and the third stress parameter 174
7-4 An example of the evolution of the two non-proportionality parameter χ and μ in the reverse loading. 175
7-5 A sketch of two step loaded specimens. (After Tai (1990)) 176
7-6 Review on tests of tension with changed notches of No. 20 steel (experimental data from Tai (1990)) 177
7-7 A test set up for reversal loading test in uniaxial testing machine (after Bao and Treitler (2004)) 178
7-8 Review on tests of reversal loading of aluminum 2024-T351 (experimental data from the type-A specimen of Bao and Treitler (2004)) 179
7-9 Test data of torsion followed by tension of the OFHC copper (After Johnson and Cook (1985)). 180
7-10 Review on tests of torsion followed by tension of OFHC cooper (experimental data from Johnson and Cook (1985)) 181
7-11 A method proposed by Khan and Jackson (1999) to calibrate the combined hardening property of materials. 182
7-12 Data points chosen on the surface of a notched round bar for optical measurement. The specimen was painted with small black dots for optical measurement. 183
7-13 Measured stress-strain curves of 1045 steel under reverse loadings: compression followed by tension. 184
7-14 Measured isotropic hardening and kinematic hardening of 1045 steel. 185
7-15 Comparison of force-displacement curves under compression-tension loading. 186
7-16 Three types of specimens: (a) un-notched round bars, (b) notched round bars, (c) flat grooved specimens. 187

7-17 Comparison of force-displacement curves for tensile tests on smooth and notched round bars. 188
7-18 Comparison of force-displacement curves for tensile tests on flat grooved specimens (groove radius = 3.97 mm). 189
7-19 Dimension of torsional tubing specimens. 190
7-20 Two torsional tubing specimens after fracture. 190
7-21 Comparison of torque-rotation curves of tubes under torsional loading. . . . 190
7-22 Finite element model with 43040 solid elements of the tubing specimen. . . . 191
7-23 A tubing specimen subject to tensile loading (after fracture). 192
7-24 Comparison of force-displacement curves of a tube under pure tensile loading. The gauge length equals to $12.7mm$. 192
7-25 Cylindrical specimens for upsetting tests. (a) the ratio of cylinder diameter to height equals to 0.8, (b) ratio of cylinder diameter to height equals to 1.0. 193
7-26 Comparison of force-displacement curves of a upsetting test (ratio of cylinder diameter to height equals to 0.8). 194
7-27 Comparison of the fracture loci of 1045 steel measured from two groups of classical specimen in the plane of equivalent strain to fracture and stress triaxiality, which clearly shows the effect of Lode angle of ductile fracture locus. 196
7-28 Projection of the fracture locus of 1045 steel from classical specimens into the plane of equivalent strain to fracture and stress triaxiality. 197
7-29 Calibrated 3D fracture locus of 1045 steel from classical specimens. 197
7-30 Butterfly specimens tested under monotonic loading conditions. 198
7-31 (a) INSTRON dual actuator loading system: 1-lower system grip, 2-upper grip, 3-upper cross-head, 4-sliding table, 5-vertical load cells, 6-horizontal load cell and actuator, 7-digital camera. (b)Schematic of the mechanical system. (photo modified after Mohr and Oswald (2007)). 199
7-32 Definition of different loading angles for butterfly specimens. 200
7-33 Comparison of force-displacement curves under pure tension (+90°). 201
7-34 Comparison of force-displacement curves under biaxial loading (+30°). . . . 201
7-35 Comparison of force-displacement curves under biaxial loading (+22°). . . . 202
7-36 Comparison of force-displacement curves under biaxial loading (+10°). . . . 202
7-37 Comparison of force-displacement curves under biaxial loading (+5°). 203
7-38 Comparison of force-displacement curves under simple shear (+0°). 203
7-39 Comparison of force-displacement curves under biaxial loading (−5°). 204

7-40 Comparison of force-displacement curves under biaxial loading ($-10°$). . . . 204
7-41 Finite element model with 28120 solid elements of the butterfly specimen. . . 205
7-42 Projection of the fracture locus of 1045 steel from butterfly specimens into the plane of equivalent strain to fracture and stress triaxiality. 207
7-43 Calibrated 3D fracture locus of 1045 steel from butterfly specimens. 207
7-44 Comparison of two fracture loci of 1045 steel calibrated from classical specimens and butterfly specimens in the plane of equivalent strain to fracture and stress triaxiality. 208
7-45 Specimens of two-stage-tension test on 1045 steel. (a) specimens after first stage tension, (b)second stage specimens with re-machining introduced notches.210
7-46 Comparison of force-displacement curves for a group of two-stage-tension tests (group A). 210
7-47 Comparison of force-displacement curves for a group of two-stage-tension tests (group B). 211
7-48 Stress-strain curves used to simulate the two-stage-tension tests. 212
7-49 Another simulation of smooth/notched round bars subjected to pure tension. This figure shows the comparison of force-displacement curves. 212
7-50 Comparison of damage accumulation for the two-stage-tension tests (case 1: for pure tension, case 2&3: group A, case 4&5: group B). 213
7-51 Specimens and experimental setup for compression-tension test on 1045 steel. 214
7-52 Comparison of two types of loading history effect on fracture under reverse loading (without any correction of loading history effect). 215
7-53 Specimens subjected to torsion followed by tension. (a)specimens after initial torsion, (b) specimens after tension of the second stage loading. 216
7-54 Comparison of torque-rotation curves for the pre-torsion part of the loading cycle. 216
7-55 Comparison of force-displacement curves for tension of the second stage loading on tubes. 217
7-56 Comparison of two types of loading history effect on fracture under torsion-tension loading. 218
7-57 Comparison of the evolution of the parameter μ between the torsion-tension loading and the compression-tension loading. 218
7-58 Correction of the loading history effect on fracture, notched round bars of 1045 steel subjected to compression followed by tension. 220

7-59 Correction of the loading history effect on fracture, tubing specimens of 1045 steel subjected to torsion followed by tension. 220
7-60 Butterfly specimens subject to the complex loading of $+0° \rightarrow +30°$. 221
7-61 Comparison of force-displacement curves under two-stage loading of ($+0° \rightarrow +30°$, test 1). 222
7-62 Comparison of force-displacement curves under two-stage loading of ($+0° \rightarrow +30°$, test 2). 222
7-63 Comparison of force-displacement curves under two-stage loading of ($+0° \rightarrow +30°$, test 3). 223
7-64 Correction of the loading history effect on fracture, butterfly specimens of 1045 steel subjected to complex loading of $+0° \rightarrow +30°$. 223
7-65 Butterfly specimens subject to the reverse loading of $-90° \rightarrow +90°$. 224
7-66 Comparison of force-displacement curves under reverse loading of ($-90° \rightarrow +90°$). 224
7-67 Correction of the loading history effect on fracture, butterfly specimens of 1045 steel subjected to reverse loading of $-90° \rightarrow +90°$. 225
7-68 Butterfly specimens subject to the reverse loading of $-0° \rightarrow +0°$. 226
7-69 Comparison of force-displacement curves under reverse loading of ($-00° \rightarrow +00°$). 226
7-70 Correction of the loading history effect on fracture, butterfly specimens of 1045 steel subjected to reverse loading of $-0° \rightarrow +0°$. 227

8-1 Photographs of the partially crushed tubes at the stage of formation of first cracks. 231
8-2 A close up view of cracks on the inner surface in tubes A and C. 232
8-3 Force-displacement responses in experiment. The observed displacements to fracture initiation are marked with circles. 233
8-4 Definition of parameters W, H and B. 234
8-5 A simple folding model with stationary plastic hinges and rotating planar elements. The shaded area represents the amount of relative transverse in plane displacement in the area adjacent to the corner line. 235
8-6 Evolution of strain obtained from numerical and analytical analysis. 236
8-7 Comparison of force-displacement responses for all four tubes. 238
8-8 Comparison of predicted deformation and fracture initiation for Tube A. The contour plot shows the distribution of the damage indicator D. 239

8-9 Comparison of predicted deformation and fracture initiation for Tube B. The contour plot shows the distribution of the damage indicator D. 239
8-10 Comparison of predicted deformation and fracture initiation for Tube D. The contour plot shows the distribution of the damage indicator D. 240

A-1 The cross-section of a flat grooved plane strain specimen and the free body diagram of its surface point on the notch 247
A-2 Diagram of the approximate stress analysis in the neighborhood of the neck of a plane strain specimen 249
A-3 Three types of specimens with necks 252

List of Tables

2.1 Material properties used in the simulation 43
2.2 A summary of the characterized dimensions of the smooth and notched round bar specimens (1045 steel) 45
2.3 A summary of the characterized dimensions of the flat grooved specimens (1045 steel) 49

3.1 Ten types of classical specimens for plasticity and fracture calibration 63
3.2 Calibrated material properties of aluminum 2024-T351 (Rolling direction) . . 77

4.1 A summary of tests of butterfly specimens under eight loading conditions (A710 steel) 94
4.2 List of locations of fracture initiation of butterfly specimens (A710 steel) . . 100
4.3 A summary of test results on A710 steel using butterfly specimens 102

5.1 A summary of Bao and Wierzbicki's test results on 2024-T351 aluminum, (experimental data after Bao (2003); Wierzbicki et al. (2005b)) 128

6.1 A summary of three typical tests for the FLD 144
6.2 Some typical forms of function $g(\lambda)$ 150
6.3 Calibrated model parameters for aluminum alloy 6111-T4 152

7.1 Some typical ductile fracture loci * 170
7.2 Some typical forms of function $g(\lambda)$ 171
7.3 Calibrated parameters of the plasticity model of 1045 steel 186
7.4 A summary of test results on 1045 steel using classical specimens 195
7.5 Calibrated parameters of the fracture locus of 1045 steel using classical specimens 196
7.6 List of locations of fracture initiation of butterfly specimens 200
7.7 A summary of test results on 1045 steel using butterfly specimens 206

7.8 Calibrated parameters of the fracture locus of 1045 steel using butterfly specimens 206
7.9 Calibrated parameters of the loading history effect on fracture of 1045 steel 219

8.1 Initial geometry of the tubes and thickness variation) 231
8.2 Parameters characterizing partially crushed tubes (refer to Fig. 8-4) 233
8.3 Calibrated parameters of the plasticity model of 2024-T351 aluminum alloy . 237
8.4 Calibrated parameters of the fracture model of 2024-T351 aluminum alloy . 237

A.1 Stress distribution inside a neck of three types of specimens 252

Chapter 1

Introduction

1.1 Ductile fracture mechanics

1.1.1 Brief background

Prediction of ductile fractures of metals in engineering structures is a topic of great importance in the automotive, aerospace, and military industries. For example, significant efforts have been recently taken by the automotive industry to reduce the weight of vehicles while maintaining performance and cost competitiveness (Walp et al., 2006). One such a solution is to use advanced high strength steels (AHSS) as the primary body materials. As the material strength of AHSS increases, its ductility will decrease, so fracture becomes a major challenge when designing vehicles with AHSS. There could be different forms of fracture, for example, forming fracture, edge crack, crushing fracture and so on. Fig. 1-1 shows examples of fracture in various structural systems. Over the past four decades, several macroscopic models have been developed to describe the ductile fracture of metals. Classical cylindrical hole growth model (McClintock, 1968), spherical hole growth model (Rice and Tracey, 1969), Gurson-Tvergaard-Needleman's (GTN) porous plasticity model (Gurson, 1975; Tvergaard and Needleman, 1984), damage mechanics (Lemaitre, 1996), empirical fracture models such as Oyane et al. (1980), Cockcroft and Latham (1968), the Wilkins et al. (1980), the Johnson and Cook (1985), and the cohesive element approach (Cirak et al., 2005) all belong to the above class. The present thesis is concerned with the macroscopic and empirical aspects of fracture.

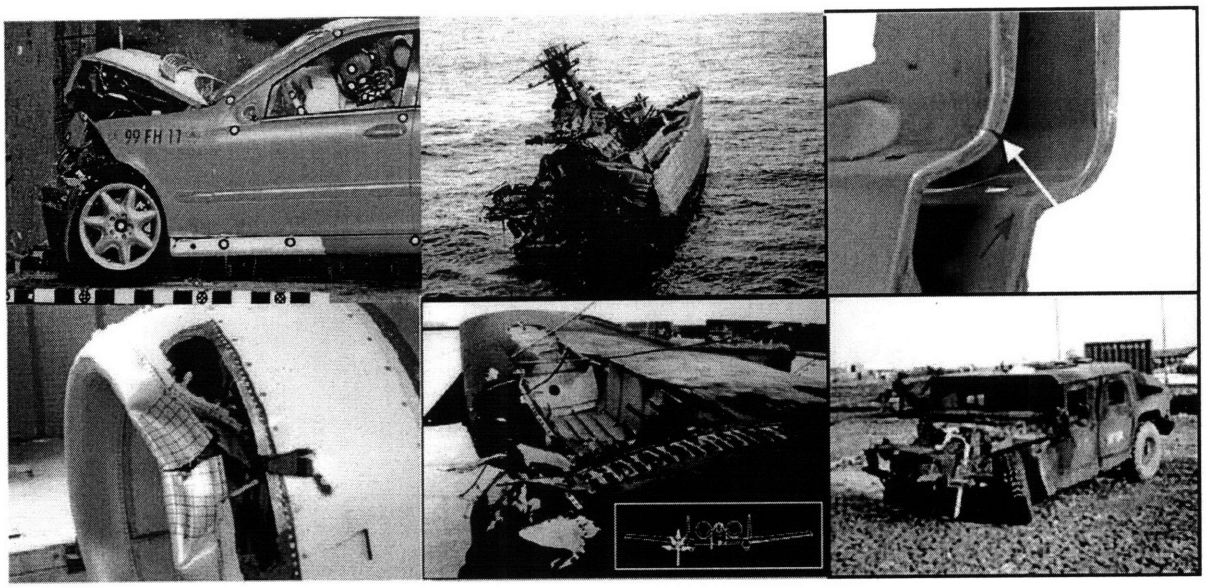

Fig. 1-1: Failures due to fracture in various structural systems

1.1.2 Fracture locus calibration under monotonic loading

Equivalent strain to fracture $\bar{\epsilon}_f$ (or the fracture strain for short) is widely used to define the material ductility. Many theoretical analyses and experimental results have shown that the material's fracture strain is not constant but changes under different loading conditions (McClintock, 1968; Rice and Tracey, 1969; Hancock and Mackenzie, 1976; Johnson and Cook, 1985; Bao, 2003). The most important fracture controlling parameter is the stress triaxiality η (normalized hydrostatic pressure, $\frac{\sigma_m}{\bar{\sigma}}$). A commonly used type of test for ductile fracture calibration is the tensile test on axisymmetric unnotched and notched round bars (Hancock and Mackenzie, 1976; Johnson and Cook, 1985), which covers only the high stress triaxiality range($\eta \geq \frac{1}{3}$). Due to the limitation of experimental methods, fracture loci determined from those tests are often extrapolated to small and even negative stress triaxiality, which is clearly a risky procedure. Another type of test is the upsetting test on cylindrical specimens (Ganser et al., 2001; Bao and Wierzbicki, 2005), which covers the negative stress triaxiality range ($-\frac{1}{3} \leq \eta \leq 0$). Bao (2003) designed and performed 15 types of tests to calibrate the fracture strain in the whole range of stress triaxiality, and found that the fracture locus is not necessary represented by a smooth, monotonic curve in the entire range of stress triaxiality due to different fracture mechanisms operating at different stress triaxiality ranges. Bao's results have recently been confirmed by Barsoum (2006), who performed tension/torsion tests

on fracture of tubular specimens. This type of calibration method is very time-consuming.

Recently, Wierzbicki and Xue (2005) revisited Wilkins' model (Wilkins et al., 1980), and incorporated the effect of Lode angle (θ) on ductile fracture. The Lode angle can be related to the third deviatoric stress invariant, which is often neglected by the plasticity theories and ductile fracture models. Introducing the Lode angle parameter (or the third deviatoric stress invariant), the calibration of fracture strain under all the loading conditions poses a great challenge. To design a new type of specimen and new experimental procedure, which covers a wide range of stress triaxiality and Lode angles, will significantly contribute to more exact prediction of ductile fracture. The present thesis makes an important step in this direction.

1.1.3 Loading history effect on fracture

While the existing fracture models have brought computational fracture mechanics to a new level of sophistication, they apply strictly to monotonic loadings. How do the existing models work for "non-monotonic", non-proportional loading or even for problems in which the loading is monotonic but the stress triaxiality changes in a wide range? What types of experiment should be performed to prove or disprove a given theory? Which of the basic hypotheses should be revisited or modified? These questions are important, and the answers are long overdue.

At the level of a unit material volume, the constitutive response depends on whether the loading is monotonic or there is a strain reversal. For monotonic loading, there is no difference between a kinematic and an isotropic hardening law. It is only in the presence of strain reversal that this difference becomes apparent. Compared to the abundance of information on *plastic behavior* under reverse loading (for example, White et al. (1990)), very little research has been reported in the literature on the effect of *loading history on fracture.* The lack of interest of the fracture mechanics community in this problem is surprising since strain reversal is present in many simple crack propagation problems. Consider, for example, three-point bending of a solid pre-notched beam. Initially, there are positive strains on the tensile side and negative strains on the compressive side. As the crack propagates towards the center of the beam, it clearly passes through a region that was initially under compression. Another example is the process of shear plugging in a high velocity impact. High compressive stresses under the projectile give way to shear as the through-thickness fracture progresses. Finally, the remaining ligament fails in tension.

The development of a new form of ductile fracture model considering the loading history effect is the main topic of the thesis. The calibration method of the loading history effect

will also be investigated.

1.2 Problem, approaches and objectives

The objective of the thesis is the development of a ductile fracture model of a crack free body and a new calibration procedure under different loading conditions, including both monotonic loading and complicated loading histories. The loading environment is *room temperature* and *quasi-static loading*. The material is assumed to be *isotropic*.

The present approaches include *experimental study, finite element (FE) simulation* and *analytical solutions*. In the experiments, both the uniaxial tests and biaxial tests will be designed and performed. In the experimental part, both the electronic measurement and optical measurement will be used. Experiments will provide the load-displacement response, the location and position of fracture initiation, as well as the fracture propagation mode. FE simulations are used to calculate all the stress states and strain components at the point of fracture initiation. Thus, the thesis makes an extensive use of a hybrid (inverse) method in which the experimental results are compared with FE simulations. The accuracy of numerical prediction depends then on the correctness of the plasticity model used.

In order to meet the above objective, the work was divided into several inter-related tasks:

- Determine the effects of pressure and the third deviatoric stress invariant (or the Lode angle parameter) on metal plasticity and fracture locus.

- Develop a new type of specimen for fracture locus calibration under different loading conditions.

- Predict the forming limit diagram (FLD) under complex loading histories using an entirely new concept.

- Reveal the loading history effect on ductile fracture through extensively experimental studies.

- Demonstrate and show the new theory by application on some engineering structures.

1.3 Outline of the thesis

The present thesis consists of nine chapters. Each chapter, except Chapter 1 and Chapter 9, addresses one specific topic. In most cases, the chapters are self-contained as they address one topic at a time and have already been published or are submitted for publication. A list of publications related to the present thesis is given in Section 1.4.

Chapter 2 analyzes the stress distribution inside the neck of a flat-grooved plane strain specimen. A Bridgman-like stress triaxiality formula is derived for the plane strain specimen. This formula is further corroborated using finite element simulations. By comparing the results of smooth/notched round bars, this type of specimen is used to study the Lode angle effect on both plasticity (this part is included in Chapter 3) and fracture. Experimental results on 1045 steel and DH36 steel are reported in this chapter.

Chapter 3 develops a generalized plasticity model for isotropic materials with both pressure and Lode angle dependence. Calibration method of the plasticity model is discussed in detail. Tests on 2024-T351 aluminum alloy were performed to calibrate the proposed plasticity model. Similarly, a generalized asymmetric 3D empirical fracture locus with *six free parameters* is proposed, which depends on both the stress triaxiality (or pressure) and the Lode angle parameter. The proposed fracture locus is calibrated using two types of methods: classical specimens under uniaxial testing, and butterfly specimens under biaxial testing. Experimental results on 2024-T351 aluminum alloy and A710 steel are used to validate the proposed fracture locus.

Chapter 4 is devoted to the design and optimization of a novel specimen with butterfly shape (called butterfly specimen). A wide range of stress state (stress triaxiality and Lode angle parameter) can be obtained through different combination of tension, shear and compression. Another important advantage of the butterfly specimen is that fracture always initiates in the center of the specimen, rather than at edges. The butterfly specimens were mounted into a customer-made universal biaxial testing device (UBTD), then loaded in the MTS uniaxial testing machine. Test results on A710 steel showed the applicability of the butterfly specimen to calibrate the 3D fracture locus. Biaxial tests of 1045 steel under the newly installed INSTRON biaxial testing machine is reported in Chapter 7.

In Chapter 5, the Mohr-Coulomb (M-C) criterion is applied to ductile fracture. M-C criterion was originally developed for the failure of brittle materials. Using the proposed generalized plasticity model, the M-C criterion is transformed from the stress space (τ^f, σ_n) to the mixed space of strain and stress invariants $(\bar{\varepsilon}_f, \eta, \bar{\theta})$ under the proportional loading assumption. It is found that the transformed M-C criterion exhibits both stress triaxial-

ity and Lode angle dependence on equivalent strain to fracture. Parametric study reveals the relationship between plasticity and fracture, which confirms that the M-C criterion is physically correct for ductile fracture prediction. The fracture tests reported by Bao (2003) and Bao and Wierzbicki (2004a) on 2024-T351 aluminum alloy are used to check the model. Using just two tests for fracture calibration, the model predicts the remaining nine tests with good accuracy. Since there are only *two free parameters* in the physically based M-C model, it has a great potential of being used as an engineering tool for predicting ductile fracture.

Chapter 6 introduces a new concept of forming severity to study the loading history effect on necking. The forming limit diagram (FLD) is transformed to the space of equivalent strain to neck and the Lode angle parameter $(\bar{\varepsilon}_n, \bar{\theta})$, which defines the necking locus of a material under proportional loading conditions. Similar to the idea of cumulative damage model (CDM) in ductile fracture mechanics, the prediction of necking is modeled in an incremental form with a non-linear accumulation rule of forming severity. Experimental data from literatures are used to check the proposed concept of necking prediction. Calibrated from only one test with non-proportional loading condition, the model is able to predict the remaining tests of complex loading paths with good accuracy.

The effect of loading history on ductile fracture, which is the main theme of the present thesis, is studied in Chapter 7. As a starting point, a suitable plasticity model under complex loading conditions and the ductile fracture locus under proportional or monotonic loading conditions are discussed. First, the combined kinematic/isotropic hardening plasticity model is proposed and calibrated from the compression-tension tests on notched round bar. Secondly, the ductile fracture locus under monotonic loading is calibrated using either "classical" specimens or the butterfly specimens in the INSTRON biaxial testing machine. Finally, several types of tests with complex loading histories were designed and performed to study the loading history effect on ductile fracture. Those tests include two-stage-tension, compression-tension, torsion-tension tests and the tests on butterfly specimens with programmed complex loading histories. Extensive experimental studies confirmed the proposed ductile fracture model.

Chapter 8 demonstrates the applicability of the above new model to the simulation of fracture of prismatic aluminum tubes under reverse straining. Crushed tests were performed for four tubes all made of 2024-T351 aluminum with different sidewall thicknesses. First fractures were observed at different locations depending on the thickness of the tube. Analytical solution on the crushed prismatic tubes shows that there is strain reversal at the fracture initiation sites. FE simulation of the crushing process confirmed the above finding.

Using the calibrated material ductile fracture model with loading history effect corrections, the proposed model is shown to be able to well predict fracture in crushed prismatic tubes.

Chapter 9 summaries the main contributions of the present thesis, and suggests some topics for future research.

1.4 List of papers published, submitted or in preparation with reference to respective chapters

Chap. 2	Bai, Y., Teng, X., and Wierzbicki, T., Derivation and application stress triaxiality formula for plane strain fracture testing, Presented on the ASME conference, Austin, TX, June 3-7, 2007.
Chap. 3	Bai, Y., Wierzbicki, T., A New Model of Metal Plasticity and Fracture with Pressure and Lode Dependence, *International Journal of Plasticity* 2007, In Press.
Chap. 4	Wierzbicki, T., Bao, Y., and Bai, Y., A new experimental technique for constructing a fracture envelope of metals under multi-axial loading, *Proceedings of the 2005 SEM Annual Conference and Exposition on Experimental and Applied Mechanics*, **2005**, 1295 - 1303.
Chap. 5	Bai, Y., Wierzbicki, T., Application of Mohr-Coulomb Criterion to Ductile Fracture, to be submitted for publication, 2007.
Chap. 6	Bai, Y., Wierzbicki, T., Forming Severity Concept for Predicting Sheet Necking under Complex Loading Histories, *International Journal of Mechanical Science*, submitted for publication, August 2007.
Chap. 7	Bai, Y., Wierzbicki, T., Study on the Loading History Effect on Ductile Fracture, to be submitted for publication, 2008.
Chap. 8	Bai, Y., Bao, Y. and Wierzbicki, T., Fracture of prismatic aluminum tubes under reverse straining, *International Journal of Impact Engineering* 2006, **32**(5).

Other related publications:

Wierzbicki, T., Bao, Y., Lee, Y., and Bai, Y., Calibration and evaluation of seven fracture models, *International Journal of Mechanical Sciences* 2005, **47**(4-5).

Mae, H., Teng, X., Bai, Y. and Wierzbicki, T., Comparison of Ductile Fracture Properties of Aluminum Castings: Sand Mold vs. Metal Mold, *International Journal of Solids and Structures*, August 2007, Accepted.

Mae, H., Teng, X., Bai, Y. and Wierzbicki, T., Calibration of Ductile Fracture Properties of a Cast Aluminum Alloy, *Materials Science and Engineering: A*, June 2007, **459**(1-2).

THIS PAGE INTENTIONALLY LEFT BLANK

Chapter 2

Derivation and application of stress triaxiality formula for plane strain fracture testing

Theoretical and experimental studies have shown that stress triaxiality is the key parameter controlling the magnitude of the fracture strain. Smooth and notched round bar specimens are mostly often used to quantify the effect of stress triaxiality on ductile fracture strain (e.g. the Johnson-Cook's fracture locus). The initial stress triaxiality inside the notch of round bar specimens can be estimated from the Bridgman's formula, so the fracture locus can be determined from the experimentally measured values. There is a mounting evidence (Bai and Wierzbicki, 2007) that in addition to the stress triaxiality, the normalized third stress invariant (equivalent to the Lode angle parameter) should also be included in characterization of ductile fracture. The calibration using round notched bars covers only a small range of possible stress states. Plane strain fracture tests provide additional important data.

Following the Bridgman's stress analysis inside the necking of a plane strain specimen, a closed-form solution is derived for the stress triaxiality inside the notch of a flat grooved plane strain specimen. The newly derived formula is confirmed by finite element simulations. The range of stress triaxiality in round notched bars and flat grooved specimens is similar, but the values of the Lode angle parameter are different. These two groups of tests are therefore very useful in constructing a general 3D fracture locus.

Results of experiments and numerical simulations on 1045 and DH36 steels have proved the applicability of the closed-form solution and have demonstrated the effect of the Lode angle parameter on the fracture locus. Furthermore, flat grooved specimens are especially

suitable for fracture testing of thin metal sheets, for which it is difficult to machine smooth or notched round specimens.

2.1 Introduction

2.1.1 Characterization of stress states

If a material is assumed to be isotropic, then material models can be formulated in terms of three invariants of the stress tensor $[\sigma]$, defined respectively by

$$p = -\sigma_m = -\frac{1}{3}tr([\sigma]) = -\frac{1}{3}(\sigma_1 + \sigma_2 + \sigma_3) \tag{2.1}$$

$$q = \bar{\sigma} = \sqrt{\frac{3}{2}[S] : [S]} = \sqrt{\frac{1}{2}\left[(\sigma_1 - \sigma_2)^2 + (\sigma_2 - \sigma_3)^2 + (\sigma_3 - \sigma_1)^2\right]} \tag{2.2}$$

$$r = \left(\frac{9}{2}[S] \cdot [S] : [S]\right)^{1/3} = \left[\frac{27}{2}det([S])\right]^{1/3} = \left[\frac{27}{2}(\sigma_1 - \sigma_m)(\sigma_2 - \sigma_m)(\sigma_3 - \sigma_m)\right]^{1/3} \tag{2.3}$$

where $[S]$ is the deviatoric stress tensor,

$$[S] = [\sigma] + p[I], \tag{2.4}$$

$[I]$ is the identity tensor and σ_1, σ_2 and σ_3 denote principal stresses. It is assumed that $\sigma_1 \geq \sigma_2 \geq \sigma_3$. It is convenient to work with the dimensionless hydrostatic pressure η, defined by

$$\eta = \frac{-p}{q} = \frac{\sigma_m}{\bar{\sigma}}. \tag{2.5}$$

The parameter η, often referred to as the triaxiality parameter, has been extensively used in the literature on ductile fracture (McClintock, 1968; Rice and Tracey, 1969; Hancock and Mackenzie, 1976; Mackenzie et al., 1977; Johnson and Cook, 1985; Bao, 2003). The second important parameter is the Lode angle θ, which is related to the normalized third invariant ξ (see Malvern (1969); Xu and Liu (1995), and Abaqus (2005)) through

$$\xi = \left(\frac{r}{q}\right)^3 = \cos(3\theta). \tag{2.6}$$

Since the range of the Lode angle is $0 \leq \theta \leq \pi/3$, the range of ξ is $-1 \leq \xi \leq 1$. The geometrical represent of Lode angle is shown in Fig. 2-1.

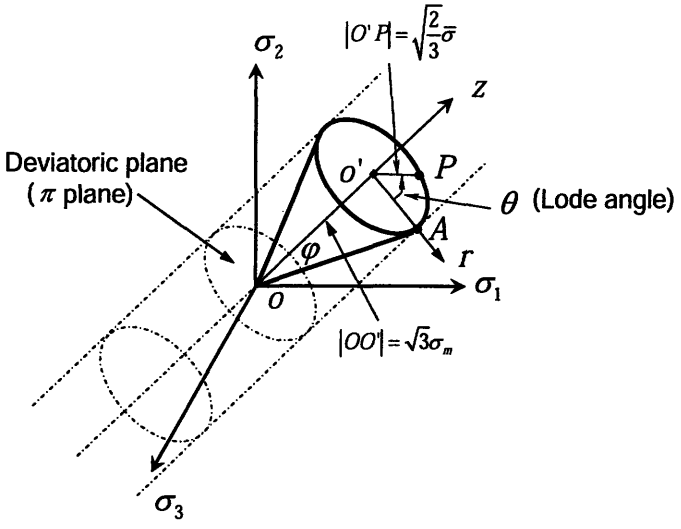

Fig. 2-1: Three types of coordinate system in the space of principal stresses

The stress state at a point in an isotropic material can be defined in three coordinate systems, as shown in Fig. 2-1. The first one is the Cartesian coordinate system $(\sigma_1, \sigma_2, \sigma_3)$, the second one is the cylindrical coordinate system $(\sigma_m, \bar{\sigma}, \theta)$, and the third one is the spherical coordinate system $(\bar{\epsilon}_f, \eta, \theta)$, where the equivalent stress $\bar{\sigma}$ is related to the equivalent strain $\bar{\epsilon}$ through the strain hardening function of a material. The coordinate φ is related to the stress triaxiality η by the following equation,

$$\eta = \frac{\sigma_m}{\bar{\sigma}} = \frac{\sqrt{2}}{3} ctan\varphi. \tag{2.7}$$

Furthermore, the Lode angle can be normalized by

$$\bar{\theta} = 1 - \frac{6\theta}{\pi} = 1 - \frac{2}{\pi} \arccos \xi. \tag{2.8}$$

The range of $\bar{\theta}$ is $-1 \leq \bar{\theta} \leq 1$. The parameter $\bar{\theta}$ will be called the Lode angle parameter hereinafter. Now, all stress directions can be characterized by the above defined set of parameters $(\eta, \bar{\theta})$. It can be shown that $\bar{\theta} = 1$ is corresponding to the axisymmtric tension, $\bar{\theta} = 0$ is corresponding to the plane strain or generalized shear loading condition, and $\bar{\theta} =$

-1 is corresponding to the axisymmtric compression (Wierzbicki and Xue, 2005; Bai and Wierzbicki, 2007a). Special attention is given to the plane stress state. It was shown by Wierzbicki and Xue (2005) that the plane stress condition ($\sigma_3 = 0$) uniquely relates the parameters η and ξ or $\bar{\theta}$ through

$$\xi = cos\left[\frac{\pi}{2}(1-\bar{\theta})\right] = -\frac{27}{2}\eta(\eta^2-\frac{1}{3}). \tag{2.9}$$

In this paper, these two parameters η and $\bar{\theta}$ will be used to describe the stress states and to formulate the fracture locus.

2.1.2 Ductile fracture models and calibration

Equivalent plastic strain to fracture $\bar{\epsilon}_f$ is widely used to characterize material ductility in engineering applications. One of the simplest fracture models is the constant fracture strain model, but it is general accepted that $\bar{\epsilon}_f$ is not constant under different loading conditions. The stress triaxiality, is an important parameter controlling material ductility (Bridgman, 1952; McClintock, 1968; Rice and Tracey, 1969; Johnson and Cook, 1985; Bao, 2003). McClintock (1968), and Rice and Tracey (1969) analyzed the void growth under hydrostatic loading, derived a simple exponential expression for the function $\hat{\epsilon}_f(\eta)$, which will be referred to as a 2-D fracture locus,

$$\bar{\varepsilon}_f = \hat{\varepsilon}_f(\eta) = C_1 e^{-C_2\eta}, \tag{2.10}$$

where C_1 and C_2 are material constants, and typically $C_2 = 1.5$. The models of void growth and their more recent extensions have become the foundation of the modern ductile fracture mechanics (McClintock, 1968; Rice and Tracey, 1969; Mackenzie et al., 1977). Johnson and Cook (1985) integrated the effect of stress triaxiality, strain rate and temperature, into a simple equation of a separable form. This model has become very popular in engineering applications, especially in high velocity impact problems (Teng and Wierzbicki, 2006). Bao (2003); Bao and Wierzbicki (2004a) designed and performed tests on several types of specimens to calibrate the fracture locus in a wide range of the stress triaxiality. He showed that the fracture strain does not have to be a monotonically decreasing function of stress triaxiality (Bao and Wierzbicki, 2005).

All of the above fracture models consider only the effect of stress triaxiality. Introducing the effect of the third stress invariant, a symmetric 3D fracture locus was introduced by Xue and Wierzbicki (Wierzbicki and Xue, 2005; Wierzbicki et al., 2005b; Xue, 2007b), which

is similar to the Wilkins model (Wilkins et al., 1980). Recently, a general 3D asymmetric fracture locus was proposed by the present authors (Bai and Wierzbicki, 2007a). This locus is constructed in the 3D space of equivalent strain to fracture $\bar{\varepsilon}_f$, stress triaxiality η, and the Lode angle parameter $\bar{\theta}$, as shown in the following equation,

$$\begin{aligned}\hat{\varepsilon}_f\left(\eta,\bar{\theta}\right) &= \left[\tfrac{1}{2}\left(\hat{\varepsilon}_f^{(+)}+\hat{\varepsilon}_f^{(-)}\right)-\hat{\varepsilon}_f^{(\circ)}\right]\bar{\theta}^2+\tfrac{1}{2}\left(\hat{\varepsilon}_f^{(+)}-\hat{\varepsilon}_f^{(-)}\right)\bar{\theta}+\hat{\varepsilon}_f^{(\circ)} \\ &= \left[\tfrac{1}{2}\left(D_1e^{-D_2\eta}+D_5e^{-D_6\eta}\right)-D_3e^{-D_4\eta}\right]\bar{\theta}^2+\tfrac{1}{2}\left(D_1e^{-D_2\eta}-D_5e^{-D_6\eta}\right)\bar{\theta}+D_3e^{-D_4\eta}\end{aligned} \tag{2.11}$$

The dependence of the equivalent strain to fracture on the stress triaxiality η is described by an exponential function while the dependence on the Lode angle parameter $\bar{\theta}$ is taken to be parabolic. Altogether, there are six material/fracture constants in the model. In Eq. (2.11), $\hat{\epsilon}_f^{(+)} = D_1e^{-D_2\eta}$ is corresponding to the bounding curve at $\bar{\theta}=1$, $\hat{\epsilon}_f^{(\circ)} = D_3e^{-D_4\eta}$ is corresponding to the bounding curve at $\bar{\theta}=0$, and $\hat{\varepsilon}_f^{(-)} = D_5e^{-D_6\eta}$ is corresponding to the bounding curve at $\bar{\theta}=-1$. The geometrical representation of the new 3D asymmetric fracture locus is shown in Fig. 2-2. The Bao-Wierzbicki fracture locus (Bao and Wierzbicki, 2004a) is a two dimensional projection of the 3D fracture locus under the plane stress condition.

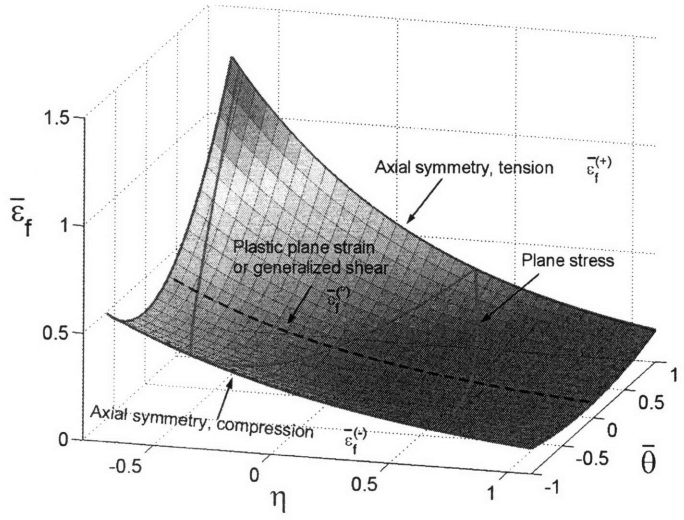

Fig. 2-2: A general 3D fracture locus newly postulated by Bai and Wierzbicki (2007a), see Chapter 3.

For practical application, an effective calibration methods are necessary. Tensile tests on round bar specimens with different notches are commonly used to investigate the effect

of stress triaxiality on fracture strain (Mackenzie et al., 1977; Johnson and Cook, 1985). Bridgman was first to analyze the stress distribution in round bar specimens with different notches (Bridgman, 1952), and derived the formula of stress triaxiality for this type of specimen, see Fig. 2-3.

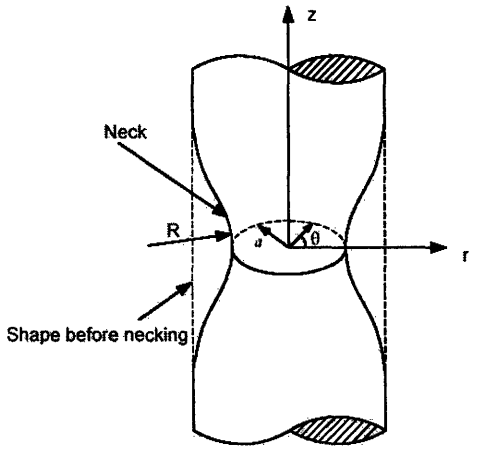

Fig. 2-3: Necking in a round bar specimen

At the center of the necked cross-section, which is the fracture initiation site, Bridgman formula reads

$$\eta = \frac{1}{3} + \ln(1 + \frac{a}{2R}), \tag{2.12}$$

where R is the local radius of a neck in the round bar specimen, and a is the radius of necking cross-section. The uniform equivalent strain at fracture in the necking cross-section of a round bar can be approximately calculated using the following formula.

$$\bar{\varepsilon}_f = 2\ln\left(\frac{a_o}{a_f}\right), \tag{2.13}$$

where a_o is the original radius of the round bar specimen, and a_f is the cross-section radius of round bar specimen at fracture. Eqs. (2.12) and (2.13) are often used to calibrate the material ductility for the Rice-Tracy (Rice and Tracey, 1969) or Johnson-Cook (Johnson and Cook, 1985) fracture models directly from the test results (Hopperstad et al., 2003).

However, there are two unresolved problems when dealing with the calibration method using smooth or notched round bars. One is that the effect of Lode angle parameter on fracture locus has not been accounted for. The range of stress state parameters in smooth or notched round bar specimens is $\eta \geq 1/3$, and $\bar{\theta} = 1$. According to the newly postulated

3D fracture locus, this type of calibration method provides only the value of one bounding curve indicated by $\hat{\epsilon}_f^{(+)}$ in Fig. 2-2. The other two bounding curves, $\hat{\epsilon}_f^{(o)}$ and $\hat{\epsilon}_f^{(-)}$, should be calibrated from other types of tests. Another shortcoming is that it is difficult to machine round specimens for thin metal sheets, which are prevalently used in industrial applications, such as automotive, aerospace and naval industries.

Clausing (1970) performed a comparative experimental study on axisymmetric and plane strain fracture of several materials, and shown that the fracture strain in plane strain condition is much lower than that of axisymmetric ones. Hancock and Brown (1983) performed another comparative experimental and numerical study on round notched bars and flat grooved plane strain specimens, and they found that the difference in Clausing's finding was due to the difference of stress triaxiality between axisymmetric tension and plane strain tension. Hancock and Brown's conclusions will be reexamined in this paper using two other types of material.

In this paper, the stress state and stress triaxiality in a flat grooved plane strain plate specimen is analyzed with the objective to provide additional information on the material ductility. Analytical solution shows that, for flat plane strain specimen without or with notches, the loading conditions are $\eta \geq 1/\sqrt{3}$ and $\bar{\theta} = 0$ because of plane strain condition. Compared with the smooth and notched round bar specimens, the range of stress triaxiality in the same in flat grooved specimens, but the value of $\bar{\theta}$ is different. Thus, this type of specimen will help to study the effect of Lode angle parameter (or the normalized third stress invariant) $\bar{\theta}$ on fracture locus. According to the newly postulated 3D fracture locus, this type of specimen can be used to calibrate the bounding curve $\hat{\epsilon}_f^{(o)}$. What's more, it is especially suitable for fracture tests on thin metal sheets.

2.2 Derivation of stress triaxiality formula for flat grooved plate plain strain specimens

A flat grooved plane strain specimen with the sketch of its cross-section is shown in Fig. 2-4, while photos of real specimens are shown in Fig. 2-12. The thickness of the specimen at the groove is $t = 2a$, and the radius of the groove is R. The thickness direction is y direction. For simplicity, the material is assumed to be rigid-perfect plastic obeying the Huber-Mises yield condition and the associated flow rule. In the Cartesian coordinate system, the equation of equilibrium is

$$\sigma_{ij,j} = 0. \tag{2.14}$$

For plane strain condition (y direction), the following conditions hold,

$$\sigma_{xy} = \sigma_{yz} = 0, \ \frac{\partial}{\partial y}[] = 0, \ and \ \epsilon_{yy} = 0. \tag{2.15}$$

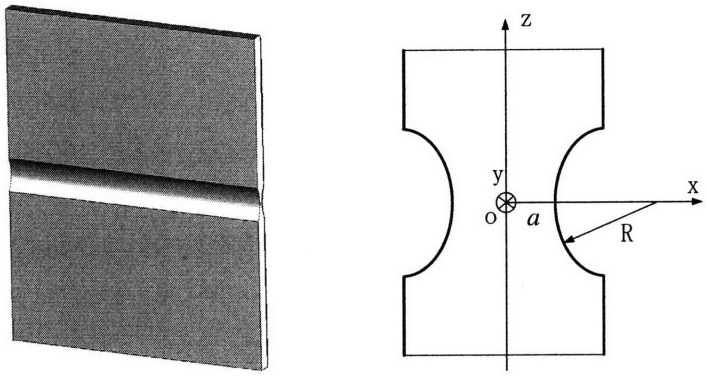

Fig. 2-4: A sketch of a flat grooved plane strain specimen(left), and the cross-section of the specimen (right).

Besides the analysis on necked round specimens in his famous book, Bridgman (1952) also gave the approximate solutions for Eq. (2.14) and (2.15) in a necked plane strain specimen, in which the stress components σ_{xx}, σ_{yy} and σ_{zz} are listed in the following three equations. (The detailed derivation can be found in Appendix A.)

$$\sigma_{xx} = F \ln\left(\frac{a^2 + 2aR - x^2}{2aR}\right), \tag{2.16}$$

$$\sigma_{yy} = F\left[\frac{1}{2} + \ln\left(\frac{a^2 + 2aR - x^2}{2aR}\right)\right], \tag{2.17}$$

$$\sigma_{zz} = F\left[1 + \ln\left(\frac{a^2 + 2aR - x^2}{2aR}\right)\right], \tag{2.18}$$

where F is a constant and can be determined by boundary conditions. Note that shear stress components at the necking cross-section are zero, so the three formulas of normal stress components are also the principal stresses. The next step is to consider the surface point on the notch ($x = a$, $z = 0$) at the neck. The stress state of this point is $\sigma_{xx} = 0$, $\sigma_{zz} = F$, and $\sigma_{yy} = F/2$. Using the von Mises yield condition, the expression of F can be

related to the equivalent stress (von Mises stress) $\bar{\sigma}$.

$$F = \frac{2}{\sqrt{3}}\bar{\sigma} \tag{2.19}$$

Considering the stress state of the central point ($x = 0$, $z = 0$) of the specimen, the mean stress and the stress triaxiality η are given respectively by the following equations.

$$\sigma_m = \frac{1}{3}(\sigma_{xx} + \sigma_{yy} + \sigma_{zz}) = \frac{2}{\sqrt{3}}\bar{\sigma}\left[\frac{1}{2} + \ln\left(1 + \frac{a}{2R}\right)\right] \tag{2.20}$$

$$\eta = \frac{\sigma_m}{\bar{\sigma}} = \frac{\sqrt{3}}{3}\left[1 + 2\ln\left(1 + \frac{a}{2R}\right)\right] = \frac{\sqrt{3}}{3}\left[1 + 2\ln\left(1 + \frac{t}{4R}\right)\right] \tag{2.21}$$

where t is the ligament thickness of the flat specimen. Equation (2.21) implies that the range of stress triaxiality at the center of a plane strain specimen is $\eta \geq 1/\sqrt{3}$. Furthermore, from Eqs. (2.16) , (2.17), (2.18) and Eqs. (2.6), (2.8), one can prove that the Lode angle parameter equals to zero ($\bar{\theta} = 0$).

The equivalent strain to fracture in the necking cross-section of a flat grooved plane strain specimen can be approximately determined using the logarithmic measure of strain,

$$\bar{\varepsilon}_f = \frac{2}{\sqrt{3}}\ln\left(\frac{t_o}{t_f}\right), \tag{2.22}$$

where t_o is the initial ligament thickness of the specimen, and t_f is the fracture ligament thickness of the specimen. This above formula defines the average strain through the cross-section.

2.3 Verification of analytical solution with finite element simulation

Bridgman's formula, Eq. (2.12), is commonly used even though it is only an approximation. Bao (2003); Wierzbicki and Bao revisited this formula using finite element simulation, and proposed a corrected equation with a coefficient $\sqrt{2}$, see Fig. 2-5 and Eq. (2.23).

$$\eta = \frac{1}{3} + \sqrt{2}\ln(1 + \frac{a}{2R}) \tag{2.23}$$

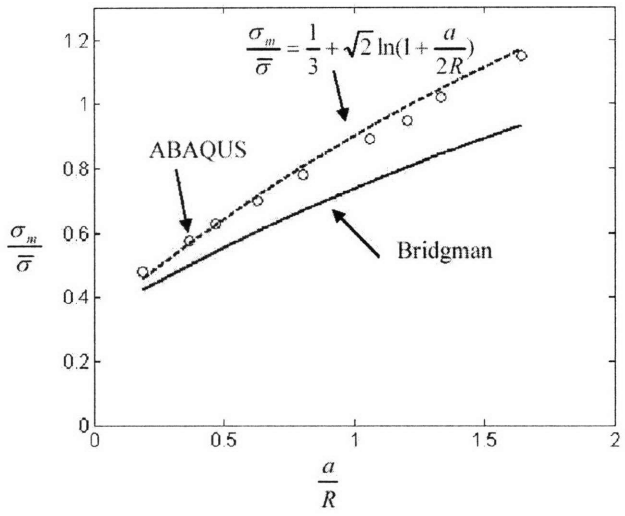

Fig. 2-5: Verification and correction of Bridgman's formula of stress triaxiality in the center of a round notch bar, after Wierzbicki and Bao.

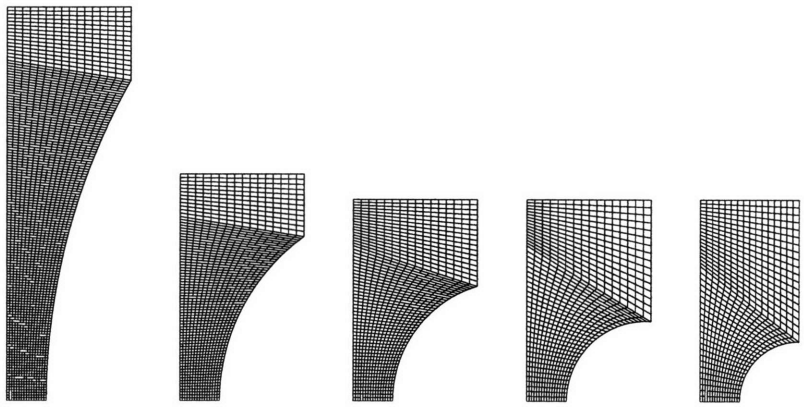

Fig. 2-6: Finite element models of flat grooved specimens with different groove radii.

To verify the formulas derived in Section 2.2, finite element models of the plane strain specimen were developed in Abaqus/Standard. Due to symmetry, only quarter models using plane strain elements were built. Five different ratios of t/R were considered. All the specimens had a constant thickness $t_o = 1.6mm$ at the groove, but the radii of the grooves are equal to 12.7mm, 3.97mm, 2.38mm, 1.59mm and 1.19mm respectively, as shown in Fig.

2-6. As an example, 1045 steel was chosen which exhibits only moderate hardening. The material properties used in the simulation are listed in the Table 2.1.

Table 2.1: Material properties used in the simulation

Density	Possion ratio	Young's Modulus	True stress-strain curve
7.8e+3 Kg/m^3	0.3	2.20e+5 MPa	see Fig. 2-11

From the simulations, the curves of stress triaxiality v.s. equivalent strain for the central elements are obtained for all five cases, as shown in Fig. 2-7. It is found that the stress triaxiality increases as the equivalent plastic strain increases. A comparison of the initial stress triaxiality from the numerical simulations with the values of analytical solution is shown in Fig. 2-8. It is seen that Eq. (2.21) gives a very good prediction of the initial stress triaxiality in the center of flat grooved specimens. The numerical simulation also reveals that the stress triaxiality is only a slowly increasing function of the equivalent plastic strain. This feature shows that the flat grooved specimens are good specimens for fracture calibration.

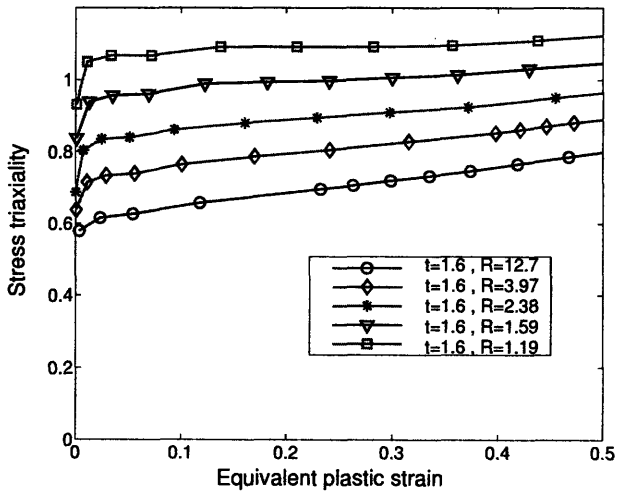

Fig. 2-7: Stress triaxiality v.s. equivalent strain in the center of flat grooved specimens from numerical simulations

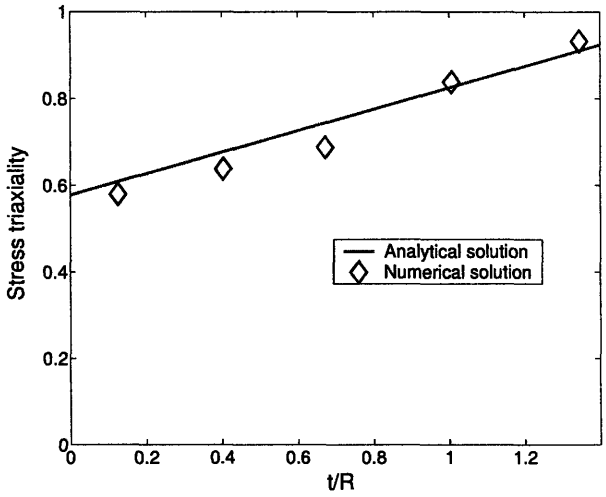

Fig. 2-8: Comparison of initial stress triaxialities from the analytical solution and numerical simulations

2.4 Results for 1045 steel

In this section, comparison will be made between the fracture response of round notched bars and flat grooved specimens on an example of 1045 steel. The objective of this study is to demonstrate the applicability of the flat grooved plate specimen and also to investigate the effect of the Lode angle parameter $\bar{\theta}$ on the fracture locus. All specimens are machined from the rolling direction of the same material block. The tests were conducted on the MTS testing machine, and an optical measurement system was used to measure the local displacement in the specimen's gauge section. The force signal measured by the MTS machine was also synchronously recorded by the optical system. The latter was used to construct the force-displacement curves.

2.4.1 Fracture tests on smooth round bar and notched round bar specimens

According to Eq. (2.12) and (2.23), the stress triaxiality η in the center of a notched round bar is controlled by the parameter a/R. Two values of a/R were assigned to specimens, $a/R = 0$(smooth round bars), and $a/R = 1/3$ (notched round bars). Two specimens of

each ratio of a/R were machined and tested, see Fig. 2-9. Table 2.2 gives a summary of the characteristic dimensions of the specimens both before tests and after tests, from which the initial stress triaxialities and equivalent fracture strain were estimated by the analytical formulas. The force-displacement curves are shown in Fig. 2-10, and the corresponding gauge section length is 20.6 mm. For axial symmetric specimens, the Lode angle parameter $\bar{\theta}$ at the fracture site is constant and equal to unity. Comparing these two tests, one can clearly see the effect of stress triaxiality on the fracture strain under a fixed Lode angle parameter ($\bar{\theta} = 1$). As the stress triaxiality increases, the equivalent fracture strain of the material decreases, as noted by a dozen of authors.

Table 2.2: A summary of the characterized dimensions of the smooth and notched round bar specimens (1045 steel)

Specimen type	Initial diameter (mm)	Fracture diameter (mm)	Notch radius (mm)	Stress triaxiality *	Fracture strain *
D9 - test A	9	7.27	∞	0.3333	0.4269
D9 - test B	9	7.28	∞	0.3333	0.4242
D9 - simulation	9	7.25	∞	0.5044	0.4892
R10.5 - test A	7	6.15	10.5	0.5513	0.2589
R10.5 - test B	7	6.17	10.5	0.5513	0.2542
R10.5 - simulation	7	6.37	10.5	0.8130	0.2312

*For the experimental results, the initial stress triaxialities are directly calculated from tests using Eq. (2.23), and the equivalent fracture strains are also directly calculated from tests using Eq. (2.13). For the simulation results, the fracture initiation sites are at the center of the specimens, and the average stress triaxialities (defined in Eq. (2.25)) are provided.

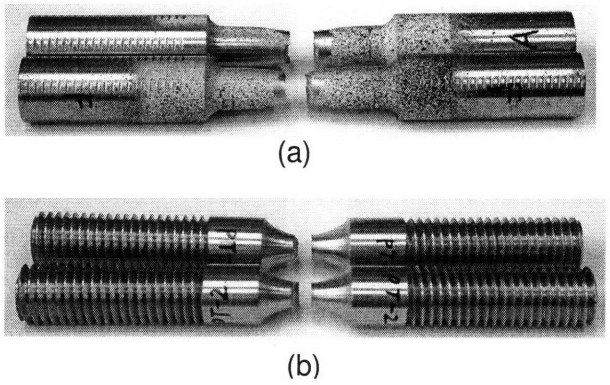

Fig. 2-9: 1045 steel round bar specimens with different notches

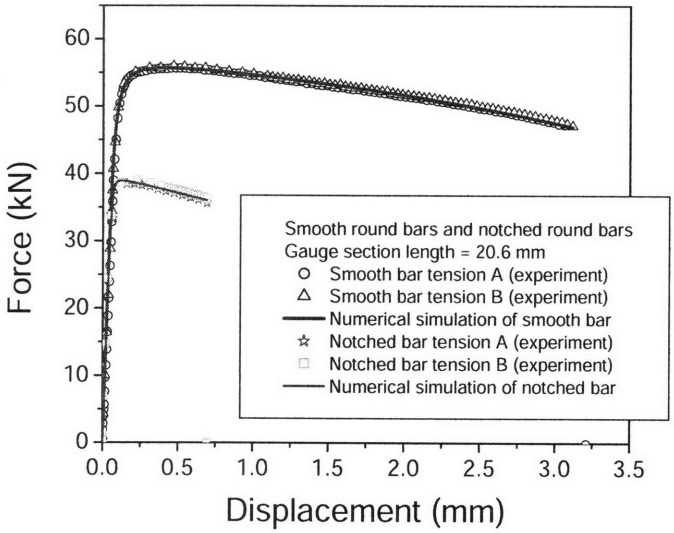

Fig. 2-10: Force displacement response of 1045 steel smooth and notched round bar specimens

Finite element models are built in ABAQUS/Standard to simulate the experiments. For round bar specimens, axisymmetric elements are used. Due to symmetry, only a quarter model was developed. The classical J2 plasticity is used. The stress-plastic strain curve used in the numerical simulations (shown in Fig. 2-11) was calibrated from the smooth round bars tensile test before and also after necking. Other material properties used in the simulations

is shown in Table 2.1.

Comparisons of force-displacement curves between numerical simulations and experimental results are illustrated in Fig. 2-10, from which it is shown that the numerical simulations using the J2 plasticity theory agree well with the experiments. From the simulations, the equivalent fracture strains (corresponding to the measured displacement to fracture) and average stress triaxialities (defined in Eq. (2.25)) are obtained and listed in Table 2.2. The characteristic dimensions of the specimens in the simulations are also listed in Table 2.2, from which it is shown again that Eq. (2.23) and (2.13) give good estimations of the stress triaxiality and the equivalent fracture strain.

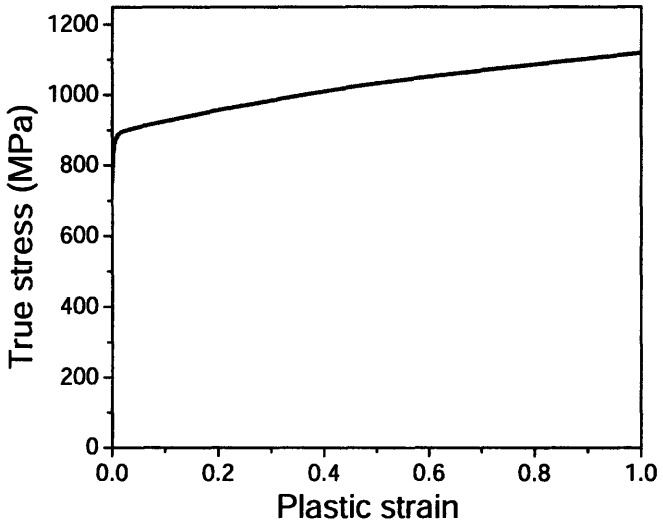

Fig. 2-11: Stress v.s. plastic strain curve of 1045 steel used in numerical simulations

2.4.2 Fracture tests on flat plane strain specimens with grooves

Referring to Eq. (2.21), the stress triaxiality η in the center of a flat grooved specimen is determined by the ratio t/R. Three values of t/R were assigned to specimens, $t/R = 0.1260$, $t/R = 0.4030$, and $t/R = 1.006$. The ligament thicknesses of the specimens at the grooves are all equal to 1.6mm, and the radii of the grooves are equal to 12.7mm, 3.97mm, and 1.59mm. The above values of the groove radii are determined by the availability of machining tools. The plate thicknesses at the specimens shoulder are all equal to 5mm, and the length of gauge section for this group of specimens is 25.9mm. Two specimens of each ratio of t/R

were machined and tested, see Fig. 2-12. Due to machining errors, there are errors on the initial thicknesses of the specimens. Table 2.3 gives a summary of the characteristic dimensions of the specimens both before tests and after tests, from which the initial stress triaxialities and equivalent fracture strain were predicted by Eqs. (2.21) and (2.22). The force-displacement curve of a typical case with the groove notch $R = 3.97mm$ is shown in Fig. 2-14.

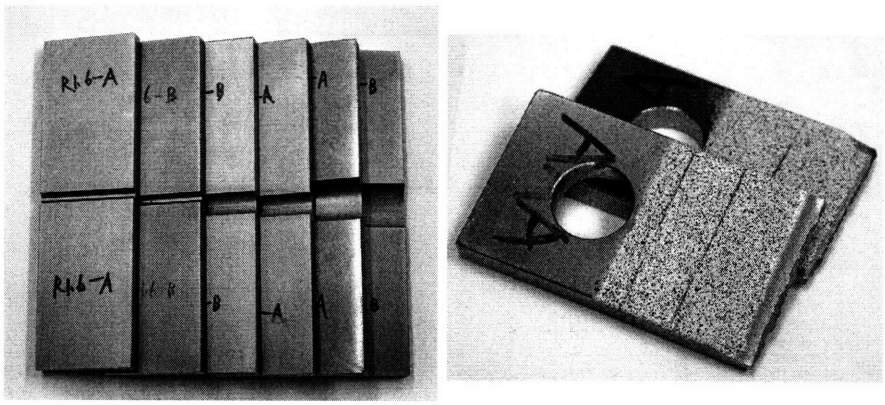

Fig. 2-12: 1045 steel plane strain flat specimens with different notches

Finite element models are built in ABAQUS/Standard to simulate the experiments. The center region of the flat grooved specimens is under plane strain condition, but the two edge region are close to plane stress condition. In order to exactly simulate the experiments, 3-D models are built using 8-node solid elements. Due to symmetries in three planes, only a 1/8 model was developed. The FE model of the case with groove notch $R = 3.97mm$ is shown in Fig. 2-13.

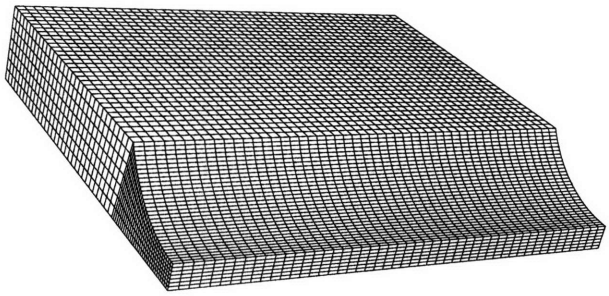

Fig. 2-13: Finite element model of flat grooved specimen, $t = 1.55mm, R = 3.97mm$.

Table 2.3: A summary of the characterized dimensions of the flat grooved specimens (1045 steel)

Specimen type	Initial thickness (mm)	Fracture thickness (mm)	Notch radius (mm)	Stress triaxiality *	Fracture strain *
R12.7 - test A	1.62	1.43	12.7 (1/2")	0.6136	0.1441
R12.7 - test B	1.48	1.32	12.7	0.6105	0.1321
R12.7 - test C	1.28	1.16	12.7	0.6061	0.1137
R12.7-A simulation	1.62	1.39	12.7	0.6705	0.2184
R3.97 - test A	1.55	1.42	3.97 (5/32")	0.6849	0.1011
R3.97 - test B	1.54	1.40	3.97	0.6842	0.1101
R3.97-A simulation	1.55	1.42	3.97	0.7799	0.1765
R1.59- test A	1.60	1.51	1.59 (1/16")	0.8365	0.0669
R1.59- test B	1.71	1.60	1.59	0.8523	0.0768
R1.59-B simulation	1.71	1.62	1.59	1.0237	0.1005

*For the experimental results, the initial stress triaxialities are directly calculated from tests using Eq. (2.21), and the fracture strains are also directly calculated from tests using Eq. (2.22). For the simulation results, the fracture initiation sites are at the center of the specimens, and the average stress triaxialities (defined in Eq. (2.25)) are provided.

Comparison of the force-displacement curve of the case with groove notch $R = 3.97mm$ between numerical simulation and experimental result is illustrated in Fig. 2-14, from which one can see that the numerical simulation agrees with the experiments reasonably well. The equivalent fracture strains and average stress triaxialities (defined in Eq. (2.25)) obtained from numerical simulations are listed in Table 2.3. The geometry dimensions of the specimens in the simulations are also listed in Table 2.3. It can be concluded from Table 2.3 that Eq. (2.21) and (2.22) give good predictions of the stress triaxiality and the equivalent fracture strain of the flat grooved plane strain specimens. For plane strain specimens, the Lode angle parameter $\bar{\theta}$ at the fracture site is constant and equal to zero.

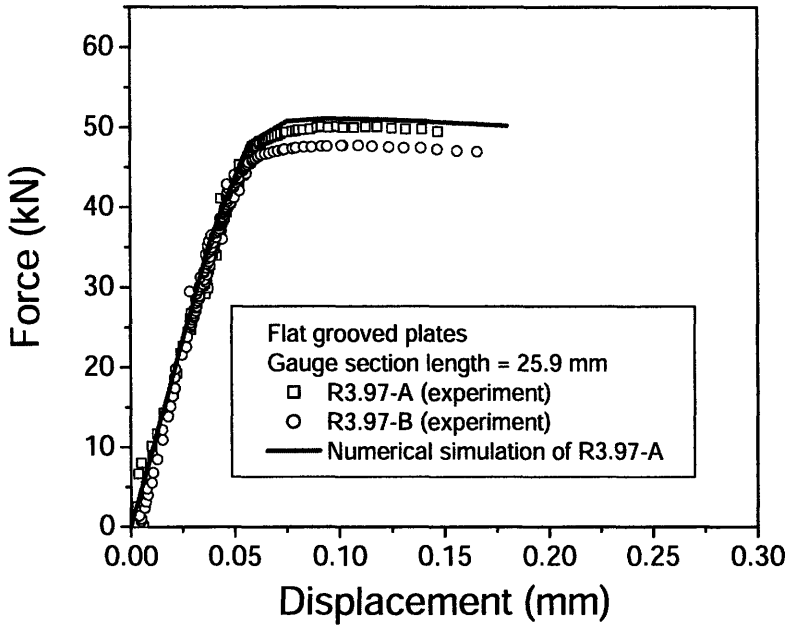

Fig. 2-14: Force displacement response of 1045 steel plane strain flat specimens with groove notch = 3.97mm

2.4.3 Fracture tests on tubular specimens in torsion

Torsion tests were conducted using Lindholm type tubular specimen (Lindholm et al., 1980; White et al., 1990). The dimensions of the specimens is shown in Fig. 2-15. Two torsional tests were conducted under quasi-static loading with zero axial force (see Fig. 2-16). The loading velocity was $0.028°/s$. In order to hold the specimen tightly, two plug-in aluminum cylinders were placed inside the two ends of the tubing specimen during the tests. The measured torque-rotation curves are shown in Fig. 2-17, from which the average rotation angle to fracture is found to be $\Delta\phi_f = 20° = 0.3491 rad$. The equivalent strain to fracture can be estimated,

$$\bar{\varepsilon}_f = \frac{r\Delta\phi_f}{\sqrt{3}L_o} = \frac{9.5 \times 0.3491}{\sqrt{3} \times 4} = 0.48. \tag{2.24}$$

The fracture initiation site was on the outer surface and around the corner, see Fig. 2-16. Because the torsion fracture is a pure shear condition, the two stress state parameters are equal to zero, $\eta = \bar{\theta} = 0$.

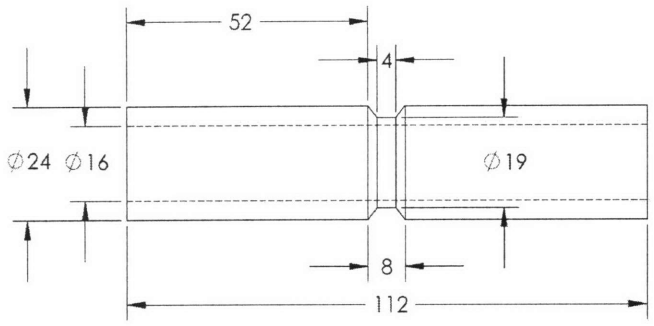

Fig. 2-15: Dimension of torsional tubing specimens.

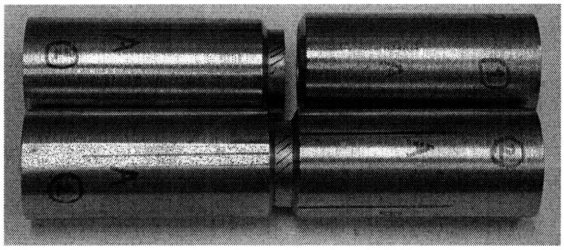

Fig. 2-16: Two torsional tubing specimens after fracture.

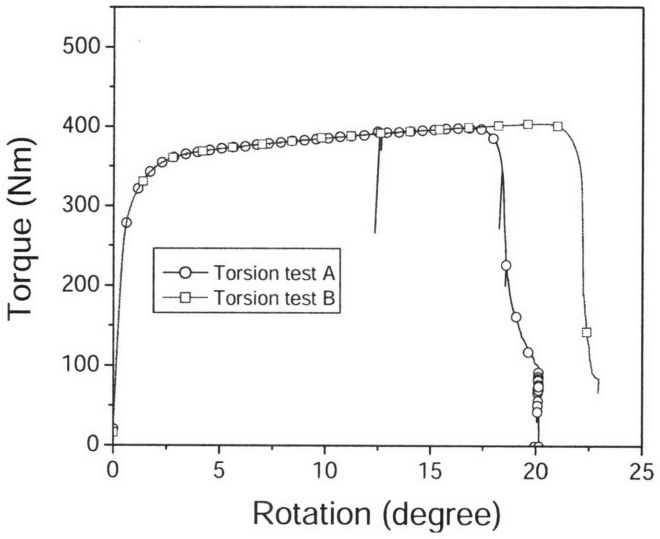

Fig. 2-17: The torque-rotation curves of tubes under torsional loading.

2.4.4 Summary of results of 1045 steel

From the experimental results in Sections 2.4.1 and 2.4.2, the fracture loci can be constructed in the space of stress triaxiality and equivalent strain to fracture. The input data to construct such plots are listed in Table 2.2 and 2.3. These two groups of specimens deformed and fractured under different values of $\bar{\theta}$, therefore, plotting these two fracture loci together will give a direct understanding of the applicability of flat grooved plate specimen to calibrate fracture locus. The results are shown in Fig. 2-18. The data points with the same value of $\bar{\theta}$ are fitted using modified Rice-Tracey type exponential function, Eq. (2.10).

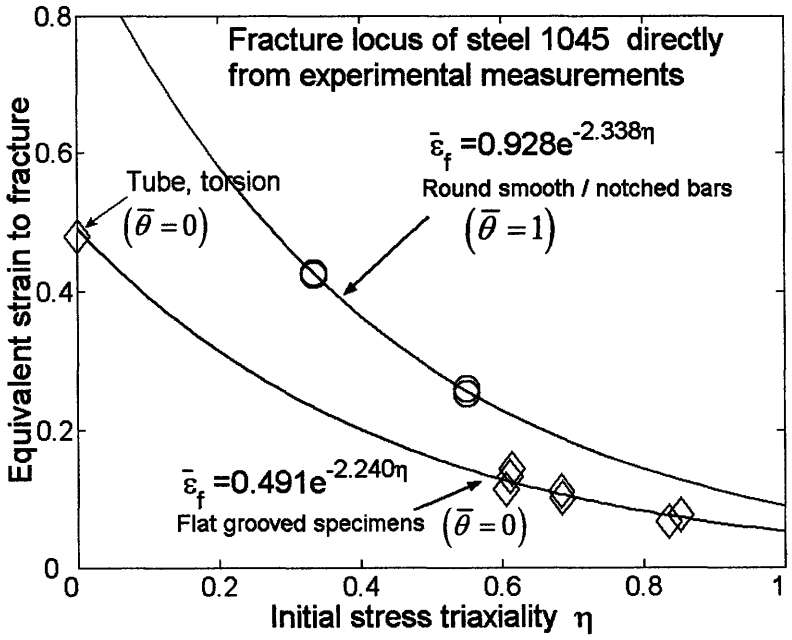

Fig. 2-18: Comparison of the fracture loci of 1045 steel measured from two groups of classical specimen in the plane of equivalent strain to fracture and *initial* stress triaxiality, which clearly shows the effect of Lode angle of ductile fracture locus.

If the data point on the torsion test, described in Section 2.4.3, is added in Fig. 2-18, then it is very interesting to find that the data point of torsion test lies exactly on the bound limit calibrated from the flat grooved specimens. The reason is that the Lode angle parameter in a torsion test is equal to zero ($\bar{\theta} = 0$), which is the same as plane strain tension tests. The following partial conclusions can be drawn from the above tests and analysis on 1045 steel.

- Ductility of both flat grooved specimen and round notched bars are diminishing in an exponential manner with stress triaxiality.

- The fracture bounding curve corresponding to flat grooved specimens and tubular specimens $\hat{\epsilon}_f^{(o)}$ is far below the bounding curve representing round bar specimens $\hat{\epsilon}_f^{(+)}$.

- The Lode angle parameter $\bar{\theta}$ has an important effect on the fracture locus

- The fracture loci shown in Fig. 2-18 were constructed on the basis of the closed-form solutions and the experimental data. No numerical simulation was needed to locate the fracture points on the 2D $(\bar{\epsilon}_f, \eta)$ plane. This method is referred to as a *direct method* of constructing the fracture locus.

An alternative method of constructing the fracture locus was developed by Bao (2003); Bao and Wierzbicki (2004a) using numerical simulation. From the numerical simulation, the histories of stress triaxiality and equivalent plastic strain are obtained, see Fig. 2-19. Since the stress triaxiality changes in the tests, a concept of average stress triaxiality, defined by Eq. (2.25), was used.

$$\eta_{av} = \frac{1}{\bar{\epsilon}_f} \int_0^{\bar{\epsilon}_f} \eta\left(\bar{\epsilon}\right) d\bar{\epsilon}. \tag{2.25}$$

The equivalent strain to fracture is defined as the strain corresponding to the measured displacement to fracture. The material's fracture locus constructed on the space of average stress triaxiality and equivalent strain to fracture, using the above inverse method, is shown in Fig. 2-19. The values of data points obtained from numerical simulations are also listed in Table 2.2 and 2.3. Again, those data points are fitted using an exponential function. Note that the values of parameters c_1 and c_2 of Eq. (2.10) are different in curve fitting using both methods.

From the analysis of data gathered in Table 2.2 and 2.3, one can see that the magnitudes of the equivalent strain to fracture in the "direct" and inverse method are similar. This means that the distribution of strain over the cross-section of round and flat specimens is almost uniform. At the same time, the initial and average stress triaxiality are different which could be expected from the analysis of Fig. 2-7. A comparison of fracture loci obtained by means of "direct" and inverse method is shown in Fig. 2-20. This difference was also noted by Borvik et al. (2003). Special attentions should be paid when the calibrated fracture loci are used to predict fractures.

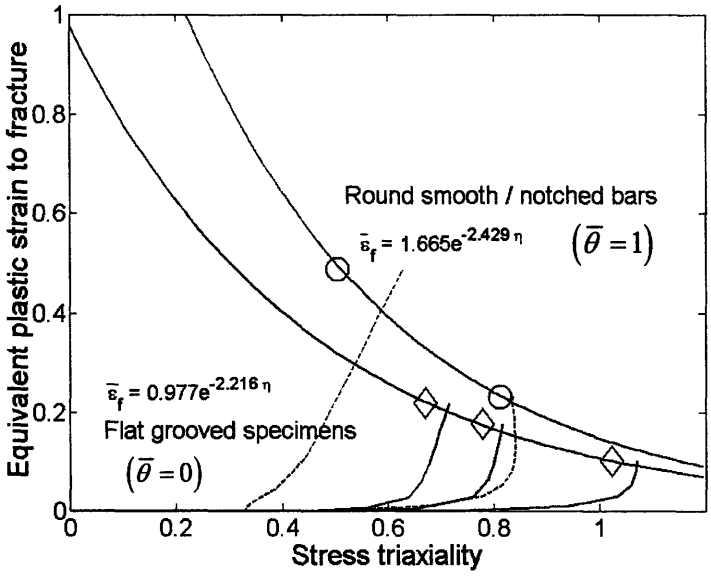

Fig. 2-19: Fracture locus of steel 1045 from numerical simulations using *average* stress triaxiality

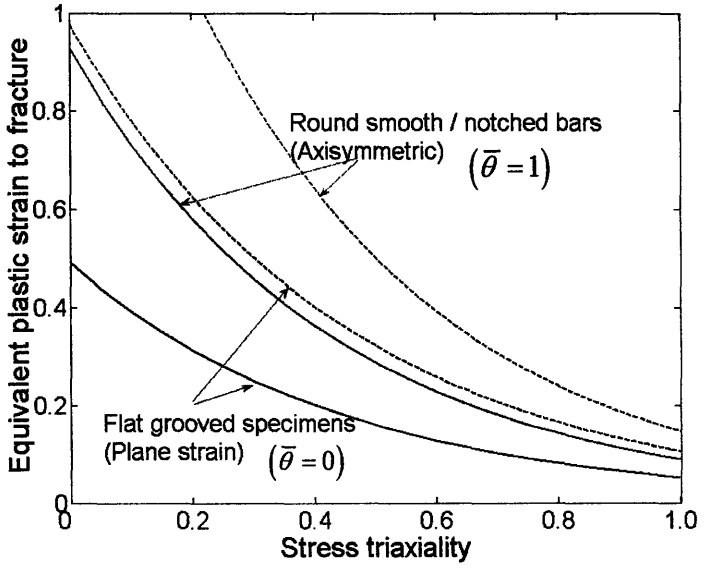

Fig. 2-20: A comparison of fracture loci constructed on the basis of the *initial* stress triaxiality (direct method, solid line) and average triaxiality (inverse method, dash line)

2.5 Results for DH36 steel

The above partial conclusion refers to fracture properties of 1045 steel. Indeed, additional study on DH36 steel tells a different story. Another round of tests and simulations was conducted on DH36 steel. All the specimens were cut and machined from a 3/8" (9.5mm) thick metal sheet. It is easier to machine flat grooved specimen than to make round notched ones from the metal sheets, but mini-size smooth and notched bars were also machined and tested to compare. The calibrated fracture loci obtained from experiments using the direct method are shown in Fig. 2-21, and the results from numerical simulations are shown in Fig. 2-22. It is found that, for DH36 steel, the effect of the Lode angle parameter $\bar{\theta}$ on the fracture locus is very weak in high stress triaxiality region, so the fracture loci calibrated from two types of specimen are almost identical. This is similar to the test results reported by Hancock and Brown (1983) on other materials. It is also noted that the present material, DH36 steel, is very ductile and deep neck develops before fracture. As a result, fracture loci determined on the basis of the initial and average stress triaxiality are remarkably different.

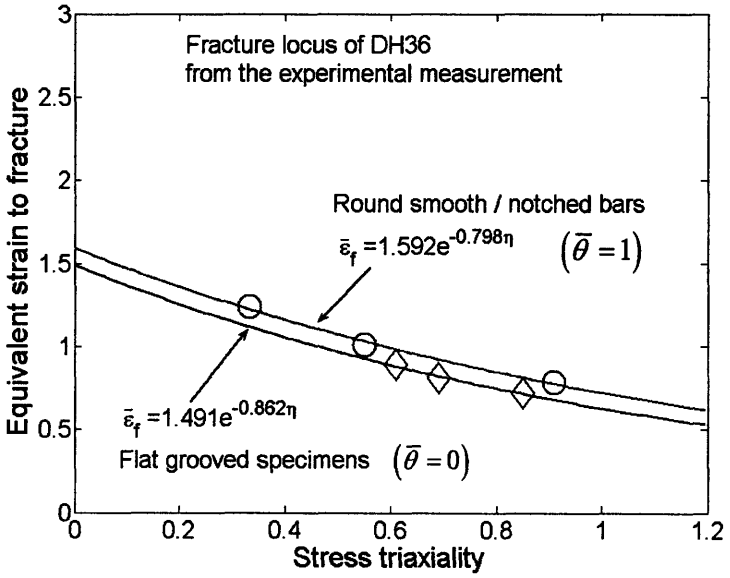

Fig. 2-21: Fracture locus of DH36 steel from experimental measurements using *initial* stress triaxiality

Although the effect of Lode angle parameter $\bar{\theta}$ on the fracture locus of DH36 steel is

weak, another interesting phenomenon is the effect of the Lode angle parameter $\bar{\theta}$ on metal plasticity. It is found that, for DH36 steel ,the stress-strain curve calibrated from the smooth round bar tensile test can not predict the force-displace response in the tests of flat grooved plane strain specimen. This shows that the classical J2 plasticity needs to be modified by including the Lode angle effect to get accurate predictions for some materials (Bai and Wierzbicki, 2007a,b).

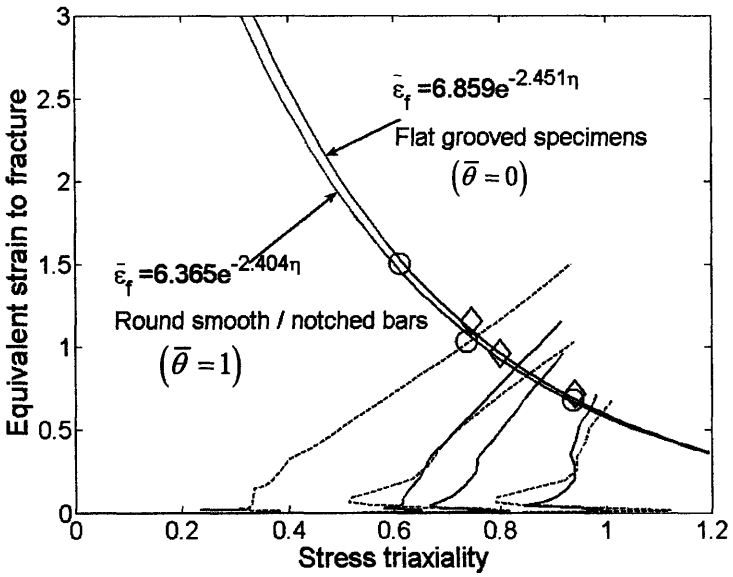

Fig. 2-22: Fracture locus of DH36 steel from numerical simulations using *average* stress triaxiality

2.6 Discussion and conclusion

The stress state inside a notch of a flat grooved plate plane strain specimen is analyzed. A Bridgman-like closed-form solution is obtained for the stress triaxiality of a flat grooved specimen. Finite element simulations has validated the accuracy of the newly derived formula. Test results of 1045 steel and DH36 steel proved the applicability of this type of specimen and the stress triaxiality formula to calibrate the effect of stress triaxiality on the fracture locus. Traditionally, the fracture locus is calibrated from smooth and notched round bars. Furthermore, the test results on DH36 steel showed that flat grooved specimens are

especially suitable for testing thin sheet metals.

The range of stress triaxiality in round notched bars and flat grooved specimens is similar, but values of the normalized third stress invariant or Lode angle parameter $\bar{\theta}$ are different. This feature makes the flat grooved plane strain specimens very suitable for studying the effect of Lode angle parameter, $\bar{\theta}$, on the fracture locus. The new test results on 1045 steel shows that the fracture locus is in fact a surface in the space of $(\bar{\epsilon}_f, \eta, \bar{\theta})$ rather than a single curve on the plane of $(\bar{\epsilon}_f, \eta)$. Accordingly, a general 3D fracture locus was introduced by Bai and Wierzbicki (2007a). These two types of specimens can be used to calibrate two bounding curves, $\hat{\epsilon}_f^{(+)}$, and $\hat{\epsilon}_f^{(\circ)}$ as shown in Fig. 2-2. If a symmetric fracture locus is assumed, $\hat{\epsilon}_f^{(+)} = \hat{\epsilon}_f^{(-)}$, then the 3D fracture loci of these two materials, 1045 steel and DH36 steel, can be plotted in Fig. 2-23.

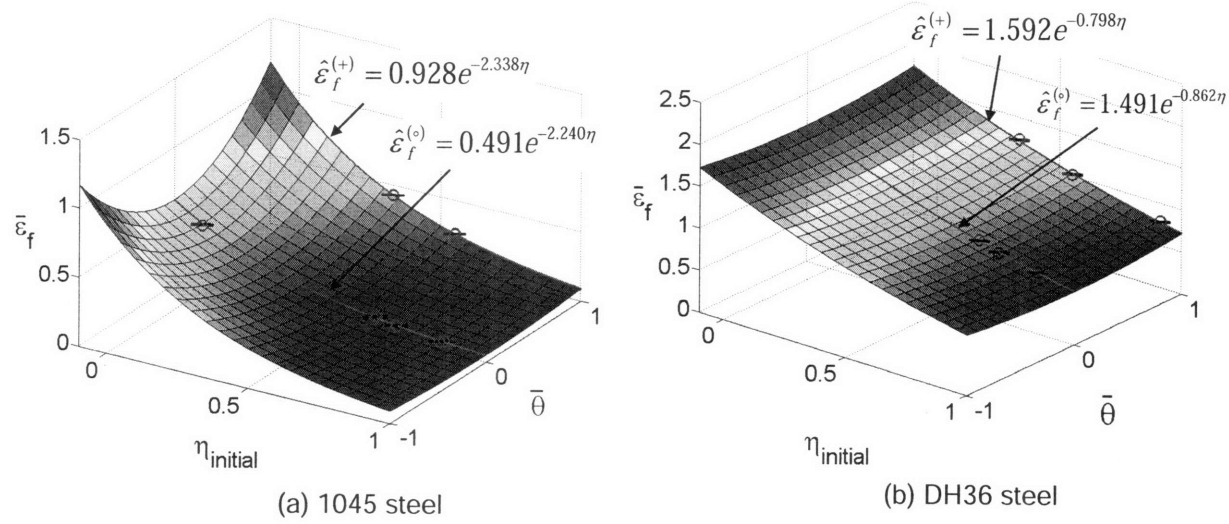

(a) 1045 steel (b) DH36 steel

Fig. 2-23: 3D fracture loci of 1045 steel and DH36 steel, data from experimental measurements, assuming symmetric fracture locus $(\hat{\epsilon}_f^{(+)} = \hat{\epsilon}_f^{(-)})$.

To experimentally calibrate the third bounding curve $\hat{\epsilon}_f^{(-)}$, upsetting tests and/or equibiaxial tension tests are suggested. It should also be noted that the tensile tests cover only the high stress triaxiality region, other types tests are need to get fracture data points for low stress triaxiality region. Every material needs comprehensive calibration to get the 3D fracture locus. For example, according to the present study and results reported by Hancock and Brown (1983), fractures of some materials such as DH36 steel are not affected by the Lode angle parameter (see Fig. 2-23(b)). It is worthy to mention that this flat grooved

specimen can also be used to study the effect of Lode angle parameter on metal plasticity, as explained by Bai and Wierzbicki (2007a), which is included in Chapter 3.

Chapter 3

A New Model of Metal Plasticity and Fracture with Pressure and Lode Dependence

Classical metal plasticity theory assumes that the hydrostatic pressure has no or negligible effect on the material strain hardening, and that the flow stress is independent of the third deviatoric stress invariant (or Lode angle parameter). However, recent experiments on metals have shown that both the pressure effect and the effect of the third deviatoric stress invariant should be included in the constitutive description of the material. A general form of asymmetric metal plasticity, considering both the pressure sensitivity and the Lode dependence, is postulated. The calibration method for the new metal plasticity is discussed. Experimental results on aluminum 2024-T351 are shown to confirmed the new material model.

From the similarity between yielding surface and fracture locus, a new 3D asymmetric fracture locus, in the space of equivalent fracture strain, stress triaxiality and the Lode angle parameter, is postulated. Two methods of calibration of the fracture locus are discussed. One is based on classical round specimens and flat specimens in uniaxial tests, and the other one uses the newly designed butterfly specimen under biaxial testing. Test results of Bao (2003) on aluminum 2024-T351, and test data points of A710 steel from butterfly specimens under biaxial testing are used to validate the postulated asymmetric 3D fracture locus.

3.1 Introduction

The classical J2 theory of metal plasticity assumes that the effect of hydrostatic pressure σ_m on plastic flow is negligible, and further assumes that the flow stress is independent of the third stress invariant of the stress deviator. For application to ductile fracture, these assumptions must be carefully examined. Ductile fracture is a local phenomenon and the state of stress and strain in potential fracture locations must be determined with great accuracy. Fracture initiation is often preceded by large plastic deformation and there are considerable stress and strain gradients around the point of fracture. In these situations, the infinitesimal J2 theory of plasticity is not accurate enough, and more refined plasticity models has to be introduced.

The soil and rock mechanics community has long recognized a need for incorporating the hydrostatic and deviatoric (Lode angle parameter) stress invariants into a constitutive descriptions (see for example (Bardet, 1990; Menetrey and Willam, 1995)). More recently Bigoni and Piccolroza (2003) proposed a general failure surface for geomaterials in the space of principal stresses that reduces in limiting cases to the Tresca hexagon or the von Mises circle. The Sandia GeoModel (Fossum and Brannon, 2006) is also formulated in the space of three invariants. The developments in geomaterials was proceeding over the decades independently of metal plasticity with the latter lagging behind the former.

Based on an extensive experimental study, Richmond and Spitzig (Richmond and Spitzig, 1980; Spitzig and Richmond, 1984) were first to demonstrate the effect of hydrostatic pressure on yielding of aluminum alloys. This conclusion has recently been confirmed by Wilson (2002), who studied notched 2024-T351 aluminum bars in tension. The concept of a shrinking yield surface with hydrostatic pressure was put forward independently by Gurson (1975) and later by Needleman and Tvergaard (1984) in their studies of ductile fracture by the nucleation, growth and coalescence of voids. The common shortcoming of these various theories of porous plasticity has been an ill-defined calibration procedure.

In general, the hydrostatic pressure is controlling the size of the yield surface while the Lode angle parameter is responsible for its shape. The determination of an adequate shape of the yield surface has become an issue in the sheet metal forming industry. It was found a long time ago that the von Mises plane stress ellipse does not lead to a correct prediction of the necking instability. There are an abundance of various modifications and generalizations of the plane stress yield curve to bring the prediction closer to reality (Karafillis and Boyce, 1993; Barlat et al., 1997, 2005; Vegter and van den Boogaard, 2006). However, most of the above theories included the effect of an in-plane anisotropy and the connection between the

shape of yield condition and the Lode angle parameter remained unnoticed.

The paper is divided into two parts. The first part is concerned with a development of a more general plasticity model. Results of 21 tests on three groups of specimens are analyzed through a finite element simulation. It is shown that the parameters of the J2 plasticity model with power hardening rule, determined from one test, can not predict correctly the load-displacement responses in the all remaining tests. A new plasticity model with correction for the hydrostatic pressure and the Lode parameter brings a perfect correlation with test results. Percentage-wise, the correction for the hydrostatic pressure is small. Physically, it could be attributed to the effect of hydrostatic pressure on metal crystal dislocations. The magnitudes of correction due to the deviatoric state parameter (Lode angle parameter) is large and in some cases reaches 20%. The effect of hydrostatic pressure is consistent with earlier finding of other authors (Richmond and Spitzig, 1980; Spitzig and Richmond, 1984; Wilson, 2002). The new yield surface is asymmetric in the space of principal stresses losing three planes of symmetry as compared to the Tresca yield condition with six plane of symmetry, so it is asymmetric in any of the Tresca's six symmetry planes.

The second part of the paper deals with the determination of the 3-D locus of the fracture initiation points. The locus is determined experimentally from two types of test procedures. One is based on classical round specimens or flat specimens in uniaxial tests, and the other one uses a series of tests on a double curvature butterfly specimen subjected to bi-axial loading under different combination of tension/shear and compression/shear. The test points are then fitted to a smooth surface which describes the dependence of the equivalent strain to fracture on the average stress triaxiality and the normalized third invariant of the deviatoric stress tensor (or Lode angle parameter). Again, it is shown that the best fit of test data is provided by a surface which is asymmetric with respect to the Lode angle parameter.

3.2 Characterization of the stress state

The extended metal plasticity model and the 3-D fracture locus will be formulated in terms of three invariants of the stress tensor $[\sigma]$, defined respectively by

$$p = -\sigma_m = -\frac{1}{3} tr([\sigma]) = -\frac{1}{3}(\sigma_1 + \sigma_2 + \sigma_3) \tag{3.1}$$

$$q = \bar{\sigma} = \sqrt{\frac{3}{2}[S] : [S]} = \sqrt{\frac{1}{2}[(\sigma_1 - \sigma_2)^2 + (\sigma_2 - \sigma_3)^2 + (\sigma_3 - \sigma_1)^2]} \tag{3.2}$$

$$r = \left(\frac{9}{2}[S]\cdot[S]:[S]\right)^{1/3} = \left[\frac{27}{2}det([S])\right]^{1/3} = \left[\frac{27}{2}(\sigma_1-\sigma_m)(\sigma_2-\sigma_m)(\sigma_3-\sigma_m)\right]^{1/3} \tag{3.3}$$

where $[S]$ is the deviatoric stress tensor,

$$[S] = [\sigma] + p[I], \tag{3.4}$$

$[I]$ is the identity tensor and σ_1, σ_2 and σ_3 denote principal stresses. Note that the parameter p is positive in compression, but σ_m is positive in tension. It is convenient to work with the dimensionless hydrostatic pressure η, defined by

$$\eta = \frac{-p}{q} = \frac{\sigma_m}{\bar{\sigma}}. \tag{3.5}$$

The parameter η, often referred to as the triaxiality parameter, has been extensively used in the literature on ductile fracture (McClintock, 1968; Rice and Tracey, 1969; Hancock and Mackenzie, 1976; Mackenzie et al., 1977; Johnson and Cook, 1985; Bao, 2003). The second important parameter is the Lode angle θ. The geometrical represent of Lode angle is shown in Fig. 2-1. The Lode angle θ is related to the normalized third deviatoric stress invariant ξ (see Malvern (1969); Xu and Liu (1995)) through

$$\xi = \left(\frac{r}{q}\right)^3 = \cos(3\theta). \tag{3.6}$$

Since the range of the Lode angle is $0 \le \theta \le \pi/3$, the range of ξ is $-1 \le \xi \le 1$. Furthermore, the Lode angle θ can be normalized by

$$\bar{\theta} = 1 - \frac{6\theta}{\pi} = 1 - \frac{2}{\pi}\arccos\xi. \tag{3.7}$$

The range of $\bar{\theta}$ is $-1 \le \bar{\theta} \le 1$. The parameter $\bar{\theta}$ will be called the Lode angle parameter hereinafter. Now, all stress directions (or called loading conditions) can be characterized by the above defined set of parameters $(\eta, \bar{\theta})$. Various stress states encountered in "classical" specimens used for plasticity and fracture testing can be uniquely characterized by the above defined set of parameters $(\eta, \bar{\theta})$, as shown in Table 3.1. The analytical expressions for the stress triaxiality η, the parameter $\bar{\theta}$ in terms of measurable quantities are all listed in Table 3.1.

Table 3.1: Ten types of classical specimens for plasticity and fracture calibration

No.	Specimen type	Analytical value or formula of stress triaxiality η^*	The Lode angle parameter $\bar{\theta}$	Analytical formula of fracture strain $\bar{\varepsilon}_f{}^*$
1	Smooth round bars, tension	$\frac{1}{3}$	1	$2\ln\left(\frac{a_o}{a_f}\right)$
2	Notched round bars, tension (Bridgman, 1952)	$\frac{1}{3}+\sqrt{2}\ln(1+\frac{a}{2R})$	1	$2\ln\left(\frac{a_o}{a_f}\right)$
3	Plastic plane strain, tension	$\frac{\sqrt{3}}{3}$	0	$\frac{2}{\sqrt{3}}\ln\left(\frac{t_o}{t_f}\right)$
4	Flat grooved plates, tension (Bai et al., 2006b)	$\frac{\sqrt{3}}{3}\left[1+2\ln\left(1+\frac{t}{4R}\right)\right]$	0	$\frac{2}{\sqrt{3}}\ln\left(\frac{t_o}{t_f}\right)$
5	Torsion or shear	0	0	$\frac{\Delta\phi_f a_o}{\sqrt{3}L_o}$
6	Cylinders, compression	$-\frac{1}{3}$	-1	$2\ln\left(\frac{a_f}{a_o}\right)$
7	Equi-biaxial tension	$\frac{2}{3}$	-1	$2\ln\left(\frac{d_f}{d_o}\right)$
8	Equi-biaxial compression	$-\frac{2}{3}$	1	$2\ln\left(\frac{d_o}{d_f}\right)$
9	Plastic plane strain, compression	$-\frac{\sqrt{3}}{3}$	0	$\frac{2}{\sqrt{3}}\ln\left(\frac{t_f}{t_o}\right)$
10	Notched round bars, compression Bridgman (1952)	$-\left[\frac{1}{3}+\sqrt{2}\ln(1+\frac{a}{2R})\right]$	-1	$2\ln\left(\frac{a_f}{a_o}\right)$

*In the above table, R is the radius of a notch or a groove, a is radius of a round bar at the notch or the outer radius of a torsional specimen, a_o is the initial radius, a_f is the radius at fracture, t is thickness of a flat grooved plat at the groove, t_o is the initial thickness, t_f is the thickness at fracture, L_o is the initial gauge length of a torsional specimen, $\Delta\phi_f$ is angular displacement to fracture of a torsional specimen, d_o is the initial grid spacing of an equi-biaxial testing specimens, and d_f is the corresponding spacing to fracture.

Special attention is given to the plane stress state. It was shown by Wierzbicki and Xue (2005) that the condition $\sigma_3 = 0$ uniquely relates the parameters η and ξ (or $\bar{\theta}$) through

$$\xi = cos\left[\frac{\pi}{2}(1-\bar{\theta})\right] = -\frac{27}{2}\eta(\eta^2-\frac{1}{3}). \tag{3.8}$$

A plot of Eq. (3.8) is shown in Fig. 3-1. Points corresponding to ten types of "classical"

specimens and tests are marked by circles. The function $\bar{\theta}$ (Eq. (3.8)) has three roots corresponding to pure shear ($\eta = 0$, $\bar{\theta} = 0$) and the transverse plastic plane strain ($\eta = \pm\frac{1}{\sqrt{3}}$, $\bar{\theta} = 0$).

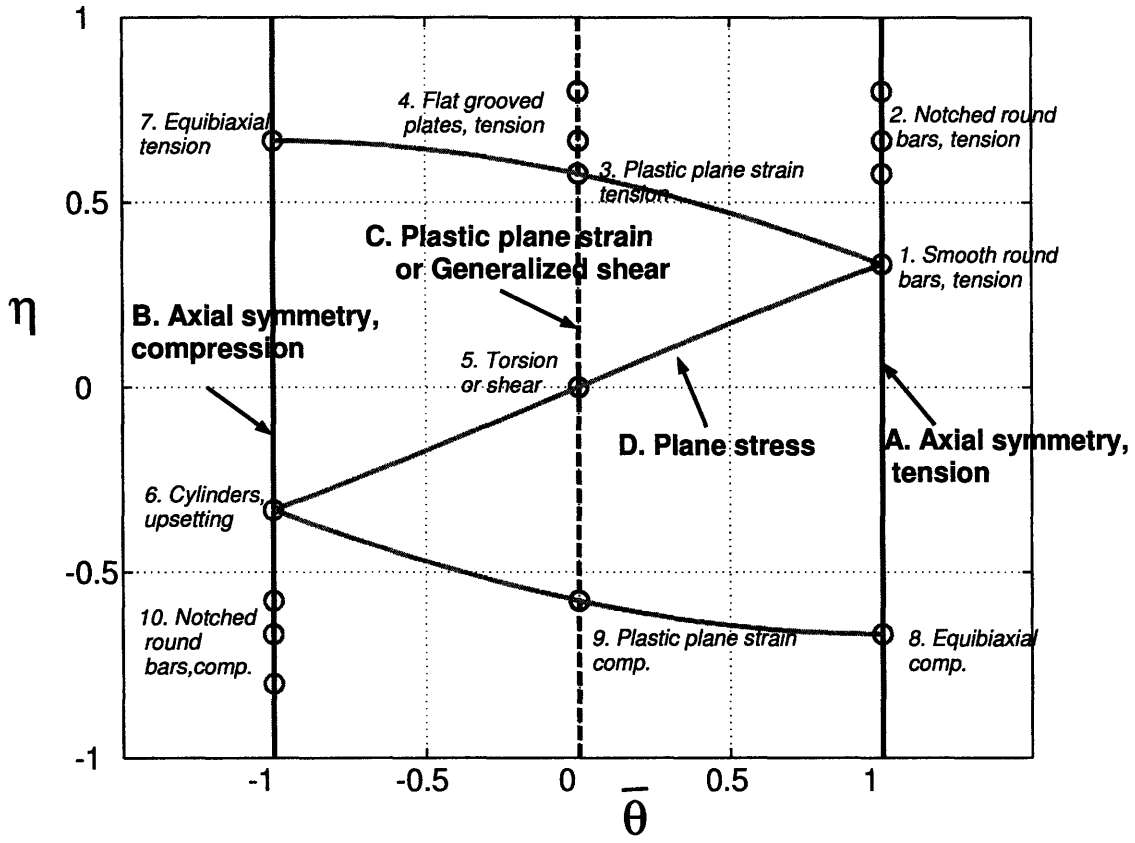

Fig. 3-1: Conceptual representation of the initial stress states on the plane of η and $\bar{\theta}$

3.3 A new form of metal plasticity

The plasticity theory to be developed in this section is valid under several assumptions. Firstly, the homogeneity and material isotropy are assumed. Secondly, the material is taken to be elastic-plastic with isotropic hardening. The extension to the combined isotropic/kinematic hardening could be made following the procedures suggested by Khan (for example Khan and Jackson (1999)). Finally, the plastic incompressibility is assumed.

3.3.1 Effect of hydrostatic pressure on yield

The concept of pressure dependent yield condition goes back to Coulomb-Mohr, and Drucker and Prager (1952). This concept, originally developed for soil and granular materials, was shown more recently in a number of publications (Richmond and Spitzig, 1980; Brownrigg et al., 1983; Spitzig and Richmond, 1984) to be applicable to metal plasticity. According to the above theories, the initial and current yield function is taken in this paper to be a linear function of the normalized pressure, η,

$$\sigma_{yld} = \bar{\sigma}(\bar{\varepsilon}_p) - \alpha I_1 = \bar{\sigma}(\bar{\varepsilon}_p)\left[1 - \frac{3\alpha\sigma_m}{\bar{\sigma}(\bar{\varepsilon}_p)}\right] = \bar{\sigma}\left(\bar{\varepsilon}_p\right)(1 - 3\alpha\eta)\,, \tag{3.9}$$

where $I_1 = 3\sigma_m$ and $\bar{\varepsilon}_p$ is the equivalent plastic strain. The proportionality parameter α should be calibrated from tests. In Eq. (3.9), the first strain hardening term, $\bar{\sigma}(\bar{\varepsilon}_p)$, represents the stress-strain curve in zero hydrostatic pressure, for example in the torsion test. In practice, tensile tests of a smooth round bar or a dogbone specimen are very commonly used to calibrate the stress-strain curve. Therefore, more generally, Eq. (3.9) can be rewritten as

$$\sigma_{yld} = \bar{\sigma}\left(\bar{\varepsilon}_p, \eta_o\right)\left[1 - 3\alpha\left(\eta - \eta_o\right)\right] = \bar{\sigma}\left(\bar{\varepsilon}_p\right)\left[1 - c_\eta(\eta - \eta_o)\right], \tag{3.10}$$

where $\bar{\sigma}(\bar{\varepsilon}_p)$ is material strain hardening function from the reference test, and η_o is the reference value of stress triaxiality from the reference test, for example, $\eta_o = 1/3$ for smooth round bar tensile test, $\eta_o = -1/3$ for cylindrical specimen compressive test, $\eta_o = 0$ for torsion test and so on. Here, c_η is a material constant need to be calibrated, which represents the hydrostatic pressure effect on material plasticity. It should also be noted that the effect of pressure on plasticity does not have to be linear. Experimental data for ices showed a non-linear pressure effect (Karr et al., 1989). A linear function is proposed in this paper for metals.

The present concept of pressure dependent yield function for metals should not be confused with Gurson type of softening (Gurson, 1975; Needleman and Tvergaard, 1984) due to the nucleation, growth and linkage of voids. In a simple tensile test, it is difficult to tell what physical mechanism is responsible for the observed softening - the suppression of dislocation motion or the growth of material porosity with deformation. The physically based Eq. (3.10) explains a relative difference in the stress-strain curves obtained in tests with various stress triaxialities, which can be measured experimentally by a few simple tests. At the same time,

the material softening in the GTN model (Needleman and Tvergaard, 1984) is an illusive concept because the reference state is the undamaged stress-strain curve for the matrix material, which can not be found from any simple tests. The reversibility of the softening is another issue even though Spitzig and Richmond (1984) did not address it directly. It is implicitly assumed that the dislocation suppression is reversible. This means that when in the loading process the hydrostatic pressure is brought back to the original value, the material will regain its initial strength. It is useful to design a test program involving a controlled change of the triaxiality to distinguish the two types of softening as discussed above. One such test could, for example, would involve two-stage tensile tests on notched round bars. After some plastic deformation the test is stopped and the gauge section of a specimen is re-machined to a larger radius. Such tests are being planned by the present authors.

3.3.2 Lode dependence

The dependence of the yield condition on the Lode angle parameter can best be explained by comparing the von Mises and Tresca yield condition. In the polar coordinate system, the equivalent stress becomes the radial coordinate while the circumferential coordinate is the Lode angle θ. In the deviatoric stress plane, the von Mises yielding condition is represented by a circle. The Tresca yielding is a hexagon inscribed on the von Mises circle, as shown in Fig. 3-2.

To take the third stress invariant into account for plasticity, a new term considering the effect of the Lode angle is introduced into Eq. (3.10). The following yield criterion is proposed,

$$\sigma_{yld} = \bar{\sigma}\left(\bar{\varepsilon}_p\right)\left[1 - c_\eta(\eta - \eta_0)\right]\left[c_\theta^s + (c_\theta^{ax} - c_\theta^s)\left(\gamma - \frac{\gamma^{m+1}}{m+1}\right)\right], \tag{3.11}$$

where γ and c_θ^{ax} are two parameters defined by

$$\gamma = \frac{\cos(\pi/6)}{1-\cos(\pi/6)}\left[\frac{1}{\cos(\theta - \pi/6)} - 1\right] = 6.4641\left[\sec(\theta - \pi/6) - 1\right], \tag{3.12}$$

$$c_\theta^{ax} = \begin{cases} c_\theta^t & for \quad \bar{\theta} \geq 0 \\ c_\theta^c & for \quad \bar{\theta} < 0 \end{cases}. \tag{3.13}$$

Equation (3.11) defines a class of function that define the shape of the yield surface. The term $\cos(\theta - \pi/6)$ in the definition of the parameter γ represents the difference between von Mises and Tresca in the deviatoric stress plane, which is obtained from the geometrical

construction by comparing the von Mises circle and the Tresca hexagon. After modification and normalization, the range of γ is $0 \leq \gamma \leq 1$, in which $\gamma = 0$ is corresponding to plane strain or shear condition, and $\gamma = 1$ is corresponding to axial symmetry. In Eq. (3.11), the leading term is linear with respect to the parameter γ, the higher order power term $(\frac{\gamma^{m+1}}{m+1})$ is introduced to make the yield surface smooth and differentiable with respect to Lode angle θ around $\gamma = 1$. The parameter m is a non-negative integer. There are four material constants, c_θ^t, c_θ^s, c_θ^c and m, need to be calibrated. The values of c_θ^t, c_θ^s, and c_θ^c are relative, and at least one of them is equal to unity. This depends on which type of reference test is used to calibrate the strain hardening function $\bar{\sigma}(\bar{\epsilon}_p)$. For example, if a smooth round bar tensile test is used, then $c_\theta^t = 1$; if a torsion test is used, then $c_\theta^s = 1$; if a cylinder specimen compressive test is used, then $c_\theta^c = 1$.

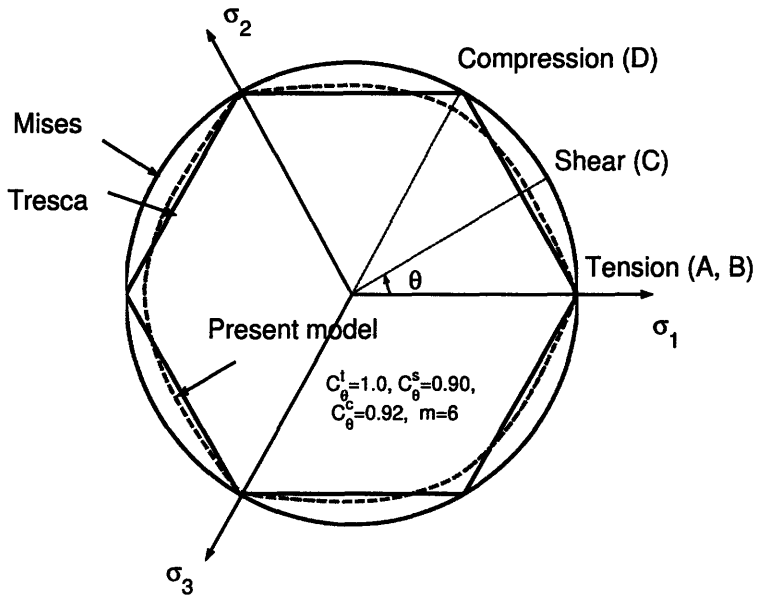

Fig. 3-2: Three yield loci in the deviatoric stress plane

It can be proved that the postulated yield function (Eq. (3.11)) is smooth and differentiable. The convexity of yield surface is controlled by the ratios of three parameters c_θ^t, c_θ^c and c_θ^s. Compared with von Mises and Tresca yield conditions, this yield surface can be plotted in the deviatoric stress plane, as shown in Fig. 3-2. Examples of yield loci are shown in Fig. 3-3 for the case of plane stress. By suitably choosing model parameters, some limiting cases are obtained. For example, assuming either $c_\eta = 0$ and $c_\theta^t = c_\theta^s = c_\theta^c = 1$ or $m = 0$ gives the von

Mises yield condition, while taking $c_\eta = 0$ and $c_\theta^s = \sqrt{3}/2, c_\theta^t = c_\theta^c = 1, m = +\infty$ gives the Tresca yield criterion. If the parameter $c_\eta \neq 0$ in above two cases, then one will get Drucker and Prager yield function (1952) and pressure-modified Tresca yield function. Most of metal plasticity theories assume that, in the deviatoric stress plane, the yield function is symmetric for uniaxial tension and uniaxial compression, which are corresponding to $\bar{\theta} = 1$ and $\bar{\theta} = -1$ respectively (for example, Tresca (1864); Mises (1913); Karafillis and Boyce (1993)). This restriction can be removed in the present model by setting $c_\theta^t \neq c_\theta^c$. It should be noted that the flattening property of the von Mises ellipse, which is needed for right prediction of the Forming Limit Curves, was introduced by many authors in the space of principal stresses using non-quadratic yield function (Hosford, 1972; Karafillis and Boyce, 1993; Barlat et al., 1997), often under plane stress assumption. Vegter and van den Boogaard (2006) modeled the plane stress yield locus by fitting Brezier curves into four test points. Working on the deviatoric plane with the Lode angle dependence is another way of controlling the shape of the yield surface in a simple and elegant way.

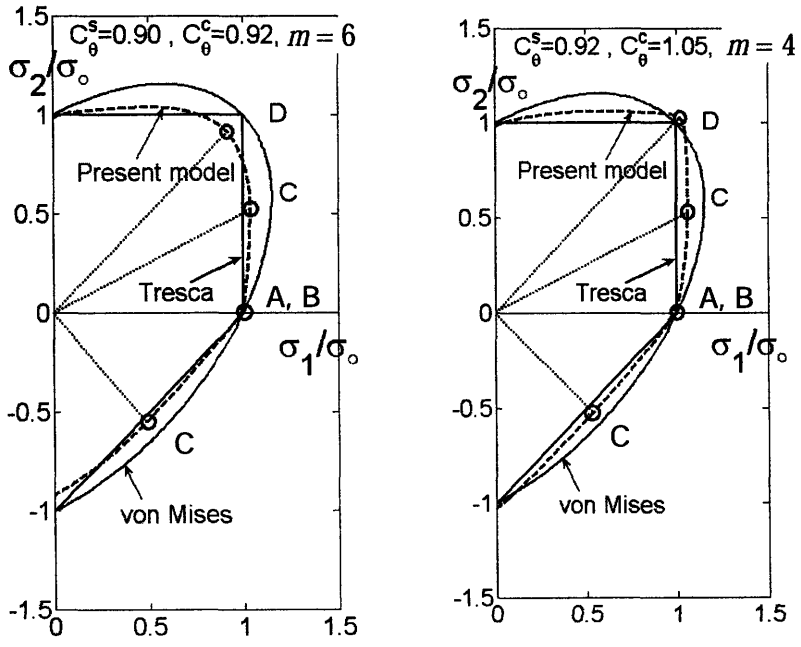

Fig. 3-3: Examples of yield locus for plane stress condition. (Here, $c_\theta^t = 1$, and the effect of hydrostatic pressure is dis-activated, $c_\eta = 0$)

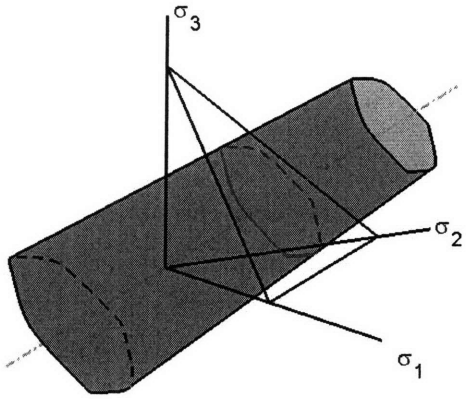

Fig. 3-4: A postulated 3D yield surface

3.3.3 The deviatoric associated flow rule

The yield surface, given by Eq. (3.11), can be visualized in the space of three principle stresses $(\sigma_1, \sigma_2, \sigma_3)$, see Fig. 3-4. According to the conventional associated flow rule,

$$d\varepsilon_{ij}^{pl} = d\lambda \frac{\partial f}{\partial \sigma_{ij}}, \tag{3.14}$$

where the plastic potential is defined by

$$f = q - \bar{\sigma}\left(\bar{\varepsilon}_p\right)\left[1 - c_\eta(\eta - \eta_0)\right]\left[c_\theta^s + \left(c_\theta^{ax} - c_\theta^s\right)\left(\gamma - \frac{\gamma^{m+1}}{m+1}\right)\right]. \tag{3.15}$$

$d\lambda$ is the equivalent plastic strain increment, and q is defined by Eq. (3.2). To implement a yield function into finite element codes, a necessary step is to derive the expression for the normal direction (or flow direction) with respect to yield locus, $\frac{\partial f}{\partial \sigma_{ij}}$. From the yield function, Eq. (3.15), one can get

$$\begin{aligned}\frac{\partial f}{\partial \sigma_{ij}} = {} & \frac{\partial q}{\partial \sigma_{ij}} + \bar{\sigma}\left(\bar{\varepsilon}^p\right) c_\eta \left[c_\theta^s + \left(c_\theta^{ax} - c_\theta^s\right)\left(\gamma - \frac{\gamma^{m+1}}{m+1}\right)\right] \frac{\partial \eta}{\partial \sigma_{ij}} \\ & - \bar{\sigma}\left(\bar{\varepsilon}^p\right)\left[1 - c_\eta\left(\eta - \eta_\circ\right)\right]\left(c_\theta^{ax} - c_\theta^s\right)\left(1 - \gamma^m\right)\frac{\partial \gamma}{\partial \sigma_{ij}},\end{aligned} \tag{3.16}$$

where $\frac{\partial q}{\partial \sigma_{ij}}$, $\frac{\partial \eta}{\partial \sigma_{ij}}$ and $\frac{\partial \gamma}{\partial \sigma_{ij}}$ can be expressed by the following equations.

$$\frac{\partial q}{\partial \sigma_{ij}} = \frac{3}{2q} s_{ij}, \tag{3.17}$$

$$\frac{\partial \eta}{\partial \sigma_{ij}} = \frac{1}{3q}\delta_{ij} - \frac{3\eta}{2q^2}s_{ij}, \tag{3.18}$$

$$\frac{\partial \gamma}{\partial \sigma_{ij}} = \left(\frac{3\sqrt{3}}{2-\sqrt{3}}\right)\left(\frac{\tan(\theta-\pi/6)}{\cos(\theta-\pi/6)}\right)\frac{1}{q\sin 3\theta}\left(\frac{\delta_{ij}}{3} + \frac{\cos 3\theta}{2q}s_{ij} - \frac{3}{2q^2}s_{ik}s_{kj}\right). \tag{3.19}$$

Although the plasticity is pressure sensitive, experiments show that the plastic dilatancy of metals is negligible (Spitzig and Richmond, 1984). To satisfy the assumption of plastic incompressibility, the first term $\frac{1}{3q}\delta_{ij}$ in Eq. (3.18) should be removed. Therefore, what is used in the present paper is a flow rule with *deviatoric associativity*, see Eq. (3.20), rather than the conventional associated flow rule, Eq. (3.16).

$$\begin{aligned} d\varepsilon_{ij}^{pl} = d\lambda \Big\{ & \tfrac{3}{2q}s_{ij} - \bar{\sigma}(\bar{\varepsilon}_p)\, c_\eta \left[c_\theta^s + (c_\theta^{ax} - c_\theta^s)\left(\gamma - \tfrac{\gamma^{m+1}}{m+1}\right)\right]\tfrac{3\eta}{2q^2}s_{ij} \\ & -\bar{\sigma}(\bar{\varepsilon}_p)\left[1 - c_\eta(\eta - \eta_o)\right](c_\theta^{ax} - c_\theta^s)(1-\gamma^m) \\ & \left(\tfrac{3\sqrt{3}}{2-\sqrt{3}}\right)\left(\tfrac{\tan(\theta-\pi/6)}{\cos(\theta-\pi/6)}\right)\tfrac{1}{q\sin 3\theta}\left(\tfrac{\delta_{ij}}{3} + \tfrac{\cos 3\theta}{2q}s_{ij} - \tfrac{3}{2q^2}s_{ik}s_{kj}\right)\Big\} \end{aligned} \tag{3.20}$$

Clearly, the presence of additional terms in Eq. (3.20) indicate that the direction of plastic flow is normal to the yield surface in the deviatoric plane but not to von Mises yield surface. In this issue, the present formulation can be classified as an intermediate flow rule between the non-associated flow rule and the conventional "fully" associated one. (It should be noted that if this model is used to model other non-mental porous materials, which are plastic compressible, then a fully associated flow rule as previous stated is necessary). This new form of metal plasticity has been implemented into Abaqus user material subroutine VUMAT using the classical mapping return algorithm. The following numerical simulations are run with the material subroutine.

3.4 Experimental calibration of 2024-T351 aluminum

A power function is introduced to describe the isotropic stain hardening for metal plasticity.

$$\bar{\sigma}(\bar{\varepsilon}_p) = A(\varepsilon_o + \bar{\varepsilon}_p)^n \qquad for \quad \bar{\sigma} \geq \sigma_y. \ , \tag{3.21}$$

where ϵ_o is the first yield strain. There are nine parameters, A,ϵ_o,n,c_η,η_o, c_θ^t, c_θ^s,c_θ^c, and m, in the present plasticity model. To validate and calibrate the model, four types of tests are required. The first test is the smooth round bar tensile test, from which the baseline stress-strain curve (parameters: A,ϵ_o and n) can be determined. Also, the reference parameters are uniquely defined: $\eta_o = 1/3$ and $c_\theta^t = 1$. The second test is the notched round bars tensile

test. Introducing a geometric notch to a smooth round bar increases the hydrostatic pressure in the materials inside the neck. Wilson (2002) conducted this type of test on aluminum 2024-T351, and calibrated the pressure effect on metal plasticity, but the effect of Lode angle was not taken into account. The third test is the tensile test of flat grooved plates, which can be used to calibrate the parameter c_θ^s. The fourth test is the cylindrical specimens' upsetting test, which can be used to calibrate the last two parameters c_θ^c and m. The corresponding stress states of these four types of tests are also respectively marked as A,B,C and D in Fig. 3-2. The analysis and a description of experimental study of the first three types of tests were described in the earlier report (Bai et al., 2006b) in detail. In this paper, emphasis is put on the numerical simulation study and plastic model calibration.

3.4.1 Smooth and notched round bars tensile tests

Smooth round bar tensile tests were used to calibrate the stress-strain curve. There are three steps involved. Firstly, the engineering stress-strain curve $\sigma_E(\varepsilon_E)$ is obtained from the force-displacement curve $P(u)$ recorded during the test. Secondly, the true stress-strain curve $\bar{\sigma}(\bar{\varepsilon})$ is calculated from the engineering stress-strain curve using the classical transformation law, $\bar{\sigma} = \sigma_E(1+\varepsilon_E)$ and $\bar{\varepsilon} = \ln(1+\varepsilon_E)$. In this step, only the data point before specimen necking can be used because the transformation equations are valid only up to necking initiation. Approximately, one can take the peak point of the force-displacement curve as the necking initiation point. Thirdly, a power function (Eq. (3.21)) is used to fit the true stress-strain curve obtained from the test. This curve is then extrapolated to get the approximate true stress-strain curve after necking.

Two methods are available to determine more precisely the true stress-strain curve after necking. If the continues measurements of the neck geometry are available, then the Bridgman correction is applicable. Alternatively, the inverse method could be used in which the stress-strain curve after necking is adjusted to get good agreement of the measured force-displacement curve. For the present material, the neck was not deep and it was not necessary to adjust the stress-strain curve after necking.

A group of tensile tests of smooth and notched round bars were conducted, refer to Fig. 3-5. The diameter of smooth round bar specimens is 9 mm. For notched round bar specimens, the diameter of the minimal cross-section is 8 mm, and two radii of notches are assigned, equal to 12 mm and 4 mm, respectively. The diameters in specimens shoulder are all equal to 15 mm, and the length of gauge section for this group of specimens is 25.5 mm. The selected material is aluminum 2024-T351. To avoid the effect of material anisotropic,

all the specimens discussed in this paper are machined from the rolling direction (or 90° direction) of a same material block. Two to four tests are conducted for each case.

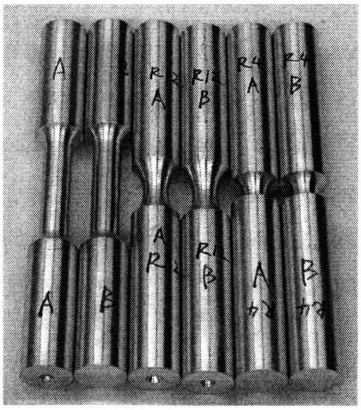

Fig. 3-5: A group of smooth and notched round bar specimens

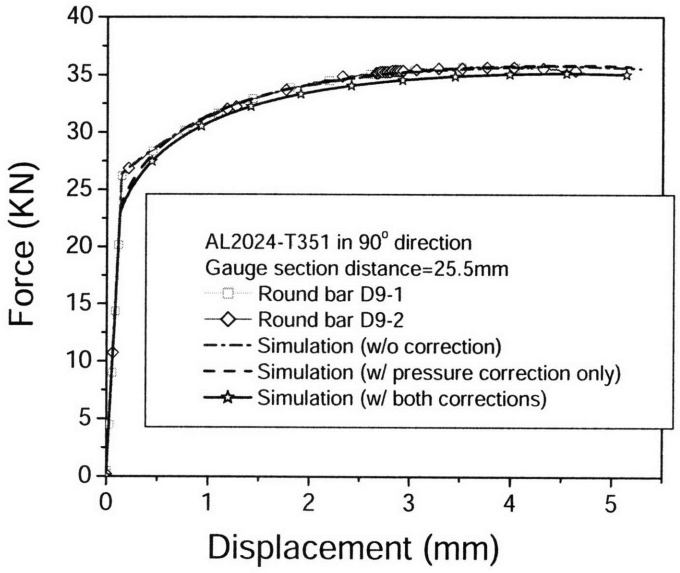

Fig. 3-6: A comparison of force-displacement curves between experimental results and simulation results: smooth round bars, diameter = 9mm

The stress-strain curve was calibrated from a smooth round bar tensile test, so $\eta_o = 1/3$. To calibrate the pressure dependence coefficient c_η, the finite element models of the

specimens were constructed with the Lode angle terms switched off. Round bar specimens are discretized by 4-node axisymmetric elements. Finite element models of Abaqus/explicit are built, in which the user material subroutine VUMAT is used. The measured force-displacement curves are shown in Fig. 3-6 and 3-7. From these figures, one can see that without any corrections, the force-displacement response of the smooth round bar simulation agrees with the experimental results very well, but the notched round bar simulations over-predict the force-displacement curves about 3%-6%. The reason is that the material points inside a notched round bar are subjected to higher pressure than the smooth round bar. This phenomenon shows the effect of hydrostatic pressure on stress-strain curve. By changing the coefficient c_η iteratively, a value of $c_\eta = 0.09$ is obtained, which makes the force-displacement curves agree with the experiment results (the errors become less than 0.8%), as shown in Fig. 3-6 and 3-7. A comparison was also done for the case with notch radius equal to 12 mm, but for the sake of brevity, it is not shown in this paper, see Ref. (Bai et al., 2006b) for a complete analysis.

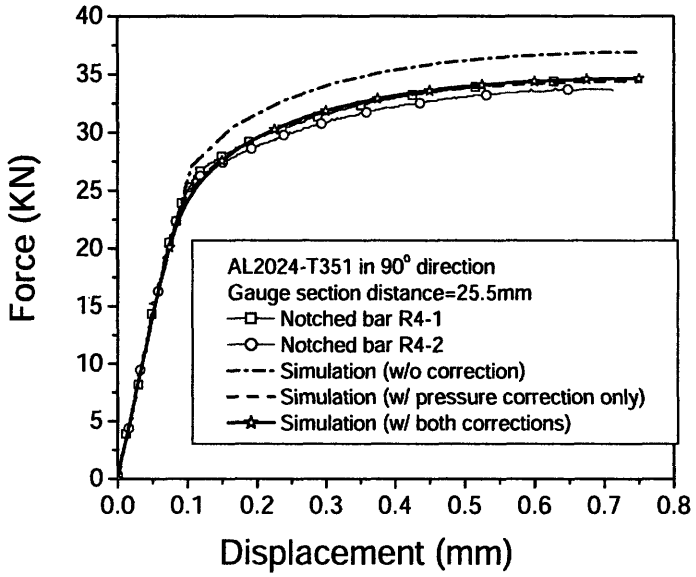

Fig. 3-7: A comparison of force-displacement curves between experimental results and simulation results: notched round bars, diameter =8mm, notch radius=4mm.

The calibrated pressure effect in Wilson's paper (Wilson, 2002) gives $\alpha = 0.03$ for apparently the same material. One can see that the present method to calibrate c_η is different

from the one Wilson suggested, but the result is similar.

3.4.2 Flat grooved plates tensile tests

Another group of tensile tests of flat grooved plates, as shown in Fig. 3-8, were conducted as described in detail in the earlier report (Bai et al., 2006b). The width of the specimens is 50mm. Four types of radii of the grooves are machined: 12.7mm, 3.97mm, 2.38mm, and 1.59mm. Two nominal thicknesses in the minimal cross-section are assigned to these specimens: $t = 2.11mm$ is assigned to the one with 1.59mm groove radius, and $t = 1.6mm$ is assigned to the other ones. The plate thicknesses at the specimens shoulder are all equal to 5mm, and the length of gauge section for this group of specimens is 25 mm. The flat grooved specimen has a same range of stress triaxiality with that of notched round bars, but the corresponding values of the Lode angle parameter $\bar{\theta}$ are different. This feature gives a direct way to see the effect of the Lode angle parameter on metal plasticity. Again, the finite element simulation of physical tests is needed to find the remaining parameters.

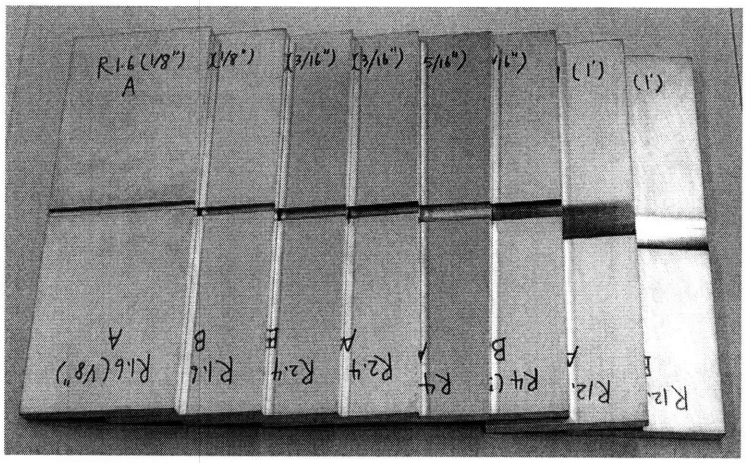

Fig. 3-8: A group of flat grooved specimens

The flat grooved specimens are discretized by 8-node solid elements. Finite element models are built and run by Abaqus/explicit with the material user subroutine. Due to symmetry condition, 1/8 of a full scale model is used. Comparisons of force-displacement curves between numerical simulations and experimental results of the case with the sharpest groove notch are illustrated in Fig. 3-9. Without any corrections, one can see large differences between numerical simulations and experiments in force responses from these figures (the

errors are about 14%-19%). If only a hydrostatic pressure effect ($c_\eta = 0.09$) is introduced, the differences between numerical simulations and experiments becomes smaller but can not be eliminated (the errors become 12%-16%). Here, it is found that the pressure effect correction is not enough, and the Lode angle parameter effect should also be taken into account. By changing the coefficient c_θ^s iteratively, a value of $c_\theta^s = 0.855$ is obtained, which makes the force-displacement curves agree well with the experiment results (the errors now become less than 2%), as shown in Fig. 3-9. The comparison was done for all four radii of the groove, but for the sake of brevity, only the result for the sharpest groove is shown (see Bai et al. (2006b) for a complete analysis). From these two groups of tests, it can be concluded that the corrections of both the hydrostatic pressure effect and the Lode dependence are necessary for aluminum 2024-T351.

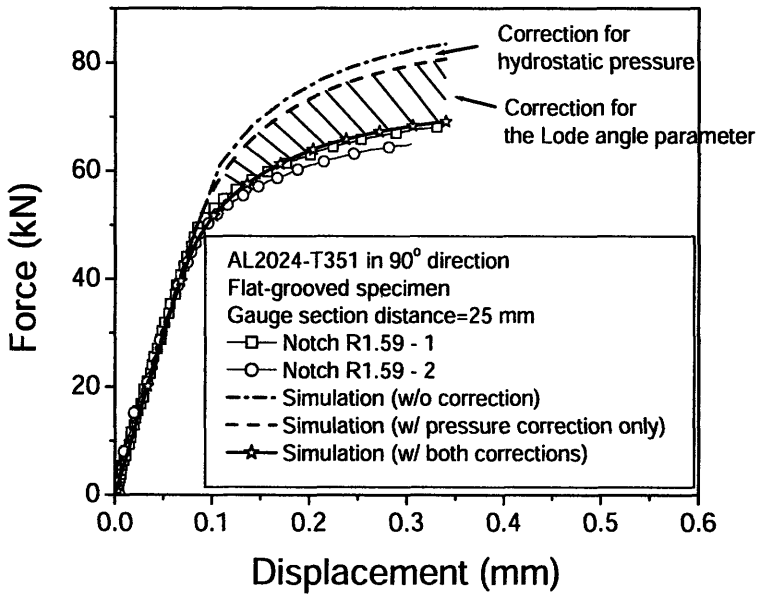

Fig. 3-9: A comparison of force-displacement curves between experimental results and simulation results: flat grooved specimens, thickness = 2.11mm, groove radius=1.59mm.

3.4.3 Cylindrical specimens upsetting tests

The remaining two parameters c_θ^c and m are found from the upsetting tests. Round bars' tensile tests and flat grooved plates' tensile tests correspond to loading conditions of $\bar{\theta} = 1$

and $\bar{\theta} = 0$ respectively. The loading condition of cylindrical specimens in the upsetting test is $\bar{\theta} = -1$ and $\eta = -1/3$. Since the pressure effect on plasticity is already calibrated in the previous two groups of tests, the upsetting tests will help to determine the shape of the yield surface at $\bar{\theta} = -1$. To check whether the yield surface is symmetric with respect to the Lode angle parameter $\bar{\theta}$ or not, a group compressive tests on cylindrical specimens were conducted. The diameters of the specimens were 8 mm, and two heights (6 mm and 11.25 mm) were assigned to two types of cylinders, as shown in Fig. 3-10.

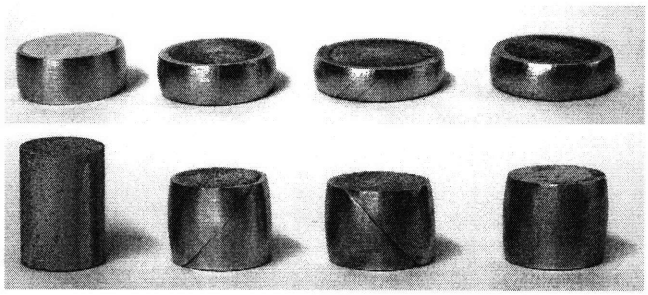

Fig. 3-10: Two groups of cylindrical specimens for upsetting tests

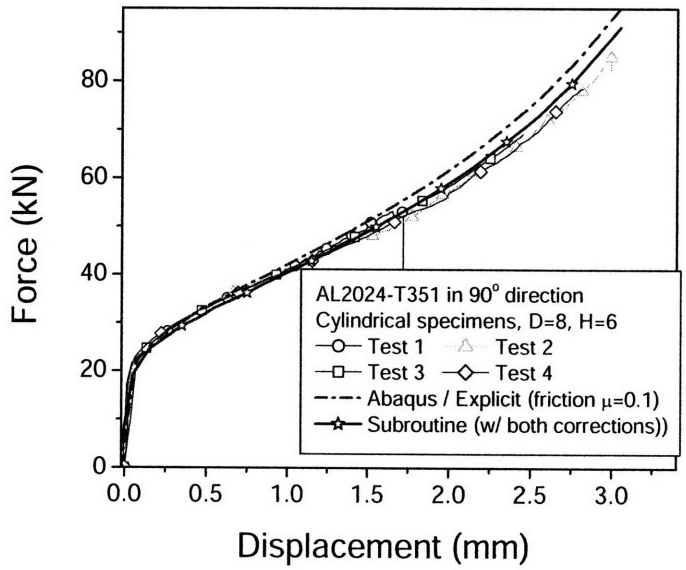

Fig. 3-11: A comparison of force-displacement curves between experimental results and simulation results: cylindrical specimens, diameter=8 mm, height=6 mm.

The cylindrical specimens are discretized by 4-node axisymmetric elements. Finite element models are built and run by Abaqus/explicit with the material user subroutine. Because the friction coefficient (μ) between specimens and the platform of the testing machine is unknown, the friction coefficient is adjusted iteratively in the simulation to make the final deformed shape of specimens agree with the experimental results. Comparisons of the force-displacement curves between numerical simulations and experimental results were made for all tests, and a typical result is shown in Fig. 3-11. The value of μ used in the simulation is also provided in the figure. It is found that, using simply the power hardening law, there is a difference between numerical simulations and experimental results (the errors are about 6%-10%). Adjusting the parameters, c_θ^c and m, iteratively in the numerical simulation, the set of parameter $c_\theta^c = 0.90$ and $m = 6$ is obtained, which makes the force-displacement curves agree well with the experimental ones (the errors become less than 2.5%), see Fig. 3-11. This proves that the yield surface of aluminum 2024-T351 is not symmetric because of $c_\theta^t \neq c_\theta^c$. In summary, the calibrated plasticity model parameters of aluminum 2024-T351 as listed in Table 3.2. This completes the calibration process of plastic behavior.

Table 3.2: Calibrated material properties of aluminum 2024-T351 (Rolling direction)

Basic material properties	Pressure effect and lode dependence constants
Density ρ= 2.7e+3 Kg/m^3	$\eta_o = 1/3$
Poisson's ratio = 0.3	$c_\eta = 0.09$
Young's Modulus E=7.115e+5 MPa	$c_\theta^t = 1.0$
Yield stress σ_y= 370 MPa	$c_\theta^s = 0.855$
Stress-strain curve $\bar{\sigma} = 908(0.0058+\bar{\epsilon}_p)^{0.1742} MPa$	$c_\theta^c = 0.90$
	$m = 6$

3.5 The asymmetric 3D fracture locus

Compared with the strain hardening, the hydrostatic pressure effect on metal plasticity is relatively small. However, the hydrostatic pressure is one of the most important parameters that controls material ductility. The equivalent plastic strain to fracture ($\bar{\epsilon}_f$) is widely used to measure material ductility. Theoretical analysis (McClintock, 1968; Rice and Tracey, 1969) and numerous experimental studies (Hancock and Mackenzie, 1976; Mackenzie et al., 1977;

Johnson and Cook, 1985; Bao, 2003) have proved that the fracture strain increases when the hydrostatic pressure increases. Wilkins et al. (1980) was first to introduce the effect of deviatoric stress ratio A, which is related to Lode angle parameter $\bar{\theta}$ or the normalized third stress invariant ξ, on ductile fracture.

$$\bar{\varepsilon}_f = w_1(p)w_2(A) = g_1(p)g_2(\bar{\theta}) = h_1(\eta)h_2(\xi). \tag{3.22}$$

Furthermore, the function g_2 was taken to be symmetric with respect to the parameter $\bar{\theta}$. In this model as well as its subsequent applications (Kamoulakos et al., 2003; Xue, 2007b), the dependence of the fracture locus on the parameter η and $\bar{\theta}$ was assumed to be separable (see Eq. (3.22)). As an extension of Wilkins' model and Johnson-Cook's model, Wierzbicki and Xue (2005) postulated a non-separable but symmetric 3D fracture locus in the space of stress triaxiality and the normalized third stress invariant ξ, $\bar{\varepsilon}_f = \hat{\varepsilon}_f(\eta, \xi)$, which is shown in Fig. 3-12.

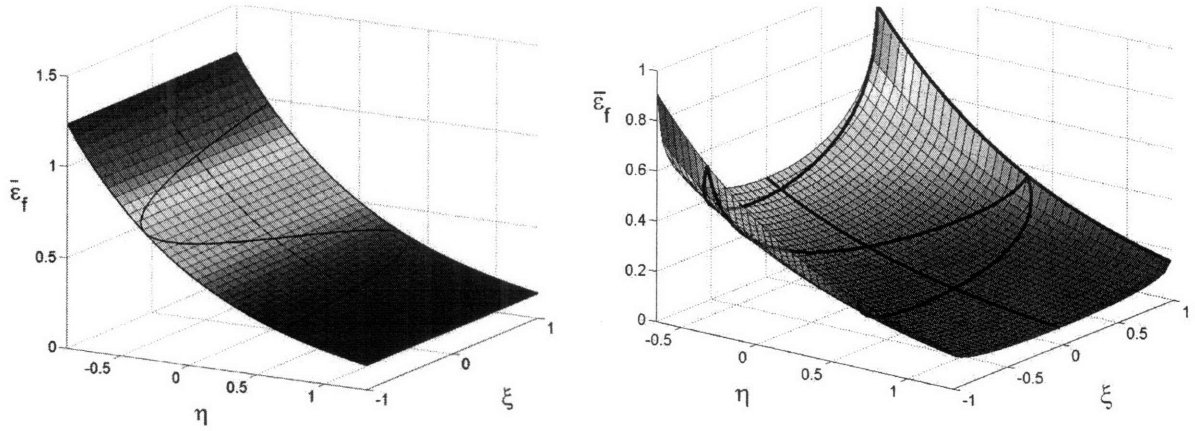

Fig. 3-12: The fracture locus independent of ξ (or $\bar{\theta}$) postulated by Johnson and Cook (1985) (left), and a 3D symmetric fracture locus accounting for ξ postulated by Wierzbicki and Xue (Wierzbicki and Xue, 2005; Wierzbicki et al., 2005b)(right)

However, the assumptions of the separable form and symmetry of the fracture locus might be too restrictive, and they were not based on the experimental evidence. Tests have shown that the effect of the third stress invariant on ductile fracture initiation becomes weak in the high range of pressures or high stress triaxiality region (Hancock and Brown, 1983; Bai et al., 2006b). In low stress triaxiality region, a cylinder's upsetting test (corresponding to the loading condition $\eta = -1/3$ and $\bar{\theta} = -1$) will give a quick check on the effect of the

third stress invariant. A common practice in the literatures is to extrapolate the fracture locus determined from high stress triaxiality region to the low stress triaxiality region. If the fracture locus is symmetric with respect to $\bar{\theta}$ as postulated by Wilkins et al., Wierzbicki and Xue (as is shown in Fig. 3-12), then the fracture strain of cylinders upsetting tests (corresponding to $\bar{\theta} = -1$) should lay on the extrapolated curve of fracture locus calibrated by notched round bars tensile tests (corresponding to the loading condition $\eta \geq 1/3$ and $\bar{\theta} = 1$).

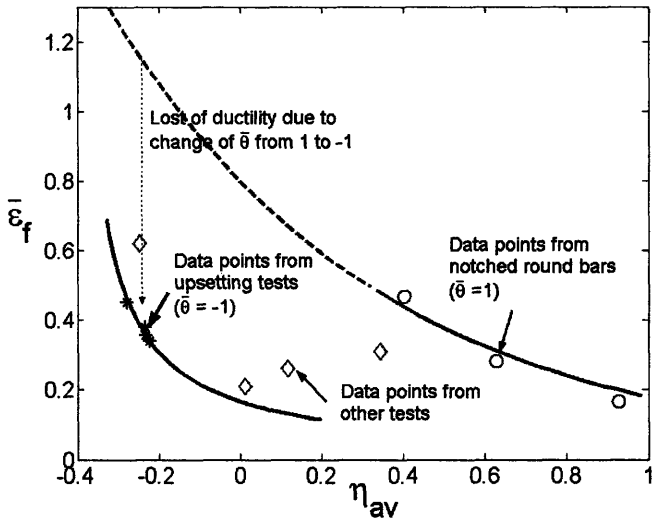

Fig. 3-13: A new interpolation of Bao's data points of aluminum 2024-T351 (experimental data from Bao's tests (Bao, 2003))

Bao (2003) designed a series of tests to calibrate the fracture strain in the entire range of stress triaxiality. It is clear from Fig. 3-13 that the fracture strains of upsetting tests are far below the extrapolated curve. In view of mounting experimental evidence, it can be hypothesized that the loss of ductility in upsetting tests are due to the Lode angle parameter $\bar{\theta}$, which changes from 1 to -1. The phenomenon is confirmed by more recent tests conducted by El-Magd et al. (2001), who performed similar tests on AlMgSil.F31 alloy.

As an extension of the 2D fracture locus, the 3D fracture locus is constructed in the space of $(\bar{\epsilon}_f, \eta, \bar{\theta})$. Since the effect of the Lode angle parameter on fracture strain is not uniform for different stress triaxialities, it is proposed to construct the fracture locus based on the

boundary limits. There are three limiting cases in the fracture locus: $\bar{\varepsilon}_f^{(-)}$ (corresponding to axial symmetry in deviatoric compression, $\bar{\theta} = -1$), $\bar{\varepsilon}_f^{(o)}$ (corresponding to plastic plane strain or generalized shear, $\bar{\theta} = 0$), and $\bar{\varepsilon}_f^{(+)}$ (corresponding to axial symmetry in deviatoric tension, $\bar{\theta} = +1$). Tests should tell which bound limit is the upper limit and which is the lower limit. There are many possibilities. Experimental data on geological materials from Han and Chen (1985) show that $\bar{\varepsilon}_f^{(-)} > \bar{\varepsilon}_f^{(+)}$, but others data from Bardet (1990) suggest that $\bar{\varepsilon}_f^{(+)} > \bar{\varepsilon}_f^{(-)}$. Theoretical analysis based on Gurson's model by Gao and Kim (2006) and cubic cell unit by Zhang et al. (2001) show that $\bar{\varepsilon}_f^{(+)} > \bar{\varepsilon}_f^{(-)}$ in high stress triaxiality region. It is also possible that these three curves will intersect when projecting the 3D surface into the plane of the equivalent fracture strain and stress triaxiality. Based on the theory of McClintock (1968) and Rice and Tracey (1969) on void growth, the exponential function for the effect of stress triaxiality on fracture strain is used. Regarding the effect of $\bar{\theta}$ on fracture locus, a parabolic function is proposed. Hence, the following form of the fracture locus is postulated,

$$\begin{aligned}\hat{\varepsilon}_f\left(\eta,\bar{\theta}\right) &= \left[\tfrac{1}{2}\left(\hat{\varepsilon}_f^{(+)}+\hat{\varepsilon}_f^{(-)}\right)-\hat{\varepsilon}_f^{(o)}\right]\bar{\theta}^2+\tfrac{1}{2}\left(\hat{\varepsilon}_f^{(+)}-\hat{\varepsilon}_f^{(-)}\right)\bar{\theta}+\hat{\varepsilon}_f^{(o)} \\ &= \left[\tfrac{1}{2}\left(D_1e^{-D_2\eta}+D_5e^{-D_6\eta}\right)-D_3e^{-D_4\eta}\right]\bar{\theta}^2+\tfrac{1}{2}\left(D_1e^{-D_2\eta}-D_5e^{-D_6\eta}\right)\bar{\theta}+D_3e^{-D_4\eta}\end{aligned} \tag{3.23}$$

In this new fracture locus function, six parameters, D_1, D_2, D_3 ,D_4, D_5, and D_6 need to be calibrated. The term $D_1e^{-D_2\eta}$ gives the $\bar{\varepsilon}_f^{(+)}$ limit of the fracture locus, $D_3e^{-D_4\eta}$ gives the $\bar{\varepsilon}_f^{(o)}$ limit of the fracture locus, and $D_5e^{-D_6\eta}$ gives the $\bar{\varepsilon}_f^{(-)}$ limit of the fracture locus. It should be noted that in this paper, the Lode angle parameter $\bar{\theta}$, instead of the normalized third stress invariant ξ, will be used to formulate the fracture locus. A geometrical representation of the new fracture locus in the 3D space is shown in Fig. 3-14. Generally speaking, $\bar{\varepsilon}_f^{(+)} \neq \bar{\varepsilon}_f^{(-)}$, which implies the asymmetry. It should be noted that a function convexity is not necessary in strain (or stress) space for the 3D fracture locus.

Many special cases of the fracture loci can be recovered from the above general function. For example, by requiring symmetry with respect to $\bar{\theta}$, $\bar{\varepsilon}_f^{(+)} = \bar{\varepsilon}_f^{(-)} = \bar{\varepsilon}_f^{(ax)}$, Eq. (3.23) becomes

$$\hat{\varepsilon}_f\left(\eta,\bar{\theta}\right) = \left[\hat{\varepsilon}_f^{(ax)}-\hat{\varepsilon}_f^{(o)}\right]\bar{\theta}^2+\hat{\varepsilon}_f^{(o)}, \tag{3.24}$$

which is similar to the Xue-Wierzbicki symmetric fracture locus. It should be noted that neither Eq. (3.23) nor Eq. (3.24) is of a separable form in η and $\bar{\theta}$ as assumed by Wilkins et al. (1980); Kamoulakos et al. (2003); Xue (2007b). If the effect of $\bar{\theta}$ on fracture locus is

taken away, $\bar{\epsilon}_f^{(ax)} = \bar{\epsilon}_f^{(\circ)}$, Eq. (3.24) becomes

$$\hat{\varepsilon}_f\left(\eta, \bar{\theta}\right) = \hat{\varepsilon}_f^{(\circ)} = D_3 e^{-D_4 \eta}, \tag{3.25}$$

which is identical to the Rice-Tracey's fracture locus and also to a reduced form of Johnson-Cooks criteria.

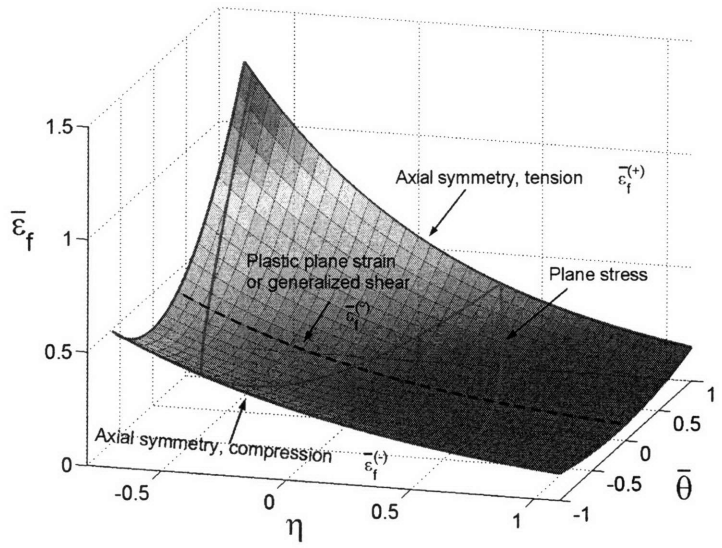

Fig. 3-14: A newly postulated 3D asymmetric fracture locus

3.6 Fracture locus calibration

3.6.1 Fracture locus calibration using "classical" specimens

There are six parameters in Eq. (3.23), so at least six different tests need to be performed to calibrate the material for fracture. Ten types of classical specimens and tests are listed in Table 3.1 and also shown in Fig. 3-1. From this table, it is suggested to choose the first seven types of specimens to calibrate the fracture locus.

An emphasis is put on two groups of tests, the smooth and notched round bars tensile tests (No. 1 and 2 in Table 3.1, $\bar{\theta} = 1$) and the flat grooved plates tensile tests (No. 3 and 4, $\bar{\theta} = 0$). In Section 3.4, these two groups of tests were used to calibrate the new form of metal plasticity. These two groups of tests are also very useful to fracture locus calibration

because the tests on smooth and notched round bars will give $\bar{\varepsilon}_f^{(+)}$, and the tests on flat grooved specimens will give $\bar{\varepsilon}_f^{(\circ)}$. Regarding the third bound limit, $\bar{\varepsilon}_f^{(-)}$, cylinders upsetting test (No. 6) and equi-biaxial tension test (No. 7) can be used.

For thin metal sheets, it is difficult to machine round specimens, so the flat dog-bone specimen tensile test (corresponding to No. 1 in Table 3.1), plane strain tension(No. 3), flat grooved plates tensile tests(No.4), shear test (No. 5), and equi-biaxial tension test (No. 7) are suggested.

A Matlab code is written to optimize the data points of tests to get the best surface fitting. An optimization function is chosen as to minimize the average error, see Eq. (3.26).

$$\underset{(D1,D2,\ldots,D6)}{Min}\,(Error)_{av} = \underset{(D1,D2,\ldots,D6)}{Min}\left[\frac{1}{N}\sum_{i=1}^{N}\left|\frac{\hat{\varepsilon}_f\left(\eta_i,\bar{\theta}_i\right)-\bar{\varepsilon}_{f,i}}{\bar{\varepsilon}_{f,i}}\right|\right] \tag{3.26}$$

The curve fitting result of Rice-Tracey criteria (Eq. (3.25)) is used as the initial values of all three limits for optimization searching process in the Matlab code. After many runs, the $\bar{\varepsilon}_f^{(+)}$ limit, $\bar{\varepsilon}_f^{(\circ)}$ limit and $\bar{\varepsilon}_f^{(-)}$ limit of the fracture locus are obtained, and the 3D fracture locus is constructed.

The above procedure is first applied to characterize fracture of 2024-T351 aluminum alloy. Bao (2003) designed and performed 14 tests on 2024-T351 aluminum for fracture locus calibration. These tests included smooth/notched round bar tensile tests, cylindrical specimens upsetting tests, plane strain test, shear test and so on. The experimental data points of all 14 tests can be found in Table 2 of Ref. (Wierzbicki et al., 2005b) or Table 5.1 in the present thesis, and ten of them is also shown in Fig. 3-13. As a first iteration, the parameters of the Rice-Tracy's criteria was determined, see Eq. (3.27).

$$\bar{\varepsilon}_f = 0.3445e^{-0.4109\eta}. \tag{3.27}$$

Taking the corresponding cylindrical surface as an initial value of the optimization process, the full 3D fracture locus was found in the form of Eq. (3.28).

$$\begin{aligned}\hat{\varepsilon}_f\left(\eta,\bar{\theta}\right) = &\left[\tfrac{1}{2}\left(0.5862e^{-1.3576\eta}+0.4859e^{-0.700\eta}\right)-0.2170e^{-0.0400\eta}\right]\bar{\theta}^2\\ &+\tfrac{1}{2}\left(0.5862e^{-1.3576\eta}-0.4859e^{-0.700\eta}\right)\bar{\theta}+0.2170e^{-0.0400\eta}.\end{aligned} \tag{3.28}$$

If a symmetric fracture locus (Eq. (3.24)) is used in surface fitting process, then a

symmetric fracture locus is obtained as follow,

$$\bar{\varepsilon}_f = \left(0.4534e^{-0.7788\eta} - 0.2147e^{-0.0400\eta}\right)\bar{\theta}^2 + 0.2147e^{-0.0400\eta}. \tag{3.29}$$

The average error of all 14 test data is reduced from 21.4% of Rice-Tracy's (Eq. (3.27)) to 7.2% of the asymmetric 3D fracture locus (Eq. (3.28)). The average error of symmetric fracture locus (Eq. (3.29)) lies in between, and is equal to 9.3%. The geometrical representation of the asymmetric 3D fracture locus is shown in Fig. 3-15.

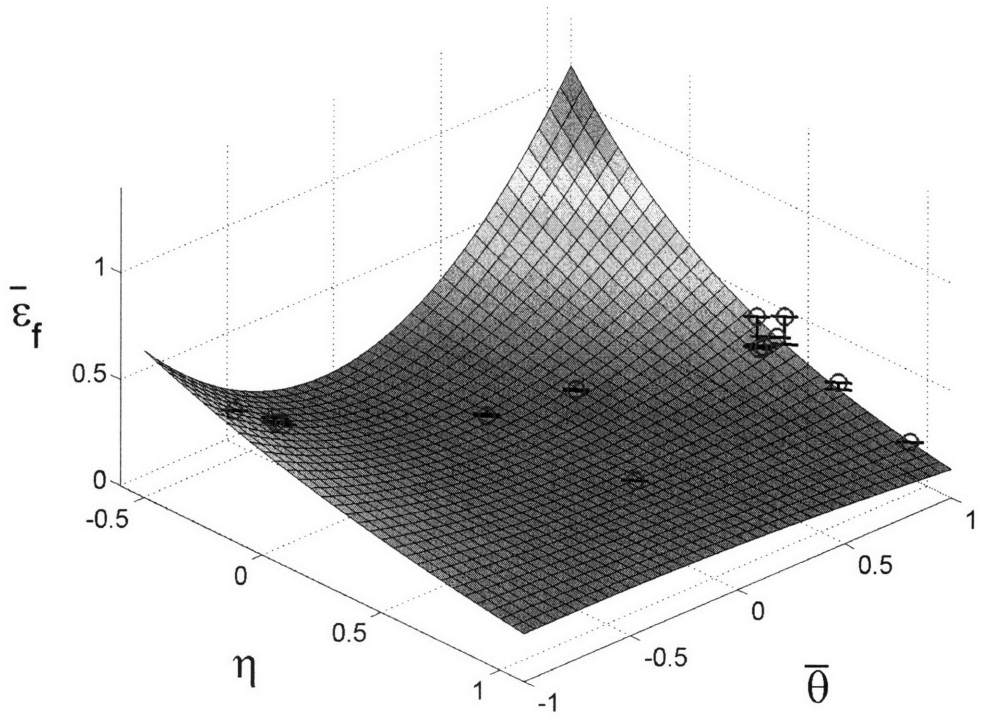

Fig. 3-15: 3D fracture locus of 2024-T351 aluminum (experimental data after Bao (2003); Wierzbicki et al. (2005b), see Table 5.1.)

It should be noted that the material block of 2024-T351 aluminum studied by Bao is different from the one studied in the present paper for metal plasticity, and different material properties are found for these two blocks.

3.6.2 Fracture locus calibration using butterfly specimens

Fracture locus calibration using "classical specimens" is complicated and time-consuming. Another shortcoming is that the classical specimens correspond all to the limiting cases of loading condition($\bar{\theta} = 0$, or $\bar{\theta} = \pm 1$), as shown in Fig. 3-1. In order to obtain data points between three limiting cases, other types of specimens and tests are need. A novel butterfly shape specimen with double curvatures, shown in Fig. 3-16, has been designed to calibrate the fracture locus in the space of stress triaxiality and equivalent fracture strain (Bao et al., 2004; Wierzbicki et al., 2005a; Mohr and Henn, 2004, 2007). The new specimen has several advantages including the same fracture initiation location (the center of the specimen) under all loading combinations, and ability to generate a wide range of stress state using only one type of specimen. The fact that one finite element model is need for all load conditions is removing partly the effect of mesh size. Also, this specimen is especially suited for application to metal sheets.

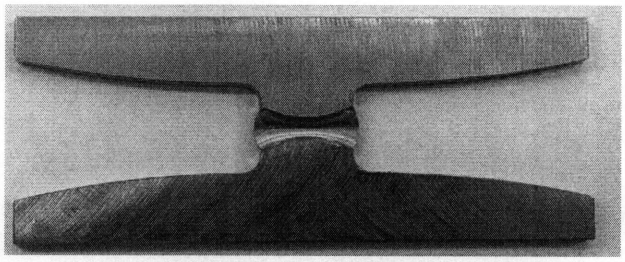

Fig. 3-16: A new type of butterfly shape specimen (A710 steel)

A710 steel is characterized by high strength and high ductility. Twenty butterfly specimens were machined and tested under eight loading conditions in a universal biaxial testing device (UBTD, see Ref. (Mohr and Doyoyo, 2004)) working in conjunction the MTS testing machine. A detailed description of these tests is given in Ref. (Bao et al., 2004). From the numerical simulations combined with experiment results, the fracture locus was plotted in the plane of stress triaxiality and equivalent fracture strain, as shown in Fig. 3-17. From the simulations, one can also get the loading conditions in the plane of stress triaxiality and the third stress parameter, as shown in Fig. 3-18. Details about the data points can be found in the Table 3 of Ref. (Wierzbicki et al., 2005a) or Table 4.3 in the present thesis. The first approximation is to fit the data points using Rice-Tracey criteria, as shown in Fig. 3-17, which gives

$$\bar{\varepsilon}_f = 2.5144 e^{-0.4185\eta}. \tag{3.30}$$

The corresponding average error of Rice-Tracey criteria (Eq. (3.30)) is 6.7%. Similar to Section 3.6.1, surface fitting of these eight date points gives three bound limits, as shown in Fig. 3-17, and the 3D fracture locus is constructed as follows

$$\begin{aligned}\hat{\varepsilon}_f\left(\eta,\bar{\theta}\right) = &\left[\tfrac{1}{2}\left(3.6421e^{-0.6892\eta} + 2.4659e^{-0.6986\eta}\right) - 2.5492e^{-0.5627\eta}\right]\bar{\theta}^2 \\ &+ \tfrac{1}{2}\left(3.6421e^{-0.6892\eta} - 2.4659e^{-0.6986\eta}\right)\bar{\theta} + 2.5492e^{-0.5627\eta}.\end{aligned} \tag{3.31}$$

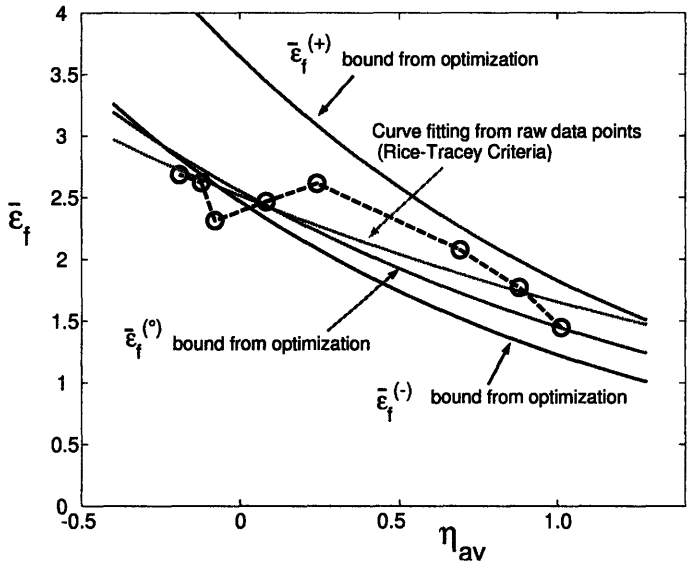

Fig. 3-17: Fracture locus of A710 steel in the space of stress triaxiality and fracture strain (experimental data from Wierzbicki et al. (2005a), see Table 4.3.)

This 3D fracture locus with the data points is shown in Fig. 3-19. Compared with Eq. (3.30), the 3D fracture locus, Eq. (3.31) makes the average error decrease from 6.7% to 3.0%. The differences between the model and the experimental value are also marked in Fig. 3-19. One can note that $\bar{\varepsilon}_f^{(+)} \neq \bar{\varepsilon}_f^{(-)}$ indicates an asymmetric fracture locus. If a symmetric fracture locus (Eq. (3.24)) is used in the surface fitting process, then a symmetric fracture locus is obtained as follow,

$$\bar{\varepsilon}_f = \left(3.2050e^{-0.400\eta} - 2.4283e^{-0.5117\eta}\right)\bar{\theta}^2 + 2.4283e^{-0.5117\eta}. \tag{3.32}$$

The corresponding average error of symmetric fracture locus (Eq. (3.32)) is 4.5%, which is between the Rice-Tracey's and the asymmetric fracture locus.

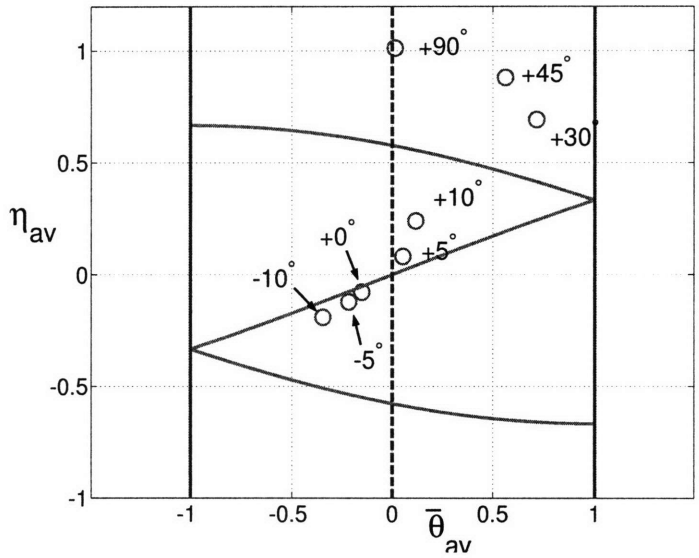

Fig. 3-18: Loading conditions of A710 steel in the plane of stress triaxiality η and the Lode angle parameter $\bar{\theta}$ (experimental data from Wierzbicki et al. (2005a), see Table 4.3.)

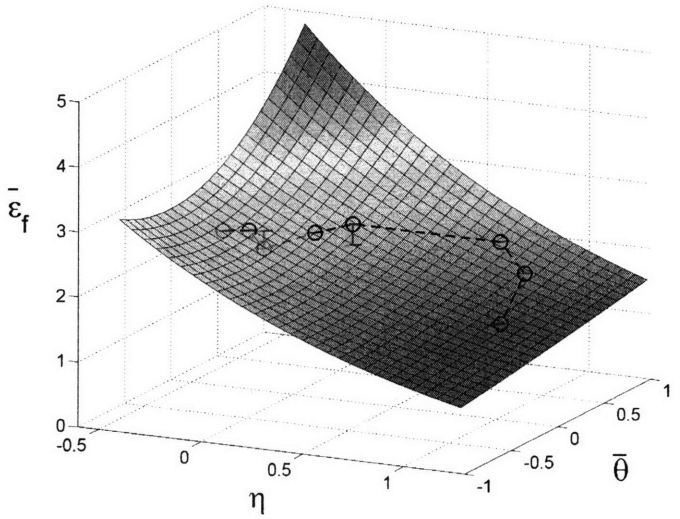

Fig. 3-19: 3D Fracture locus of A710 steel in the space of stress triaxiality, the Lode angle parameter and fracture strain (data points from Wierzbicki et al. (2005a), see Table 4.3.)

3.7 Damage evolution rule

Besides the fracture locus, discussed extensively in the preceding section, the rule of damage evolution is an integral part of the fracture predictive technology. Here, a linear incremental relationship is assumed between the damage indicator D and the equivalent plastic strain $\bar{\epsilon}_p$,

$$D\left(\bar{\varepsilon}_p\right) = \int_0^{\bar{\varepsilon}_p} \frac{d\bar{\varepsilon}_p}{f\left(\eta, \bar{\theta}\right)}, \tag{3.33}$$

where the stress state parameters $\eta(\bar{\varepsilon}_p)$, $\bar{\theta}(\bar{\varepsilon}_p)$ are unique functions of the equivalent plastic strain. A material element is considered to fail when the limit of ductility is reached, $\bar{\varepsilon}_p = \bar{\varepsilon}_f$, so that $D(\bar{\epsilon}_f) = D_c = 1$. In the limiting case (for example proportional loading), when the parameters $(\eta, \bar{\theta})$ are constant over the loading cycle, Eq. (3.33) can be integrated to give

$$\bar{\varepsilon}_f = f\left(\eta, \bar{\theta}\right) = \hat{\varepsilon}_f\left(\eta, \bar{\theta}\right), \tag{3.34}$$

which reduces to the 3D fracture locus $\hat{\varepsilon}_f\left(\eta, \bar{\theta}\right)$. However, in most tests on various types of specimens, the stress state parameters $(\eta, \bar{\theta})$ are variable. The shape of the fracture locus will then depend on whether the initial, final or some average value of these parameters is considered.

The above discussion emphasized the intrinsic difficulty in constructing a unique fracture locus. In this paper, it is proposed to determine the fracture locus based on the average value of the parameters $(\eta, \bar{\theta})$ in the loading process.

$$\eta_{av} = \tfrac{1}{\bar{\varepsilon}_f} \textstyle\int_0^{\bar{\varepsilon}_f} \eta\left(\bar{\varepsilon}_p\right) d\bar{\varepsilon}_p \quad , \quad \bar{\theta}_{av} = \tfrac{1}{\bar{\varepsilon}_f} \textstyle\int_0^{\bar{\varepsilon}_f} \bar{\theta}\left(\bar{\varepsilon}_p\right) d\bar{\varepsilon}_p. \tag{3.35}$$

The function $\eta(\bar{\varepsilon}_p)$ and $\bar{\theta}(\bar{\varepsilon}_p)$ are known from the numerical simulation of the tests and the equivalent strain to fracture $\bar{\epsilon}_f$ is determined from mapping of the measured displacement to fracture into calculated strain to fracture. In all the calibration efforts presented in the preceding section, the average parameters $(\eta_{av}, \bar{\theta}_{av})$, defined by Eq. (3.35) were used. The 3D fracture locus constructed on the bases of the average values is then used as a reference surface for more complex loading paths.

3.8 Discussion and conclusion

Classical metal plasticity J2 theory assumes that the hydrostatic pressure has no effect or negligible effect on the material strain hardening, and that the flow stress is independent of the third stress invariant (or Lode angle parameter). However, new experiments coupled with numerical simulations have shown that both the pressure effect and the effect of the third stress invariant should be included in the metal plasticity. A new form of an asymmetric metal plasticity model, considering both these two effects, is postulated. Calibration methods are discussed. Experimental results on aluminum 2024-T351 validated the new plasticity model.

From the similarity between yielding surface and fracture locus, the asymmetric 3D fracture locus, in the space of equivalent fracture strain $\bar{\epsilon}_f$, stress triaxiality η and the Lode angle parameter $\bar{\theta}$, is developed. Two methods of calibration of the fracture locus are suggested and discussed. One uses "classical" specimens and tests, another one uses the newly designed butterfly specimen under biaxial testing. The test results of Bao (2003) on aluminum 2024-T351 and the data points of A710 steel validated the postulated 3D asymmetric fracture locus.

The work in this paper proposes an extension to the classical metal plasticity and ductile fracture locus, but this extension may not be necessary for all metal materials. For example, the 1045 steel shows no obvious effect of hydrostatic pressure and Lode angle dependence on metal plasticity (Bai et al., 2006b), and the DH36 steel shows no apparent dependence on the Lode angle parameter on the fracture locus (Bai et al., 2006b). Hence, every material needs a careful executed calibration procedure with regards to both plasticity and fracture. A linear incremental dependence of the damage function $D(\bar{\varepsilon}_p)$ on the equivalent plastic strain (see Eq. (3.33)) was shown to work well for monotonic loading. In the case of reverse straining or more complicated loading paths, a nonlinear incremental rule must be considered (Bai et al., 2006a). This subject will be studied in Chapter 7.

Chapter 4

Design of butterfly specimen

In this chapter, a novel experimental technique is presented to characterize the fracture behavior of metals under bi-axial and tri-axial states of stress. A unique feature of this technique is that a wide range of stress triaxiality η and Lode angle parameter $\bar{\theta}$ is achieved using only one type of suitably designed specimens. These specimens are mounted in a custom-made testing equipment designed to work with a universal 200 KN kinematically driven testing machine. By suitably changing orientation of the specimen with respect to the loading direction, one can obtain various stress states from pure tension through tension/shear, shear, shear/compression, and all the way to axial compression. An optical measurement system was used to acquire an accurate displacement field of the specimen. Local stresses and strains are determined from a detailed numerical simulation of the new compound curvature "butterfly" specimen. The true stress-strain was obtained through an iterative procedure and served as an input to ABAQUS/Standard FE modeling of the specimen response. A good correlation was obtained between numerical simulations and tests in terms of global force-displacement response and the deformed shapes of specimen's gauge section at the point of fracture. By comparing the test with simulation, one can determine the magnitude of the equivalent strain at the point of fracture as well as the history of stress triaxiality and the Lode angle parameter. Based on these results, a 3D fracture locus was constructed in the space of equivalent strain to fracture, stress triaxiality and the Lode angle parameter.

4.1 Introduction

There are two types of classical specimens for fracture study. One is compression of short cylinders (the so-called upsetting test), which are often performed to investigate fracture of ductile materials under negative stress triaxiality. Ductile fracture in upsetting tests was first studied experimentally by Kudo and Aoi (1967), who established an empirical fracture locus in the space of principal strains. This result was later confirmed by a number of investigators (eg. Kuhn and Dieter (1977); Thomason (1968, 1969); Ganser et al. (2001)). Wierzbicki et al. (2002); Bao and Wierzbicki (2005) analytically transformed the fracture locus from the space of the principal strains into the space of the equivalent strain to fracture and stress triaxiality.

Another commonly used type of test in ductile fracture is the tensile test on unnotched and notched round bars (eg. Hancock and Mackenzie (1976); Johnson and Cook (1985); Mirza et al. (1996); Hopperstad et al. (2003)). It should be noted that those specimens cover the range of high stress triaxiality. Due to the limitation of experimental method, fracture loci determined from those tests are often extrapolated to small and even negative stress triaxiality (eg. Johnson and Cook (1985)), which is clearly a far reaching assumption.

Bao and Wierzbicki (2004a,b) found that the fracture locus is not necessary represented by a smooth, monotonic curve in the entire range of stress triaxiality due to different fracture mechanisms operating at different stress triaxiality ranges. A total of eleven distinct tests including shear, shear/tension tests, conventional upsetting and tensile tests were carried out. In the above test program, specimens with different shapes such as short cylinders, round bars with notches, and flat specimens were used. It is not convenient in the industrial environment to machine different types of specimens and construct the fracture envelope based on those specimens. Also, round specimens are not easy to be manufactured from sheets and plates, which are widely used in the automotive and airplane industry.

In this chapter, a novel type of a flat compound curvature specimen, which is suitable to characterize fracture behavior of metals under a wide range of stress triaxiality, is developed. Using a custom-made Universal Biaxial Testing Device (UBTD), new specimens are loaded under different angles to obtain fracture properties in different stress states. Local stresses and strains are determined from detailed numerical simulations. The detailed methodology of determination of fracture properties of ductile materials is illustrated by constructing the fracture locus for A710 steel.

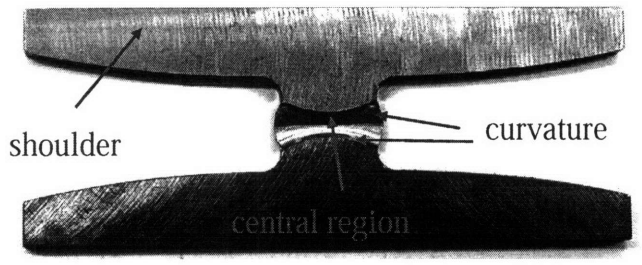

Fig. 4-1: A newly designed specimen which has a gauge section with a double curvature profile.

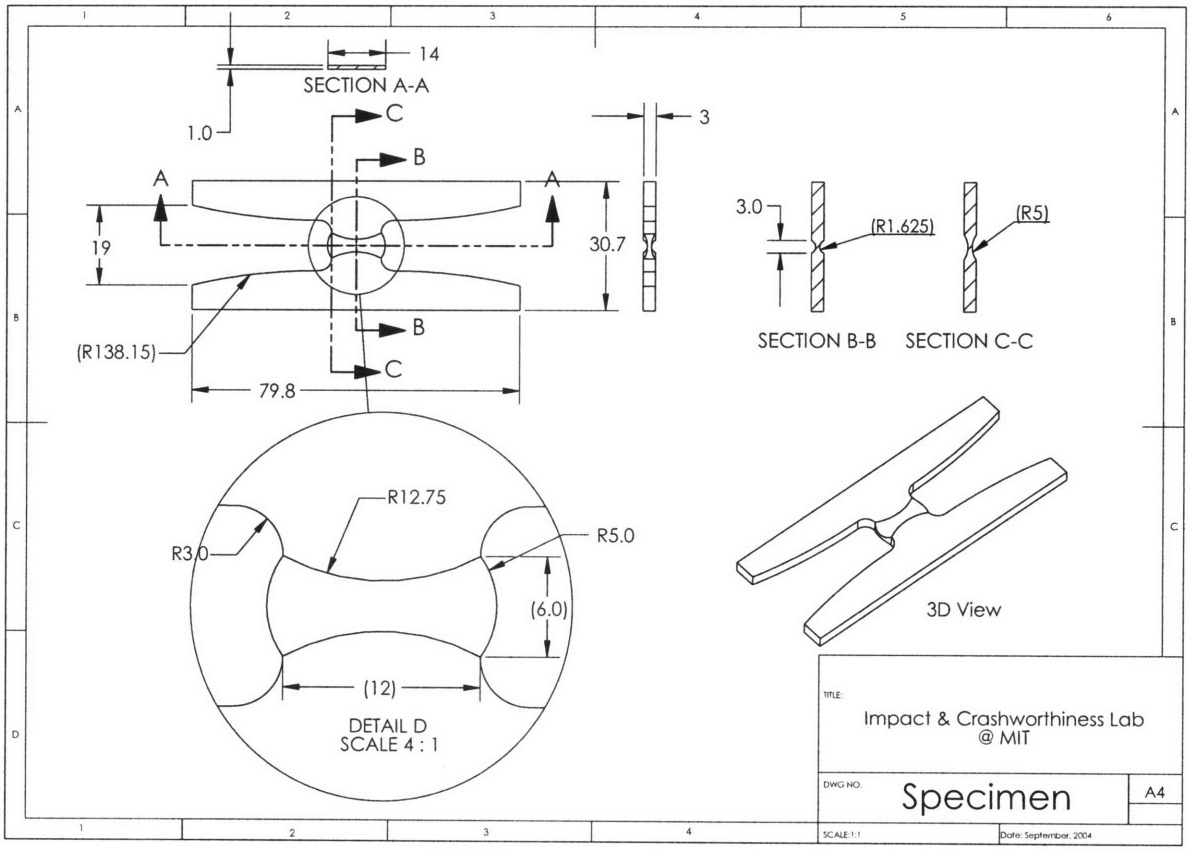

Fig. 4-2: Detailed geometry of the newly designed specimen

4.2 Specimen design

The challenge of the design process is to determine geometry of a flat specimen such that fracture initiates at the desired gauge area instead of free boundaries, and at the same time the specimen experience a wide range of stress states at the location of crack formation under different loadings. This is a difficult task because due to imperfections crack may start unexpectedly at boundaries, which is the case with the Iosipescu shear test.

The gauge section of the novel specimen involves two curvatures (see Fig. 4-1) in order to ensure that strain is highly localized in the central region, which dramatically reduces the possibility of crack formation at the boundaries. The long shoulders of the specimen provide sufficient gripping area, which is important to hold the specimen securely. Another feature of the specimen is the jump of the thickness between the shoulder and gauge section, which makes the shoulder stay rigid during the entire loading process. The detailed geometry of the specimen in shown in Fig. 4-2.

4.3 Methodology

As an example, material A710 steel is taken to demonstrate the new technique for the determination of the fracture properties of ductile metals. The technique consists of both physical testing and numerical simulation.

4.3.1 Testing

Specimens are mounted in a custom-made testing equipment (UBTD) designed to work with a universal 200 KN kinematically driven machine, see Fig. 4-3. By suitably changing orientation of the specimen with respect to the loading direction, one can obtain various stress states from pure tension through tension/shear, shear, shear/compression, and all the way to axial compression. The setup shown in Fig. 4-3 corresponds to $\Theta = 10°$, which represents either a shear/tension or shear/compression condition. One LVDT (Linear Variable Displacement Transducer) and two load cells were built in to the UBTD to measure the travel of the left part of the UBTD and horizontal forces acting on the device, respectively. The vertical force acting on the UBTD is measured by the MTS universal testing machine with a 200 KN load cell. A detailed description of the UBTD can be found in a recent paper by Mohr (2003); Mohr and Doyoyo (2004).

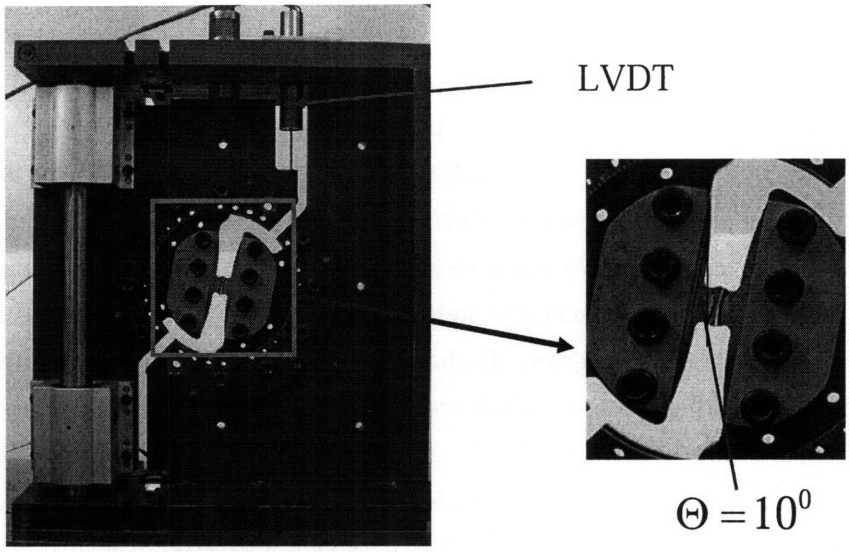

Fig. 4-3: A universal biaxial testing device designed by Mohr and Doyoyo (2004). Specimen is positioned for 10° loading.

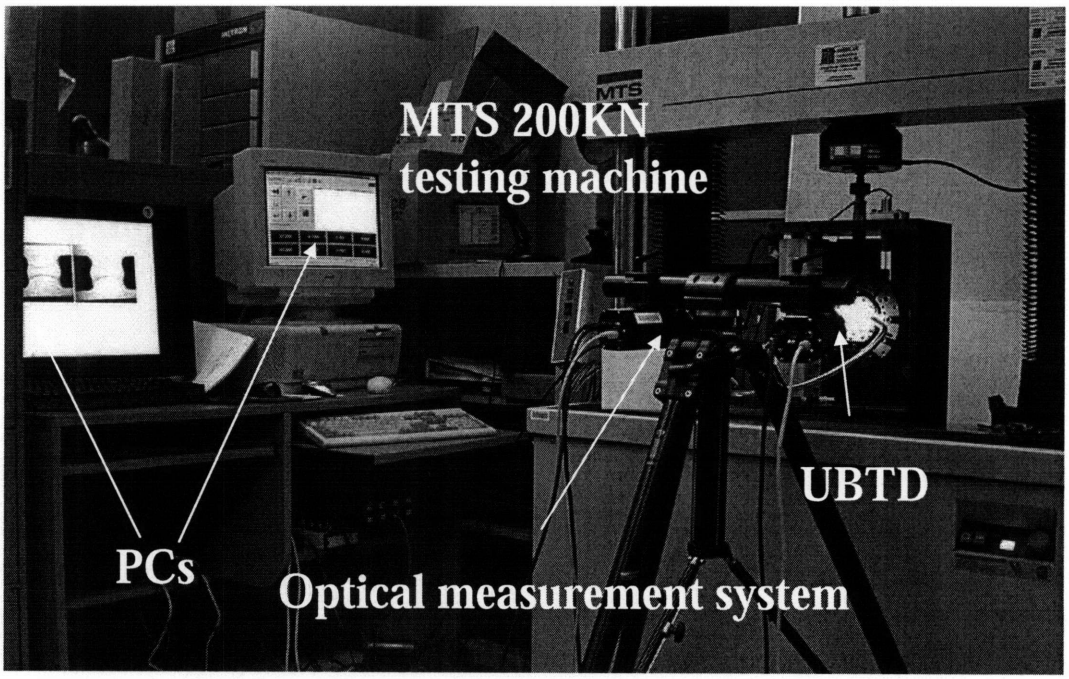

Fig. 4-4: The experimental set-up.

An optical measurement system developed by Correlated Solutions Inc. is employed to determine the displacement field of the specimen. The specimen is painted before testing with a fine spectrum of dots for that purpose. The optical system consists of two high-resolution cameras, a digital photo acquisition device, and a post-processing program. The cameras are calibrated and remain in the same position during the entire series of experiments. Digital images are taken from two different viewpoints simultaneously during the test based on the setup of the two cameras. The displacement field of specimen is then calculated from those images using the post-processing program. It should be noted that the optical measurement system and the MTS load-displacement measurement system are synchronized. The whole experimental system is illustrated in Fig. 4-4. A total of 17 specimens were tested under 8 different loading conditions $-10°$, $-5°$, $+0°$, $+5°$, $+10°$, $+30°$, $+45°$ and $+90°$. A detailed description of the tests is listed in Table 4.1. All the specimens after fracture are shown in Fig. 4-5.

Table 4.1: A summary of tests of butterfly specimens under eight loading conditions (A710 steel)

Loading cases	Loading condition	Number of specimens tested
1	$-10°$, compression and shear	2
2	$-5°$, compression and shear	1
3	$+0°$, shear	2
4	$+5°$, tension and shear	2
5	$+10°$, tension and shear	2
6	$+30°$, tension and shear	2
7	$+45°$, tension and shear	2
8	$+90°$, tension	4

All of the tests were run at a very low speed, 0.1 mm/min, in order to capture the initiation of crack. Due to high ductility of the material, the tests were able to be stopped before the specimen is completely fractured for all the loading cases except for 0 degree tension (pure shear case). A post-mortum examination of those specimens provides a good indicator of the location of crack initiation. It can be seen that the crack initiates at the center of the gauge section in all seven cases, which is exactly what the specimen was designed for. It is believed that this is also the case for 0 degree tension. As an example, the crack for the 90 degrees tension loading case is displayed in Fig. 4-6.

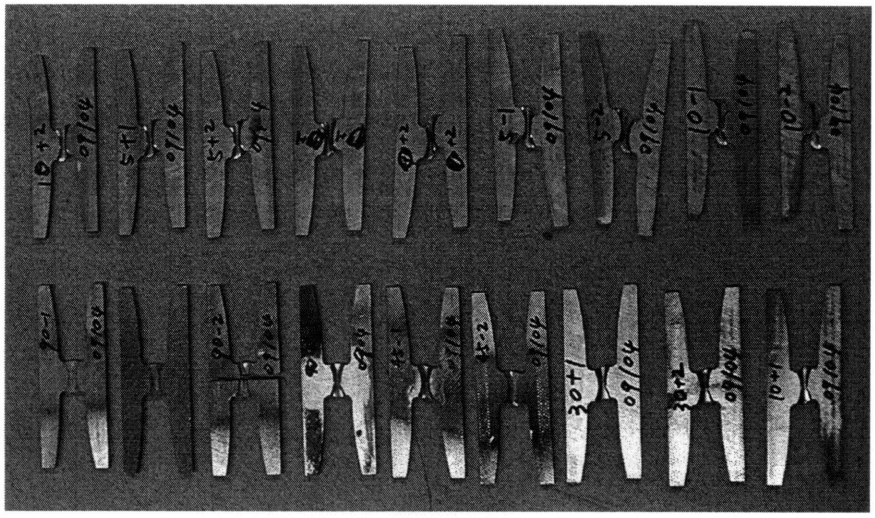

Fig. 4-5: All the specimens of A710 steel after fracture.

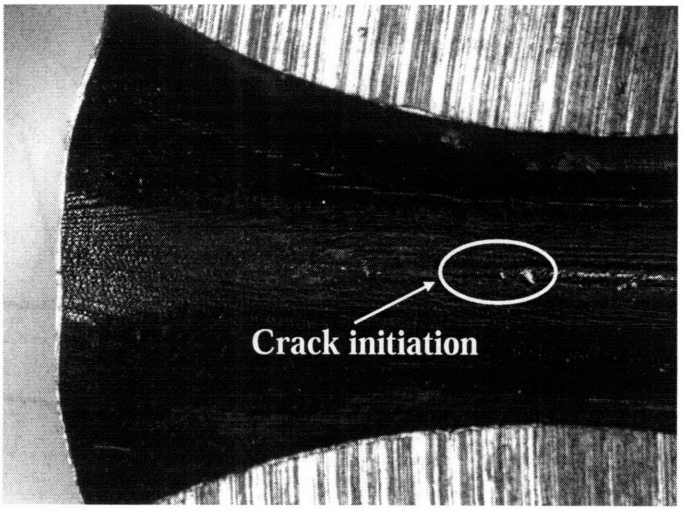

Fig. 4-6: Crack initiation in 90° tension.

4.3.2 Finite element simulation

It was postulated that fracture is governed by the local stresses, strains and their histories. However, it is very difficult or even impossible to determine individual components of stress and strain tensors at the location of fracture directly from physical experiments, which brings the finite element analysis to this study.

Corresponding numerical simulations of all the eight tests were performed using a commercial finite element code, ABAQUS/STANDARD, in order to obtain individual components of stress and strain tensors at the location of fracture. The specimen was modeled as 8-node solid elements (Fig. 4-7). The whole model consists of 52776 solid elements with smaller elements at the gauge section and larger ones at the shoulder. The size of the smallest elements is $0.03 \times 0.08 \times 0.15mm$.

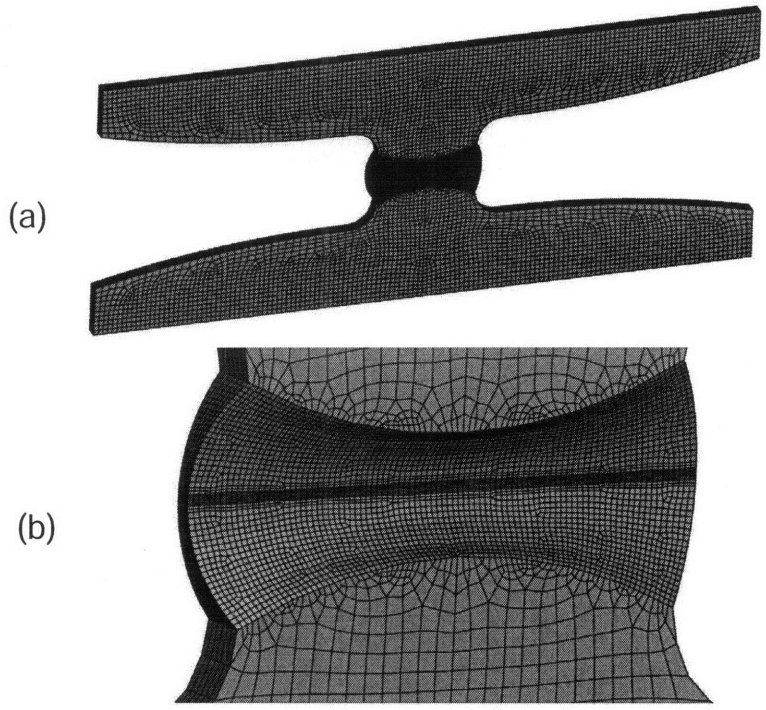

Fig. 4-7: (a) Finite element discretization of butterfly specimen (A710 steel), (b) a close view of the central region of the specimen.

During the tests, the horizontal loading cells measured compression forces when the specimens were mounted before the test. Still, the J2 plasticity material model was used in this study because the initial imposed compression force was too small to cause the material to yield, and there was no need to introduce kinematic hardening. The material input consists of the stress-strain curve (Fig. 4-8), which was determined from standard tensile tests on flat dog-bone specimens and corresponding numerical simulations based on the method developed in an earlier report Bao et al. (2004). Both the dog-bone specimens and the compound specimens were cut from the same block of A710 steel.

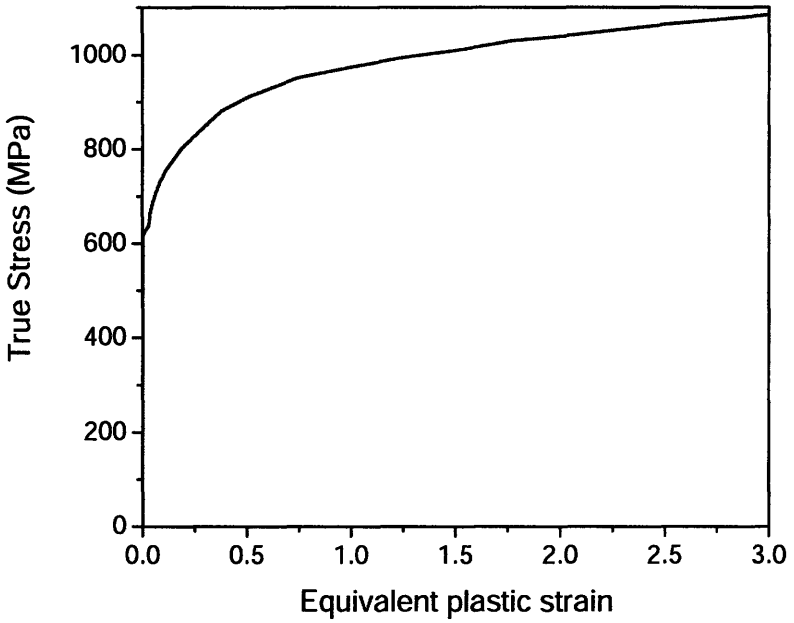

Fig. 4-8: Calibrated stress-strain curve of A710 steel.

A constant vertical velocity is imposed to one end of the model of the compound specimen while the other end is fixed. Additionally, initial horizontal forces detected by the two horizontal load cells are introduced in the FE model. It should be noted that the stiffness of the UBTD is limited because of the use of the aluminum bearings. In order to simulate the boundary conditions applied to the specimen more accurately, horizontal springs are introduced at every node located in the clamped area. The position and area of the clamped region are measured from deformed specimens. A number of runs were performed with different spring stiffness for each loading case in order to quantify the magnitude of the stiffness until the best correlation with experimental results was achieved (Bao et al., 2004).

Indeed, the correlations between experiments and numerical simulations are very good for each case in terms of deformed shape of specimens and force-displacement responses. As an example, Fig. 4-9 shows the comparison of deformed specimens at or right after the point of fracture for loading cases #6. The numerical simulation successfully captured the highly localized deformation at the gauge section and also the deformed shape of edge curvatures. The comparison of the force-displacement response for all eight cases is shown in Fig. 4-10. It should be emphasized that there are two types of output from the experimental results. One is the direct output from the MTS machine, i.e. applied vertical loading vs. travel of

the LVDT; the other is the output from the optical measurement system. It is seen that the numerically-obtained force-displacement response correlates very well with the one that is made up of the measured displacement from the optical system for all of the cases. The curves have a perfect agreement with the response acquired directly from the MTS machine for all eight cases except for the 90 degree tension case, in which a slight slip between the grips and the specimen is observed due to the high level of force (11kN). It is clear that the shoulder of the specimen remains rigid during the tests and the vertical stiffness of the whole system is sufficiently large.

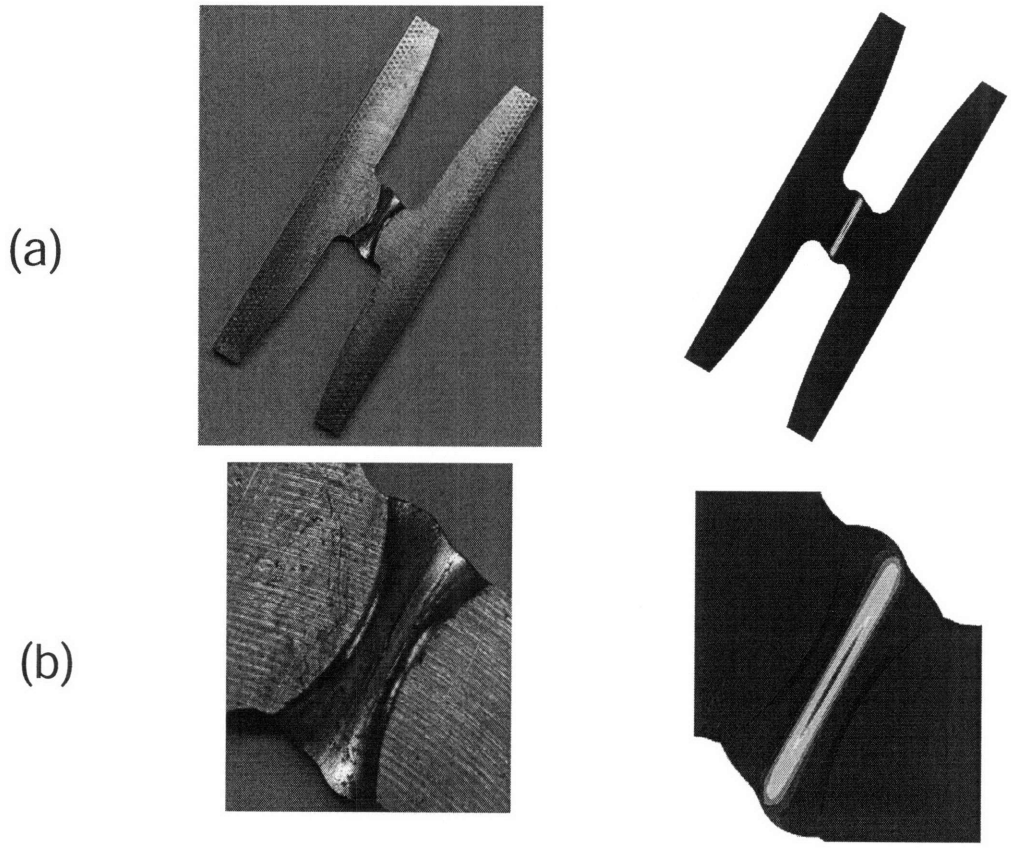

Fig. 4-9: (a) Comparison of deformed butterfly specimens under +30° loading (A710 steel), (b) a close view of the central region of the specimen.

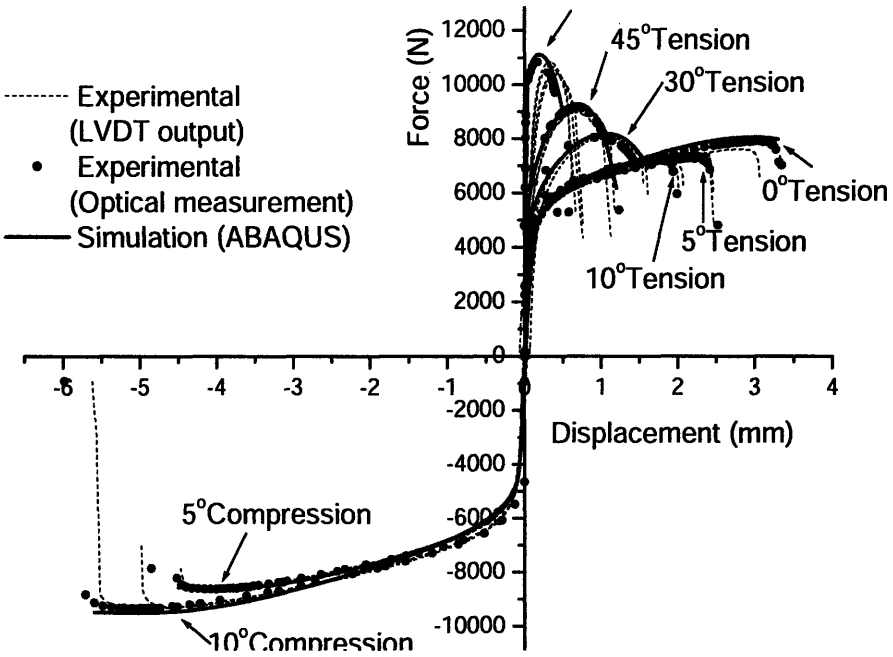

Fig. 4-10: Comparison of force-displacement response for all eight cases (A710 steel).

4.4 Analysis of the results

The numerical simulation provides the magnitudes of the individual components of stress and strain tensors at the locations of crack formation. The correlation of the experimental and numerical results is almost perfect in terms of the force-displacement response and the deformation shapes for all the cases considered in this study. It is recognized that getting the force-displacement response right does not guarantee the agreement in terms of local quantities. However, getting a correct force-displacement response is a necessary condition for a perfect simulation. With the perfect correlation on the force-displacement response and the deformed shape, the local quantities obtained from simulations are believed to reasonably represent the real values.

A careful examination of the fractured specimens indicates that cracks initiate at the center of the gauge section in all the cases. However, it is difficult to determine directly from the experiments whether fracture starts from the middle of the cross-section or from the surface. In other words, the experiments only explicitly gave the location of crack imitation in the main plane but not in the thickness direction.

The strain gradient through the thickness is small (the difference of strain between the

middle of thickness and the surface is less than 5%) due to the small thickness of the gauge section of the specimen. However, the difference of the stress triaxiality is not negligible and in fact is about 20% between those two locations. Therefore, the exact location of crack formation is determined from numerical simulations by checking all the elements located at the center of the gauge section from the middle of thickness to the surface. There is sufficient experimental evidence that in both the negative stress triaxiality range and high stress triaxiality range, the equivalent strain to fracture decreases with stress triaxiality. Therefore, it is likely that the crack initiates at the location with the highest stress triaxiality because the strain gradient through the thickness is small. The locations of the crack in the last column of Table 4.2 were based on this above condition. A summary of the locations of crack formation is given in Table 4.2. The magnitudes of the displacement to fracture u_f (taken from the tests) are also collected in Table 4.2.

Table 4.2: List of locations of fracture initiation of butterfly specimens (A710 steel)

No.	Loading condition	Displacement to fracture (mm) *	Location in the main plane	Location in the thickness direction
1	$-10°$	$u_f = -5.59$	Center	Surface
2	$-5°$	$u_f = -4.48$	Center	Surface
3	$+0°$	$u_f = 3.27$	Center	Surface
4	$+5°$	$u_f = 2.40$	Center	Middle of thickness
5	$+10°$	$u_f = 1.94$	Center	Middle of thickness
6	$+30°$	$u_f = 1.43$	Center	Middle of thickness
7	$+45°$	$u_f = 1.08$	Center	Middle of thickness
8	$+90°$	$u_f = 0.41$	Center	Middle of thickness

* *The combined displacement to fracture is denoted by* u_f.

In order to determine the fracture locus in the space of the equivalent strain to fracture, stress triaxiality and the Lode angle parameter, one needs to examine the stress triaxiality, the Lode angle parameter and equivalent strain that the material experiences at the location of crack initiation. The numerical simulations provide the values of stress and strain components and also load-displacement responses. The relationship between displacement and equivalent strain at the critical location can be obtained from the numerical simulation for each case. Also, the equivalent strain to fracture can be determined as the equivalent strain, which corresponds to the measured displacement to fracture. The displacement to fracture is acquired by both observations during experiments and the force-displacement responses.

There is a significant load drop in the force-displacement responses in all the tests. This drop is taken as the point of fracture initiation in this study. It is true that load could still increase even if structure starts to crack because of material hardening. However, the strain hardening of this material is small, and it is observed that cracks grow rapidly during the tests. Therefore, it is reasonable to take the beginning of the drop as an approximate indication of the onset of fracture since those two stages are close to each other.

Life would have been easier if the stress triaxiality and the Lode angle parameter were constant during plastic deformation. The evolution of these two parameters for all eight loading cases are shown in Fig. 4-11 and 4-12. In order to construct the fracture locus in the space of equivalent strain, stress triaxiality and the Lode angle parameter, as a first approximation, an average stress triaxiality and an average Lode angle parameter, defined by

$$\eta_{av} = \frac{1}{\bar{\varepsilon}_f}\int_0^{\bar{\varepsilon}_f} \eta\left(\bar{\varepsilon}_p\right) d\bar{\varepsilon}_p \quad , \quad \bar{\theta}_{av} = \frac{1}{\bar{\varepsilon}_f}\int_0^{\bar{\varepsilon}_f} \bar{\theta}\left(\bar{\varepsilon}_p\right) d\bar{\varepsilon}_p. \tag{4.1}$$

are introduced. A summary of the results of all eight loading cases is listed in Table 4.3. Each data point includes the average stress triaxiality, average Lode angle parameter and the equivalent strain to fracture. If more than one tests were done for a loading case, a mean value of all tests is provided.

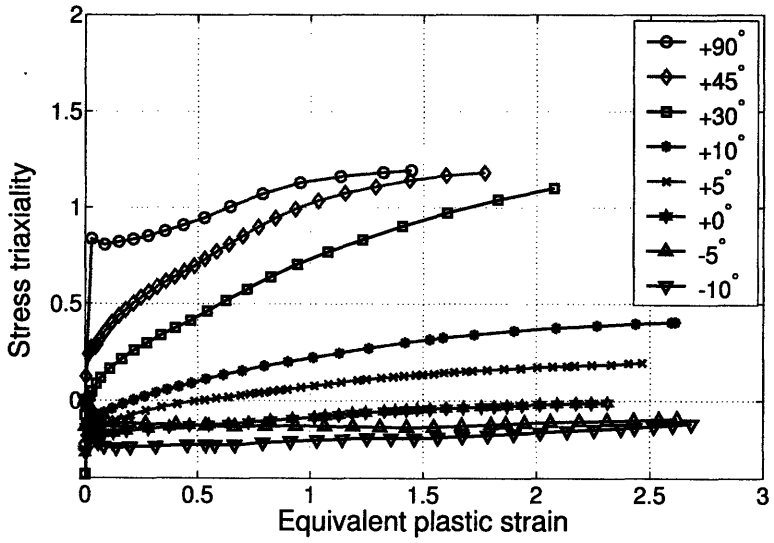

Fig. 4-11: Evolution of the stress triaxiality parameter for all eight loading cases (A710 steel).

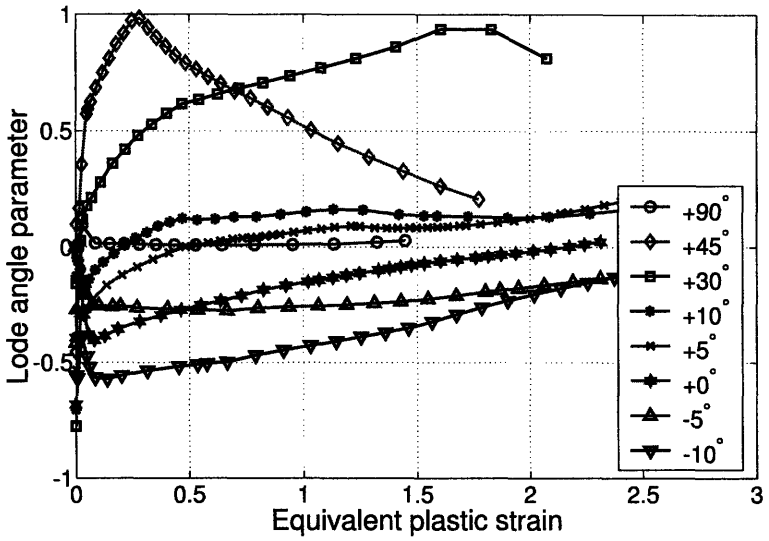

Fig. 4-12: Evolution of the Lode angle parameter for all eight loading cases (A710 steel).

Table 4.3: A summary of test results on A710 steel using butterfly specimens

No.	Loading condition	η_{av}	$\bar{\theta}_{av}$	$\bar{\epsilon}_f$
1	$-10°$, compression and shear	-0.1906	-0.3459	2.6842
2	$-5°$, compression and shear	-0.1216	-0.2164	2.6210
3	$+0°$, shear	-0.0783	-0.1513	2.3136
4	$+5°$, tension and shear	0.0814	0.0532	2.4660
5	$+10°$, tension and shear	0.2405	0.1174	2.6127
6	$+30°$, tension and shear	0.6917	0.7146	2.0754
7	$+45°$, tension and shear	0.8798	0.5617	1.7706
8	$+90°$, tension	1.0118	0.0149	1.4471

For each test, a data point is plot in the space of equivalent strain to fracture and stress triaxiality. There are eight cases with a total of 17 points. For every case, other than case #2, there are at least 2 data points. Now, the 2D fracture locus proposed by Bao (2003) can be constructed in the plane of the equivalent strain to fracture and the average stress triaxiality. A curve is fitted through the average data points, as shown in Fig. 4-13.

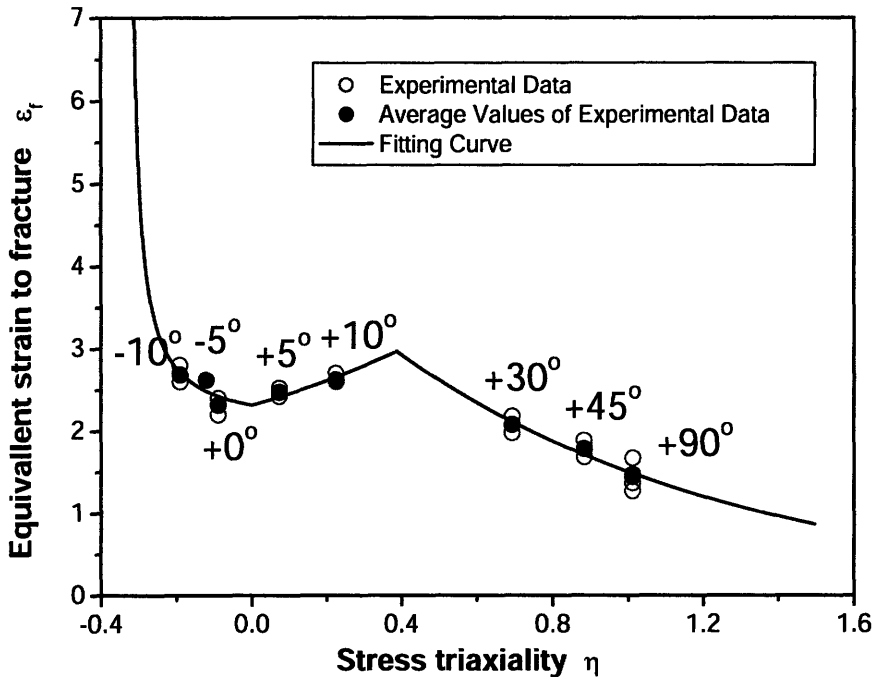

Fig. 4-13: The fracture locus of A710 steel in the space of equivalent strain to fracture and stress triaxiality.

The local cusp around $\eta = \frac{1}{3}$ in Fig. 4-13 vanishes if those data points are re-plotted into a 3D space by introducing the Lode angle parameter $\bar{\theta}$. Construction of the 3D fracture locus using the obtained data points (Table 4.3) is presented in Section 3.6.2.

4.5 Discussion and conclusion

A novel experimental technique to characterize fracture behavior of metals under bi-axial and tri-axial state of stress is developed in this study. This technique needs only one type of suitably designed specimen and one finite element mesh for a wide range of stress triaxiality and Lode angle parameter. Based on the results of physical tests and the corresponding numerical simulation, a fracture envelope for A710 steel is constructed in the space of equivalent strain to fracture and stress triaxiality. These data is also used to construct the 3D fracture locus $\hat{\varepsilon}_f(\eta, \bar{\theta})$, see Section 3.6.2.

It should be noted that the results presented are based on the numerical simulation on the finite element model with over 50,000 solid elements. Another model was developed with

double size of elements in the gauge section (very fine mesh size) to further assess the effect of mesh size. The difference between those two models in terms of the equivalent strain at the location of crack initiation is about 3-12%. Although the effect of mesh size needs more work in the future, the 3D fracture locus calibrated from butterfly specimens is already partially removed the mesh size effect since only one mesh is used for all simulations.

The tests on A710 steel presented in this chapter were conducted on the MTS uniaxial testing machine with the UBTD device. A further improvement of the present experimental technique is to perform the tests on butterfly specimens of 1045 steel using INSTRON biaxial testing machine. See Section 7.5 for details.

Chapter 5

Application of Mohr-Coulomb Criterion to Ductile Fracture

The Mohr-Coulomb (M-C) failure criterion is revisited with an objective of describing ductile fracture of isotropic crack-free solids. This criterion has been extensively used in rock and soil mechanics as it correctly accounts for the effects of hydrostatic pressure as well as the Lode angle parameter. It turns out that these two parameters, which are critical for characterizing failure of geo-materials, also control fracture of ductile metals (Wilkins et al., 1980; Bai and Wierzbicki, 2007a; Xue, 2007a; Barsoum, 2006).

The local form of the M-C criterion is transformed to the spherical coordinate system, where the axes are the equivalent strain to fracture $\bar{\epsilon}_f$, the stress triaxiality η, and the normalized Lode angle parameter $\bar{\theta}$. For a proportional loading, the fracture surface is shown to be an asymmetric function of $\bar{\theta}$. A detailed parametric study is performed to demonstrate the effect of model parameters on fracture. It was found that the M-C fracture locus predicts almost exactly the exponential decay of the material ductility with stress triaxiality, which is in accord with theoretical analysis of Rice and Tracey (1969) and the empirical equation of Johnson and Cook (1985). The M-C criterion also predicts a form of Lode angle dependence which is close to parabolic. The fracture tests reported by Bao (2003) and Bao and Wierzbicki (2004a) on 2024-T351 aluminum alloy are used to check the model. Calibrated from just two tests for fracture, the model predicts the remaining nine tests with good accuracy.

Another advantage of the M-C failure model is that it predicts uniquely the orientation of the fracture surface. It is shown that the direction cosines of the unit normal vector to the fracture surface are functions of the "friction" coefficient in the M-C criterion. Since there

are only two free parameters in the physically based M-C model, it has a great potential to be used as an engineering tool for predicting ductile fracture.

5.1 Introduction

The Mohr-Coulomb (M-C) failure criterion (Coulomb, 1776; Mohr, 1914) has been widely used in rock and soil mechanics (e.g. Zhao (2000); Palchik (2006)) and other relatively brittle materials (e.g. Lund and Schuh (2004)). This is a physically sound and simple failure model. Fundamentals and applications of this model can be found in many textbook, monographs and research papers. As a stress-based criterion, the Mohr-Coulomb model has good resolution for materials that fail in the elastic range and/or under small strain plasticity, such as rock, soil, concrete and so on.

There have recently been several successful applications of this model for predicting fracture of ceramics under static and dynamic loading (Fossum and Brannon, 2006). The M-C criterion is a special case of the Sandia GeoModel (Fossum and Brannon, 2005). A unique feature of the M-C model is an explicit dependence on the Lode angle parameter, which is missing in almost all existing models of ductile fracture. The purpose of the present paper is to demonstrate the applicability of the M-C criterion to ductile fracture of uncracked bodies.

Meanwhile, the ductile fracture community took a different path. In search for a physically based fracture model, the mechanism of nucleation, growth and coalescence of void was identified and extensively studied. Due to fundamental work by McClintock (1968); Rice and Tracey (1969); Gurson (1975); Tvergaard and Needleman (1984), it was determined that ductile fracture is mostly affected by the hydrostatic pressure. Accordingly, the equivalent strain to fracture, which is a measure of material ductility, was made dependent on the first invariant of the stress tensor. The mixed stress-strain formulation of a fracture criterion is justifiable because, well into the plastic range, the resolution of strains is much larger than stresses, as explained in Fig. 5-1. Another feature of the Gurson-Tvergaard-Needleman (GTN) model (Tvergaard and Needleman, 1984) is that it describes well the predominate tensile fracture, characterized by relatively high stress triaxiality, but fails to predict shear fracture. Attempts are currently underway to extend the void growth and coalescence model to describe shear fracture (Xue, 2007a; Nahshon and Hutchinson, 2007). The M-C criterion

is an extension of the maximum shear stress failure criterion and therefore it is well poised to predict shear fracture.

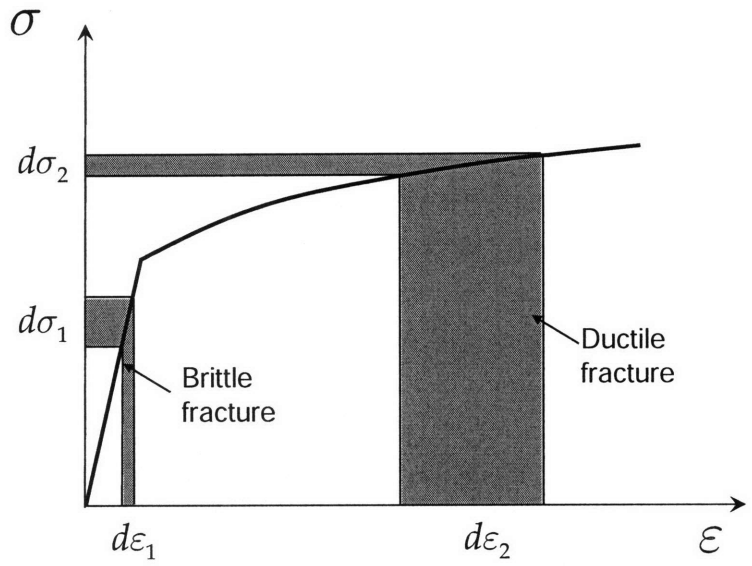

Fig. 5-1: Different resolution quality of strain and stress parameters: the stress parameters have good resolutions in elastic region, and the strain parameters have good resolutions in plastic region.

In parallel with the "physically based" models of ductile fracture, a number of empirical fracture models have earned a permanent place in the literature (Cockcroft and Latham, 1968; Hancock and Mackenzie, 1976; Wilkins et al., 1980; Johnson and Cook, 1985; Bao and Wierzbicki, 2004a; Wierzbicki and Xue, 2005; Bai and Wierzbicki, 2007a). These models were based on extensive test programs on bulk material and/or sheets. One of the most comprehensive series of experiments involving tensile tests on unnotched and notched round bars, upsetting tests and shear tests was reported by Bao (2003); Bao and Wierzbicki (2004a). Even more recently, Wierzbicki et al. (2005a) performed a series of fracture tests on specially designed butterfly specimens under combined tension/shear/compression loading. Results of bi-axial fracture tests on tubular specimens in the tension/torsion loading frame was published by Barsoum and Faleskog (2007). All of these recent tests have proven that the material ductility depends on both stress triaxiality and the Lode angle parameter. These two effects are actually captured by the M-C model, as will be shown in the paper.

A particular case of Mohr-Coulomb criterion is the maximum shear stress criterion. It

has been shown by Lee (2005) that the maximum shear stress criterion predicts well plane stress fracture for 2024-T351 aluminum alloy, see Fig. 5-2. A comparison of maximum shear stress criterion with other models was reported by Wierzbicki et al. (2005b). One main shortcoming of the maximal shear stress fracture criterion is the missing pressure dependence. The M-C criterion removes this shortcoming. To increase resolution of the ductile fracture prediction, the M-C criterion is transformed to a strain-based formula under the assumption of monotonic loading. A parametric study is performed to get a better insight into this fracture model. The experimental results of Bao and Wierzbicki on 2024-T351 aluminum alloy (Bao, 2003; Bao and Wierzbicki, 2004a; Wierzbicki et al., 2005b) are used to validate the new form of the Mohr-Coulomb criterion.

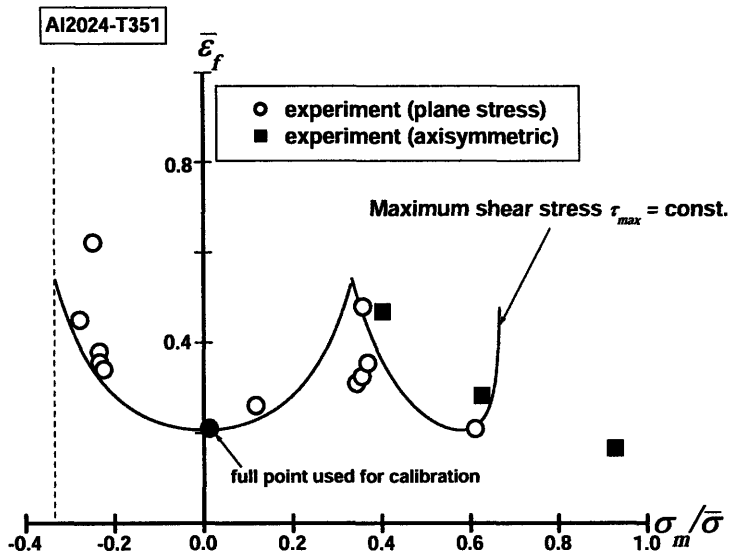

Fig. 5-2: Application of maximum shear stress failure criterion to ductile fracture for plane stress condition (Lee, 2005; Wierzbicki et al., 2005b).

5.2 Characterization of the stress state

The three invariants of a stress tensor $[\sigma]$ are defined respectively by

$$p = -\sigma_m = -\frac{1}{3}tr([\sigma]) = -\frac{1}{3}(\sigma_1 + \sigma_2 + \sigma_3) \tag{5.1}$$

$$q = \bar{\sigma} = \sqrt{\frac{3}{2}[S] : [S]} = \sqrt{\frac{1}{2}\left[(\sigma_1 - \sigma_2)^2 + (\sigma_2 - \sigma_3)^2 + (\sigma_3 - \sigma_1)^2\right]} \tag{5.2}$$

$$r = \left(\frac{9}{2}[S] \cdot [S] : [S]\right)^{1/3} = \left[\frac{27}{2} det([S])\right]^{1/3} = \left[\frac{27}{2}(\sigma_1 - \sigma_m)(\sigma_2 - \sigma_m)(\sigma_3 - \sigma_m)\right]^{1/3} \tag{5.3}$$

where $[S]$ is the deviatoric stress tensor,

$$[S] = [\sigma] + p[I], \tag{5.4}$$

$[I]$ is the identity tensor and σ_1, σ_2 and σ_3 denote principal stresses. It is assumed that $\sigma_1 \geq \sigma_2 \geq \sigma_3$. Note that the parameter p is positive in compression, but σ_m is positive in tension. It is convenient to work with the dimensionless hydrostatic pressure η, defined by

$$\eta = \frac{-p}{q} = \frac{\sigma_m}{\bar{\sigma}}. \tag{5.5}$$

The parameter η, often referred to as the triaxiality parameter, has been extensively used in the literature on ductile fracture (McClintock, 1968; Rice and Tracey, 1969; Hancock and Mackenzie, 1976; Mackenzie et al., 1977; Johnson and Cook, 1985; Bao, 2003). The second important parameter is the Lode angle θ, which is related to the normalized third invariant ξ through

$$\xi = \left(\frac{r}{q}\right)^3 = \cos(3\theta). \tag{5.6}$$

One can see that that the normalized third deviatoric stress invariant can be expressed in terms of the Lode angle θ (see Malvern (1969); Xu and Liu (1995); ABAQUS, 2005; the derivation is also summarized in Section 5.3.1). Since the range of the Lode angle is $0 \leq \theta \leq \pi/3$, the range of ξ is $-1 \leq \xi \leq 1$. The geometrical represent of Lode angle is shown in Fig. 5-3.

As shown in Fig. 5-3, one can think of three types of coordinate systems to describe the stress state. The first is the Cartesian coordinate system $(\sigma_1, \sigma_2, \sigma_3)$, the second is the cylindrical coordinate system $(\sigma_m, \bar{\sigma}, \theta)$, and the third is the spherical coordinate system $(\bar{\epsilon}_f, \eta, \theta)$, where the equivalent stress $\bar{\sigma}$ is related to the equivalent strain $\bar{\epsilon}$ through the strain hardening function of a material. The coordinate φ is related to the stress triaxiality η by the following equation,

$$\eta = \frac{\sigma_m}{\bar{\sigma}} = \frac{\sqrt{2}}{3} cotan\varphi. \tag{5.7}$$

Furthermore, the Lode angle can be normalized by

$$\bar{\theta} = 1 - \frac{6\theta}{\pi} = 1 - \frac{2}{\pi}\arccos\xi. \tag{5.8}$$

The range of $\bar{\theta}$ is $-1 \leq \bar{\theta} \leq 1$. The parameter $\bar{\theta}$ will be called the Lode angle parameter hereinafter. Now, all stress directions (or loading conditions) can be characterized by the above defined set of parameters $(\eta, \bar{\theta})$. It is easy to show (Wierzbicki and Xue, 2005; Bai and Wierzbicki, 2007a) that $\bar{\theta} = 1$ corresponds to the axisymmtric tension, $\bar{\theta} = 0$ corresponds to the generalized shear (or plastic plane strain) loading condition, and $\bar{\theta} = -1$ corresponds to the axisymmtric compression. Special attention is given to the plane stress state. It was shown by Wierzbicki and Xue (2005); Bai and Wierzbicki (2007a) that the plane stress condition uniquely relates the parameters η and ξ or $\bar{\theta}$ through

$$\xi = cos(3\theta) = cos\left[\frac{\pi}{2}(1-\bar{\theta})\right] = -\frac{27}{2}\eta\left(\eta^2 - \frac{1}{3}\right). \tag{5.9}$$

In this paper, the Mohr-Coulomb model will be reformulated in the spherical coordinate system.

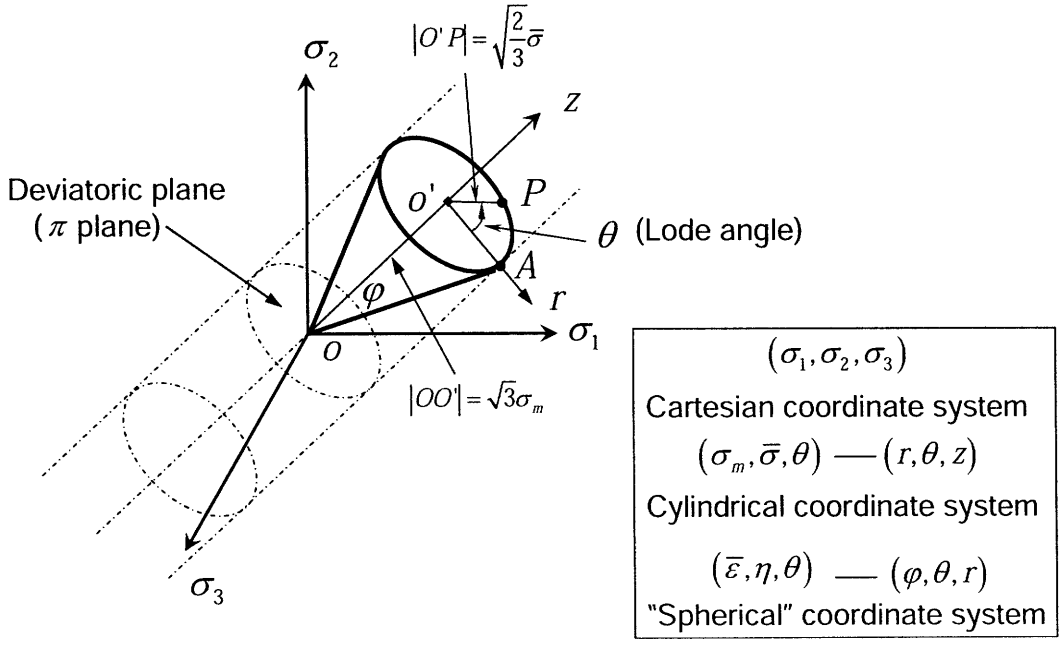

Fig. 5-3: Three types of coordinate system in the space of principal stresses

5.3 Transformation of Mohr-Coulomb to the space of $(\bar{\epsilon}_f, \eta, \bar{\theta})$

Consider a material element subjected to three principal stresses σ_1, σ_2, and σ_3. At an arbitrary cutting plane defined by the unit normal vector (ν_1, ν_2, ν_3), the shear stress and the corresponding normal stress are given by

$$\tau = \sqrt{\nu_1^2\nu_2^2\left(\sigma_1-\sigma_2\right)^2 + \nu_2^2\nu_3^2\left(\sigma_2-\sigma_3\right)^2 + \nu_3^2\nu_1^2\left(\sigma_3-\sigma_1\right)^2}, \tag{5.10}$$

$$\sigma_n = \nu_1^2\sigma_1 + \nu_2^2\sigma_2 + \nu_3^2\sigma_3, \tag{5.11}$$

where the three components ν_1, ν_2 and ν_3 are constrained by $\nu_1^2 + \nu_2^2 + \nu_3^2 = 1$.

The Mohr-Coulomb failure criterion says that fracture occurs when the combination of normal stress and shear stress reach a critical value, according to

$$\left(\tau + c_1\sigma_n\right)_f = c_2, \tag{5.12}$$

where c_1, c_2 are material constants. The constant c_1 is often referred to as a "friction" coefficient, and c_2 is shear resistance. The ranges of c_1 and c_2 are $c_1 \geq 0$ and $c_2 > 0$. In the limiting case of $c_1 = 0$, the M-C criterion reduces to the maximal shear stress criterion.

The applicability of the M-C failure criterion to capture ductile fracture will be shown in Section 5.8. In order to find on which cutting plane the M-C criterion will be met first, one must solve the following maximum value problem:

$$\begin{cases} Max\left\{\sqrt{\nu_1^2\nu_2^2\left(\sigma_1-\sigma_2\right)^2 + \nu_2^2\nu_3^2\left(\sigma_2-\sigma_3\right)^2 + \nu_3^2\nu_1^2\left(\sigma_3-\sigma_1\right)^2} + c_1\left(\nu_1^2\sigma_1 + \nu_2^2\sigma_2 + \nu_3^2\sigma_3\right)\right\} \\ Subject\ \ to \quad \nu_1^2 + \nu_2^2 + \nu_3^2 = 1 \end{cases} . \tag{5.13}$$

Recalling that $\sigma_1 \geq \sigma_2 \geq \sigma_3$, the solution of the maximum value problem using the Lagrangian multiplier technique is

$$\begin{cases} \nu_1^2 = \dfrac{1}{1+\left(\sqrt{1+c_1^2}+c_1\right)^2} \\ \nu_2^2 = 0 \\ \nu_3^2 = \dfrac{1}{1+\left(\sqrt{1+c_1^2}-c_1\right)^2} \end{cases} , \tag{5.14}$$

where ν_1, ν_2, and ν_3 are direction cosines of maximum, intermediate, and minimum principal

stresses, respectively. Substituting Eq. (5.14) into Eq. (5.13), the M-C criterion can be expressed in terms of principal stresses,

$$\left(\sqrt{1+c_1^2}+c_1\right)\sigma_1-\left(\sqrt{1+c_1^2}-c_1\right)\sigma_3=2c_2. \tag{5.15}$$

In view of enormous literature on the M-C failure criterion, the solution to the above maximum value problem must have been published earlier. However, the present authors were unable to find any reference on this topic. Here, only the final results are given. It should be noted that the orientation of the failure plane depends only on the friction coefficient c_1, while the onset of failure is controlled by both c_1 and c_2. In order to transform the Mohr-Coulomb criterion to the space of $(\bar{\epsilon}_f, \eta, \bar{\theta})$, one needs to express principal stresses in terms of σ_m, η and θ. Similar transformation equations can be found, for example, in Malvern (1969). However, for the consistency of notation, the required transformation is derived here from the geometrical construction in Section 5.3.1.

5.3.1 Formulas for principal stresses in terms of σ_m, η and θ

The principal stresses and principal deviatoric stesses can be geometrically represented on the deviatoric plane (π plane), as shown in Fig. 5-4. Note that all the components are scaled because of the inclined angle between the deviatoric plane and the principal axis (see Fig. 5-3). From the geometrical construction, one can easily obtain the expressions of the deviatoric principal stresses in terms of $\bar{\sigma}$ and θ,

$$\left\{\begin{array}{c}\sqrt{\frac{3}{2}}s_1=\sqrt{\frac{2}{3}}\bar{\sigma}\cos\theta\\ \sqrt{\frac{3}{2}}s_2=\sqrt{\frac{2}{3}}\bar{\sigma}\cos\left(\frac{2}{3}\pi-\theta\right)\\ \sqrt{\frac{3}{2}}s_3=\sqrt{\frac{2}{3}}\bar{\sigma}\cos\left(\frac{4}{3}\pi-\theta\right)\end{array}\right. \Rightarrow \left\{\begin{array}{c}s_1=\frac{2}{3}\bar{\sigma}\cos\theta\\ s_2=\frac{2}{3}\bar{\sigma}\cos\left(\frac{2}{3}\pi-\theta\right)\\ s_3=\frac{2}{3}\bar{\sigma}\cos\left(\frac{4}{3}\pi-\theta\right)\end{array}\right. . \tag{5.16}$$

It should be noted that the constraint of deviatoric principal stresses,

$$s_1+s_2+s_3=\frac{2}{3}\bar{\sigma}\left[\cos\theta+\cos\left(\frac{2}{3}\pi-\theta\right)+\cos\left(\frac{4}{3}\pi-\theta\right)\right]=0, \tag{5.17}$$

is satisfied automatically. Using Eq. (5.16), one can express the three principal stresses in

terms of σ_m, η and θ.

$$\begin{cases} \sigma_1 = \sigma_m + s_1 = \sigma_m + \frac{2}{3}\bar{\sigma}\cos\theta = \left[1 + \frac{2\cos\theta}{3\eta}\right]\sigma_m \\ \sigma_2 = \sigma_m + s_2 = \sigma_m + \frac{2}{3}\bar{\sigma}\cos\left(\frac{2}{3}\pi - \theta\right) = \left[1 + \frac{2\cos\left(\frac{2}{3}\pi - \theta\right)}{3\eta}\right]\sigma_m \\ \sigma_3 = \sigma_m + s_3 = \sigma_m + \frac{2}{3}\bar{\sigma}\cos\left(\frac{4}{3}\pi - \theta\right) = \left[1 + \frac{2\cos\left(\frac{4}{3}\pi - \theta\right)}{3\eta}\right]\sigma_m \end{cases} \tag{5.18}$$

Since the range of Lode angle is $0 \leq \theta \leq \pi/3$, it can be proved that $\sigma_1 \geq \sigma_2 \geq \sigma_3$ is satisfied for the three principal stresses in Eq. (5.18). Using Eq. (5.18), one can also show the equivalence of the normalized third deviatoric invariant ξ and the Lode angle θ expressed earlier in Eq. (5.6). Also, the condition of plane stress (Eq. (5.9)) can be easily proved by using the above transformation formulas.

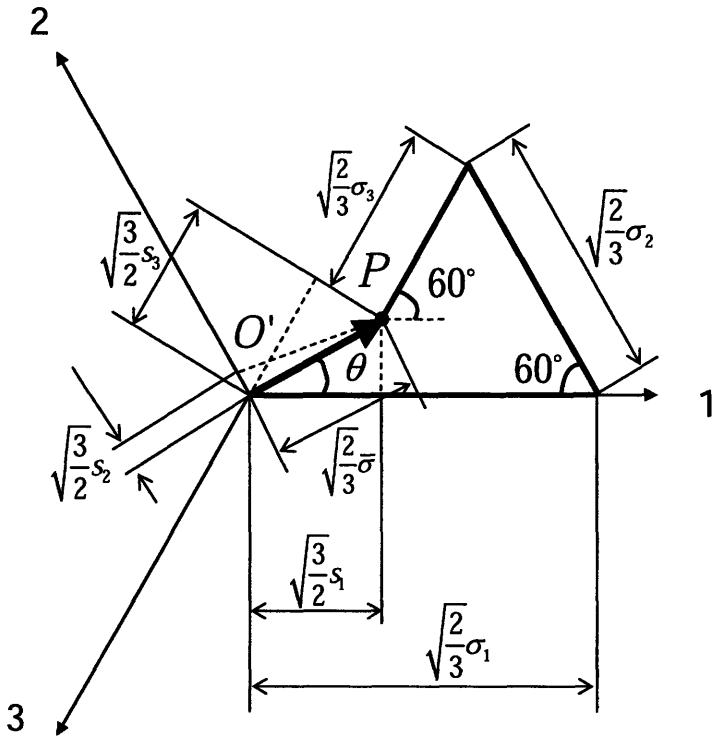

Fig. 5-4: Geometry representation of principal stresses $(\sigma_1, \sigma_2, \sigma_3)$, deviatoric stresses (s_1, s_2, s_3), equivalent stress $(\bar{\sigma})$ and Lode angle (θ) on the deviatoric plane (π plane)

5.3.2 A new form of the Mohr-Coulomb model

Substituting Eq. (5.18) into Eq. (5.15), one can express the M-C criterion in terms of $\bar{\sigma}$, η and θ,

$$\bar{\sigma} = c_2 \left[\sqrt{\frac{1+c_1^2}{3}} \cos\left(\frac{\pi}{6} - \theta\right) + c_1 \left(\eta + \frac{1}{3}\sin\left(\frac{\pi}{6} - \theta\right)\right)\right]^{-1}. \tag{5.19}$$

This is a stress space representation. As explained in Fig. 5-1, the resolution of the onset of ductile fracture is much better if a strain representation is used. To this end, one must express the equivalent stress in term of equivalent strain. This will be done in the present paper assuming monotonic loading and a power law material hardening function. Bai and Wierzbicki (2007a) proposed a generalized hardening rule with pressure and Lode angle dependence in the form,

$$\bar{\sigma} = A\bar{\varepsilon}_f^n \left[1 - c_\eta(\eta - \eta_\circ)\right] \left[c_\theta^s + (c_\theta^{ax} - c_\theta^s)\gamma\right], \tag{5.20}$$

where A is a material constant, n is the strain hardening exponent, and c_η, $\eta_\circ$, c_θ^s and c_θ^{ax} are parameters to describe both the pressure dependence and Lode angle dependence of the material plasticity. Altogether, there are six parameters defining the plasticity model. In what follows, only a special case of $c_\theta^{ax} = 1$ is considered, which means that the yield surface is symmetric with respect to the Lode angle parameter. There are no basic difficulties to retain the property of asymmetry, but this would require one more calibration test. A discussion about the effect of the parameter c_θ^{ax} on the yield locus can be found in (Bai and Wierzbicki, 2007a). The parameter γ in Eq. (5.20) is related to the Lode angle by

$$\gamma = \frac{\sqrt{3}}{2-\sqrt{3}}\left[sec(\theta - \frac{\pi}{6}) - 1\right] = \frac{\sqrt{3}}{2-\sqrt{3}}\left[sec\left(\frac{\bar{\theta}\pi}{6}\right) - 1\right]. \tag{5.21}$$

Some limiting cases of yielding function are obtained by suitably choosing model parameters. For example, $c_\eta = 0$, $c_\theta^{ax} = c_\theta^s = 1$ gives the von-Mises yielding function; while $c_\eta = 0$, $c_\theta^{ax} = 1$, $c_\theta^s = \sqrt{3}/2$ corresponds to the Tresca yielding function. At the point of fracture, the equivalent stress and corresponding equivalent strain are denoted by $\bar{\sigma}_f$ and $\bar{\varepsilon}_f$, respectively.

Substituting Eq. (5.20) and Eq. (5.21) into Eq. (5.19), the Mohr-Coulomb fracture criterion is transformed from the stress-based form into the mixed space of $(\bar{\varepsilon}_f, \eta, \bar{\theta})$.

$$\bar{\varepsilon}_f = \left\{ \frac{A}{c_2}\left[1 - c_\eta(\eta - \eta_\circ)\right]\left[c_\theta^s + \frac{\sqrt{3}}{2-\sqrt{3}}(c_\theta^{ax} - c_\theta^s)\left(sec\left(\frac{\bar{\theta}\pi}{6}\right) - 1\right)\right]\left[\sqrt{\frac{1+c_1^2}{3}}\cos\left(\frac{\bar{\theta}\pi}{6}\right) + c_1\left(\eta + \frac{1}{3}\sin\left(\frac{\bar{\theta}\pi}{6}\right)\right)\right]\right\}^{-n} \tag{5.22}$$

A total of eight parameters $(A, n, c_\eta, \eta_\circ, c_\theta^{ax}, c_\theta^s, c_1, c_2)$ need to be found, but only two have to be calibrated from fracture tests. If a von Mises yielding function is used ($c_\eta = 0$, $c_\theta^{ax} = c_\theta^s = 1$), then Eq. (5.22) reduces to

$$\bar{\varepsilon}_f = \left\{ \frac{A}{c_2} \left[\sqrt{\frac{1+c_1^2}{3}} \cos\left(\frac{\bar{\theta}\pi}{6}\right) + c_1 \left(\eta + \frac{1}{3} \sin\left(\frac{\bar{\theta}\pi}{6}\right) \right) \right] \right\}^{-\frac{1}{n}}. \tag{5.23}$$

In the case of Tresca yield function ($c_\eta = 0$, $c_\theta^{ax} = 1$, $c_\theta^s = \sqrt{3}/2$), and Eq. (5.22) reduces to

$$\bar{\varepsilon}_f = \left\{ \frac{A}{c_2} \left[\frac{\sqrt{1+c_1^2}}{2} + c_1 \frac{\sqrt{3}}{2} sec\left(\frac{\bar{\theta}\pi}{6}\right) \left(\eta + \frac{1}{3} \sin\left(\frac{\bar{\theta}\pi}{6}\right) \right) \right] \right\}^{-\frac{1}{n}}. \tag{5.24}$$

In the above two limiting cases, the simplified plasticity model depends on only two parameters, A and n, which can be found from the same tests as the fracture tests. From the application point of view, the ease and practicality of the M-C failure criterion in terms of finding model parameters from experiments can not be overemphasized.

5.4 A limiting case: maximum shear stress criterion

In the limiting case of $c_1 = 0$, the Mohr-Coulomb fracture criterion reduces to the maximum shear stress fracture criterion. For example, if the von Mises yield function is used, then Eq. (5.23) reduces to

$$\bar{\varepsilon}_f = \left[\frac{\sqrt{3}}{3} \frac{A}{c_2} \cos\left(\frac{\bar{\theta}\pi}{6}\right) \right]^{-\frac{1}{n}}, \tag{5.25}$$

which is pressure independent. At the same time, the direction cosines of the fracture plane, defined by Eq. (5.14), are constant and equal to $\left(\frac{1}{\sqrt{2}}, 0, \frac{1}{\sqrt{2}}\right)$. A geometric representation of this criterion is shown in Fig. 5-5. The fracture locus depends only on the Lode angle parameter and forms a half tube in the space of $(\bar{\varepsilon}_f, \eta, \bar{\theta})$. The corresponding fracture locus for plane stress condition (Eq. (5.9)) is a three-branch curve lying on the half tube. The projection of the plane stress fracture locus onto the plane of equivalent strain to fracture and the stress triaxiality is shown in Fig. 5-2, on which only two branches are plotted.

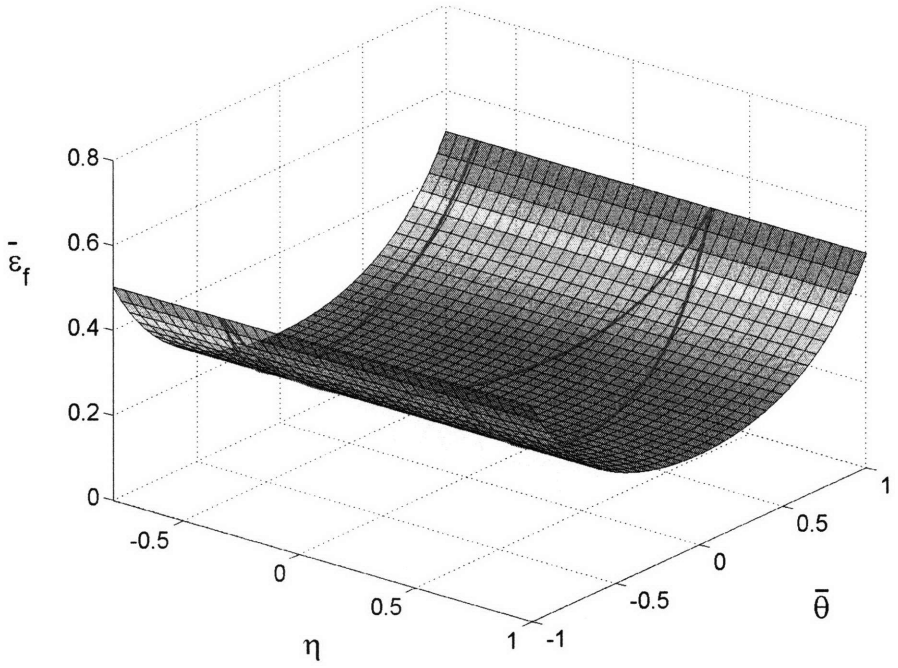

Fig. 5-5: 3D geometry representation of maximum shear fracture criterion ($A = 740MPa$, $n = 1/6$, $c_\eta = 0$, $c_\theta^{ax} = c_\theta^s = 1$, $c_1 = 0.0$, and $c_2 = 330MPa$). The curve on the surface represents the plane stress curve.

If the Tresca yielding condition is used, the maximum shear stress criterion, Eq. (5.24), reduces to the constant fracture strain criterion.

$$\bar{\varepsilon}_f = \left(\frac{A}{2c_2}\right)^{-\frac{1}{n}}. \tag{5.26}$$

5.5 Representation of Mohr-Coulomb fracture criterion in 3D space of invariants

The new form of Mohr-Coulomb fracture model, Eq. (5.22), can be geometrically represented in the 3D space of $(\bar{\epsilon}_f, \eta, \bar{\theta})$, see Fig. 5-6. Here, an example group of parameters is used: $A = 740MPa$, $n = 1/6$, $c_\eta = 0$, $c_\theta^{ax} = c_\theta^s = 1$, $c_1 = 0.1$, and $c_2 = 330MPa$. The 3D fracture locus is seen to be a monotonic function of the stress triaxiality and an asymmetric function with respect to the Lode angle parameter $\bar{\theta}$.

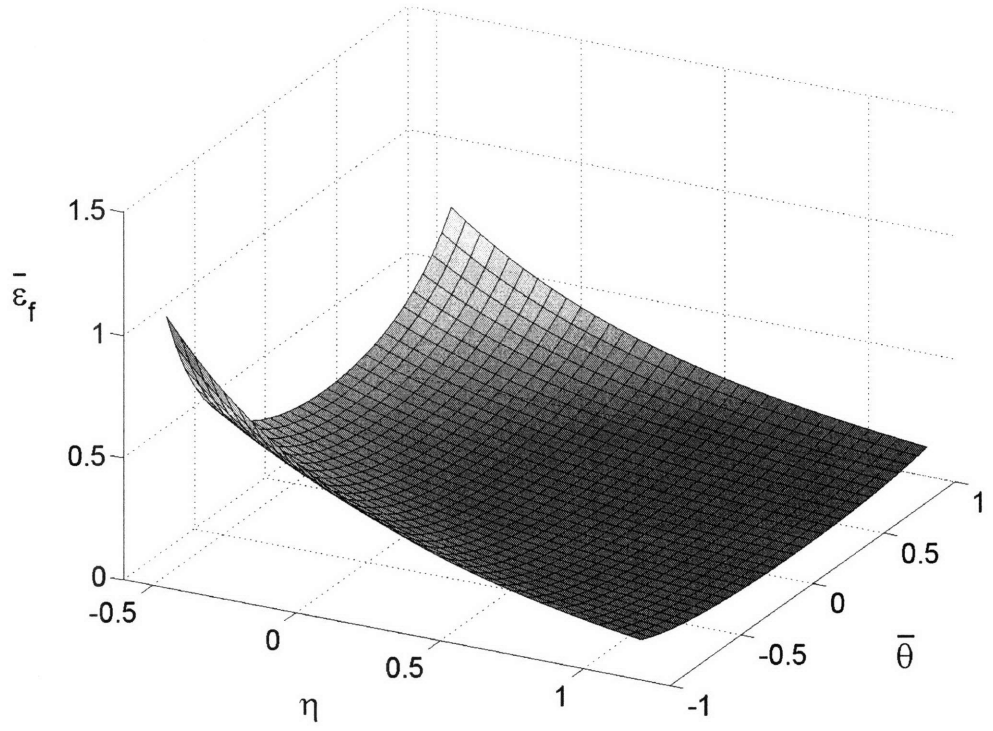

Fig. 5-6: 3D geometry representation of Mohr-Coulomb fracture model ($A = 740MPa$, $n = 1/6$, $c_\eta = 0$, $c_\theta^{ax} = c_\theta^s = 1$, $c_1 = 0.1$, and $c_2 = 330MPa$).

5.5.1 Pressure dependence

If a von-Mises yielding function is used ($c_\eta = 0$, $c_\theta^{ax} = c_\theta^s = 1$), and the Lode angle parameter $\bar{\theta}$ in Eq. (5.22) is fixed at a certain value, for example $\bar{\theta} = 0$, then Eq. (5.22) reduces to

$$\bar{\varepsilon}_f = \left[\frac{A}{c_2}\left(\sqrt{\frac{1+c_1^2}{3}} + c_1\eta\right)\right]^{-\frac{1}{n}}. \tag{5.27}$$

which is a nonlinear hyperbolic function of stress triaxiality η. An example plot of Eq. (5.27) is shown in Fig. 5-7. It is found that an exponential function $D_3e^{-D_4\eta}$ fits Eq. (5.27) for a wide range of stress triaxiality. So, the Mohr-Coulomb criterion provides an interesting physical interpretation of the effect of stress triaxiality on ductile fracture, which is originally based on the theory of void growth (McClintock, 1968; Rice and Tracey, 1969).

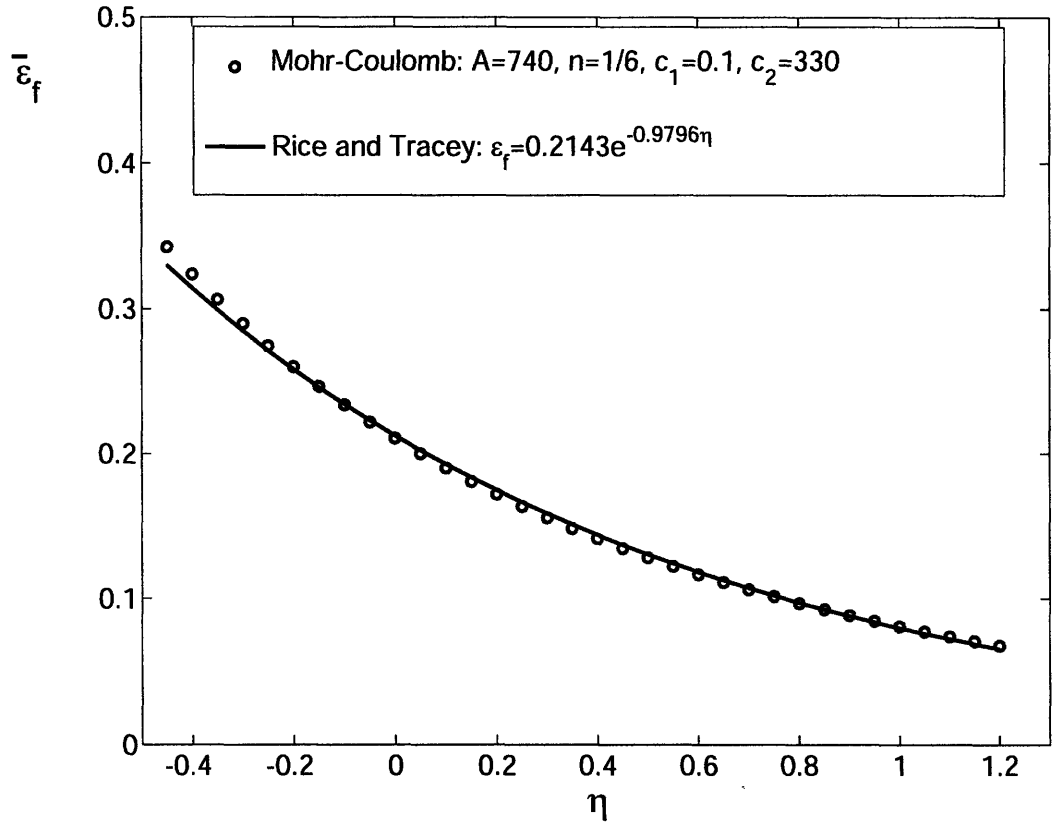

Fig. 5-7: Mohr-Coulomb criterion in the space of equivalent strain to fracture and stress triaxiality (assuming $\bar{\theta} = 0$)

5.5.2 Lode angle dependence

If the von-Mises yielding function is used again ($c_\eta = 0$, $c_\theta^{ax} = c_\theta^s = 1$), and the stress triaxiality η in Eq. (5.22) is fixed at a certain value, for example $\eta = 0$, then Eq. (5.22) becomes

$$\bar{\varepsilon}_f = \left\{ \frac{A}{c_2} \left[\sqrt{\frac{1+c_1^2}{3}} \cos\left(\frac{\bar{\theta}\pi}{6}\right) + \frac{c_1}{3} \sin\left(\frac{\bar{\theta}\pi}{6}\right) \right] \right\}^{-\frac{1}{n}}. \tag{5.28}$$

An example plot of Eq. (5.28) is shown in Fig. 5-8. A parabolic function controlled by three points, $\bar{\epsilon}_f(\bar{\theta} = 1)$, $\bar{\epsilon}_f(\bar{\theta} = 0)$ and $\bar{\epsilon}_f(\bar{\theta} = -1)$, is used to fit the curve. It follows from Fig. 5-8 that a parabolic function provides a good functional dependence of the Lode angle parameter on ductile fracture. It should be noted that the minimum value of the function

does not occur at $\bar{\theta} = 0$ but it is slightly shifted, which makes the 3D fracture locus an asymmetric function.

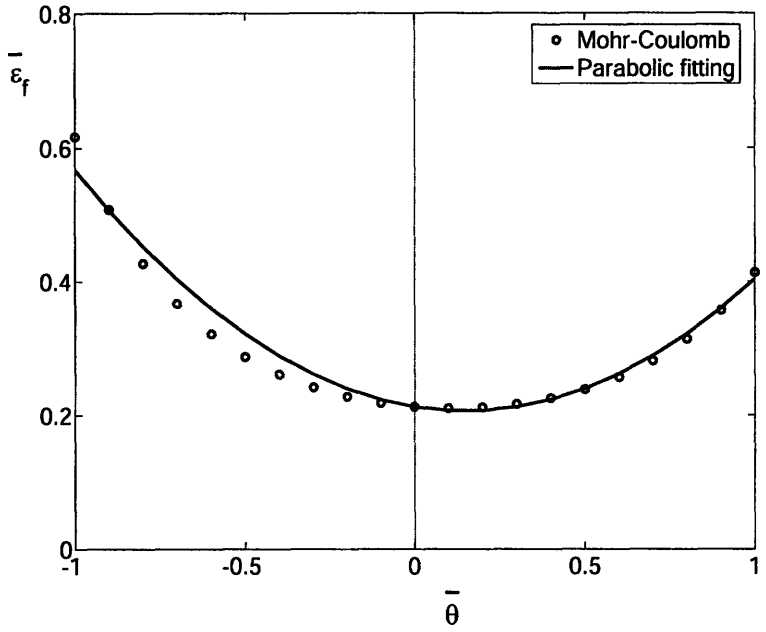

Fig. 5-8: Mohr-Coulomb criterion on the space of equivalent strain to fracture and the Lode angle parameter (assuming $\eta = 0$)

5.6 Parametric study

There are eight parameters (A, n, c_1, c_2, c_η, η_o, c_θ^s and c_θ^{ax}) in the Mohr-Coulomb failure criterion. In this section, a parameter study is performed to get a better understanding of new forms of Mohr-Coulomb criterion. In particular, some qualitative features of model parameters on the fracture locus are demonstrated. As a starting point, a combination of model parameters, $A = 740MPa$, $n = 1/6$, $c_\eta = 0$, $\eta_o = 0$, $c_\theta^{ax} = c_\theta^s = 1$, $c_1 = 0.1$ and $c_2 = 330MPa$, is considered.

5.6.1 Effect of c_1

Keeping other parameters unchanged, the new form of the Mohr-Coulomb criterion is plotted for three values of c_1 ($c_1 = 0$, 0.1, and 0.2) on the same planes as those in Sections 5.5.1 and 5.5.2, see Fig. 5-9. It is found that as c_1 increases, the fracture strain becomes more

pressure dependent (see Fig. 5-9(a)), and the fracture locus becomes more asymmetric (see Fig. 5-9(b)). The limiting case $c_1 = 0$, which corresponds to the maximum shear stress criterion, implies a symmetric fracture locus with respect to Lode angle parameter $\bar{\theta}$.

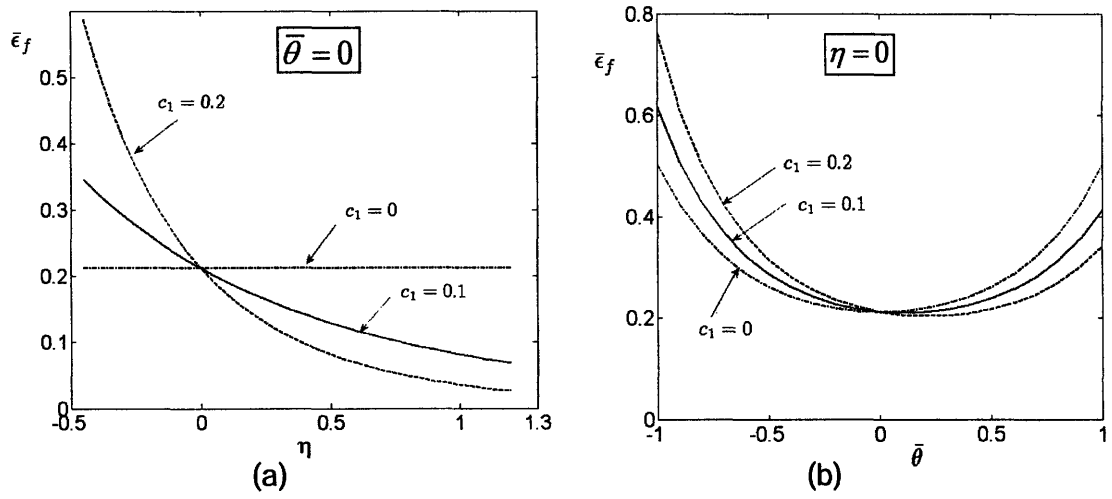

Fig. 5-9: Effect of c_1 on the new form of the Mohr-Coulomb criteria

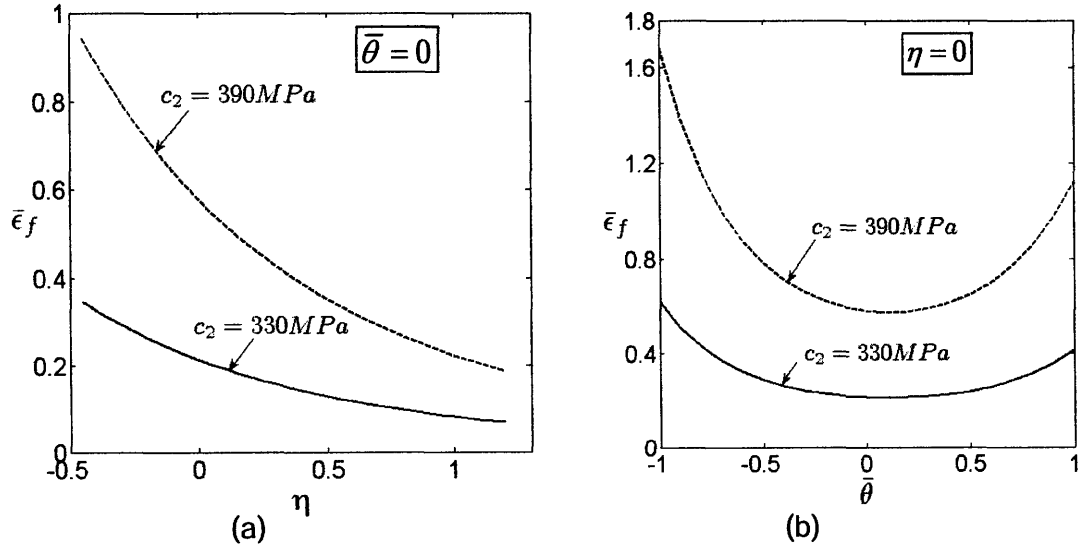

Fig. 5-10: Effect of c_2 on the new form of the Mohr-Coulomb criteria

5.6.2 Effect of c_2

Keeping other parameters unchanged, two values of c_2 are used to plot the new form of the Mohr-Coulomb criteria, see Fig. 5-10. It is found that the value of c_2 affect only the "height" of the fracture locus while the shape of the fracture locus is unchanged. A larger value of c_2 scales up the fracture locus.

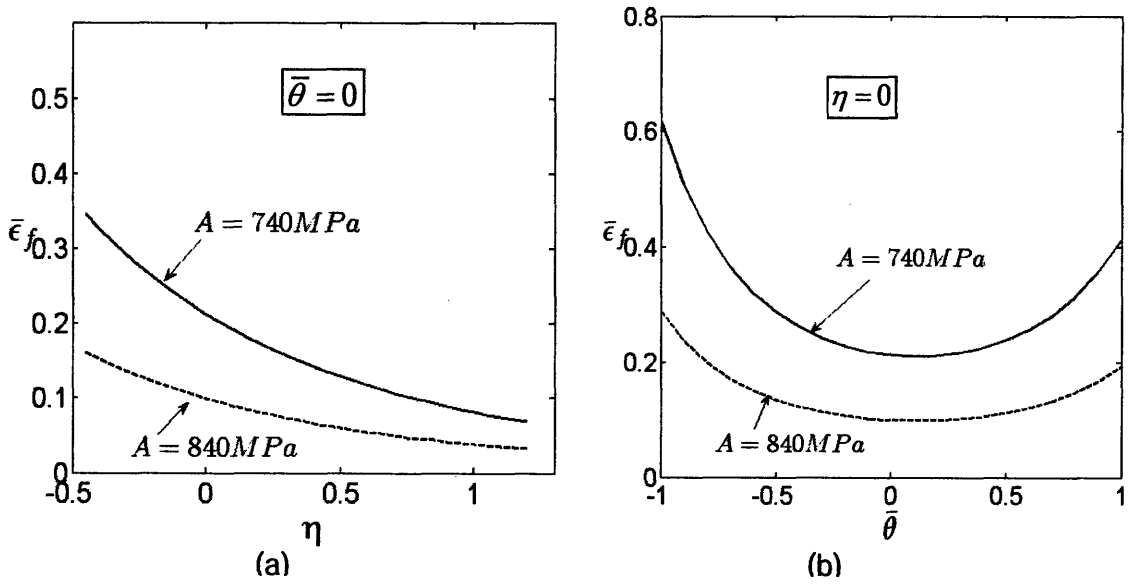

Fig. 5-11: Effect of A on the new form of the Mohr-Coulomb criteria

5.6.3 Effect of A

Similarly, two values of A are used to plot the new form of the Mohr-Coulomb criteria, see Fig. 5-11. It is found that the parameter A has a similar effect as that of parameter c_2, but the effect of A on fracture locus is in the opposite direction of that of c_2. A larger value of A scales down the fracture locus. In other words, if a material gains more strength in the plastic range, then it loses some of its ductility. This point has been proven in many advanced high strength steels (Pfestorf, 2005).

5.6.4 Effect of strain hardening exponent n

Again, two values of the strain hardening exponent, n, are used to plot the new form of the Mohr-Coulomb criteria, see Fig. 5-12. One obvious effect of the strain hardening exponent

n is that it raises the fracture locus.

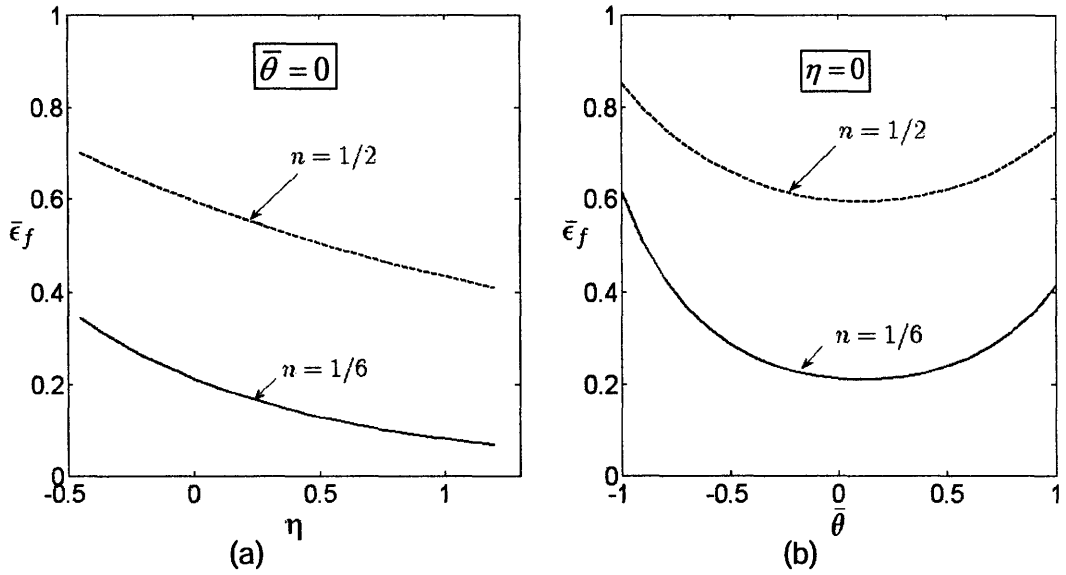

Fig. 5-12: Effect of n on the new form of the Mohr-Coulomb criteria

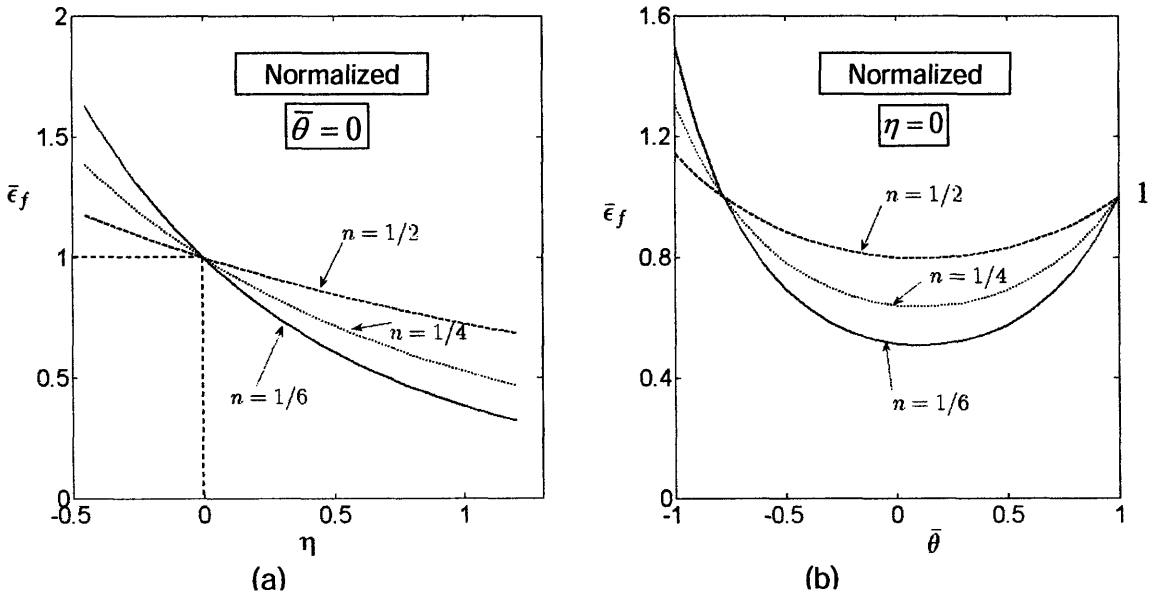

Fig. 5-13: A normalized plot to show the effect of n on the new form of the Mohr-Coulomb criteria

Three values of n ($\frac{1}{6}$, $\frac{1}{4}$ and $\frac{1}{2}$) are chosen in Fig. 5-13 to further demonstrate the effect of n. In Fig. 5-13(a), all three curves are normalized with respect to $\bar{\epsilon}_f(\eta = 0)$, and in Fig. 5-13(b), all curves are normalized with respect to $\bar{\epsilon}_f(\bar{\theta} = 1)$. From Fig. 5-13(a), one can see that a higher value of n decreases the pressure dependence of fracture locus. From Fig. 5-13(b), one can see that a higher value of n decreases the dependence of fracture locus on the Lode angle parameter, which was first noted by Xue (2007a) using the Stören and Rice necking criterion (Storen and Rice, 1975).

5.6.5 Effect of c_η

Taking into account the pressure effect on material plasticity, for example, $c_\eta = 0.09$ and $\eta_o = 0$ with other parameters kept unchanged, a comparison of fracture locus is shown in Fig. 5-14. It is found that changing the parameter c_η has no effect on the Lode angle dependence of the fracture locus (see Fig. 5-14(b)), but increasing c_η will decrease the pressure dependence of the fracture locus (see Fig. 5-14(a)). In other words, if a material has more pressure dependence on plasticity, then it will have less pressure dependence on fracture. This result should also be further investigated experimentally on different materials.

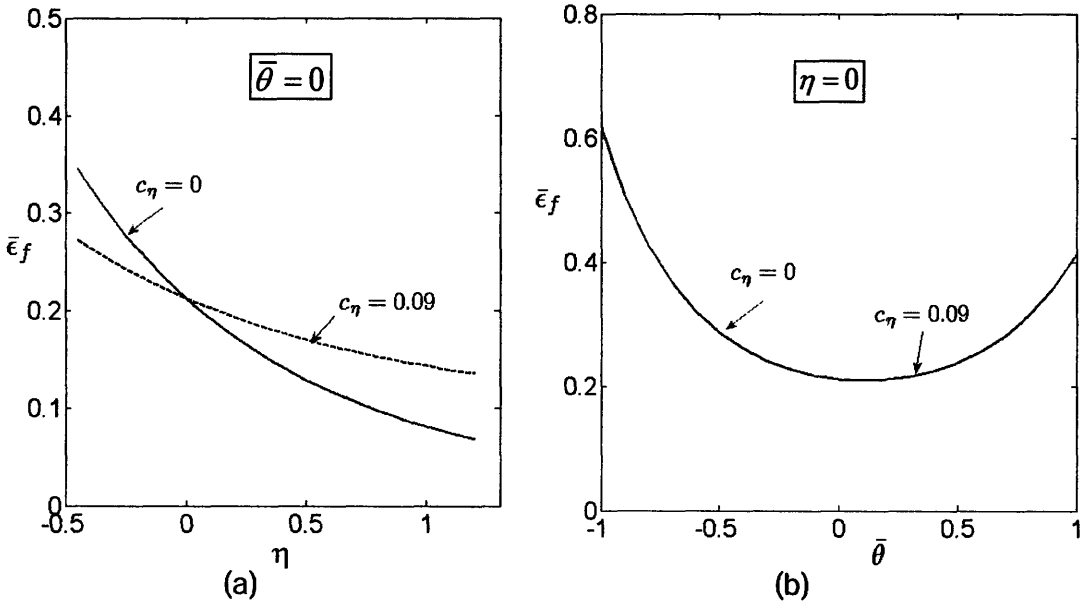

Fig. 5-14: Effect of c_η on the new form of the Mohr-Coulomb criteria

5.6.6 Effect of c_θ^s

The effect of the Lode angle effect on material plasticity is studied assuming $c_\theta^{ax} = 1$, and three values of c_θ^s (1.0, 0.93 and $\frac{\sqrt{3}}{2} = 0.866$), see Fig. 5-15. One can see that decreasing the parameter c_θ^s will raise the fracture locus (see Fig. 5-15(a)). On the other hand, decreasing c_θ^s will decrease the Lode dependence of the fracture locus (see Fig. 5-15(b)). In other words, if a material has stronger Lode dependence on plasticity, then it will have weaker Lode dependence on fracture. This point has been confirmed by comparing fracture data of two steels (1045 steel and DH36 steel), see (Bai et al., June 3-7, 2007). The 1045 steel has no Lode angle dependence on plasticity but exhibits a Lode angle dependence on fracture locus. On the other hand the DH36 exhibits a Lode angle dependence on plasticity but not on fracture. Referring to Section 5.6.4, it is found that the parameters, c_θ^s and n, are the two key parameters controlling the Lode angle effect on the fracture locus. This conclusion emphasizes the importance of developing an accurate plasticity model to predict fracture.

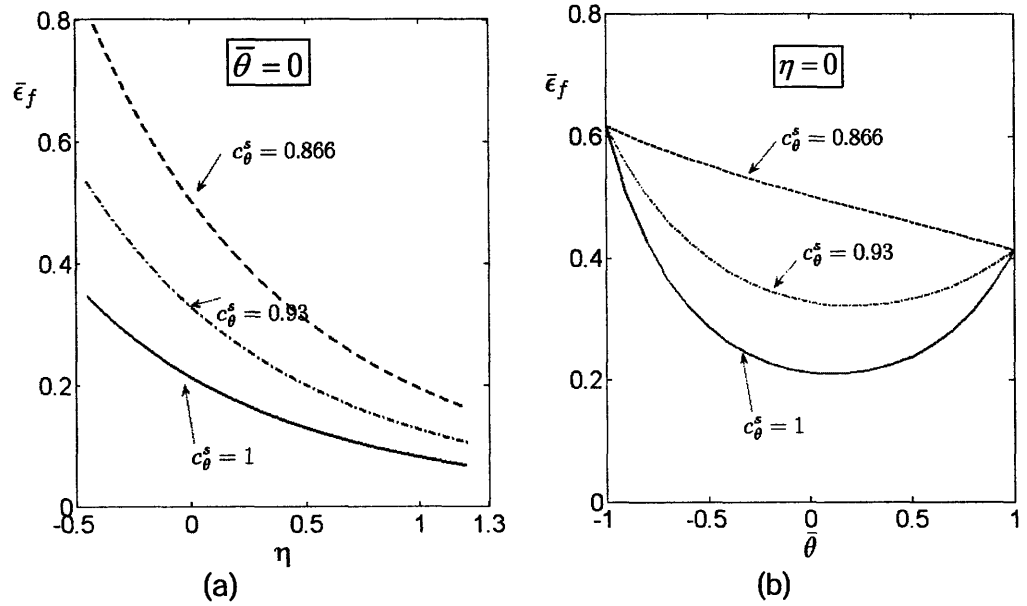

Fig. 5-15: Effect of c_θ^s on the new form of the Mohr-Coulomb criteria

5.6.7 Existence of a cutoff region

The existence of a cutoff value in the low stress triaxiality region has been revealed by Bao (2003); Bao and Wierzbicki (2005) and Teng (2004). Based on analysis of upsetting tests and

Bridgman's tests (Bridgman, 1952), Bao and Wierzbicki (2005) discovered that the cutoff value for fracture occurs at $\eta_{cutoff} = -\frac{1}{3}$. No fracture can occur below this critical value. Teng (2004) confirmed the importance of a cutoff value in high velocity impact simulation.

Introducing the Lode angle parameter $\bar{\theta}$ into the ductile model, the cutoff region in the plane of the stress directions $(\eta, \bar{\theta})$ of the 3D fracture locus appears automatically as a consequence of the M-C model. From Eq. (5.22), it is found that the fracture strain will go to infinity when the following condition is satisfied,

$$\sqrt{\frac{1+c_1^2}{3}}\cos\left(\frac{\bar{\theta}\pi}{6}\right) + c_1\left(\eta + \frac{1}{3}\sin\left(\frac{\bar{\theta}\pi}{6}\right)\right) \leq 0. \tag{5.29}$$

This cutoff region in the stress state plane $(\eta, \bar{\theta})$ is shown in Fig. 5-16 with a shaded area. In Fig. 5-16, an arbitrary value $c_1 = 0.57$ is assumed.

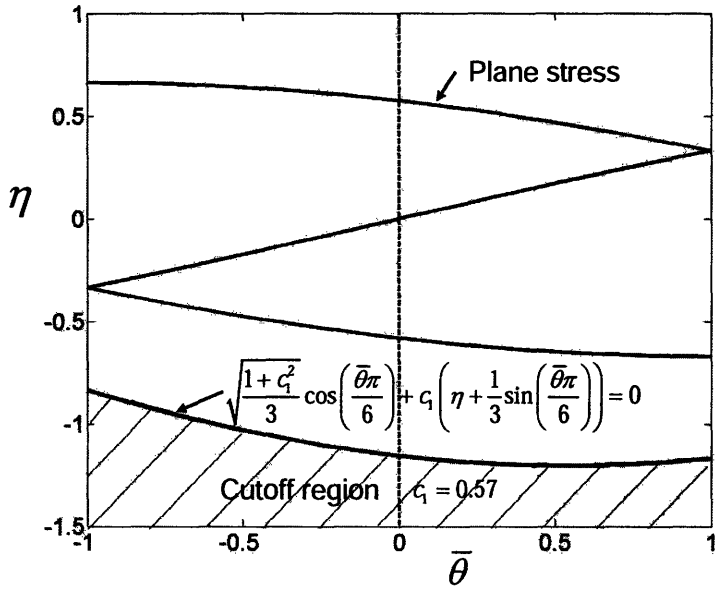

Fig. 5-16: A proposed shape of cutoff region of fracture one the plane of $(\eta, \bar{\theta})$ with $c_1 = 0.57$.

The above property of the cutoff region can be justified by revoking the physical concept of die-cone in the friction force, see Fig. 5-17. When the stress triaxiality η is less than a certain value, the vector of total force will be contained within the die-cone, under which condition slips will not occur during the material deformation. This gives an interesting physical interpretation of cutoff region using the Mohr-Coulomb criterion together with the

concept of die-cone. Tests should be designed and carried out in the future to validate this idea.

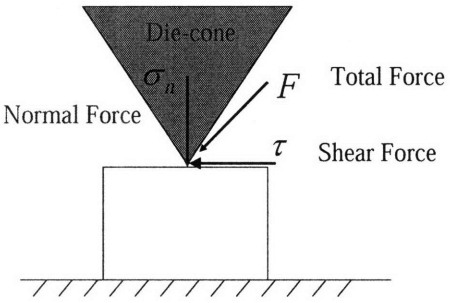

Fig. 5-17: A physical interpretation of existence cutoff region using the concept of die-cone in friction.

5.7 Crack directions in the plane stress and uni-axial stress

An important feature of M-C criterion is that it tells not only when a material point fails but also in which direction the material element cracks. In the general case, the crack plane is defined by Eq. (5.14). For the plane stress condition, it is convenient to consider a 2D representation of fracture planes, see Fig. 5-18. This picture was constructed taking $c_1 = 0.1$ as an example. The asymmetric hexagon represents the locus of crack directions. For example, in the first quadrant, there will be slant fracture through thickness, but in the planar view, the crack forms perpendicular to the maximum principal stress. In the second and fourth quadrant, the through thickness crack is normal to the middle surface of a sheet, but follows an inclined planar direction. It is interesting to note that the planar vector of the crack direction is perpendicular to unit normal vector of the M-C failure surface.

To simulate the crack propagation, the currently used technique in finite element simulation is based either on element deletion or element split along element edges. Neither of these two methods correctly simulates the boundary condition after a crack initiates, which is critical to predict the crack propagation, especially the slant fractures. It is suggested to use an extended element split technique in the spirit of an enriched FE shell element model suggested by Belytschko (for example, Areias and Belytschko (2005)). The direction of local element split surface will then follow from the M-C criterion. This is a technique requiring

the joint efforts of both physical fracture modeling and finite element coding.

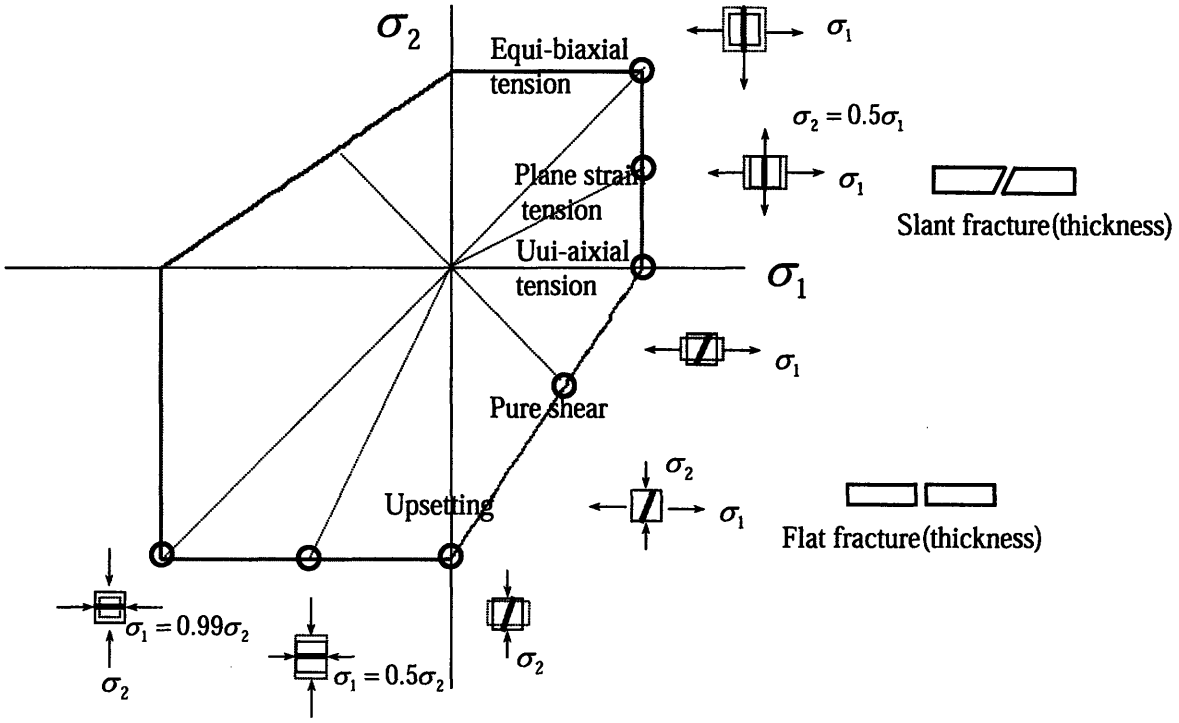

Fig. 5-18: According to Mohr-Coulomb fracture criterion, a crack direction locus is proposed for plane stress conditions.

5.8 Experiment calibration and verification

Bao and Wierzbicki (Bao, 2003; Bao and Wierzbicki, 2004a; Wierzbicki et al., 2005b) performed a series of tests to calibrate the fracture locus of 2024-T351 aluminum alloy in a wide range of stress triaxiality, see Fig. 5-19. All the data from the 15 types of tests done by Bao and Wierzbicki are re-processed to calculate the Lode angle parameter $\bar{\theta}$, which was not provided by Bao and Wierzbicki. Since the two stress state parameters are variable during the loading process, average values are used, according to the definitions given in Section 5.9. A list of the stress state parameters, η and $\bar{\theta}$, and the equivalent strain to fracture $\bar{\epsilon}_f$ is shown in Table 5.1. The corresponding specimens of all the data points are labeled in Fig. 5-19. These tests, except test No.9 (where there were no obvious observed cracks), will be reviewed in this section using the new form of the Mohr-Coulomb criterion.

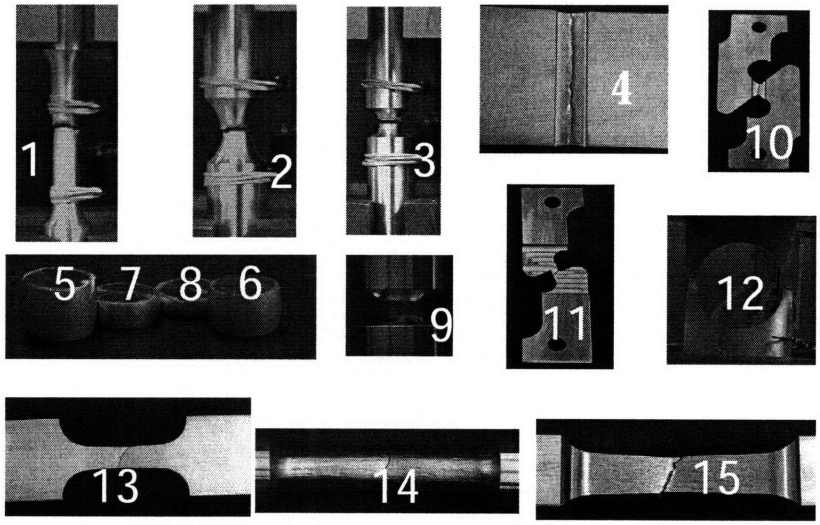

Fig. 5-19: Specimens used by Bao to calibrate the fracture locus for the wide range of stress triaxialtiy (Bao, 2003; Wierzbicki et al., 2005b)

Table 5.1: A summary of Bao and Wierzbicki's test results on 2024-T351 aluminum, (experimental data after Bao (2003); Wierzbicki et al. (2005b))

No.	Specimen description	η_{av}	$\bar{\theta}_{av}$	$\bar{\epsilon}_f$
1	Smooth round bar,tension	0.4014	0.9992	0.4687
2	Round large notched bar,tension	0.6264	0.9992	0.2830
3	Round small notched bar,tension	0.9274	0.9984	0.1665
4	Flat grooved,tension	0.6030	0.0754	0.2100
5	Cylinder($d_o/h_o = 0.5$),compression	-0.2780	-0.8215	0.4505
6	Cylinder($d_o/h_o = 0.8$),compression	-0.2339	-0.6809	0.3800
7	Cylinder($d_o/h_o = 1.0$),compression	-0.2326	-0.6794	0.3563
8	Cylinder($d_o/h_o = 1.5$),compression	-0.2235	-0.6521	0.3410
9	Round notched, compression	-0.2476	-0.7141	0.6217
10	Simple shear	0.0124	0.0355	0.2107
11	Combination of shear and tension	0.1173	0.3381	0.2613
12	Plate with a circular hole	0.3431	0.9661	0.3099
13	Dog-bone specimen, tension	0.3570	0.9182	0.4798
14	Pipe, tension	0.3557	0.9286	0.3255
15	Solid square bar,tension	0.3687	0.9992	0.3551

Plasticity: This section summarizes the determination of material constants appearing in Eq. (5.22). For that purpose, no new tests are performed, but rather experimental data on 2024-T351 aluminum reported by Bao (2003) will be used. The parameters of the basic hardening curve, $A = 740MPa$, $n = 0.15$, were found from the best fit of the stress-strain curve corresponding to the upsetting test (No. 6). The analysis of data on unnotched and notched round bar experiments (test No. 1, 2 and 3) indicate that there is a negligible effect of hydrostatic pressure on plasticity. Therefore, c_η is taken to be zero ($c_\eta = 0$), while the other parameter is $\eta_o = -\frac{1}{3}$. In order to quantify the effect of Lode angle on plasticity (constant c_θ^s), axial-symmetric (test No. 1 or 6) and plane strain (test No. 4) experiments should be compared, as described by Bai and Wierzbicki (2007a). Such a comparison was performed by Bao (2003) showing that there is a very little Lode angle effect on plasticity. Therefore, for the purpose of the present analysis, the parameter is set to unity ($c_\theta^s = 1$). Finally, $c_\theta^{ax} = 1$, as discussed in Section 5.3.2. This completes determination of all six plasticity constants.

Fracture: The M-C fracture criterion involves two material constants, so only two tests are needed to calibrate this criterion. For that purpose, fracture test No. 6 and 10 of Table 5.1 are used. Substituting the experimental data (η_{av}, $\bar{\theta}_{av}$ and $\bar{\varepsilon}_f$) into Eq. (5.22), a set of two nonlinear algebraic equations for c_1 and c_2 are obtained. The solution of this system yields $c_1 = 0.0345$ and $c_2 = 338.6MPa$. Now all eight parameters describing plasticity and fracture of 2024-T351 aluminum have been determined. The plot of the resulting fracture locus is shown in Fig. 5-20. Tests No. 6 and 10, used for fracture calibration, are displayed as diamonds. The "half tube" surface passes exactly through those two points. Points corresponding to the remaining twelve tests are denoted by circles. They appears to be very close to the 3D surface, except for three points corresponding to unnotched and notched round bars. It has been shown by many investigators that the fracture in round bars in tension involves a mechanism of void growth and linkage. Clearly this is not well captured by the M-C fracture criterion. In other words, the M-C model describes shear type of fracture well but not fracture produced by void growth and linkage. It can be concluded that the M-C model calibrated from just two fracture tests is able to capture, with an engineering accuracy, shear fracture of 2024-T351 aluminum in a wide range of stress triaxiality and Lode angle parameter.

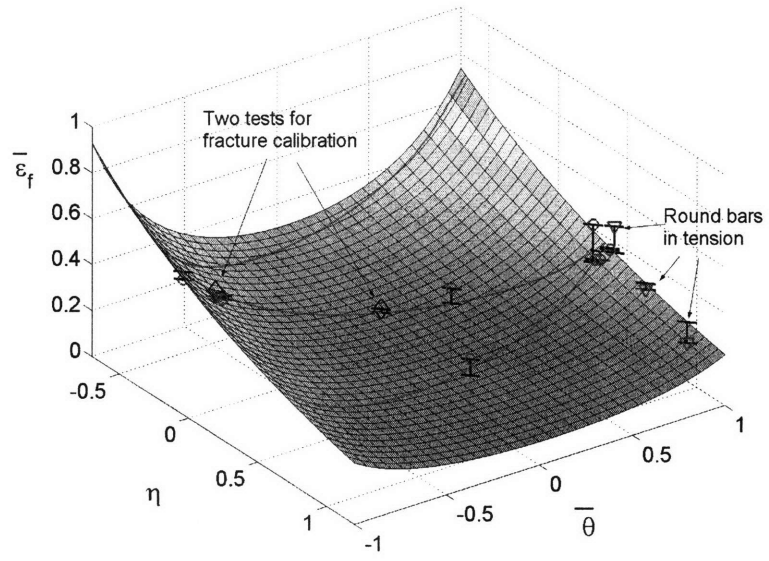

Fig. 5-20: 3D geometric representation of Mohr-Coulomb fracture locus for 2024-T351 aluminum alloy

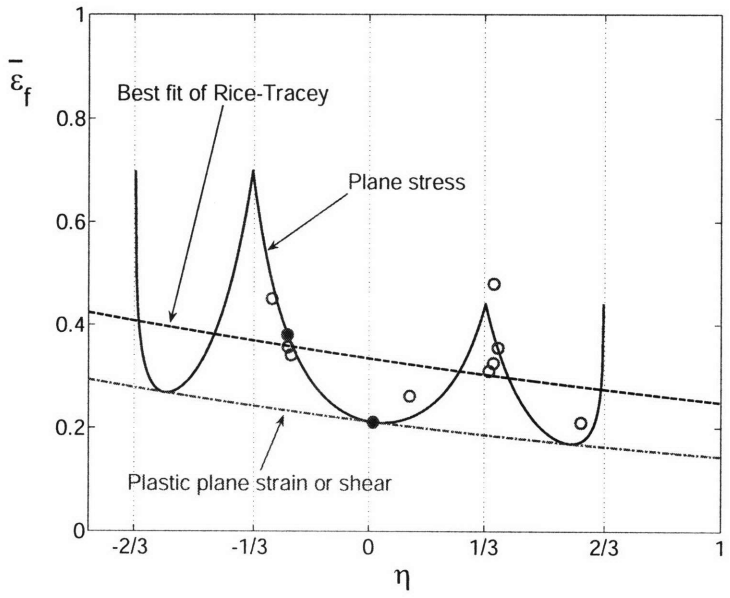

Fig. 5-21: Mohr-Coulomb fracture locus for 2024-T351 on the plane of equivalent strain to fracture and stress triaxiality.

Most of the tests done by Bao and Wierzbicki were in plane stress condition, except for three round bars tensile tests (No. 1, 2 and 3). It follows from Eq. (5.9) that the plane stress data points lie on the "s"-shaped curve of plane stress condition. By substituting Eq. (5.9) into Mohr-Coulomb criterion, Eq. (5.22), the fracture locus of plane stress condition can be plotted on the plane of equivalent strain to fracture and the stress triaxiality (refer to Fig. 5-21). One can see that the fracture locus of plane stress consists of three half-cycles. This phenomenon was first revealed by Wierzbicki and Xue (Wierzbicki and Xue, 2005; Xue, 2007a) from a symmetric 3D fracture locus. The experimental data points used for calibration are marked in Fig. 5-21 by full circles. It is found that the calibrated Mohr-Coulomb criterion predicts the trends of experimental results very well. At the same time the Rice-Tracey fracture model (Rice and Tracey, 1969) can not predict the trend of plane stress fracture.

5.9 Damage evolution rule

Besides the fracture locus, discussed extensively in the preceding section, the rule of damage evolution is an integral part of the fracture predictive technology. Here, a linear incremental relationship is assumed between the damage indicator, D, and the equivalent plastic strain $\bar{\varepsilon}_p$,

$$D\left(\bar{\varepsilon}_p\right) = \int_0^{\bar{\varepsilon}_p} \frac{d\bar{\varepsilon}_p}{f\left(\eta, \bar{\theta}\right)}, \tag{5.30}$$

where the stress direction parameters, $\eta(\bar{\varepsilon}_p)$, and $\xi(\bar{\varepsilon}_p)$, are unique functions of the equivalent plastic strain. A material element is considered to fail when the limit of ductility is reached, $\bar{\varepsilon}_p = \bar{\varepsilon}_f$, so that $D(\bar{\epsilon}_f) = D_c = 1$. In the limiting case (for example proportional loading), when the parameters $(\eta, \bar{\theta})$ are constant over the loading cycle, Eq. (5.30) can be integrated to give

$$\bar{\varepsilon}_f = f\left(\eta, \bar{\theta}\right) = \hat{\varepsilon}_f\left(\eta, \bar{\theta}\right), \tag{5.31}$$

which reduces to the 3D fracture locus $\hat{\varepsilon}_f\left(\eta, \bar{\theta}\right)$. However, in most tests on various types of specimens, the stress state parameters $(\eta, \bar{\theta})$ are variable. The shape of the fracture locus will then depend on whether the initial, final or some average value of these parameters is considered.

The above discussion emphasized the intrinsic difficulty in constructing a unique fracture locus. In this paper, it is proposed to determine the fracture locus based on the average

value of the parameters $(\eta, \bar{\theta})$ in the loading process.

$$\eta_{av} = \frac{1}{\bar{\varepsilon}_f} \int_0^{\bar{\varepsilon}_f} \eta\left(\bar{\varepsilon}_p\right) d\bar{\varepsilon}_p \quad , \quad \bar{\theta}_{av} = \frac{1}{\bar{\varepsilon}_f} \int_0^{\bar{\varepsilon}_f} \bar{\theta}\left(\bar{\varepsilon}_p\right) d\bar{\varepsilon}_p. \tag{5.32}$$

The functions, $\eta(\bar{\varepsilon}_p)$ and $\bar{\theta}(\bar{\varepsilon}_p)$, are known from the numerical simulation of the tests and the equivalent strain to fracture $\bar{\varepsilon}_f$ is determined from mapping the measured displacement to fracture into the calculated strain to fracture. In all of the calibration efforts presented in the preceding section, the average parameters $(\eta_{av}, \bar{\theta}_{av})$ defined by Eq. (5.32) were used. The 3D fracture locus constructed on the basis of the average values is then used as a reference surface for more complex loading paths.

A linear incremental dependence of the damage function $D\left(\bar{\varepsilon}_p\right)$ on the equivalent plastic strain (Eq. (5.30)) was shown to work well for monotonic loading. In the case of reverse straining or more complicated loading paths, a nonlinear incremental rule and new terms for history effect correction must be considered (see Chapter 7).

5.10 Discussion and conclusion

In this paper, the transformation formulas between the principal stresses and the stress state parameters (the stress triaxiality η and the Lode angle parameter $\bar{\theta}$) are derived. For monotonic loading conditions, the Mohr-Coulomb criterion is transformed from a local representation in terms of a shear stress and a normal stress, to the mixed strain-stress representation of $(\bar{\epsilon}_f, \eta, \bar{\theta})$. The corresponding fracture locus of the Mohr-Coulomb criterion is shown to be described by a monotonically decreasing function of the stress triaxiality coupled with an asymmetric function of Lode angle parameter. A parametric study on the new form of the Mohr-Coulomb criterion was performed and the results are summarized as follows.

- Increasing the friction parameter c_1 increases both the dependence of fracture locus on pressure and the asymmetry of the fracture locus.
- Increasing the shear resistance parameter c_2 shifts the fracture locus upward without changing its shape.
- Increasing the amplitude of the power hardening law, parameter A, shifts the fracture locus down, but its shape remains the same. In other words, increasing the material's strength will decrease its ductility.

- Increasing the power exponent n shifts the fracture locus upward, but decreases both the pressure dependence and the Lode angle dependence of the fracture locus. In other words, less strain hardening materials will have more pressure and Lode angle dependence on fracture.

- Increasing the parameter c_η will decrease the pressure dependence of the fracture locus, but leave no effect on the shape of the fracture locus.

- Decreasing the parameter c_θ^s will increase the whole height of the fracture locus, and decrease the effect of Lode angle on the fracture locus. In other words, if a material exhibits more Lode dependence on plasticity, then it has less Lode dependence on fracture, and vice versa.

- There exists a cutoff region on the stress state plane $(\eta, \bar{\theta})$, see Eq. (5.29), where fracture will not occur.

Bao and Wierzbicki's experimental results on 2024-T351 aluminum alloy are revisited using the new form of the Mohr-Coulomb criterion. Using two types of test to calibrate the Mohr-Coulomb criterion, the model predicts the remaining nine tests with good accuracy, especially for plane stress fracture. While the Mohr-Coulomb criterion predicts most of the shearing dominated fracture well, there are still some limitations of this fracture criterion. For example, it does not provide a good prediction of the fracture of round bars in tension, which satisfy the axial symmetry condition. At the same time, fracture in upsetting tests occurs at the equatorial region of the outer surface. This is a plane stress fracture, and it is predicted well by the M-C criterion.

The M-C criterion predicts not only crack initiation sites but also crack directions. Providing a given material element crack direction in conjunction with the arbitrary element splitting technique can predict crack path with greater accuracy. Since there are only two parameters in the Mohr-Coulomb criterion, this ductile fracture model has great potential for many engineering application.

THIS PAGE INTENTIONALLY LEFT BLANK

Chapter 6

Forming Severity Concept for Predicting Sheet Necking under Complex Loading Histories

A new method of predicting neck formation in sheets under non-proportional loading is proposed, based on the concept of the "cumulative forming severity". This concept is borrowed from a macroscopic model of ductile fracture where the crack initiation is governed by the accumulated equivalent plastic strain modified by the stress triaxiality and the Lode angle parameters. Such an approach necessitates a representation of the Forming Limit Diagram (FLD) in the space of the equivalent strain to neck and the Lode angle parameter.

Another new factor is the assumption of the nonlinear accumulation rule of forming severity for non-proportional and complex loading histories. A class of nonlinear weighting function is proposed with only one free parameter. A starting point in the derivation is the known FLD corresponding to proportional loading. This can be either determined from Hill's and Stören and Rice analytical solutions or from numerical simulation or else taken directly from experiments. In the case of proportional loading, necking depends on the final state of stress or strain, so it does not matter if necking severity index is accumulated in a linear or nonlinear way. For non-proportional loading, the unknown free parameter of the nonlinear accumulation rule must be determined from a test.

Experimental data on FLDs under complex strain paths for two types of material, aluminum alloy 6111-T4 (Graf and Hosford, 1994) and aluminum-killed sheet steel (Muschenborn and Sonne, 1975), found in the literature are revisited by the proposed model. Calibrated from only one test with non-proportional loading condition, the model is able to

predict the remaining tests of complex loading paths with good accuracy.

6.1 Introduction

The Forming Limit Diagram (FLD) originally developed by Keeler and Backhofen (1964) and Goodwin (1968) is widely used in the sheet metal forming industry (Atkins and Mai, 1985). The conventional FLD is defined in the space of two in-plane principal strains, the major strain ε_1 and the minor strain ε_2. Figure 6-1 shows an example of FLD of aluminum alloy 6111-T4 reported by Graf and Hosford (1994). The FLD is defined and calibrated under proportional loading assumption, under which the ratio of two principal strain increments, given by Eq. (6.1), is constant. For example, the uni-axial tension loading corresponds to $\alpha = -0.5$, the plane strain tension corresponds to $\alpha = 0$, and the equi-biaxial tension is $\alpha = 1$. The range of α of interest to the FLD is $-0.5 \leq \alpha \leq 1$. When $\alpha < -0.5$, the failure mode of metal sheet is either shear fracture or wrinkling.

$$\frac{d\varepsilon_2}{d\varepsilon_1} \triangleq \alpha. \tag{6.1}$$

An important feature of the experimental strain-based FLD is that it is strongly strain path dependent, which means that the FLD is not unique under complex loading histories or non-proportional loading conditions (Muschenborn and Sonne, 1975; Graf and Hosford, 1994; Stoughton, 2000; Stoughton and Zhu, 2004). A great deal of modeling effort were devoted in the past to predict the effect the loading history on the FLD (Marciniak and Kuczynski, 1967; Cao et al., 2000; Chow et al., 2001). A stress-based FLD was proposed by Stoughton (2000), which was found to be less strain path dependent. However, there are two drawbacks of the stress-based FLD. One is that the stress components can not be easily measured during experiments as opposed to strain components. The other is that the stress-based criteria have relatively poor resolutions as compared to the strain-based criteria, especially for ductile material with high forming limit. A comprehensive review of all these models is presented by Stoughton and Zhu (2004). Their prediction give correctly qualitative trends of complex loading history using only equations of plane stress plasticity theory. At the same time, the present method will introduce one more free parameter, and therefore its accuracy could be much better.

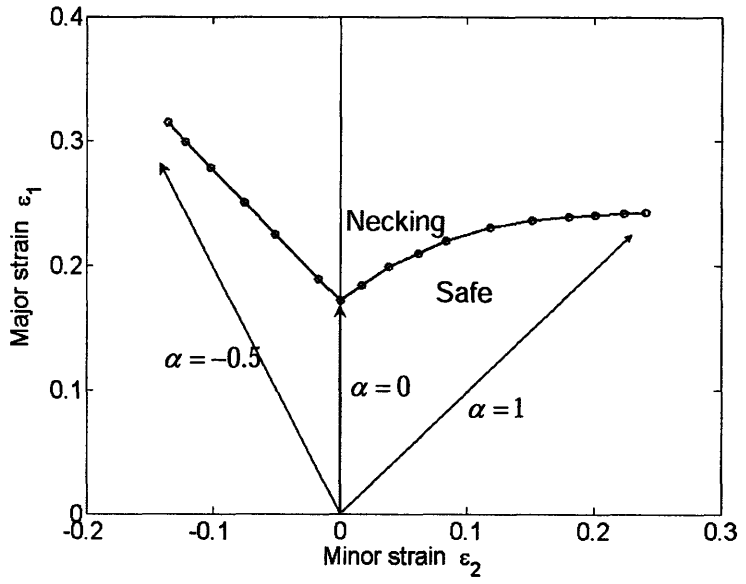

Fig. 6-1: An example of forming limit diagram (FLD) of the transverse direction of aluminum alloy 6111-T4 (experimental data after Graf and Hosford (1994))

In this paper, the loading history effect on FLD will be accounted for in three steps. The starting point of the analysis is the known FLD under proportional loading conditions. In the second step, the strain-based conventional FLD is transformed and approximately formulated in the space of equivalent strain to neck and the Lode angle parameter, $(\bar{\varepsilon}_n, \bar{\theta})$. Finally, the loading history effect is taken into account by considering the onset of the necking as a non-linear accumulative process of forming severity. Examples on two materials are given to illustrate the procedure.

6.2 Transformation of FLD to different spaces under plane stress

6.2.1 Basic formulas for space transformation under plane stress

Although the FLD is usually expressed in the plane of $(\varepsilon_1, \varepsilon_2)$, it can also be represented in other spaces using the known transformation formulas for plane stress plasticity (see Stoughton (2000); Lee (2005)). If a proportional loading path is assumed, then the increment

of principal strains follow the equation,

$$d\varepsilon_1 : d\varepsilon_2 : d\varepsilon_3 = 1 : \alpha : -(1+\alpha), \tag{6.2}$$

where the material is taken to be incompressible and isotropic. The material is further assumed to obey the von Mises yield condition and the associated flow rule.

$$\sigma_y = \bar{\sigma} = \sqrt{\frac{1}{2}\left[(\sigma_1-\sigma_2)^2 + (\sigma_2-\sigma_3)^2 + (\sigma_3-\sigma_1)^2\right]}, \tag{6.3}$$

$$d\varepsilon_{ij} = d\Lambda \frac{\partial \bar{\sigma}}{\partial \sigma_{ij}} = \frac{3}{2}\frac{d\Lambda}{\bar{\sigma}} s_{ij}, \tag{6.4}$$

where σ_{ij} are stress components, σ_1, σ_2 and σ_3 are principal stresses, s_{ij} are deviatoric stress components, $d\Lambda$ is the plasticity multiplier, and $d\varepsilon_{ij}$ is the strain increments. It is recognized that neck formation in the first quadrant may be facilitated by a non-associated flow rule (see Storen and Rice (1975) or Stoughton (2002)). However, for simplicity, Eq. (6.4) is assumed to hold for both positive and negative α. Defining the stress ratios,

$$\frac{\sigma_2}{\sigma_1} \triangleq \beta, \tag{6.5}$$

$$\frac{\sigma_3}{\sigma_1} \triangleq \gamma, \tag{6.6}$$

Eq. (6.4) can be rewritten in the principal stress and strain space.

$$\begin{cases} d\varepsilon_1 = \left(\frac{3}{2}\frac{d\Lambda}{\bar{\sigma}}\right) s_1 = \left(\frac{3}{2}\frac{d\Lambda}{\bar{\sigma}}\right)\left[1 - \frac{1}{3}(1+\beta+\gamma)\right]\sigma_1 \\ d\varepsilon_2 = \left(\frac{3}{2}\frac{d\Lambda}{\bar{\sigma}}\right) s_2 = \left(\frac{3}{2}\frac{d\Lambda}{\bar{\sigma}}\right)\left[\beta - \frac{1}{3}(1+\beta+\gamma)\right]\sigma_1 \\ d\varepsilon_3 = \left(\frac{3}{2}\frac{d\Lambda}{\bar{\sigma}}\right) s_3 = \left(\frac{3}{2}\frac{d\Lambda}{\bar{\sigma}}\right)\left[\gamma - \frac{1}{3}(1+\beta+\gamma)\right]\sigma_1 \end{cases} \tag{6.7}$$

Note that the present notation is consistent with the book of literature but is different from the notation used by Smith et al. (2003), who interchanged parameters α and β. Substituting Eq. (6.7) into Eq. (6.1), one can get a known relationship between strain ratios and stress ratios under proportional loading condition,

$$\alpha = \frac{2\beta - \gamma - 1}{2 - \beta - \gamma}. \tag{6.8}$$

A special case of plane stress, $\sigma_3 = 0$, imposes a unique relation between two parameters characterizing the stress state, the stress triaxiality η and the Lode angle parameter $\bar{\theta}$, defined

respectively by Eq. (6.11) and (6.12) (see Bai and Wierzbicki (2007a)). From Eq. (6.6), the parameter γ vanishes, and Eq. (6.8) reduces to

$$\alpha = \frac{2\beta - 1}{2 - \beta}. \tag{6.9}$$

The inverted form of Eq. (6.9) reads

$$\beta = \frac{2\alpha + 1}{2 + \alpha}. \tag{6.10}$$

Now, the stress triaxiality η and the Lode angle parameter $\bar{\theta}$, can be expressed in terms of the stress ratio β, according to the respective definitions,

$$\eta = \frac{\sigma_m}{\bar{\sigma}} = \frac{\beta + 1}{3\sqrt{\beta^2 - \beta + 1}}, \tag{6.11}$$

$$\bar{\theta} = 1 - \frac{2}{\pi}\arccos\xi = 1 - \frac{2}{\pi}\arccos\left[\frac{(\beta+1)(\beta-2)(2\beta-1)}{2(\beta^2-\beta+1)^{3/2}}\right], \tag{6.12}$$

where $\xi = \frac{27}{2}\frac{(\sigma_1-\sigma_m)(\sigma_2-\sigma_m)(\sigma_3-\sigma_m)}{\bar{\sigma}^3}$ is the normalized third deviatoric stress invariant of the stress tensor, and σ_m is the mean stress. Details regarding the above derivation can be found, for example, in Bai and Wierzbicki (2007a,b). In the reminder of this section, the conventional FLD will be transformed to four different spaces.

6.2.2 Space of $(\bar{\varepsilon}_n, \alpha)$

The increment of equivalent strain is defined in terms of increments of principal strain components,

$$d\bar{\varepsilon} = \sqrt{\frac{2}{3}(d\varepsilon_1^2 + d\varepsilon_2^2 + d\varepsilon_3^2)}. \tag{6.13}$$

Substitute Eq. (6.2) into Eq. (6.13), one gets

$$d\bar{\varepsilon} = \sqrt{\frac{4}{3}[1 + \alpha + \alpha^2]}d\varepsilon_1. \tag{6.14}$$

Under the proportional loading of plane stress condition, the strain ratio α is constant, so that Eq. (6.14) can be integrated and the equivalent strain $\bar{\epsilon}$ can be expressed in terms of

the major strain ε_1 and the parameter α,

$$\bar{\varepsilon} = \frac{2\varepsilon_1}{\sqrt{3}}\sqrt{1+\alpha+\alpha^2}, \tag{6.15}$$

where now $\alpha = \frac{d\varepsilon_2}{d\varepsilon_1} = \frac{\varepsilon_2}{\varepsilon_1}$. Using Eq. (6.15), the forming limit diagram can be transformed to the space of $(\bar{\varepsilon}_n, \alpha)$. The experimental data points of 6111-T4 aluminum alloy (transverse direction) shown in Fig. 6-1 is re-drawn in the new space in Fig. 6-2. Such a representation of forming diagram was proposed among others by Hooputra et al. (Oct. 2003, 2004).

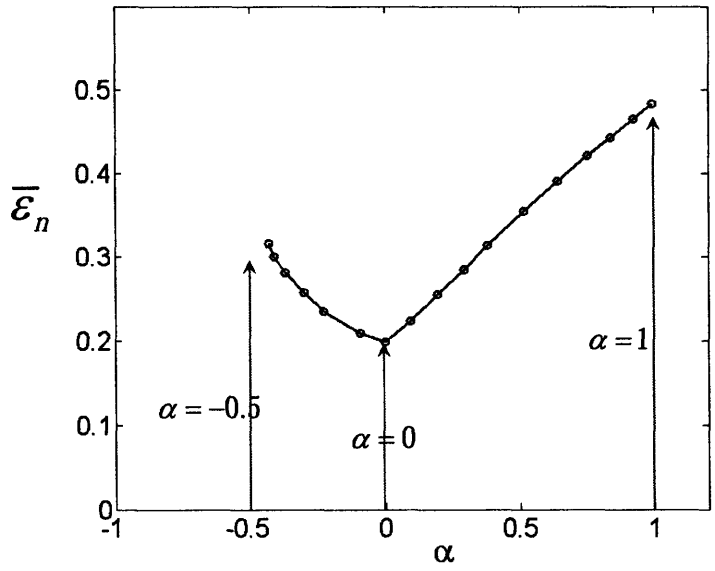

Fig. 6-2: Transformation from FLD to the space of $(\bar{\varepsilon}_n, \alpha)$ for 6111-T4 aluminum.

6.2.3 Space of $(\bar{\varepsilon}_n, \eta)$

Using Eq. (6.15),(6.11) and (6.10), the forming limit diagram can also be transformed to the space of $(\bar{\varepsilon}_n, \eta)$. The basic procedure of transformation is to use Eqs. (6.10) and (6.11) and eliminate the parameter β between three equations, which involves the following steps: $(\varepsilon_1, \varepsilon_2) \rightarrow (\varepsilon_1, \alpha) \rightarrow (\bar{\varepsilon}_n, \alpha) \rightarrow (\bar{\varepsilon}_n, \beta) \rightarrow (\bar{\varepsilon}_n, \eta)$. The experimental data points of 6111-T4 aluminum alloy (transverse direction) shown in Fig. 6-1 is re-drawn in this new space, as shown in Fig. 6-3. A FLD in the space of $(\bar{\sigma}_n, \sigma_m)$, which is similar to the current one $(\bar{\varepsilon}_n, \eta)$ was used to study the effect of pressure on FLD in hydroforming by Worswick's team (Hari Manoj Simha et al., 2007).

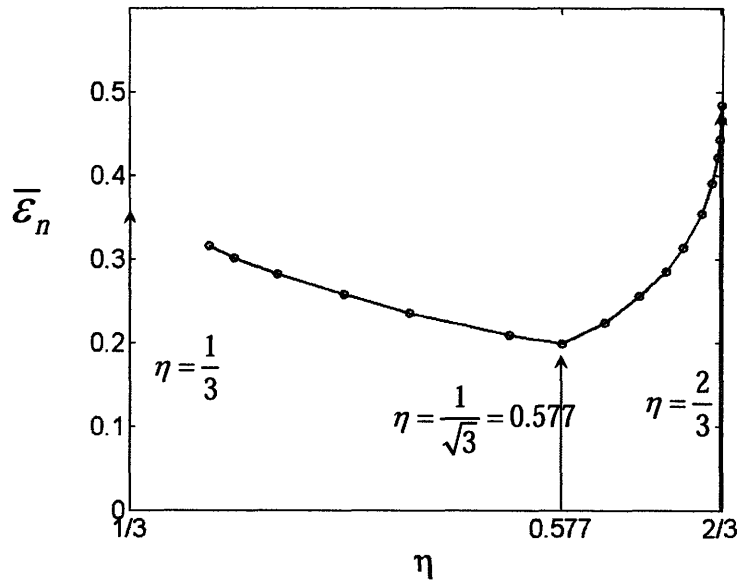

Fig. 6-3: Transformation from FLD to the space of $(\bar{\varepsilon}_n, \eta)$ for 6111-T4 aluminum.

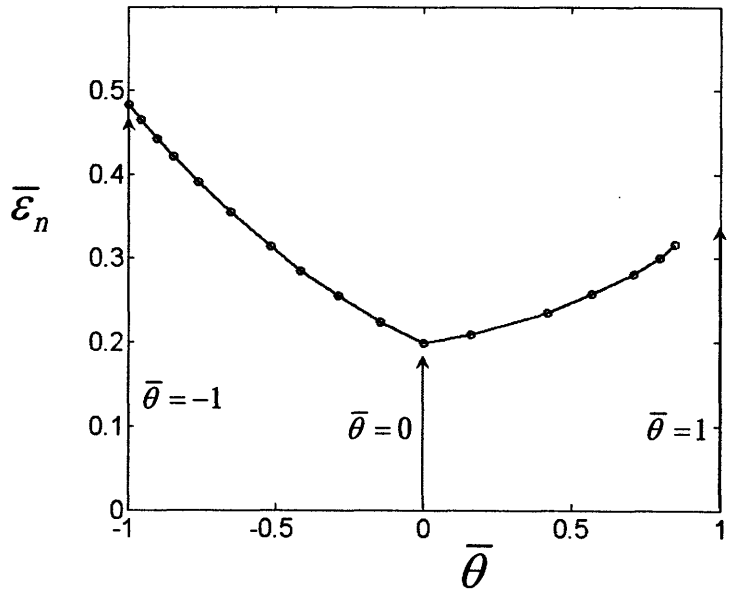

Fig. 6-4: Transformation from FLD to the space of $(\bar{\varepsilon}_n, \bar{\theta})$ for 6111-T4 aluminum.

6.2.4 Space of $(\bar{\varepsilon}_n, \bar{\theta})$

Similarly, using Eq. (6.15),(6.12) and (6.10), the forming limit diagram can be transformed to the space of $(\bar{\varepsilon}_n, \bar{\theta})$. The basic procedure is $(\varepsilon_1, \varepsilon_2) \rightarrow (\varepsilon_1, \alpha) \rightarrow (\bar{\varepsilon}_n, \alpha) \rightarrow (\bar{\varepsilon}_n, \beta) \rightarrow \left(\bar{\varepsilon}_n, \bar{\theta}\right)$. The experimental data points of 6111-T4 aluminum alloy (transverse direction), which is shown in Fig. 6-1 and mapped into this new space, is given in Fig. 6-4. It must be noted that all four representations of FLD are equivalent and carry the same amount of information.

6.2.5 Space of (σ_1, σ_2)

From the definition of equivalent stress (Eq. (6.3)), the two principal stresses (σ_1, σ_2) of a plane stress loading can be expressed in terms of the equivalent stress $\bar{\sigma}$ and the stress ratio β.

$$\begin{cases} \sigma_1 = \frac{\bar{\sigma}}{\sqrt{1-\beta+\beta^2}} \\ \sigma_2 = \frac{\beta\bar{\sigma}}{\sqrt{1-\beta+\beta^2}} \end{cases} . \tag{6.16}$$

To transform the FLD to the stress space (σ_1, σ_2), the material hardening law is needed to relate the equivalent strain $\bar{\varepsilon}$ and the equivalent stress $\bar{\sigma}$. A power hardening law is assumed.

$$\bar{\sigma} = A\bar{\varepsilon}^n, \tag{6.17}$$

where A and n are two material constants. Substitute Eq. (6.17) into Eq. (6.16), the relationship between the principal stresses and the equivalent strain $\bar{\varepsilon}$ is obtained.

$$\begin{cases} \sigma_1 = \frac{A\bar{\varepsilon}^n}{\sqrt{1-\beta+\beta^2}} \\ \sigma_2 = \frac{\beta A\bar{\varepsilon}^n}{\sqrt{1-\beta+\beta^2}} \end{cases} . \tag{6.18}$$

Using Eq. (6.15),(6.18) and (6.10), the forming limit diagram can be transformed to the space of two principal stresses. The basic procedure consists of the following steps: $(\varepsilon_1, \varepsilon_2) \rightarrow (\varepsilon_1, \alpha) \rightarrow (\bar{\varepsilon}_n, \alpha) \rightarrow (\bar{\varepsilon}_n, \beta) \rightarrow (\sigma_1, \sigma_2)$. Similar transformation was performed by Stoughton (2000) and others. The strain hardening property of the 6111-T4 aluminum alloy in the transverse direction are defined by $A = 540MPa$ and $n = 0.244$ (experimental data after Graf and Hosford (1994)). The transformed FLD to the space of principal stress is shown in Fig. 6-5. This is called the stress-based FLD extensively studied by Stoughton (2000); Smith et al. (2003); Stoughton and Zhu (2004).

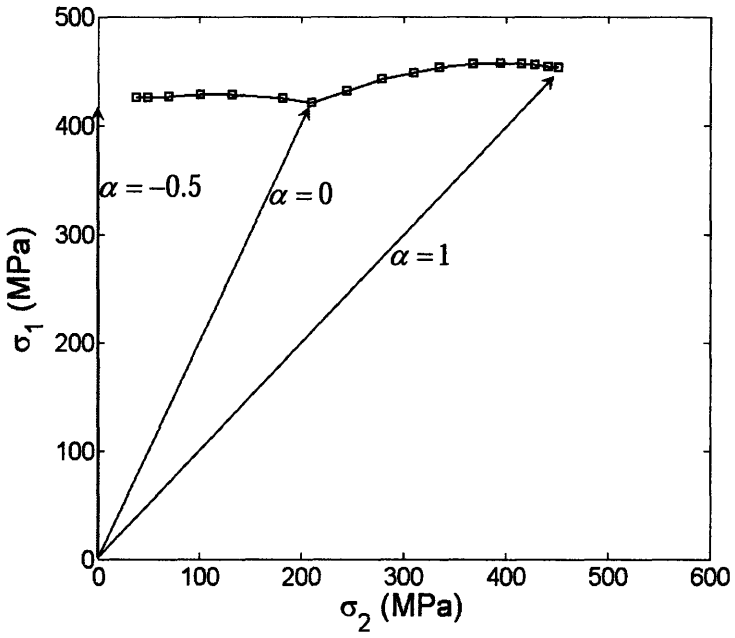

Fig. 6-5: Transformation from FLD to the space of (σ_1, σ_2) for 6111-T4 aluminum.

6.2.6 Analytical representation of FLD under proportional loading

The range of strain ratio α of interest to FLD is $-0.5 \leq \alpha \leq 1$, the range of stress triaxiality η is $\frac{1}{3} \leq \eta \leq \frac{2}{3}$, and the range of the Lode angle parameter $\bar{\theta}$ is $-1 \leq \bar{\theta} \leq 1$. Since there is a one to one correspondence between three parameters in the particular range, any parameter can be used to distinguish different loading conditions. Referring to the extensive work about the effect of Lode angle parameter on ductile fracture locus (Bai and Wierzbicki, 2007a; Bai et al., June 3-7, 2007; Bai and Wierzbicki, 2007b), the Lode angle parameter is chosen in this paper to be an independent parameter in formulating the FLD. For the purpose of predicting FLD under non-proportional loading paths, it is first necessary to provide data on proportional loading FLD, $\bar{\varepsilon}_n(\bar{\theta})$, as a reference value.

Curve fitting method using experimental data

The next step in the present methodology is to acquire information on the FLD under proportional loading. This can be either determined from Hill's and Stören and Rice analytical

solutions or from numerical simulation or else taken directly from experiments.

There are three typical loading conditions in sheets: uni-axial tension, plane strain tension and equi-biaxial tension. The corresponding values of stress state parameters of these three tests are summarized in Table 6.1.

Table 6.1: A summary of three typical tests for the FLD

State parameters	Uni-axial tension	Plane strain tension	Equi-biaxial tension
strain ratio α	-0.5	0	1
stress triaxiality η	$\frac{1}{3}$	$\frac{1}{\sqrt{3}}$	$\frac{2}{3}$
Lode angle parameter $\bar{\theta}$	1	0	-1
$\bar{\varepsilon}_n$, experimentally determined equivalent necking strain	$\bar{\varepsilon}_n^{UA}$	$\bar{\varepsilon}_n^{PE}$	$\bar{\varepsilon}_n^{BA}$

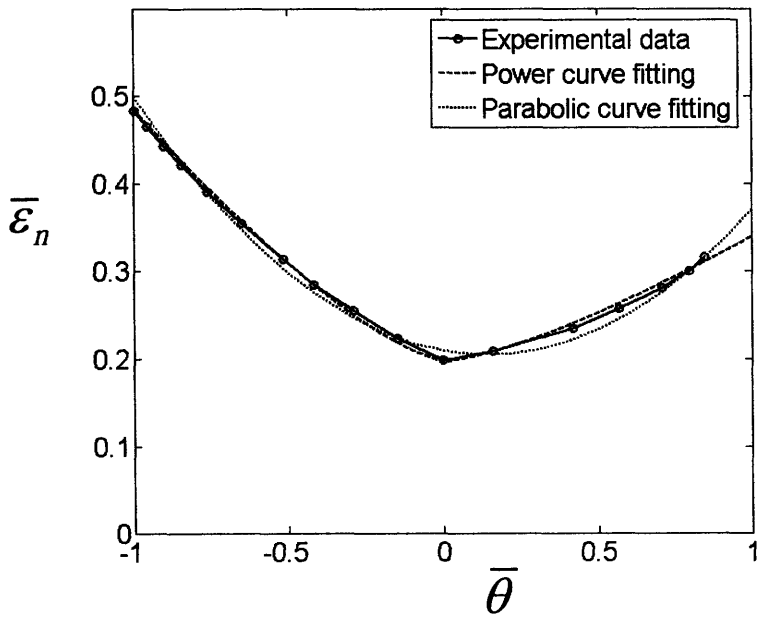

Fig. 6-6: Two types of curve fitting of FLD in the space of $(\bar{\varepsilon}_n, \bar{\theta})$

Similar to the effect of the Lode angle parameter on ductile fracture locus (Bai and Wierzbicki, 2007a,b), one can assume that the equivalent strain to necking is a parabolic

function of the Lode angle parameter,

$$\bar{\varepsilon}_n = \hat{\varepsilon}_n\left(\bar{\theta}\right) = \left[\frac{1}{2}\left(\bar{\varepsilon}_n^{UA} + \bar{\varepsilon}_n^{BA}\right) - \bar{\varepsilon}_n^{PE}\right]\bar{\theta}^2 + \frac{1}{2}\left(\bar{\varepsilon}_n^{UA} - \bar{\varepsilon}_n^{BA}\right)\bar{\theta} + \bar{\varepsilon}_n^{PE}. \tag{6.19}$$

A distinction should be made between $\bar{\varepsilon}_n$ and $\hat{\varepsilon}_n(\bar{\theta})$. The former is the equivalent strain to necking, while the latter is the function of equivalent strain to necking for different Lode angle parameters $\bar{\theta}$. There are three free parameters in Eq. (6.19), which are the equivalent strain to necking for three typical loading conditions. As an illustration, consider the empirical locus of necking points for 6111-T4 aluminum alloy represented in the $(\bar{\varepsilon}_n, \bar{\theta})$ space (Fig. 6-4). Minimizing the mean square error between Eq. (6.19) and the transformed FLD, the following combination of three parameters is obtained: $\bar{\varepsilon}_n^{UA} = 0.37$, $\bar{\varepsilon}_n^{PE} = 0.21$, and $\bar{\varepsilon}_n^{BA} = 0.50$. It is shown in Fig. 6-6 that this formula gives a good approximation to the FLD. The accuracy of curve fitting can be further improved if one more parameter is introduced, using a power function representation, see Eq. (6.20).

$$\bar{\varepsilon}_n = \hat{\varepsilon}_n\left(\bar{\theta}\right) = \bar{\varepsilon}_n^{PE} + \left(\bar{\varepsilon}_n^{AX} - \bar{\varepsilon}_n^{PE}\right)\left|\bar{\theta}\right|^M, \tag{6.20}$$

where, the parameter $\bar{\varepsilon}_n^{AX}$ is defined as

$$\bar{\varepsilon}_n^{AX} = \begin{cases} \bar{\varepsilon}_n^{UA} & for \quad \bar{\theta} \geq 0 \\ \bar{\varepsilon}_n^{BA} & for \quad \bar{\theta} < 0 \end{cases}. \tag{6.21}$$

The additional parameter is the power index M. The curve fitting result using Eq.(6.20) is also shown in Fig. 6-6. Curve fitting gives the combination of four parameters: $\bar{\varepsilon}_n^{UA} = 0.340$, $\bar{\varepsilon}_n^{PE} = 0.197$, $\bar{\varepsilon}_n^{BA} = 0.485$, and $M = 1.35$. The results of curve fitting can also be transformed back to the space of $\varepsilon_1, \varepsilon_2$ using the inverse methods described in Section 6.2.4. As shown in Fig. 6-7, a very good correlation is now achieved between the empirical FLD and its analytical representation given by Eq. (6.20). Equation (6.20) will be used in this paper to describe the FLD under proportional loading. Using this approximate formula with four parameters, four types of tests would be needed to calibrate the FLD under proportional loading condition.

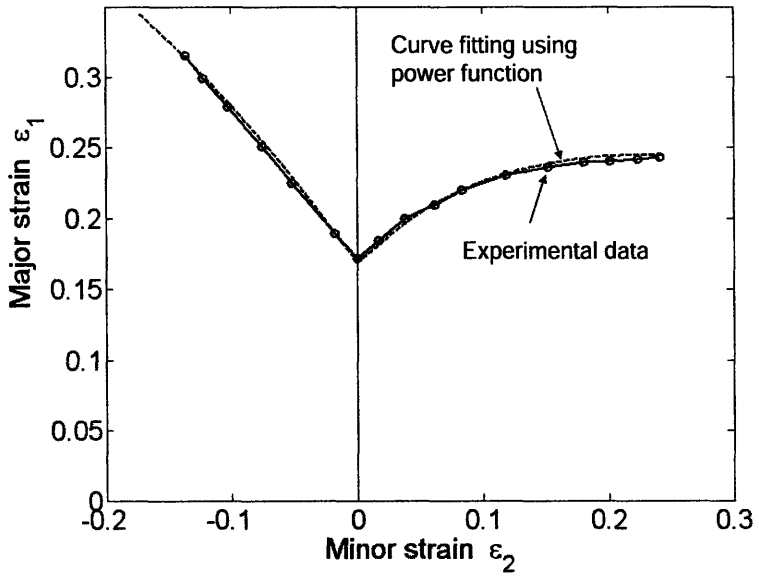

Fig. 6-7: Power function curve fitting of FLD in the $(\bar{\varepsilon}_n, \bar{\theta})$ compared with the experimental results in the space of $(\varepsilon_1, \varepsilon_2)$ (transverse direction of 6111-T4 aluminum alloy, $\bar{\varepsilon}_n^{UA} = 0.340$, $\bar{\varepsilon}_n^{PE} = 0.197$, $\bar{\varepsilon}_n^{BA} = 0.485$, and $M = 1.35$).

Curve fitting method using existing closed-form solutions

Hill (1952) developed a theory to analyze the localized necking in metal sheets, which gives the forming limit for the range between uni-axial tension and plane strain tension.

$$\varepsilon_{1n} = \frac{n}{1+\alpha} \qquad for \quad -0.5 \leq \alpha \leq 1 \ , \tag{6.22}$$

where n is the strain hardening exponent defined in Eq. (6.17). Storen and Rice (1975) used theoretical bifurcation analysis and provided an expression for the FLD in the first tension-tension quadrant,

$$\varepsilon_{1n} = \frac{3\alpha^2 + n\,(2+\alpha)^2}{2\,(2+\alpha)\,(1+\alpha+\alpha^2)} \qquad for \quad 0 \leq \alpha \leq 1 \ . \tag{6.23}$$

From Hill's formulation (Eq. (6.22)), one can estimate necking strains in uni-axial tension ($\bar{\varepsilon}_n^{UA}$) and plane strain tension ($\bar{\varepsilon}_n^{PE}$). Meanwhile, from the Stören and Rice's analysis (Eq. (6.23)), the necking strain under equi-biaxial tension ($\bar{\varepsilon}_n^{BA}$) can also be predicted. The three

necking reference strains, calculated from Eq. (6.22) and Eq. (6.23) are

$$\begin{cases} \bar{\varepsilon}_n^{UA} = 2n & for \quad \alpha = -0.5 \\ \bar{\varepsilon}_n^{PE} = \frac{2}{\sqrt{3}}n & for \quad \alpha = 0 \\ \bar{\varepsilon}_n^{BA} = n + \frac{1}{3} & for \quad \alpha = 1 \end{cases} . \tag{6.24}$$

The fourth parameter in the approximate formula of FLD (Eq. (6.20)) is the power exponent M. It is suggested that $M = 1 \sim 2$. If one takes $M = 2$ in Eq. (6.20), a comparison between the approximate formula and the theoretical analysis is shown in Fig. 6-8. One can see that the approximate formula fits very well with two analytical solutions. It should be noted that these parameter estimations are tentative, but they are good for engineering application in the absence of a sufficient number of experimental data.

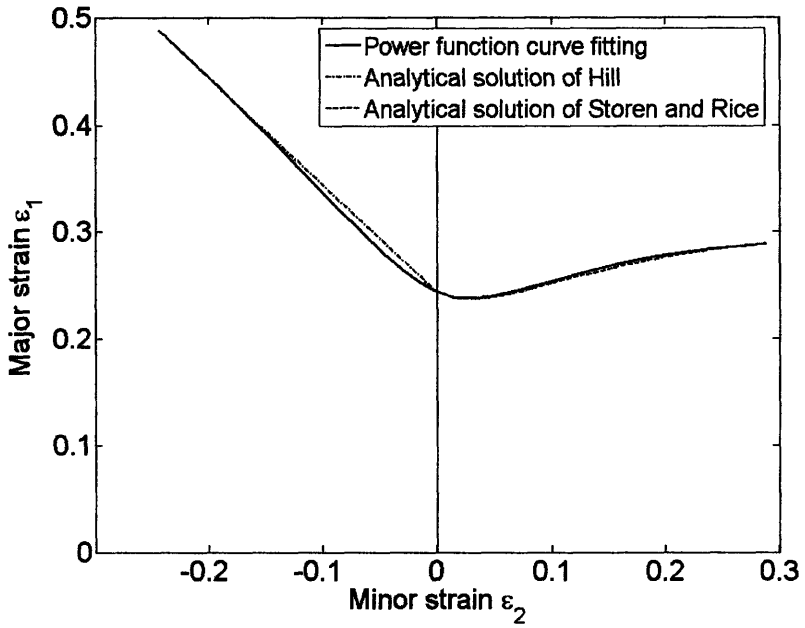

Fig. 6-8: An example of the proposed power function curve fitting of FLD compared with analytical solution from Hill, Stören and Rice ($n = 0.244$ for analytical solution, and $\bar{\varepsilon}_n^{UA} = 0.488$, $\bar{\varepsilon}_n^{PE} = 0.2817$, $\bar{\varepsilon}_n^{BA} = 0.5773$, $M = 2$ for the power function).

6.3 A new model considering the loading history effect on sheet necking

In Section 6.2.6, the FLD under proportional loading was discussed and re-formulated in the space of $(\bar{\varepsilon}_n, \bar{\theta})$. However, in many practical press shop stamping operations, the strain-path changes in a continuous or abrupt manner. A large effect of the loading history on FLD was demonstrated experimentally by many authors (Muschenborn and Sonne, 1975; Graf and Hosford, 1994; Zhao et al., 1996). Attempts have also been made to predict this effect theoretically (Marciniak and Kuczynski, 1967; Cao et al., 2000; Stoughton, 2000).

According to an FLD, necking will occur once a combination of two principal strains exceed a limiting value. Instead of this commonly accepted viewpoint, the onset of sheet necking can be treated as an accumulative process of "forming severity". A scalar variable N, which is a measure of how far a given material point is from the onset of necking, is introduced. By analogy to the concept of the cumulative damage model (Wilkins et al., 1980; Johnson and Cook, 1985; Bao, 2003; Bai et al., 2006a), the onset of necking is said to occur when the integral of equivalent strain with a suitable weighting function of the stress state parameter $\bar{\theta}$ reaches a critical value N_c, see Eq. (6.25).

$$N = \int_0^{\bar{\varepsilon}} f\left(\bar{\theta}\right) d\bar{\varepsilon}. \tag{6.25}$$

At the necking point, $\bar{\varepsilon} = \bar{\varepsilon}_n$ and $N = N_c$. Now, the goal is to find a suitable weighting function $f(\bar{\theta})$, so that necking could be predicted under all loading cases. It is convenient to introduce a normalized critical forming severity index, which from now on will be denoted by N. Now necking occurs when $N_c = 1$. Under proportional loading conditions, the Lode angle parameter $\bar{\theta}$ is constant, and Eq. (6.25) can be integrated to give

$$f\left(\bar{\theta}\right) \bar{\varepsilon}_n = N_c = 1. \tag{6.26}$$

Using Eq. (6.26), Eq. (6.25) can be written in an alternative form,

$$N_c = \int_0^{\bar{\varepsilon}_n} \frac{1}{\hat{\varepsilon}_n\left(\bar{\theta}\right)} d\bar{\varepsilon} = 1, \tag{6.27}$$

where $\hat{\varepsilon}_n(\bar{\theta})$ is the necking locus discussed in Section 6.2.6. For non-proportional loading, in which $\bar{\theta}$ changes along the loading path, the integral (Eq. (6.27)) can still be evaluated

and the critical equivalent strain to necking $\bar{\varepsilon}_n$ could be determined. Such an approach was proposed, for example, by the BMW-MATFEM team (Hooputra et al., Oct. 2003; Werner et al., Oct. 2004; Hooputra et al., 2004). The evolution of necking severity index can be represented in a differential form, $dN = d\lambda$, where λ is defined by

$$\lambda \triangleq \frac{\bar{\varepsilon}}{\hat{\varepsilon}_n\left(\bar{\theta}\right)}, \tag{6.28}$$

which implies a linear accumulation of the forming severity in the loading process. To make sure that the necking severity N is an increasing function, the increment $d\lambda$ is defined as,

$$d\lambda = \frac{d\bar{\varepsilon}}{\hat{\varepsilon}_n\left(\bar{\theta}\right)}, \tag{6.29}$$

where, from the definition, $d\bar{\varepsilon}$ is non-negative. This limitation of linearity is now removed, and instead, a non-linear necking accumulation rule is proposed as

$$dN = g(\lambda)d\lambda., \tag{6.30}$$

where the function $g(\lambda)$ should be non-negative. Now the necking is assumed to occur when

$$g(\lambda) \geq 0 \quad , \quad \int_0^{\lambda_f} g(\lambda)d\lambda = 1. \tag{6.31}$$

A similar nonlinear accumulation rule applied to the problem of onset of ductile fracture was considered in Bonora (1997); Bai et al. (2006a); Xue (2007b).

Different forms of function $g(\lambda)$ can be postulated based on different assumptions. Some possible representatives of a family of $g(\lambda)$, expressed in terms of elementary functions, are listed in Table 6.2. In this paper, the function $g(\lambda)$ is postulated to be a solution of the following simple differential equation subjected to the initial condition, $N\,|_{\lambda=0} = 0$, and the normalization condition, $N\,|_{\lambda=1} = 1$.

$$\frac{dN}{d\lambda} = b + c_g N \quad , \quad N\,|_{\lambda=0} = 0 \quad , \quad N\,|_{\lambda=1} = 1. \tag{6.32}$$

The first term in this equation corresponds to the linear rate of forming severity, while the second term accounts for the accelerated growth. The solution of the first order differential equation involves one integration constant, which is found from the initial condition. The normalization condition provides a unique relationship between two coefficients in the differ-

ential equation, $b = \frac{c_g}{e^{c_g}-1}$. Therefore, the solution of the two-point boundary value problem takes finally the form,

$$N(\lambda) = \frac{e^{c_g\lambda} - 1}{e^{c_g} - 1}. \tag{6.33}$$

From Eq. (6.33), the increment of N is

$$dN = \frac{c_g}{e^{c_g} - 1} e^{c_g\lambda} d\lambda. \tag{6.34}$$

Comparison of Eq. (6.30) and Eq. (6.34) gives an expression for the weighting function $g(\lambda)$, which is listed in row No. 6 in Table 6.2.

Table 6.2: Some typical forms of function $g(\lambda)$

No.	Formula of $g(\lambda)$	Remark
1	1	Linear assumption for forming severity accumulation
2	$\delta(\lambda - 1)$	Final value assumption, δ is the Dirac's delta function.
3	$\frac{H(\lambda - c_g)}{1 - c_g}$	Threshold value assumption, H is the step function.
4	$\begin{cases} c_g\lambda - \frac{c_g}{2} + 1 & for \quad c_g \leq 2 \\ c_g\lambda - c_g + \sqrt{2c_g} & for \quad c_g > 2 \end{cases}$	Linear weighting function
5	$(c_g + 1)\lambda^{c_g}$	Power weighting function
6	$\frac{c_g}{e^{c_g}-1} e^{c_g\lambda}$	Exponental weighting function

Note that all functions listed in Table 6.2 involve only one free parameter c_g, which has to be determined from suitable tests. A comparison of four weighting function from Table 6.2 is shown in Fig. 6-9(a). The above functions have been normalized, so that in all case $N_c = 1$, see Fig. 6-9(b). In this paper, the exponential weighting function (case No. 6 in Table 6.2) is chosen for all illustrative examples, so that Eq. (6.31) takes the following particular form,

$$N_c = \int_0^{\lambda_f} \left(\frac{c_g}{e^{c_g} - 1} \right) e^{c_g\lambda} d\lambda = 1, \tag{6.35}$$

where λ is defined in Eq. (6.28). It should be noted that in the case of complex loading history, the denominator in Eq. (6.28) may assume different values in various segments of the loading history. This implies in general discontinuity in the variable λ. Only for proportional loading, λ is a continuous variable. In the above formulation, there is only one free parameter, c_g, so that at least one type of test with non-proportional loading is needed for calibration.

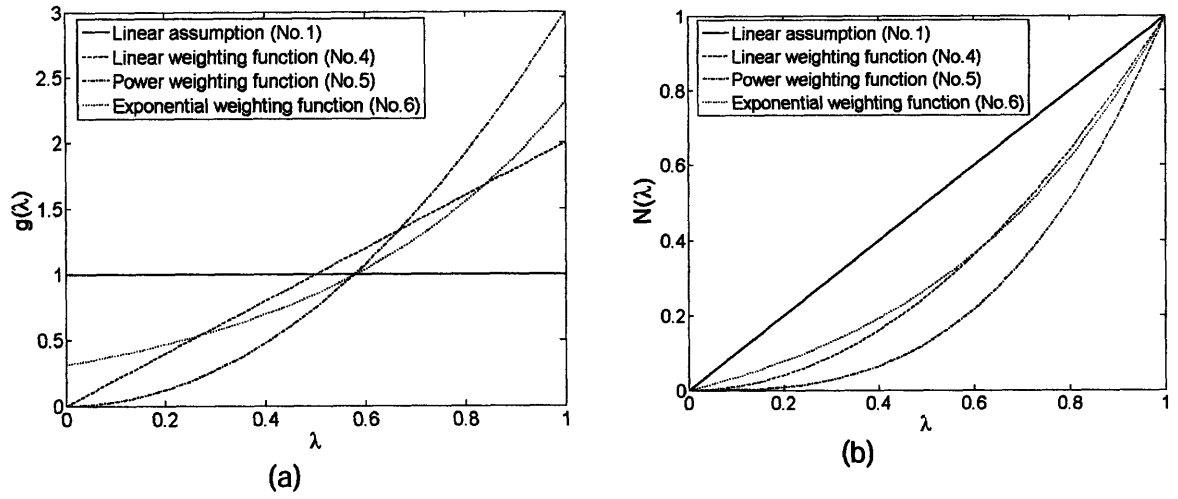

Fig. 6-9: Comparison of different weighting functions for the case of $c_g = 2$.

It is important to note that Eq. (6.35) reduces to the necking locus of the conventional FLD under proportional loading, where λ is a continuously increasing variable. This can be proved by performing the integration, which gives the following condition,

$$\frac{e^{c_g \lambda_f} - 1}{e^{c_g} - 1} = 1. \tag{6.36}$$

The solution of this equation is $\lambda_f = 1$, which, according to the definition of λ, gives the necking locus defined under proportional loading, $\bar{\varepsilon}_n = \hat{\varepsilon}_n(\bar{\theta})$. Under non-proportional or complex loading conditions, the parameter λ could be discontinuous. Referring to Eq. (6.32) for the exponential weighting function $g(\lambda)$, the Eq. (6.35) can be rewritten as an incremental form,

$$dN = \left(c_g N + \frac{c_g}{e^{c_g} - 1}\right) \frac{d\bar{\varepsilon}^p}{\hat{\varepsilon}_n\left(\bar{\theta}\right)}, \tag{6.37}$$

and a material element is assumed to neck when $N = 1$. The incremental form is convenient in the implementation to finite element codes, and the integral form is easier for analytical solutions under piece-wise loading conditions. The merit of working with Eq. (6.35) or Eq. (6.37) is that it can predict necking under complex loading path, which will be validated by experimental data in the subsequent sections.

6.4 Model calibration

In the following sections, experimental data of two types of material are used to calibrate and validate the proposed necking model. One is aluminum alloy 6111-T4 (Graf and Hosford, 1994), the other is aluminum-killed sheet steel (Muschenborn and Sonne, 1975). The present procedure includes three steps: curve fitting of FLD under proportional loading, calibrating the loading history function (parameter c_g), and predicting FLD under complex loading conditions.

Graf and Hosford (1994) performed a series of tests to determine the forming limit of aluminum alloy 6111-T4 under complex loading conditions. These data is revisited in this section. The curve fitting of FLD under proportional loading for aluminum alloy 6111-T4 (transverse direction) is presented in Section 6.2.6. Similarly, the FLD for the major strain on the rolling direction is also fitted using Eq. (6.20). A summary of the model parameters for both direction is listed in Table 6.3.

Table 6.3: Calibrated model parameters for aluminum alloy 6111-T4

Direction	$\bar{\varepsilon}_n^{UA}$	$\bar{\varepsilon}_n^{PE}$	$\bar{\varepsilon}_n^{BA}$	M	c_g
Transverse direction (TD)	0.340	0.197	0.485	1.35	1.24
Rolling direction (RD)	0.275	0.250	0.555	1.45	1.24

As one additional test with non-proportional loading is needed to calibrate the free parameter c_g, chosen is one typical test with two-stage proportional loading reported by Graf and Hosford (1994). This is the equi-biaxial tension ($\bar{\theta} = -1$, $\Delta\bar{\varepsilon} = 0.03 \times 2 = 0.06$, see $\overline{OA}$ in Fig. 6-11) followed by plane strain tension ($\bar{\theta} = 0$, $\Delta\bar{\varepsilon}' = 0.13 \times \frac{2}{\sqrt{3}} = 0.15$, see $\overline{AB}$ in Fig. 6-11). According to Eq. (6.35), the integral of the forming severity is broken into two stages,

$$N = N_1 + N_2 = \int_0^{\lambda_1} \left(\frac{c_g}{e^{c_g} - 1}\right) e^{c_g \lambda} d\lambda + \int_{\lambda_1'}^{\lambda_2'} \left(\frac{c_g}{e^{c_g} - 1}\right) e^{c_g \lambda'} d\lambda' = 1, \tag{6.38}$$

where limits of the above two integral, λ_1, λ_1' and λ_2' are evaluated as follows,

$$\lambda_1 = \frac{\Delta\bar{\varepsilon}}{\hat{\bar{\varepsilon}}_n^{(TD)}\left(\bar{\theta} = -1\right)} = \frac{0.06}{0.485} = 0.1237, \tag{6.39}$$

$$\lambda_1' = \frac{\Delta\bar{\varepsilon}}{\hat{\bar{\varepsilon}}_n^{(TD)}\left(\bar{\theta} = 0\right)} = \frac{0.06}{0.197} = 0.3046, \tag{6.40}$$

$$\lambda_2^{'} = \frac{\Delta\bar{\varepsilon} + \Delta\bar{\varepsilon}^{'}}{\hat{\varepsilon}_n^{(TD)}\left(\bar{\theta}=0\right)} = \frac{0.06+0.15}{0.197} = 1.066, \tag{6.41}$$

where $\Delta\bar{\varepsilon}$ is the increment of equivalent strain in prestraining stage (see $\overline{OA}$ in Fig. 6-11), and $\Delta\bar{\varepsilon}^{'}$ is the increment of equivalent strain in the second stage (see $\overline{AB}$ in Fig. 6-11). Substituting Eqs (6.39),(6.40) and (6.41) into Eq. (6.38), the parameter c_g is found numerically to be $c_g = 1.24$.

6.5 Prediction of necking after initial prestraining

Four types of prestrain tests were reported by Graf and Hosford in their study on the loading history effect on FLD: biaxial prestraining, uni-axial prestraining in transverse direction, plane strain prestraining, and uni-axial prestraining in rolling direction (RD). All four types of tests will be compared with the prediction of the newly calibrated necking model. Since all the experimental loading conditions consist of two stages of proportional loadings, the model prediction using Eq. (6.35) can be transformed to the plane of $(\varepsilon_1, \varepsilon_2)$. The procedure of deriving modified FLD is explained for the case of two stage loading, expressed by Eq. (6.38). Given the prestraining $\left(\Delta\varepsilon_1^{(I)}, \Delta\varepsilon_2^{(I)}\right)$, since the parameter c_g has already been calibrated, the unknown in the above equation is the amount of relative straining, $\lambda_2^{'}$, corresponding to the onset of necking in the second stage. Integrating Eq. (6.38) and solving for $\lambda_2^{'}$ yields

$$\lambda_2^{'} = \frac{1}{c_g}\ln\left(e^{c_g} - e^{c_g\lambda_1} + e^{c_g\lambda_1^{'}}\right), \tag{6.42}$$

where the λ_1 and $\lambda_1^{'}$ are calculated/defined by

$$\lambda_1 = \frac{\Delta\bar{\varepsilon}^{(I)}}{\hat{\varepsilon}_n\left[\bar{\theta}^{(I)}\right]}, \tag{6.43}$$

$$\lambda_1^{'} = \frac{\Delta\bar{\varepsilon}^{(I)}}{\hat{\varepsilon}_n\left(\bar{\theta}_i\right)}. \tag{6.44}$$

The $\bar{\theta}_i$ in Eq. (6.44) denotes an arbitrary loading condition in the second stage loading. Then, from the definition of $\lambda_2^{'}$, the increment of equivalent strain in the second stage,$\Delta\bar{\varepsilon}^{(II)}$ can be solved.

$$\lambda_2^{'} = \frac{\Delta\bar{\varepsilon}^{(I)} + \Delta\bar{\varepsilon}^{(II)}}{\hat{\varepsilon}_n\left(\bar{\theta}_i\right)} \tag{6.45}$$

$$\Delta\bar{\varepsilon}^{(II)} = \lambda_2' \hat{\varepsilon}_n \left(\bar{\theta}_i\right) - \Delta\bar{\varepsilon}^{(I)} \tag{6.46}$$

Knowing the $\Delta\bar{\varepsilon}^{(II)}$ and $\bar{\theta}_i$, the strain increments in two principal directions, $\left(\Delta\varepsilon_1^{(II)}, \Delta\varepsilon_2^{(II)}\right)$, can be evaluated. Therefore, the predicted necking point, $(\varepsilon_1, \varepsilon_2)$, in the FLD is obtained. The steps involved in the procedure are shown in Fig. 6-10.

Stage (I) (Prestraining) :

$$\begin{bmatrix} \Delta\varepsilon_1^{(I)} \\ \Delta\varepsilon_2^{(I)} \end{bmatrix} \rightarrow \begin{bmatrix} \bar{\theta}^{(I)} \\ \Delta\bar{\varepsilon}^{(I)} \end{bmatrix} \rightarrow \begin{bmatrix} N_1 \\ \Delta\bar{\varepsilon}^{(I)} \end{bmatrix}$$

Stage (II) (FLD calibration, for every $\bar{\theta}_i$) :

$$\begin{bmatrix} -1 \le \bar{\theta}_i \le 1 \\ N_2 = 1 - N_1 \\ \Delta\bar{\varepsilon}^{(I)} \end{bmatrix} \rightarrow \begin{bmatrix} \bar{\theta}_i \\ \Delta\bar{\varepsilon}^{(II)} \end{bmatrix} \rightarrow \begin{bmatrix} \Delta\varepsilon_1^{(II)} \\ \Delta\varepsilon_2^{(II)} \end{bmatrix} \rightarrow \begin{bmatrix} \varepsilon_1 = \Delta\varepsilon_1^{(I)} + \Delta\varepsilon_1^{(II)} \\ \varepsilon_2 = \Delta\varepsilon_2^{(I)} + \Delta\varepsilon_2^{(II)} \end{bmatrix}$$

Fig. 6-10: A sketch of transformation of model prediction for two-stage loading to the $(\varepsilon_1, \varepsilon_2)$ plane.

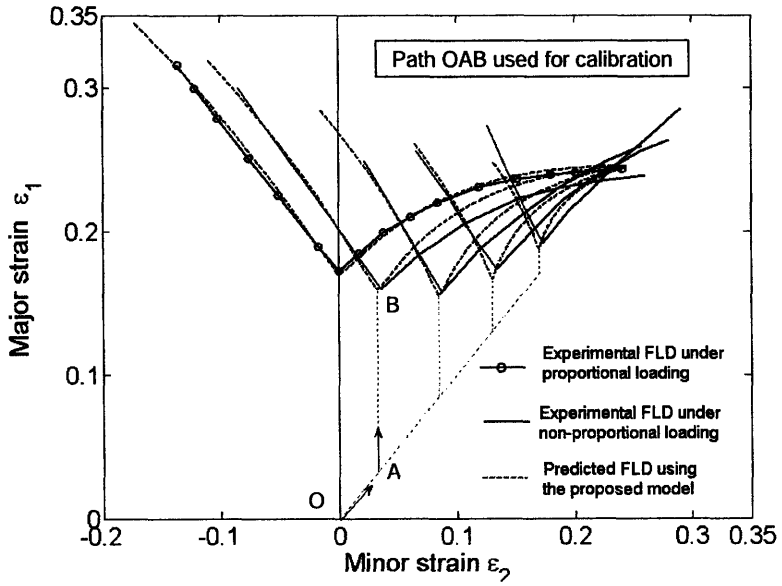

Fig. 6-11: Comparison between model prediction (dashed curves) and experimental results (solid curves) on the plane of $(\varepsilon_1, \varepsilon_2)$ after different equi-bixial-prestraining. The FLD is for aluminum 6111-T4 in transverse direction. Path OAB is used for calibration.

Prestraining in equi-biaxial tension: The solid curves in Fig. 6-11 show the experimental FLDs of aluminum alloy 6111-T4 prestrained in equi-biaxial tension. Four different amount of prestraining are included, which are the major strain $\Delta\varepsilon_1^{(I)}$ equal to 0.03, 0.085, 0.13 and 0.17. (The corresponding $\Delta\bar{\varepsilon}$ are 0.06, 0.17, 0.26 and 0.34.) The dashed curves in Fig. 6-11 show the FLDs predicted by the model. It is found that the FLDs from model prediction agree very well with the experimental results. It should be noted that circles in Figs 6-11 through 6-16 do not refer to specific experimental data points but rather distinguish the curve corresponding to FLD obtained experimentally under proportional loading.

Prestraining in uni-axial tension in transverse direction: The solid curves in Fig. 6-12 are the measured FLDs of aluminum alloy 6111-T4 prestrained in uni-axial tension. Four different amount of prestraining were applied, which are the major strain $\Delta\varepsilon_1^{(I)}$ equal to 0.05, 0.095, 0.14 and 0.18. (The corresponding $\Delta\bar{\varepsilon}$ is equal to $\Delta\varepsilon_1^{(I)}$ for uni-axial tension.) The dashed curves in Fig. 6-12 are the FLDs predicted by the model. Again, one can see that the model predictions follow the trend of the experimental results.

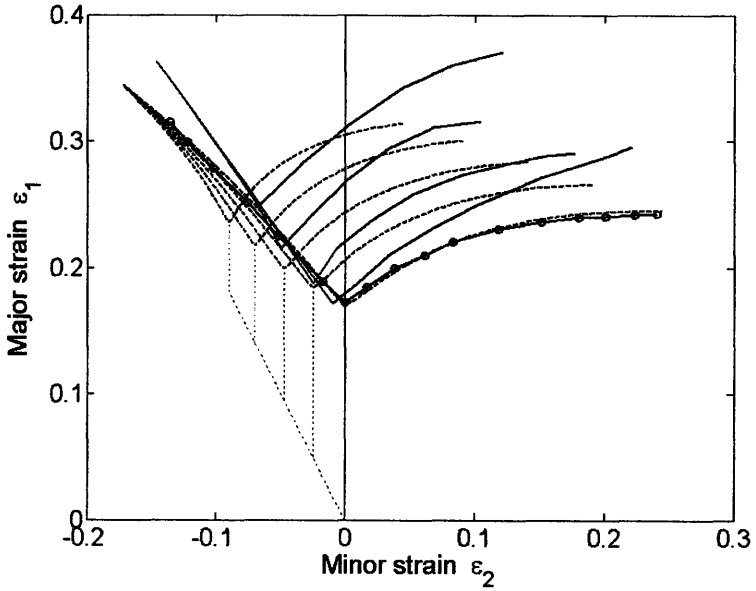

Fig. 6-12: Comparison between model prediction (dashed curves) and experimental results (solid curves) on the plane of $(\varepsilon_1, \varepsilon_2)$ after different uni-axial-prestraining. The FLD is for aluminum 6111-T4 in transverse direction.

Prestraining in plane strain tension in transverse direction: The solid curves in Fig. 6-13 show the measured FLDs of aluminum alloy 6111-T4 prestrained in plane strain

tension. Two different amount of prestraining were tested, which are the major strain $\Delta\varepsilon_1^{(I)}$ equal to 0.05, and 0.11. (The corresponding $\Delta\bar{\varepsilon}$ are 0.0577 and 0.127.) The dashed curves in Fig. 6-13 are the corresponding model predictions.

The predicted FLD corresponding to both amounts of prestraining were found to be very close to the reference proportional loading FLD curve. At the same time, the experimental curves are somewhat higher. This point was brought up under discussion by the authors of the test themselves. They noted that, in the case of plane strain loading path, there was no change in the strain trajectory from single stage to double stage loading cases. Therefore, there should not be any effect of the loading history. On further scrutiny, they concluded that the difference is due to the effect of strain recovery as the first stage and the second stage tests were done on different days. When adjusting for this effect, the experimental FLD should be much closer to the one predicted by the present method.

The question of accuracy of Graf and Hosford's experiments was brought by Stoughton. He pointed out that because there must have been an error in the tests with plane strain prestraining, the same error might propagate to other tests such as uni-axial tension prestraining. More tests under complex loading histories are need to clarify this point.

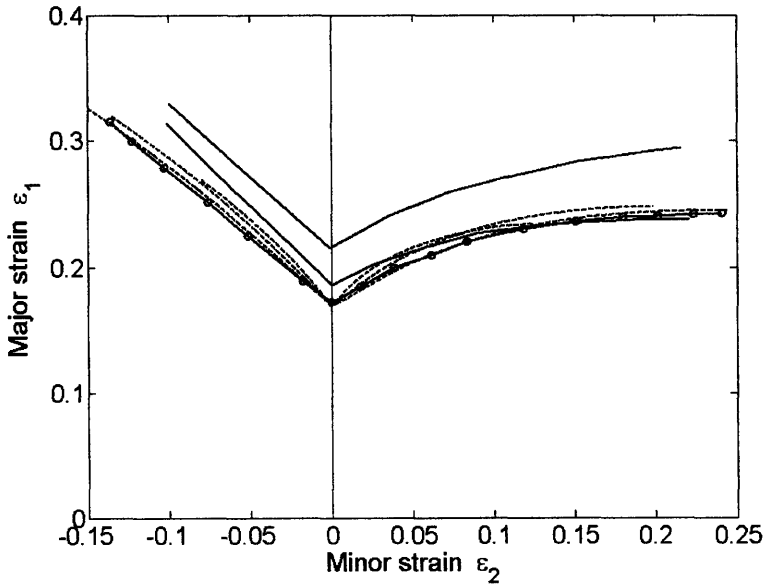

Fig. 6-13: Comparison between model prediction (dashed curves) and experimental results (solid curves) on the plane of $(\varepsilon_1, \varepsilon_2)$ after different plane strain prestraining. The FLD is for aluminum 6111-T4 in transverse direction.

Prestraining in uni-axial tension in rolling direction: Experimental results have shown that the FLD of aluminum 6111-T4 is anisotropic. There is an obvious difference between two FLDs under proportional loading for rolling direction and transverse direction, see Table 6.3. Figure 6-14 shows the FLDs in transverse direction after prestraining with uni-axial tension in rolling direction. Even though the development of the present theory is done under the assumption of material isotropy, the effect of in-plane sheet anisotropy is partially taken into account by introducing different necking loci in rolling and transverse directions (see Table 6.3). In the model prediction, the FLD for rolling direction is used for the first stage uni-axial tension, and the FLD for transverse direction is used for the second stage loadings. The dashed curves in Fig. 6-14 show the results of model prediction. It is seen that the model predicts the FLD under this type of complex loading condition with very good accuracy.

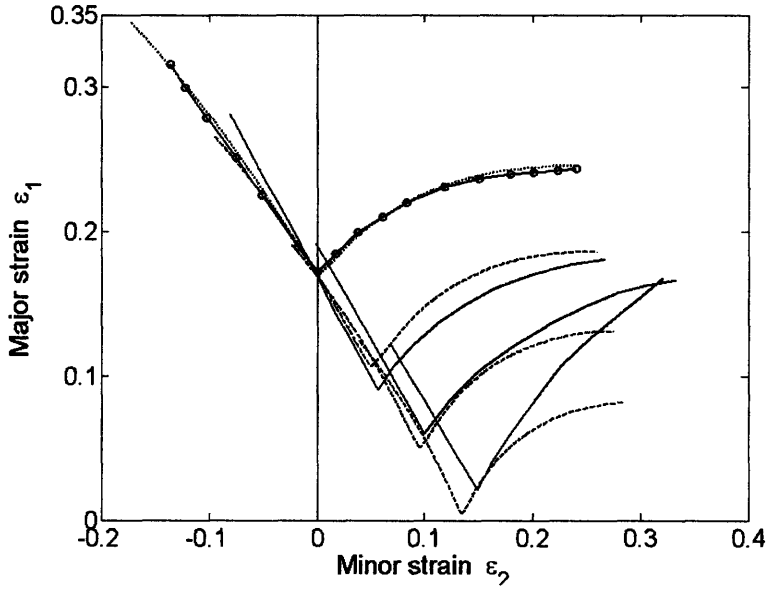

Fig. 6-14: Comparison between model prediction (dashed curves) and experimental results (solid curves) on the plane of $(\varepsilon_1, \varepsilon_2)$ after different uni-axial-prestraining in rolling direction. The FLD is for aluminum 6111-T4 in transverse direction.

Although only one additional parameter, c_g, is introduced to the necking prediction model, from the comparisons of all four types of complex loading (Figs. 6-11, 6-12, 6-13 and 6-14), it can be concluded that the proposed necking model works well for both proportional loading and complex loading conditions.

6.6 Further application to steel sheets

Another material to be reviewed in this paper is the aluminum-killed sheet steel. A series of necking tests on aluminum-killed sheet steel were performed by Muschenborn and Sonne (1975). These tests included proportional loading tests to calibrate the FLD and two types of loading with complex strain path, which are prestrained under uni-axial tension and equi-biaxial tension, respectively. It should be noted that neither Eq. (6.19) nor Eq. (6.20) can adequately describe a rather smooth experimental reference FLD. Therefore, a third option is used here, in which an experimental data from the reference FLD is introduced directly to the present calculation routine. In other words, the function $\hat{\varepsilon}_n(\bar{\theta})$ is represented by a set of data points rather than an analytical formula.

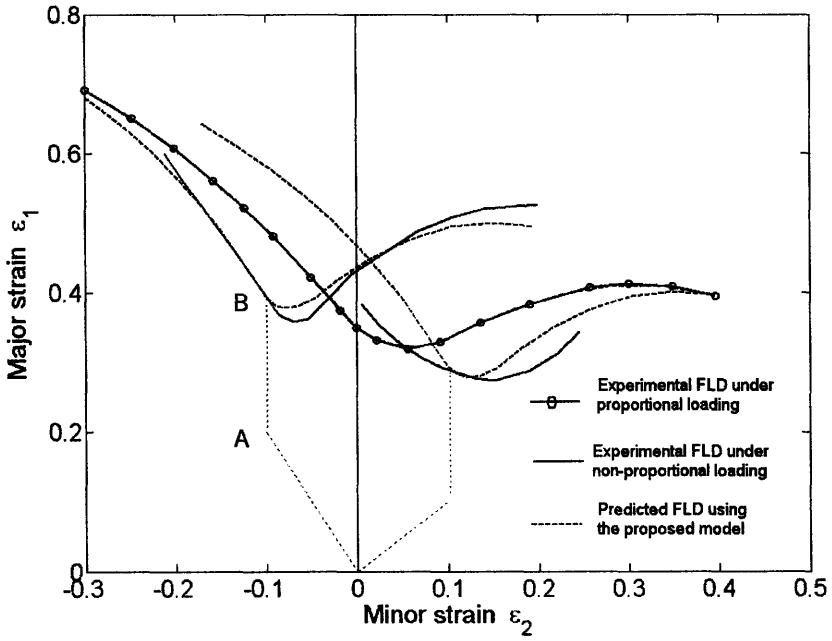

Fig. 6-15: Comparison between model prediction (dashed curves) and experimental results (solid curves) on the plane of $(\varepsilon_1, \varepsilon_2)$ under both proportional loading and with different prestraining. The FLD is for aluminum-killed sheet steel.

The test used for calibrating the parameter c_g is the uni-axial tension followed by plane strain tension (path OAB in Fig. 6-15). The calibrated parameter is $c_g = 2.5$. The present necking model is then used to predict FLD under complex strain path. The comparison between model predictions and experiments is illustrated in Fig. 6-15. It is found that the

proposed necking model well predicts the trends of the effect of strain path on sheet metal necking. One can see that the accuracy of the present calculations is very good in the case of uni-axial tension prestraining. In the case of equi-biaxial prestraining, the differences are larger, but this could be attributed to an insufficient accuracy of the reference FLD.

6.7 Discussion and conclusion

The currently used strain-based FLD depends strongly on the loading history. Under the proportional loading assumption, the FLD is transformed to several different spaces such as $(\bar{\varepsilon}_n, \alpha)$, $(\bar{\varepsilon}_n, \eta)$, $(\bar{\varepsilon}_n, \bar{\theta})$, and (σ_1, σ_2). An approximate formula for FLD is constructed based in the $(\bar{\varepsilon}_n, \bar{\theta})$ space. A class of elementary function with four parameters is proposed to fit the experimental data points of aluminum alloy 6111-T4 (Graf and Hosford, 1994). The theoretical analysis by Hill, and Stören and Rice can also be well fitted by the approximate formula.

Under the non-proportional loading conditions, in analogy to the cumulative damage models, a new form of necking prediction formula is proposed based on the idea of cumulate forming severity. From the assumption of non-linear forming severity accumulation rate, a normalized weighting function is introduced to the necking model to account for the loading history effect on necking. An exponential weighting function, with one additional parameter, is used in this paper.

Experimental data of FLDs under complex strain paths for two types of material, aluminum alloy 6111-T4 (Graf and Hosford, 1994) and aluminum-killed sheet steel (Muschenborn and Sonne, 1975), are revisited by the proposed model. Calibrated from one test with non-proportional loading condition, the model predicts the remaining tests with good accuracy. From the present comparison, it transpires that the accuracy of predicting necking is much better on the descending branch of FLD rather on the ascending branch. One reason is that there is always an inherent uncertainty in experimentally determining the onset of necking. A definition of necking has been evolving over the years from simply visual or tactile information, through the analysis of inscribed circle technique, to the most recent digital image correlation methods. The error in finding experimentally FLD has been discussed neither by Graf and Hosford nor in the present paper. It is possible that this error might be responsible for some of the discrepancy between test and prediction on the ascending branch of FLD.

The effect of the free parameter c_g on the predicted FLD under pice-wise linear loading

path is worth further investigation. From the calibration study, it was found that $c_g = 1.24$ for the aluminum sheet and $c_g = 2.5$ for the steel sheet. A comparison of model predictions with different values of c_g for the aluminum-killed steel sheet is shown in Fig. 6-16. It is found that there is no significant difference between the solutions corresponding to $c_g = 1.0$ and $c_g = 2.5$. The above parametric study suggests that the constant c_g is responsible for fine tuning of the predicted FLD. However, the main effect of shifting the curves is already included in the integral representation of the forming severity index. When no test results are available under initial prestraining, one can assume a "universal" calibration constant, for example $c_g = 1.5$. It would appear that one can provide estimates on FLDs under complex loading paths knowing only a single material constant - the exponent n of the power hardening law.

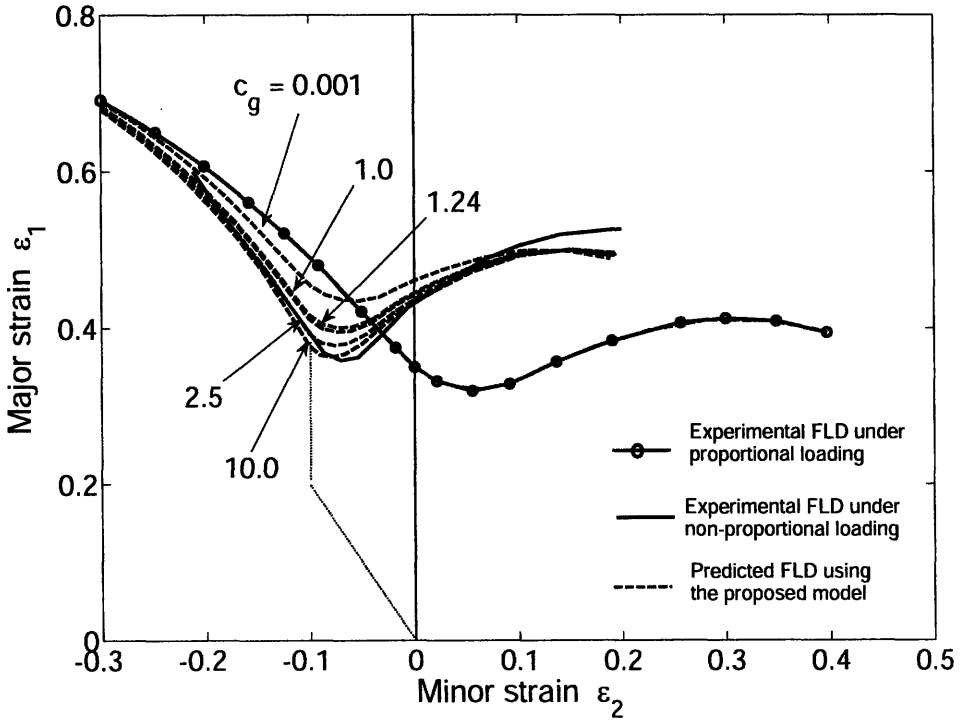

Fig. 6-16: Comparison of model predictions with different values of c_g for the aluminum-killed steel sheet

In the present model, the Lode angle parameter $\bar{\theta}$ is defined for the plane stress condition, which means varnishing of the through thickness normal stress component. It is generally known that the hydrostatic pressure (or the normalized parameter, stress triaxiality η) is a

key parameter controlling ductile fracture (Bridgman, 1952; Johnson and Cook, 1985; Bao and Wierzbicki, 2004a; Bai and Wierzbicki, 2007a). Determination of sheet metal necking with non-zero through thickness normal stress ($\sigma_3 \neq 0$) is of great interest to the hydro-forming technology and other press shop activities (Smith et al., 2003; Hari Manoj Simha et al., 2007). The present model is strictly valid under plane stress assumption, but it can be extended to the case of 3D reference necking surface defined in terms of two stress state parameters, for example $\hat{\varepsilon}_n(\eta, \bar{\theta})$. This is a similar idea to the 3D fracture surface, proposed by the present authors (Bai and Wierzbicki, 2007a,b). In other words, the reference function $\hat{\varepsilon}_n(\bar{\theta})$ appearing in Eqs. (6.27) and (6.28) should now be replaced by a similar function of two independent variables, $\hat{\varepsilon}_n(\eta, \bar{\theta})$. The basic framework of the present approach would remain unchanged.

In the sheet metal forming industry, a safety margin is often defined as a fixed offset from the strain-based conventional FLD (Stoughton and Zhu, 2004). The concept of forming severity index N is this paper is an alternative means for safety control in the design of forming operations. Unsafe design (producing necking) is when $N \geq 1$. Clearly, a safe design would require to take $N < 1$, and it is up to users to decide what should be the required safety margin.

THIS PAGE INTENTIONALLY LEFT BLANK

Chapter 7

Study on the Loading History Effect on Ductile Fracture

In the chapter, a new form of ductile fracture model considering the loading history effect was proposed. As an extension to the conventional linear damage evolution assumption, two weighting functions were introduced to the damage indicator calculation. One considers the non-linear damage evolution under proportional loading, the other accounts for the effect of change in Loading directions. Test results with complicated (non-proportional)loading paths from the literatures were reviewed using the newly proposed ductile fracture model. These tests include two-stage-tension test, compression-tension test and torsion-tension test.

A round of comprehensive fracture tests on 1045 steel was conducted to check the proposed fracture model. Firstly, the plasticity model with kinematic/isotropic hardening was calibrated using compression-tension tests. Secondly, the 3D fracture locus of 1045 steel was calibrated by two methods: uniaxial tests on "classical specimens" and biaxial loading on butterfly specimens. Thirdly, the proposed correction of loading history effect is studied and calibrated by "classical" specimens under complicated loading conditions. Two different kinds of loading history effect are found. Test results of butterfly specimens under complex loading conditions confirmed the proposed ductile fracture model.

7.1 Introduction

7.1.1 Ductile fractures under complex loading conditions

The effect of loading history on metal sheets necking has been recognized for many years (Muschenborn and Sonne, 1975; Graf and Hosford, 1994; Stoughton, 2000). The strain-based forming limit diagram (FLD) is not unique under non-proportional loading conditions. The effect of loading history on FLD was also studied by (Atkins and Mai, 1985; Stoughton, 2000; Cao et al., 2000; Chow et al., 2001; Bai and Wierzbicki, 2007c). However, the effect of loading history on fracture is still well noted by the community of fracture mechanics. Both the physically-based fracture models (for example Tvergaard and Needleman (1984)) and empirical fracture models(for example Wilkins et al. (1980); Johnson and Cook (1985); Hooputra et al. (2004)) are usually calibrated and validated by tests under monotonic loading conditions. A fracture model calibrated only from monotonic loading usually fails to predict fracture under complex loading conditions. For example, it was pointed by Johnson and Cook (1985) that the total damage is always less than unity at fracture (up to 40%) when the material is subjected to torsion followed by tension.

Recently, the effect of strain reversal on fracture was studied by Bao (2003); Bao and Treitler (2004); Bai et al. (2006a), which is an common phenomena is mechanics. Consider for example three-point bending of a solid section beam. Initially, there are positive strains on the tensile side and negative strains on the compressive side. As the crack propagates towards the center of the beam, it clearly passes through a region that was initially under compression. This interesting phenomenon has been described by Bao (2003); Bao and Treitler (2004), who also introduced a modified form of damage function to account for the effect of pre-compression. Another practical example in which the strain rate ratio changes sign is an axially compressed prismatic tube. Wierzbicki and Thomas (1993); Dyrli (1999) proved through a simple analytical model and finite element simulation that the strain in the transverse direction (perpendicular to the axis of the tube) changes from compression to tension. This problem was revisited by Bai et al. (2006a) using a continuum damage model with a nonlinear damage accumulation law.

The objective of the present paper is to study the loading history effect on fracture through a round of comprehensive experimental study. Firstly, the 3D fracture locus of 1045 steel is calibrated under monotonic loading conditions. Secondly, tests with complex loading conditions are designed and conducted. These tests includes two-stage-tension test, compression-tension test, torsion-tension test, and tests on a specially designed butterfly

specimen subjected to complicated loading conditions in a biaxial testing machine. A new form of ductile fracture model is proposed and validated based on the experimental results.

7.1.2 Characterization of the stress state

The three invariants of a stress tensor $[\sigma]$ are defined respectively by

$$p = -\sigma_m = -\frac{1}{3}tr([\sigma]) = -\frac{1}{3}(\sigma_1 + \sigma_2 + \sigma_3) \tag{7.1}$$

$$q = \bar{\sigma} = \sqrt{\frac{3}{2}[S_o] : [S_o]} = \sqrt{\frac{1}{2}\left[(\sigma_1 - \sigma_2)^2 + (\sigma_2 - \sigma_3)^2 + (\sigma_3 - \sigma_1)^2\right]} \tag{7.2}$$

$$r = \left(\frac{9}{2}[S_o] \cdot [S_o] : [S_o]\right)^{1/3} = \left[\frac{27}{2}det([S_o])\right]^{1/3} = \left[\frac{27}{2}(\sigma_1 - \sigma_m)(\sigma_2 - \sigma_m)(\sigma_3 - \sigma_m)\right]^{1/3} \tag{7.3}$$

where $[S_o]$ is the deviatoric stress tensor,

$$[S_o] = [\sigma] + p[I], \tag{7.4}$$

$[I]$ is the identity tensor and σ_1, σ_2 and σ_3 denote principal stresses. It is assumed that $\sigma_1 \geq \sigma_2 \geq \sigma_3$. It should be noted that if a isotropic/kinematic hardening rule is used, then the stress tensor $[\sigma]$ in Eq. (7.4) will be replaced by $[\sigma] - [S_{back}]$,

$$[S_o] = [S] + p[I] = [\sigma] - [S_{back}] + p[I], \tag{7.5}$$

where $[S_{back}]$ denotes the back stress tensor, and $[S]$ denotes the stress tensor measured from the center of the back stress. Also note that the parameter p is positive in compression, but σ_m is positive in tension. It is convenient to work with the dimensionless hydrostatic pressure η, defined by

$$\eta = \frac{-p}{q} = \frac{\sigma_m}{\bar{\sigma}}. \tag{7.6}$$

The parameter η, often referred to as the triaxiality parameter, has been extensively used in the literature on ductile fracture (McClintock, 1968; Rice and Tracey, 1969; Hancock and Mackenzie, 1976; Mackenzie et al., 1977; Johnson and Cook, 1985; Bao, 2003). The second important parameter is the Lode angle θ, which is related to the normalized third invariant ξ through

$$\xi = \left(\frac{r}{q}\right)^3 = \cos(3\theta). \tag{7.7}$$

One can see that that the normalized third deviatoric stress invariant can be expressed in terms of the Lode angle θ (see Malvern (1969); Xu and Liu (1995); ABAQUS, 2005). Since the range of the Lode angle is $0 \leq \theta \leq \pi/3$, the range of ξ is $-1 \leq \xi \leq 1$. The geometrical represent of Lode angle is shown in Fig. 7-1.

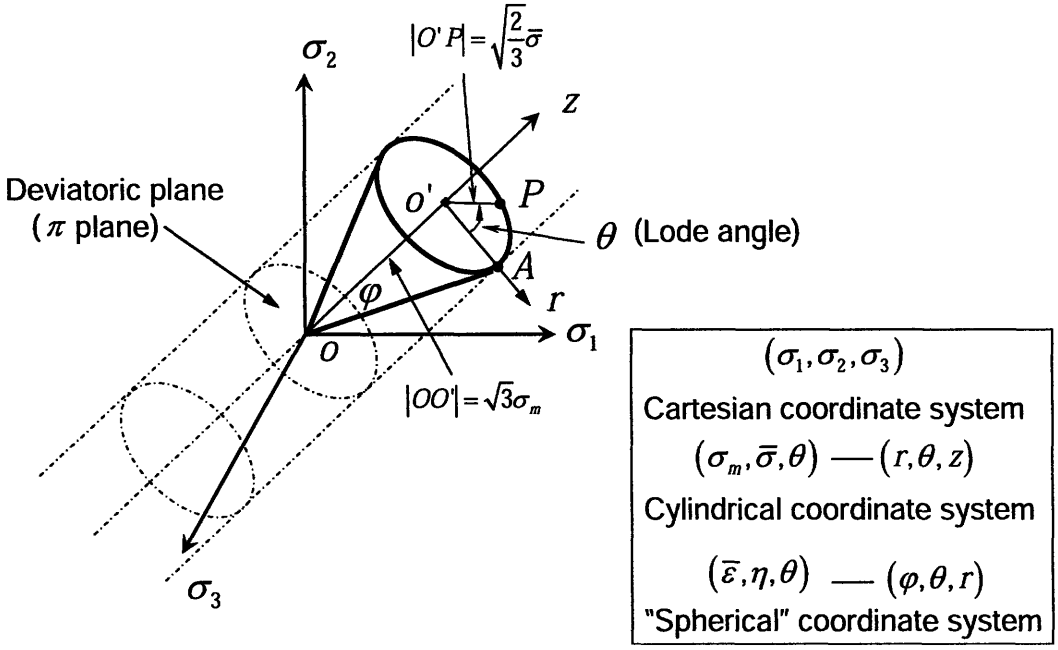

Fig. 7-1: Three types of coordinate system in the space of principal stresses

As shown in Fig. 7-1, one can think of three types of coordinate systems to describe the stress state. The first is the Cartesian coordinate system $(\sigma_1, \sigma_2, \sigma_3)$, the second is the cylindrical coordinate system $(\sigma_m, \bar{\sigma}, \theta)$, and the third is the spherical coordinate system $(\bar{\epsilon}_f, \eta, \theta)$, where the equivalent stress $\bar{\sigma}$ is related to the equivalent strain $\bar{\epsilon}$ through the strain hardening function of a material. The coordinate φ is related to the stress triaxiality η by the following equation,

$$\eta = \frac{\sigma_m}{\bar{\sigma}} = \frac{\sqrt{2}}{3} cotan\varphi. \tag{7.8}$$

Furthermore, the Lode angle can be normalized by

$$\bar{\theta} = 1 - \frac{6\theta}{\pi} = 1 - \frac{2}{\pi} \arccos\xi. \tag{7.9}$$

The range of $\bar{\theta}$ is $-1 \leq \bar{\theta} \leq 1$. The parameter $\bar{\theta}$ will be called the Lode angle parameter

hereinafter. Now, all stress directions (or loading conditions) can be characterized by the above defined set of parameters $(\eta, \bar{\theta})$. It is easy to show (Wierzbicki and Xue, 2005; Bai and Wierzbicki, 2007a) that $\bar{\theta} = 1$ corresponds to the axisymmtric tension, $\bar{\theta} = 0$ corresponds to the generalized shear (or plastic plane strain) loading condition, and $\bar{\theta} = -1$ corresponds to the axisymmtric compression. Special attention is given to the plane stress state. It was shown by Wierzbicki and Xue (2005); Bai and Wierzbicki (2007a) that the plane stress condition uniquely relates the parameters η and ξ or $\bar{\theta}$ through

$$\xi = cos(3\theta) = cos\left[\frac{\pi}{2}(1-\bar{\theta})\right] = -\frac{27}{2}\eta\left(\eta^2 - \frac{1}{3}\right). \tag{7.10}$$

In this paper, the ductile fracture model will be reformulated in the spherical coordinate system.

7.2 Constitutive modeling

7.2.1 A plasticity model considering combined hardening rule

In order to simulate a test under complex loading paths, the isotropic hardening rule described in Eq. (7.12) is not enough, so the kinematic hardening of the material has to be introduced. According to the work of Armstrong and Frederick (1966); Chaboche (1977), the evolution of the back stress is given by

$$d[S_{back}] = \frac{2}{3}C[d\varepsilon^p] - \Gamma[S_{back}]d\bar{\varepsilon}^p, \tag{7.11}$$

where C and Γ are material constants and S_{back} is the back stress tensor. The isotropic hardening takes the form of the asymmetric plasticity model proposed by the authors (Bai and Wierzbicki, 2007a), which assumes that a isotropic yield surface is controlled by both hydrostatic pressure and Lode angle parameter. The following isotropic yield surface is proposed,

$$\sigma_{yld} = f\left(\bar{\varepsilon}_p, [\sigma] - [S_{back}]\right) = \bar{\sigma}_{iso}\left(\bar{\varepsilon}_p\right)\left[1 - c_\eta(\eta - \eta_0)\right]\left[c_\theta^s + (c_\theta^{ax} - c_\theta^s)\left(\gamma - \frac{\gamma^{m+1}}{m+1}\right)\right], \tag{7.12}$$

where γ and c_θ^{ax} are two parameters defined by

$$\gamma = \frac{\cos(\pi/6)}{1-\cos(\pi/6)}\left[\frac{1}{\cos(\theta-\pi/6)}-1\right] = 6.4641\left[\sec(\theta-\pi/6)-1\right], \tag{7.13}$$

$$c_\theta^{ax} = \begin{cases} c_\theta^t & for \quad \bar{\theta} \geq 0 \\ c_\theta^c & for \quad \bar{\theta} < 0 \end{cases} . \tag{7.14}$$

The range of γ is $0 \leq \gamma \leq 1$, in which $\gamma = 0$ is corresponding to plane strain or shear condition, and $\gamma = 1$ is corresponding to axial symmetry. The parameter m is a non-negative integer. There are four material constants, c_θ^t, c_θ^s, c_θ^c and m, need to be calibrated. The values of c_θ^t, c_θ^s, and c_θ^c are relative, and at least one of them is equal to unity. This depends on which type of reference test is used to calibrate the isotropic strain hardening function $\bar{\sigma}_{iso}(\bar{\epsilon}_p)$. It can be proved that the postulated isotropic yield surface (Eq. (7.12)) is smooth and differentiable. Two specific types of isotropic hardening rules are suggested. One uses a power function to describe the isotropic stain hardening for metal plasticity.

$$\bar{\sigma}_{iso}\left(\bar{\varepsilon}_p\right) = A\left(\varepsilon_\circ + \bar{\varepsilon}_p\right)^n \qquad for \quad \bar{\sigma} \geq \sigma_y. \ , \tag{7.15}$$

where $\epsilon_\circ$ is the first yield strain. The second one is a specific definition used by Chaboche (1977); Lee and Zavenl (1978).

$$\sigma_{iso}\left(\bar{\varepsilon}^p\right) = \sigma_\circ + \sigma_{st}\left(1-e^{-b\bar{\varepsilon}^p}\right), \tag{7.16}$$

where $\sigma_\circ$ is the first yield stress, and the stabilized value is $\sigma_\circ + \sigma_{st}$. If a material is assumed to be isotropic hardening only, then Eq. (7.15) will be used. If the material is assumed to follow a combined hardening rule, then Eq. (7.16) will be used. In this paper, the latter is used. Experimental calibration of these two types of hardening rule will be described in section 7.4.1.

7.2.2 A new form of ductile fracture model considering the loading history effect

From a cumulative damage point of view, one can use a damage indicator D to account for the damage accumulation, which is controlled by different stress states of a loading history. Furthermore, it is assumed that a damage will initiate when the damage indicator D exceeds a critical value D_c. In the classical plasticity theory, the equivalent plastic strain $\bar{\varepsilon}^p$ is an

ever increasing parameter, so the loading path can be replaced by $\Phi[\eta(\bar{\varepsilon}^p), \theta(\bar{\varepsilon}^p)]$. This idea can be described by the following equation.

$$D_c = \int_0^{t_f} \Phi\left[\sigma_{ij}(t), \varepsilon_{ij}(t)\right] dt = \int_0^{\bar{\varepsilon}_f} \Phi\left[\sigma_{ij}(\bar{\varepsilon}^p), \varepsilon_{ij}(\bar{\varepsilon}^p)\right] d\bar{\varepsilon}^p, \tag{7.17}$$

where σ_{ij} and ϵ_{ij} are all the stress and strain components.

For isotropic materials, the material properties can be described in the space of three principal stresses $\sigma_1, \sigma_2, \sigma_3$. Since the space of principal stresses is a Cartesian coordinate system, it is more convenient to describe the loading path in spherical coordinate system by two dimensionless parameters $\Phi[\eta(t), \bar{\theta}(t)]$, where η is the stress triaxiality and θ is the Lode angle. Stress triaxiality η is an important parameter in constructing the fracture locus, and Lode angle parameter $\bar{\theta}$ is a parameter to describe the loading condition, such as tension, compression or shear. Therefore, equation (7.17) can be rewritten as the following equation.

$$D_c = \int_0^{\bar{\varepsilon}_f} \Phi\left[\eta(\bar{\varepsilon}^p), \bar{\theta}(\bar{\varepsilon}^p)\right] d\bar{\varepsilon}^p \tag{7.18}$$

A lot of effort has been made to find the fracture locus $\hat{\varepsilon}_f\left(\eta, \bar{\theta}\right)$, which is defined by equivalent plastic strain to fracture $\bar{\epsilon}_f$ as a function of the stress state parameters under a restricted proportional loading. Theoretical analysis (McClintock, 1968; Rice and Tracey, 1969) and experimental studies (Mackenzie et al., 1977; Johnson and Cook, 1985; Hancock and Brown, 1983) have shown that the stress triaxiality is an important parameter controlling the fracture locus. The equivalent plastic strain to fracture $\bar{\epsilon}_f$ increases as the stress triaxiality decreases. Recent work are done to study the effect of Lode angle parameter on ductile fracture locus Wierzbicki and Xue (2005); Bai and Wierzbicki (2007a). If the reciprocal of a fracture locus is used as the weighting function in equation (7.18), then the critical damage indicator is normalized $D_c = 1$.

$$D_c = \int_0^{\bar{\varepsilon}_f} \frac{1}{\hat{\varepsilon}_f\left(\eta, \bar{\theta}\right)} d\bar{\varepsilon}^p = 1 \tag{7.19}$$

This is currently the mostly widely used ductile fracture model Wierzbicki et al. (2005b). Some typical fracture loci are listed in Table 7.1, for example Johnson and Cook (1985), Wilkins et al. (1980), Werner et al. (Oct. 2004) and so on.

Table 7.1: Some typical ductile fracture loci *

No.	Formula of $\hat{\varepsilon}_f$	Remark
1	$\hat{\epsilon}_f = \bar{\varepsilon}_f$	Constant fracture strain
2	$\hat{\epsilon}_f(\eta) = c_1 e^{c_2 \eta}$	Rice and Tracey (1969)
3	$\hat{\varepsilon}_f(\sigma_m, A) = D_c (1 - a\sigma_m)^{\lambda} (2 - A)^{-\mu}$	Wilkins et al. (1980)
4	$\hat{\sigma}_f(\sigma_m, \theta) = \frac{1}{2a}\left[-(b\cos\theta + c) + \sqrt{(b\cos\theta + c)^2 - 4a(\sqrt{3}d\sigma_m - 1)}\right]$	Han and Chen (1985)
5	$\hat{\varepsilon}_f(\eta, \dot{\varepsilon}, T) = \left(D_1 + D_2 e^{D_3 \eta}\right)\left[1 + D_4 \ln(\dot{\varepsilon}/\dot{\varepsilon}_0)\right]\left[1 + D_5\left(\frac{T - T_0}{T_M - T_0}\right)^m\right]$	Johnson and Cook (1985)
6	Three branches fracture locus	Bao and Wierzbicki (2004a)
7	$\hat{\varepsilon}_f(\eta, \xi) = c_1 e^{-c_2\eta} - (c_1 e^{-c_2\eta} - c_3 e^{-c_4\eta})\left(1 - \xi^M\right)$	Wierzbicki and Xue (2005)
8	$\begin{cases} \textit{Instability} & \\ \hat{\varepsilon}_f(\eta) = d_0 e^{-c\eta} + d_1 e^{c\eta} \quad \textit{ductile fracture} & \\ \hat{\varepsilon}_f(\theta^*) = d_2 e^{-f\theta^*} + d_3 e^{f\theta^*} \quad \textit{shear fracture} & \end{cases}$	BMW - MATFEM team, (Werner et al., Oct. 2004)
9	$\hat{\varepsilon}_f(\eta, \bar{\theta}) = \left[\frac{1}{2}\left(\hat{\varepsilon}_f^{(+)} + \hat{\varepsilon}_f^{(-)}\right) - \hat{\varepsilon}_f^{(o)}\right]\bar{\theta}^2 + \frac{1}{2}\left(\hat{\varepsilon}_f^{(+)} - \hat{\varepsilon}_f^{(-)}\right)\bar{\theta} + \hat{\varepsilon}_f^{(o)}.$	Bai and Wierzbicki (2007a)

* *Please refer to the oringinal papers for the notations of each formula.*

Equation (7.19) implies that the damage indicator D increases linearly under a proportional loading in which $\hat{\varepsilon}_f\left(\eta, \bar{\theta}\right)$ keeps constant, as shown in equation (7.20).

$$D = \frac{\bar{\varepsilon}^p}{\hat{\varepsilon}_f\left(\eta, \bar{\theta}\right)} \tag{7.20}$$

Generally speaking, the damage accumulation is not linear even under proportional loading. To correct this question, a new parameter λ defined in equation (7.21), which is used to describe the different loading stage under a proportional loading, was introduced by Bai et al. Bai et al. (2006a), and a new weighting function $g(\lambda)$ is also introduced into the fracture model. From equation (7.19), it can be inferred that the restrictions for $g(\lambda)$ are that its value is always positive and its integral between $0 \leq \lambda \leq 1$ should be unity, see equation (7.22).

$$\lambda \triangleq \frac{\bar{\varepsilon}^p}{\hat{\varepsilon}_f\left(\eta, \bar{\theta}\right)} \tag{7.21}$$

$$g(\lambda) \geq 0 \quad , \quad \int_0^1 g(\lambda) d\lambda = 1 \tag{7.22}$$

The weighting function $g(\lambda)$ is found to be very important to predict necking under complex loading paths (Bai and Wierzbicki, 2007c). Different forms of function $g(\lambda)$ can be postulated based on different assumptions. This part will be discussed in details in Section 7.3.1. Some example forms are listed in the following Table 7.2, where c_g is a material constant to be calibrated.

Table 7.2: Some typical forms of function $g(\lambda)$

No.	Formula of $g(\lambda)$	Remark
1	1	No history effect
2	$\delta(\lambda - 1)$	Final value assumption (Non-CDM model), δ is the Dirac's delta function.
3	$\frac{H(\lambda - c_g)}{1 - c_g}$	Threshold value assumption, H is the step function.
4	$\begin{cases} c_g\lambda - \frac{c_g}{2} + 1 & for \quad c_g \leq 2 \\ c_g\lambda - c_g + \sqrt{2c_g} & for \quad c_g > 2 \end{cases}$	Linear weighting function
5	$(c_g + 1)\,\lambda^{c_g}$	Power weighting function
6	$\frac{c_g}{e^{c_g} - 1} e^{c_g \lambda}$	Exponental weighting function

However, in real problems, the loading paths are usually not proportional except the specially design calibration tests for construction fracture locus. The integral form of equation (7.19) takes this effect into account only *partially* (Bai et al., 2006a). A new parameter χ is introduced to describe the stress state of non-proportionality,

$$\chi \triangleq \left\| \frac{\sigma}{\|\sigma\|} - \frac{S_{back}}{\|S_{back}\|} \right\| = \left\| \tilde{\sigma} - \tilde{S}_{back} \right\|, \tag{7.23}$$

which denotes the difference between the directions of current stress and back stress. It can be proven that the range of χ is $0 \leq \chi \leq 2$. A new parameter μ, defined by

$$\mu \triangleq 10 \cdot \int_0^{\bar{\varepsilon}^p} \chi d\bar{\varepsilon}^p = 10 \cdot \int_0^{\bar{\varepsilon}^p} \left\| \tilde{\sigma} - \tilde{S}_{back} \right\| d\bar{\varepsilon}^p, \tag{7.24}$$

is introduced to measure the accumulated amount of non-proportionality during the loading process, For convenience, a coefficient 10 is used to make the range of coefficient μ vary around unity.

To consider the non-proportionality of loading conditions, a form of weighting function

$h(D,\mu)$ is also introduced, see Eq. (7.25)

$$h(D,\mu) = (1 + c_h D^{\beta_1} \mu^{\beta_2})^k, \tag{7.25}$$

where c_h, β_1, β_2 and k are four material constants to calibrate. The parameter k is equal to +1 or -1, which captures two possible types of non-proportional loading effects on ductile fracture (delaying or accelerating onset of fracture). Up to now, a new form of ductile fracture model considering the loading history effect is proposed, as shown in equation (7.26). Totally, there are five material parameters, c_g, c_h β_1, β_2, and k, to characterizing the loading history effect.

$$D_c = \int_0^{\bar{\varepsilon}_f} g(\lambda) h(D,\mu) \frac{d\bar{\varepsilon}^p}{\hat{\varepsilon}_f(\eta,\bar{\theta})} = 1. \tag{7.26}$$

7.3 Damage accumulation process

7.3.1 Damage accumulation under proportional loading

If the two stress state parameters(η and $\bar{\theta}$) of a loading keep constant or the parameter χ keeps zero, then the loading is called proportional loading. When calibrating the fracture locus $\hat{\epsilon}_f(\eta,\bar{\theta})$, one has to design specimens under proportional loading conditions. Experimental results have shown that in proportional loading conditions, the damage accumulation is still not linear (Bonora, 1997). Bonora (1997) proposed three types of possibilities of the damage accumulation: linear accumulation, accelerating accumulation and decelerating accumulation, as shown in Fig. 7-2. In Bonora's model, the damage indicate D is defined and experimentally measured by the reduction of Young's modulus E during the tensile loading, which is the same as that of Lemaitre (Lemaitre, 1996). The experimental data on several metal materials verified this assumption about three types of damage accumulation (Bonora, 1997).

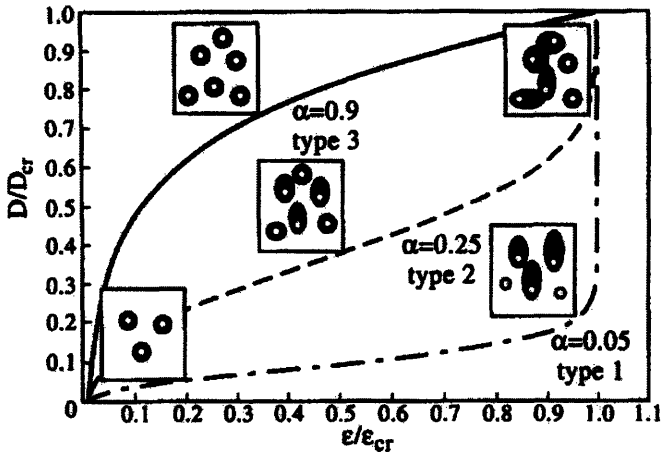

Fig. 7-2: Three possibilities of damage accumulation under monotonic loading postulated by Bonora (1997).

Although the definition of damage indicator D in the paper is different from that of Bonora or Lemaitre, the same idea is assumed in the present paper. If the acceleration of damage is assumed to be a constant c_g, then one can get a simple differential equation

$$\frac{d^2D}{d\lambda^2} = c_g \quad , \quad D|_{\lambda=0} = 0 \quad , \quad D|_{\lambda=1} = 1, \tag{7.27}$$

where c_g is a material constant. The condition $c_g = 0$ means linear damage accumulation, $c_g > 0$ means accelerated damage accumulation, and $c_g < 0$ means decelerated damage accumulation. Integral Eq. (7.27), then D can be solved.

$$\begin{cases} D = \frac{1}{2}c_g\lambda^2 + \left(1 - \frac{1}{2}c_g\right)\lambda \\ g(\lambda) = \frac{dD}{d\lambda} = c_g\lambda - \frac{1}{2}c_g + 1 \end{cases} \tag{7.28}$$

From Eq. (7.28), one linear form of weight function $g(\lambda)$ is obtained, which is corresponding to No. 4 in Table 7.2. Similarly, the power weighting function is corresponding to differential equation (7.29), and the exponential weighting function is corresponding to Eq. (7.30).

$$\frac{d^2D}{d\lambda^2} = c_g\left(c_g + 1\right)\ \lambda^{c_g - 1} \quad , \quad D|_{\lambda=0} = 0 \quad , \quad D|_{\lambda=1} = 1. \tag{7.29}$$

$$\frac{dD}{d\lambda} = c_g D + \frac{c_g}{e^{c_g} - 1} \quad , \quad D|_{\lambda=0} = 0 \quad , \quad D|_{\lambda=1} = 1. \tag{7.30}$$

7.3.2 Damage accumulation under non-proportional loading

A simple way to describe non-proportional loading paths

If the two stress state parameters(η and $\bar{\theta}$) change under a loading path or the parameter μ increases away from zero, then the loading is called non-proportional loading. A non-proportional loading can be described by two features. One feature is that, in the plane of stress direction, $(\eta, \bar{\theta})$, a proportional loading corresponds to a fixed point in the $(\eta, \bar{\theta})$ plane, but an arbitrary loading path corresponds to a curve in the $(\eta, \bar{\theta})$ plane, as shown in Fig. 7-3. Since the range of Lode angle is $0 \leq \theta \leq \pi/3$, the change of the loading path is partially captured by the variation of these two stress state parameter, $\Delta\eta$ and $\Delta\bar{\theta}$.

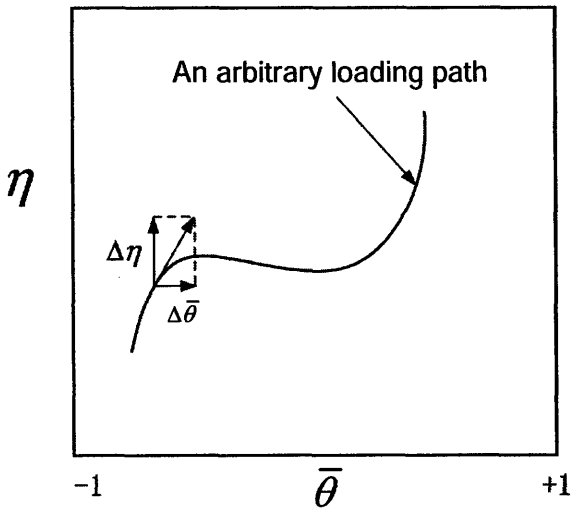

Fig. 7-3: An arbitrary loading path in the plane of stress triaxiality and the third stress parameter

The second feature is the change of the parameters χ and μ. The evolution of these two parameters in an example of reverse loading, compression followed by tension in a notched round bar, is shown in Fig. 7-4. One can see that the parameter χ changes from zero to two in the beginning of a reverse loading, and it reduces to zero after a certain amount of continuing loading. The parameter μ keeps increasing if there is any change in the loading path ($\chi \neq 0$). It is shown that the parameter μ can distinguish different stages of a non-proportional loading process.

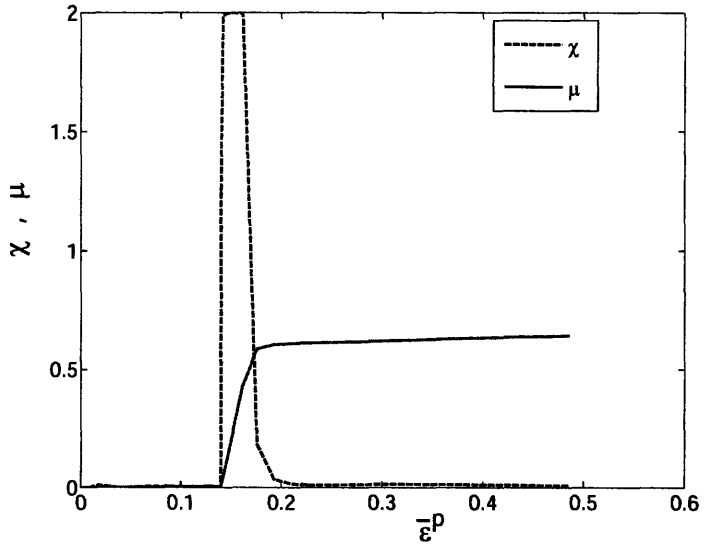

Fig. 7-4: An example of the evolution of the two non-proportionality parameter χ and μ in the reverse loading.

Because the fracture locus $\hat{\varepsilon}_f(\eta, \bar{\theta})$ is defined and calibrated only under proportional loading conditions, additionally designed experiments with non-proportional loadings are necessary to calibrate the loading history effect on fracture initiation, which are corresponding to two functions, $g(\lambda)$ and $h(D, \mu)$, in Eq. (7.26). The proposed ductile fracture model, Eq. (7.26), can also be written in an incremental form, which will be used in the implementation of the material subroutine. In this paper, the exponential weighting function (No. 6 in Table 7.2) is used. Referring to Eq. (7.30) for the exponential weighting function $g(\lambda)$, the incremental form of ductile fracture model is shown in Eq. (7.31), and material points are assumed to fracture when $D = 1$.

$$dD = \left(c_g D + \frac{c_g}{e^{c_g} - 1}\right)\left(1 + c_h D^{\beta_1} \mu^{\beta_2}\right)^k \frac{d\bar{\varepsilon}^p}{\hat{\varepsilon}_f\left(\eta, \bar{\theta}\right)}. \tag{7.31}$$

In the paper, the fracture locus $\hat{\varepsilon}_f\left(\eta, \bar{\theta}\right)$ is defined as

$$\begin{aligned}\hat{\varepsilon}_f\left(\eta, \bar{\theta}\right) &= \left[\tfrac{1}{2}\left(\hat{\varepsilon}_f^{(+)} + \hat{\varepsilon}_f^{(-)}\right) - \hat{\varepsilon}_f^{(o)}\right]\bar{\theta}^2 + \tfrac{1}{2}\left(\hat{\varepsilon}_f^{(+)} - \hat{\varepsilon}_f^{(-)}\right)\bar{\theta} + \hat{\varepsilon}_f^{(o)} \\ &= \left[\tfrac{1}{2}\left(D_1 e^{-D_2\eta} + D_5 e^{-D_6\eta}\right) - D_3 e^{-D_4\eta}\right]\bar{\theta}^2 + \tfrac{1}{2}\left(D_1 e^{-D_2\eta} - D_5 e^{-D_6\eta}\right)\bar{\theta} + D_3 e^{-D_4\eta}\end{aligned}, \tag{7.32}$$

which is the case 9 in Table 7.1.

In this section, some test results with non-proportional loading conditions from the literatures will be reviewed using the newly proposed fracture model with loading history effect correction.

Review on Tai's test: Tension with changed notches

A new type of two stages loading test on round bars was designed and performed by Tai (1990), see Fig. 7-5. In the first stage, the material inside the notch is subjected to a value of stress triaxiality η_1. After a certain amount of tensile loading, the test is paused and a new specimen is machined from the deformed specimen with a different ratio of notch radius to the cross-section radius. In the second stage, the material inside the notch is subjected to a different value of stress triaxiality η_2. In this test, the Lode angle parameter $\bar{\theta}$ keeps constant ($\bar{\theta} = 1$), and the loading remains radial or proportional, so the parameter $\mu = 0$, and then the function $h(D, \mu) = 1$. Therefore, this type of test can be used to calibrate the function $g(\lambda)$.

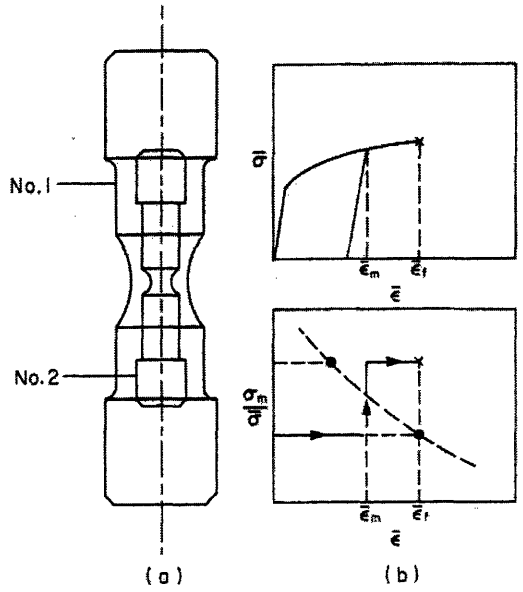

Fig. 7-5: A sketch of two step loaded specimens. (After Tai (1990))

In Tai's paper, the ductile fracture locus of No. 20 steel can be found from the tensile tests data on round bars with different notches, which reads

$$\hat{\varepsilon}_f(\eta) = 1.6478e^{-1.0826\eta}. \tag{7.33}$$

Tai's tests result on No.20 steel is shown in Fig. 7-6, where the histories of stress triaxiality η and damage indicate D are plotted as a function of the equivalent plastic strain. It is shown that Eq. (7.19) gives a good prediction fracture initiations for all those loading cases, so $c_g = 0$. The history effect correction $g(\lambda)$ is not needed for this material in this group of two-stage loading tests. Because in the real tests, the stress triaxiality will increases after the specimen necks in tensile loading, it should be noted that in this analysis the initial values of stress triaxiality η are used.

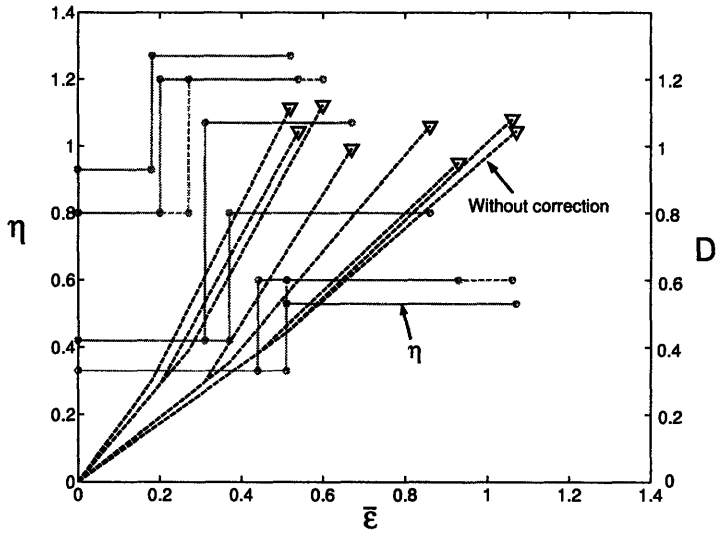

Fig. 7-6: Review on tests of tension with changed notches of No. 20 steel (experimental data from Tai (1990))

Review on Bao's reversal loading test: Compression followed by tension

A type of reverse loading test on round notched bars was designed and performed by Bao and Treitler (2004) to study the effect of reverse loading on ductile fracture, see Fig. 7-7. In this type of test, round notched bars are subjected to compression firstly to a certain amount, then they are subjected to tension all the way to fracture. In this type of reverse loading test, the stress state of the material inside the notch change is reversed. The stress triaxiality η changes from $-\eta$ to $+\eta$ (see Fig. 7-8), and the Lode angle parameter $\bar{\theta}$ changes from -1 to $+1$. The studied material is 2024-T351 aluminum alloy. Tensile test results on round bars with different notches were used to calibrate the ductile fracture locus of this

material (Bao and Treitler, 2004), which is

$$\hat{\varepsilon}_f(\eta) = \frac{1}{6.7\eta} \quad for \quad \eta \geq \tfrac{1}{3}. \tag{7.34}$$

It is further assumed that there is a cut-off value for fracture at $\eta \leq -\frac{1}{3}$ for this material (Bao and Wierzbicki, 2005). The histories of stress triaxiality and damage indicator D as a function of equivalent plastic strain in the reverse loading tests are shown in Fig. 7-8. It is found that a ductile fracture model without loading history correction (Eq. (7.19)) over-predicts the material ductility. As shown in Fig. 7-8 with triangles, the critical damage indicator to fracture D_c decreases as the amount of pre-compression strain increases. This phenomena means that the reverse loading decreases the material ductility for 2024-T351 aluminum alloy.

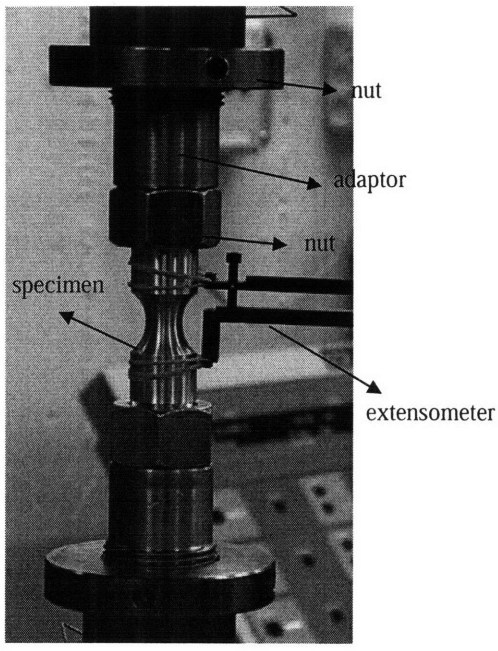

Fig. 7-7: A test set up for reversal loading test in uniaxial testing machine (after Bao and Treitler (2004))

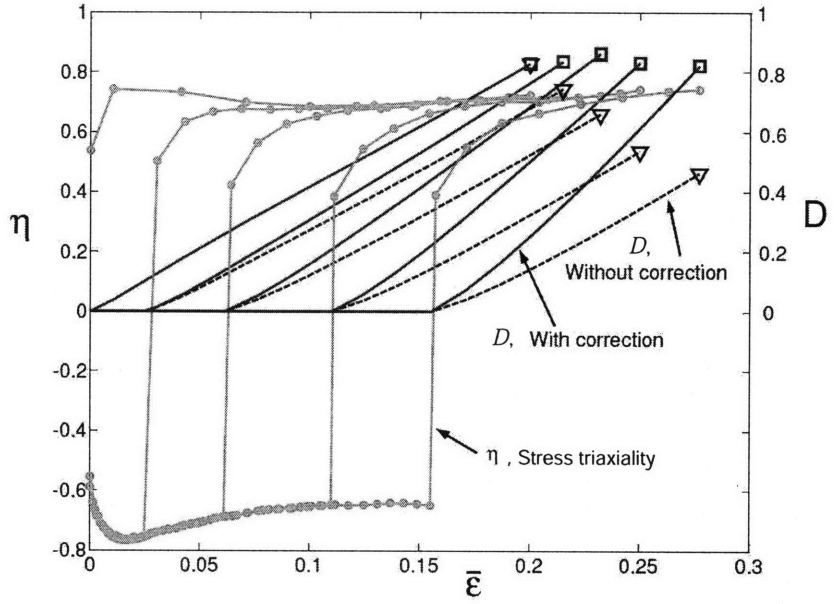

Fig. 7-8: Review on tests of reversal loading of aluminum 2024-T351 (experimental data from the type-A specimen of Bao and Treitler (2004))

The effect was corrected by Bai et al. (2006a) using a linear weighting function $g(\lambda)$ (No. 4 in Table 7.2), and a value of $c_g = 1.25$ is obtained. If the second weighting function $h(D, \mu)$ is used to consider the effect of reverse loading, then a combination of $c_g = 0$, $c_h = 1.8$, $\beta_1 = 1$, $\beta_2 = 3.5$ and $k = 1$ gives a very good prediction on fracture initiation on the reverse loading test, see Fig. 7-8. It should be noted that in this test, both two stress state parameters (η and $\bar{\theta}$) change during the loading process. Since no two-stage-tension tests (see Section 7.3.2) were performed on aluminum 2024-T351 to calibrate the parameter c_g, a single type of tests can not be used to calibrate both two weighting function, $g(\lambda)$ and $h(D, \mu)$, therefore, one can not tell the weighting of each correction.

Review on Johnson-Cook's test: Torsion followed by tension

Johnson and Cook (1985) found that the total damage indicator is less than unity under the loading condition of torsion followed by tension, see Fig. 7-9. The total damage indicator D_{Tot} decreases as the initial torsion damage D_s increase in the beginning, then D_{Tot} increases after a certain value of D_s. This problem had been unsolved for long time although the Johnson-Cook fracture model (Johnson and Cook, 1985) has been widely used. It is should

be noted that a linear damage accumulation (see Eq. (7.19)) is assumed in Johnson-Cook's model.

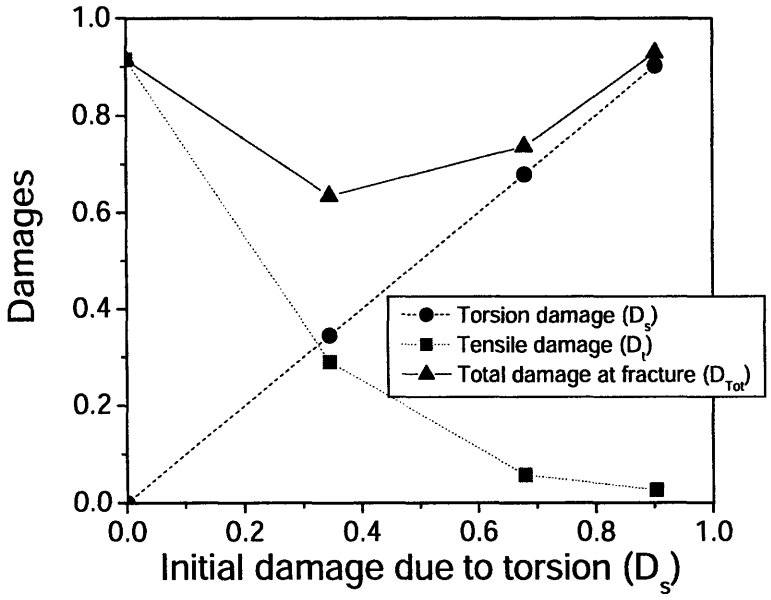

Fig. 7-9: Test data of torsion followed by tension of the OFHC copper (After Johnson and Cook (1985)).

In the test of torsion followed by tension, the stress triaxiality η changes from 0 to $\frac{1}{\sqrt{3}}$ (thin tubes in tension), and the Lode angle parameter $\bar{\theta}$ changes from 0 to +1. The material used in Johnson and Cook's test was a very ductile material, OFHC copper. The first stage torsional loading is proportional (the parameter $\mu = 0$), so the damage accumulation D_s should be kept unchanged. In order to have a unity total damage indicator, the damage accumulation in the second stage tensile loading should be accelerated due to change of loading direction. Because there is no detail data available for those tests, an approximate correction formula (similar to the function $h(D, \mu)$) is used, which modifies the damage accumulation at the second stage tensile loading,

$$D'_{Tot} = D_s + D'_t = D_s + D_t(1 + c_h D_s). \tag{7.35}$$

It is found that a value of $c_h = 3.2$ gives good prediction on fracture initiation on the torsion-tension loading test, see Fig. 7-10. Review on Johnson-Cook's data helps to explain

the second function of loading history effect, $h(D, \mu)$.

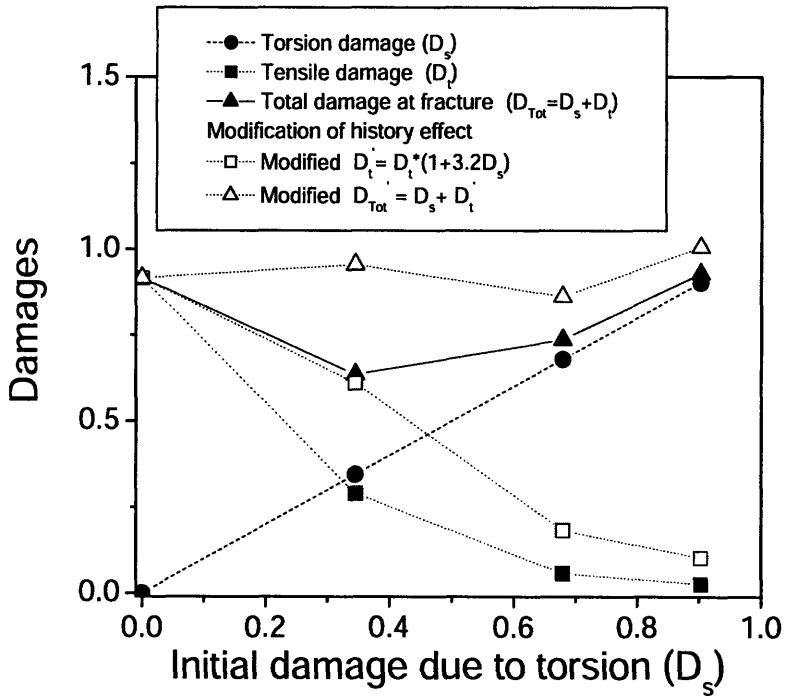

Fig. 7-10: Review on tests of torsion followed by tension of OFHC cooper (experimental data from Johnson and Cook (1985))

7.4 Fracture locus calibration on 1045 steel using "classical" specimens

In Section 7.3.2, several types of tests with non-proportional loading from the literatures are reviewed using the newly proposed ductile fracture model. The shortcoming of the review is that all three types of tests are for different materials. In order to validate the new ductile fracture model, a round of comprehensive fracture tests are designed and performed on the same material, 1045 steel. These tests includes fracture locus calibration under proportional loading, two-stage-tension tests, compression-tension tests, torsion-tension tests, and biaxial testing on butterfly specimens under both monotonic and complex loading conditions. All the tests will be described in sections 7.4, 7.5, 7.6, and 7.7.

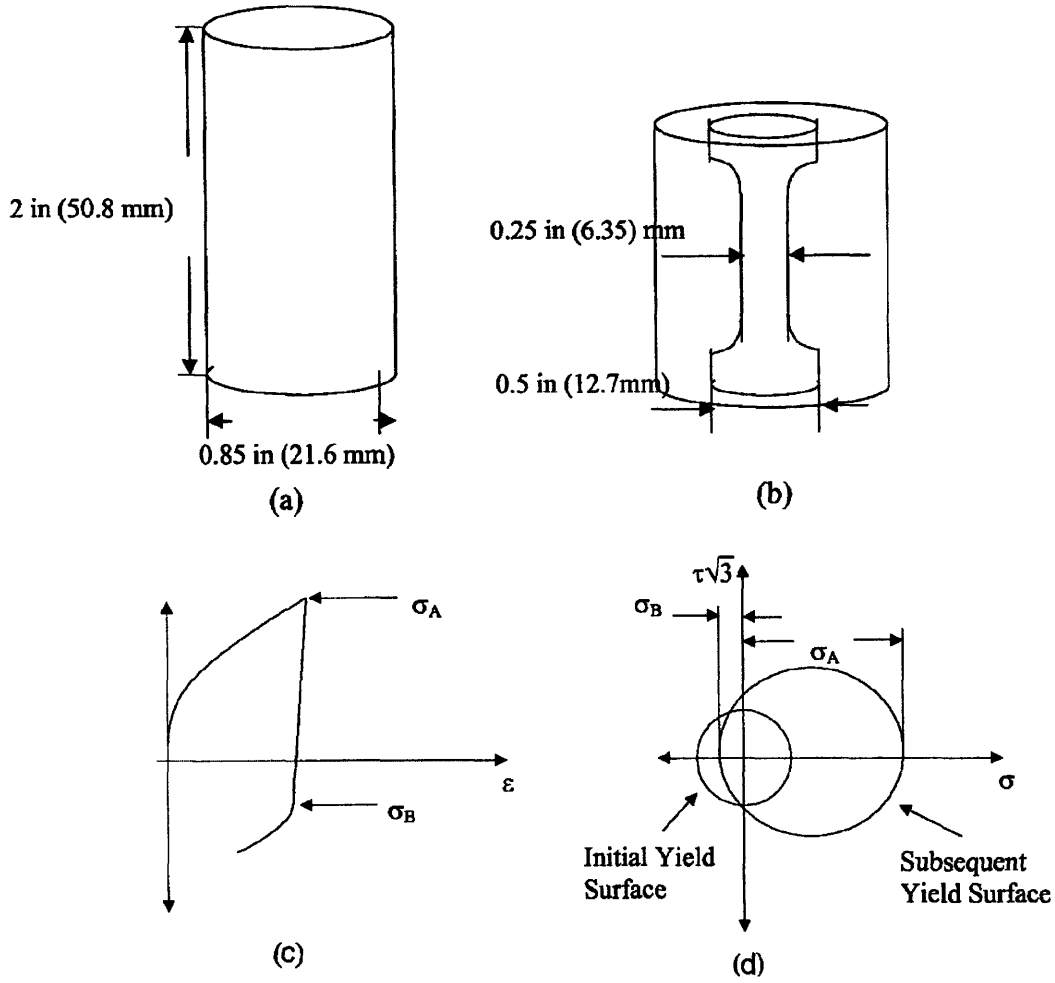

Fig. 7-11: A method proposed by Khan and Jackson (1999) to calibrate the combined hardening property of materials.

7.4.1 Calibration of plasticity model with combined hardening rule

To get the accurate stress and strain components in fracture tests, finite element simulations will be performed. The first step of running simulations is to calibrate the plasticity model. Khan and Jackson (1999) proposed a method of finding parameters of both isotropic hardening and kinematic hardening of materials. The method uses a compression tests followed by tension tests after re-machining, as shown in Fig. 7-11(a) and (b). If the yield stress in compression test at the point of unloading, denoted by σ_A, and the corresponding yield stress

under reverse loading, denoted by σ_B, are found, then the stress contributions of isotropic and kinematic hardening can be determined by the following two equations. The procedure is illustrated in Fig. 7-11(c) and (d). Khan and Jackson (1999) also found that the isotropic and kinematic hardening (σ_{IH} and σ_{KH}) depend on the yield definition.

$$\sigma_{IH} = (\sigma_A - \sigma_B)/2, \tag{7.36}$$

$$\sigma_{KH} = (\sigma_A + \sigma_B)/2. \tag{7.37}$$

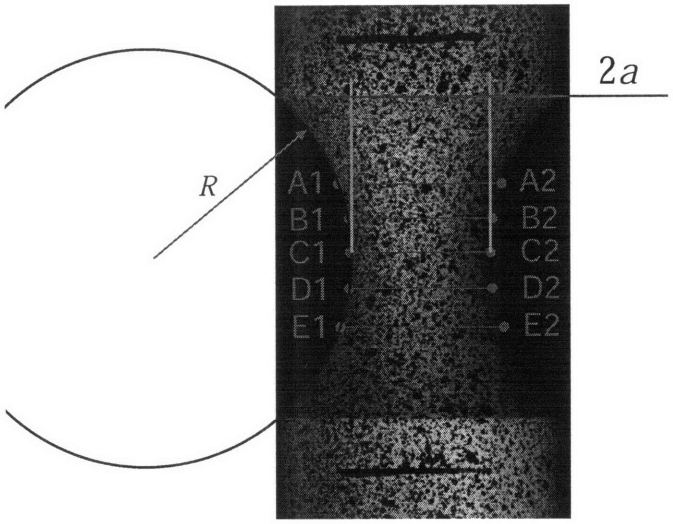

Fig. 7-12: Data points chosen on the surface of a notched round bar for optical measurement. The specimen was painted with small black dots for optical measurement.

In this paper, a type of reverse loading test on notched round bars with compression followed by tension is used for calibration (specimens and experimental setup is shown in Fig. 7-51). The diameter at the cross-section is 7mm, and the radius of the notch is 10.5 mm. Optical measurement is used to precisely measure the deformation process of the specimen. An optical method of measuring the geometry of a neck is proposed by Walters (2006). Accordingly, a series of points of interest are chosen on the two surfaces of a notched round bar, as shown in Fig. 7-12. The optical measurement system is able to capture and record the displacement of all the points. From the relative positions of the these points, the cross-section diameter, $2a$, and the radius of the notch, R, are obtained for every loading step. A Matlab code is written is post-process all the data to calculate the center and radius of the notch and the diameter of the minimum cross-section. According

to the Bridgman's correction (Bridgman, 1952), the equivalent stress $\bar{\sigma}$ is calculated using the following equation.

$$\bar{\sigma} = \frac{\frac{P}{\pi a^2}}{\left(1 + \frac{2R}{a}\right) \ln\left(1 + \frac{a}{2R}\right)}, \tag{7.38}$$

where P is the force at yield. The equivalent strain is measured from the area variation of cross-section using

$$\bar{\varepsilon} = 2ln\left(\frac{a}{a_o}\right), \tag{7.39}$$

where a_o is the initial radius of the neck, and a is the current radius. Using Eq. (7.38) and (7.39), the measured stress-strain curves under reverse loading conditions are shown in Fig. 7-13.

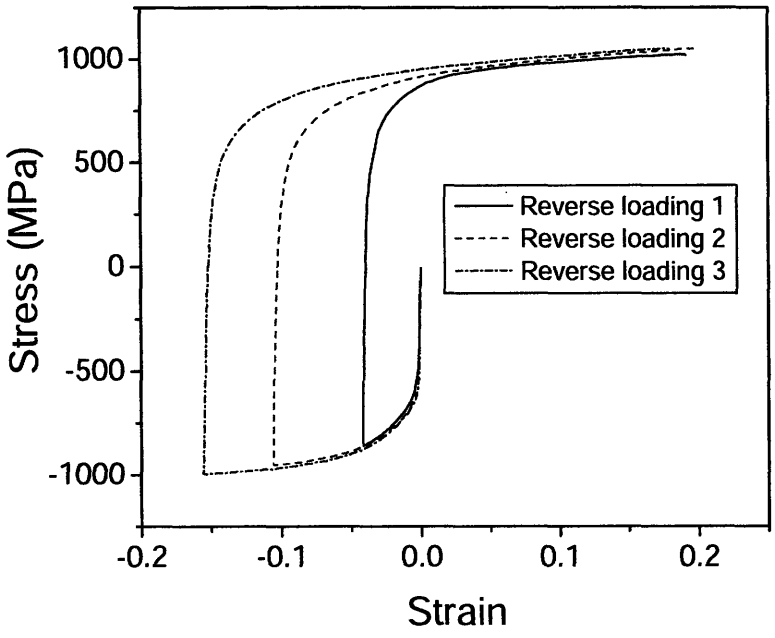

Fig. 7-13: Measured stress-strain curves of 1045 steel under reverse loadings: compression followed by tension.

From Fig. 7-13, one can see that there are no obvious yield points at the second stage loading of tension. If the yield is defined as the stress at 1.5% strain, then the contributions of isotropic hardening and kinematic hardening can be determined using Eq. (7.36) and (7.37). The results as well as the total strain hardening are illustrated in Fig. 7-14.

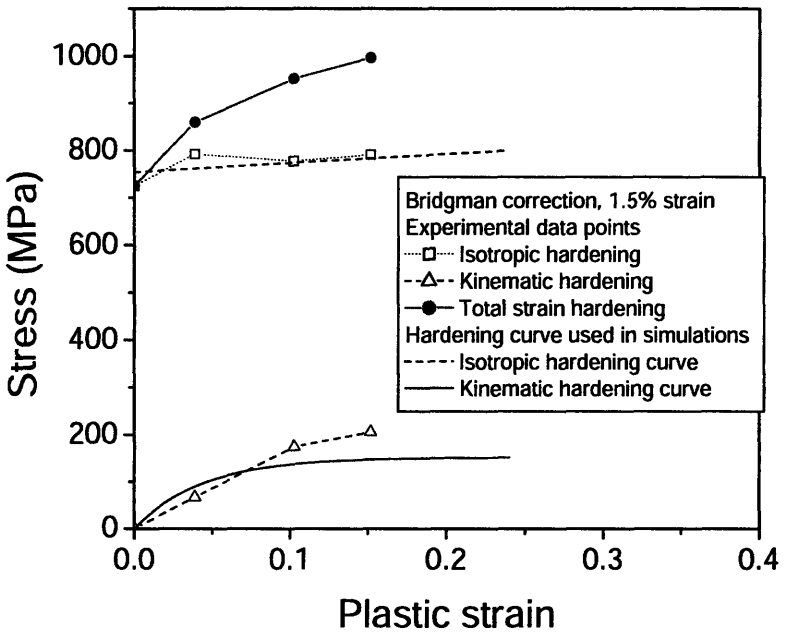

Fig. 7-14: Measured isotropic hardening and kinematic hardening of 1045 steel.

In the 1-D case, the kinematic hardening rule, Eq. (7.11) can be rewritten as

$$d\sigma_{KH} = Cd\bar{\varepsilon}^p - \Gamma\sigma_{KH}d\bar{\varepsilon}^p. \tag{7.40}$$

Solving this differential equation, one can get that

$$\sigma_{KH} = \frac{C}{\Gamma}\left(1 - e^{-\Gamma\bar{\varepsilon}^p}\right). \tag{7.41}$$

Using Eq. (7.16) and Eq. (7.41) to fit the two measured hardening data respectively, the parameters for the both isotropic hardening and kinematic hardening are obtained: $\sigma_o = 730MPa$, $\sigma_{st} = 1000MPa$, $b = 0.41$, $C = 1787MPa$ and $\Gamma = 1.79$.

It is shown in Ref. (Bai et al., June 3-7, 2007) that the material of 1045 steel has neither pressure dependence nor Lode angle dependence on plasticity, so the following parameters of plasticity are assumed: $c_\eta = 0.0$, $\eta_o = -0.72$, $c_\theta^s = c_\theta^t = c_\theta^c = 1.0$, and $m = 6$. In this particular case, the proposed plasticity model reduces to a combined isotropic/kinematic hardening model with von Mises type of flow. This particular model is already available in both ABAQUS/Standard and ABAQUS/Explicit, so all the numerical simulations in this paper were done using the ABAQUS code.

Finite element model using 4-node axisymmetric elements (CAX4R) is built to simulate the notched round bar subjected to compression-tension loading. Since the experimental data of hardening are only up to $\bar{\varepsilon}^p = 0.152$ that is far below the maximum equivalent plastic strains occurring in the tests, the hardening parameters are adjusted around the experimentally calibrated values at each iterate run. Finally, a very good correlation of the force-displacement curves between experiments and numerical simulation is achieved, as shown in Fig. 7-15. The finally calibrated parameters of the plasticity model is listed in Table. 7.3. A comparison of two hardening curves between the initial calibration and final adjustment is shown in Fig. 7-14. This group of parameters will be used for all the remaining tests.

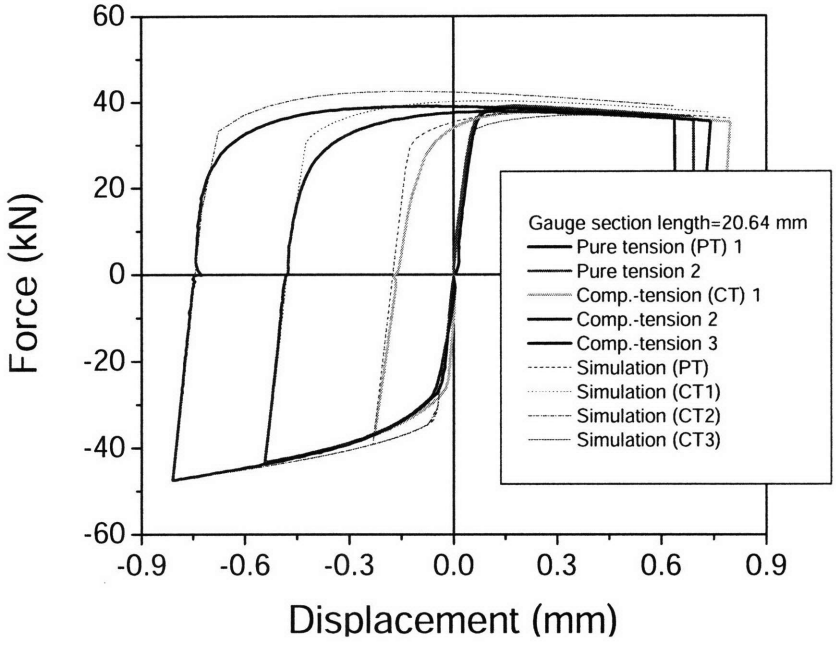

Fig. 7-15: Comparison of force-displacement curves under compression-tension loading.

Table 7.3: Calibrated parameters of the plasticity model of 1045 steel

E	ν	$\sigma_\circ$	σ_{st}	b	C	Γ
2.2e+5MPa	0.3	754 MPa	500 MPa	0.4	3500 MPa	23
c_η	$\eta_\circ$	c_θ^s	c_θ^t	c_θ^c	m	
0.0	-0.72	1.0	1.0	1.0	6	

7.4.2 Fracture tests on unnotched/notched round bars and flat grooved specimens

Two groups of specimens, smooth/notched round bars and flat grooved specimens, were subjected to quasi-static tension until fracture in the MTS uniaxial testing machine, see Fig. 7-16. The loading velocity for round bars was $0.4mm/min$, and the loading velocity for flat grooved specimen was $0.2mm/min$. There were three different ratios of thickness to groove radius in the flat grooved specimens. Each type of test were repeated twice. Details about the dimensions of the specimens both before test and after fracture can be found in Ref. (Bai et al., June 3-7, 2007). The round bars fractured in a cup-cone mode, and the flat grooved specimen showed shear dominant slat fracture. Using the analytical solutions for stress triaxiality and Lode angle parameter (Bai et al., June 3-7, 2007), the initial stress state parameters can be determined from the specimen geometries. Also, from the measured area reduction or thickness reduction, the equivalent strains to fracture can be estimated. A summary of those test results is listed in Table 7.4. The measured force-displacement curves are shown in Fig. 7-17 and 7-18.

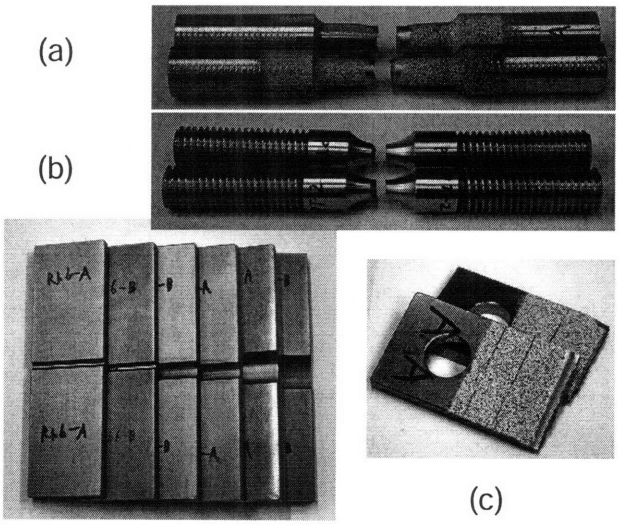

Fig. 7-16: Three types of specimens: (a) un-notched round bars, (b) notched round bars, (c) flat grooved specimens.

Finite element models were built in ABAQUS/Standard to simulate the experiments.

For the round bars, 4-node axisymmetric elements (CAX4R) were used, and for flat grooved plane strain specimens, 8-node solid elements (C3D8R) were used. The material parameters used in the simulation are listed in Table 7.3. Comparisons of force-displacement curves between experimental results and numerical simulations are shown in Fig. 7-17 and 7-18. Good correlations are achieved for flat grooved specimen, but intermediate errors are reported for the round bars. It should be noted that those two groups of test, tensile tests on round bars and flat grooved specimens, were also simulated using the classical J2 plasticity model with isotropic hardening defined by an input of stress-strain curve. A much better correlation than the present results was obtained for the same tensile tests of round bars. See Ref. (Bai et al., June 3-7, 2007) or Section 7.6.1 for details. However, since this paper is focused on the loading history effect, it is more important to use the same plasticity model for all the simulations. An exception is made in Section 7.6.1 of this paper, in which the classical J2 plasticity model with the calibrated stress-strain curve will be used to simulate the two-stage-tension tests.

The sites of fracture initiation were always in the center of the specimens. From the numerical simulations, the average stress triaxiality η_{av}, the Lode angle parameter $\bar{\theta}_{av}$ and the corresponding equivalent strain to fracture $\bar{\varepsilon}_f$ at the fracture initiation sites were obtained. The results are summarized in Table 7.4.

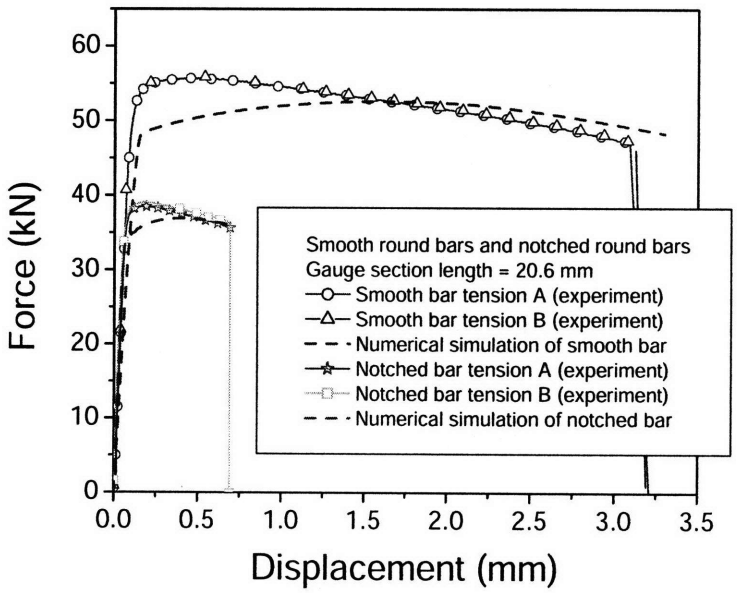

Fig. 7-17: Comparison of force-displacement curves for tensile tests on smooth and notched round bars.

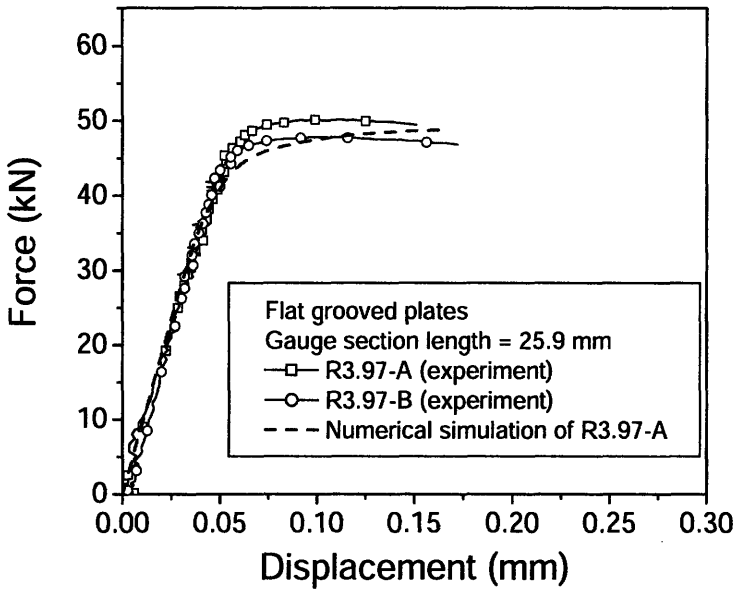

Fig. 7-18: Comparison of force-displacement curves for tensile tests on flat grooved specimens (groove radius = 3.97 mm).

7.4.3 Fracture tests on tubular specimens

Torsion tests were conducted using Lindholm type tubular specimen (Lindholm et al., 1980; White et al., 1990). The dimensions of the specimens is shown in Fig. 7-19. Two torsional tests were conducted under quasi-static loading with zero axial force (see Fig. 7-20). The loading velocity was $0.028°/s$. In order to hold the specimen tightly, two plug-in aluminum cylinders were placed inside the two ends of the tubing specimen during the tests. The measured torque-rotation curves are shown in Fig. 7-21, from which the average rotation angle to fracture is found to be $\Delta\phi_f = 20° = 0.3491 rad$. The equivalent strain to fracture can be estimated,

$$\bar{\varepsilon}_f = \frac{r\Delta\phi_f}{\sqrt{3}L_o} = \frac{9.5 \times 0.3491}{\sqrt{3} \times 4} = 0.48. \tag{7.42}$$

The fracture initiation site was on the outer surface and around the corner, see Fig. 7-20. Because the torsion fracture is a pure shear condition, the two stress state parameters are equal to zero, $\eta = \bar{\theta} = 0.0$.

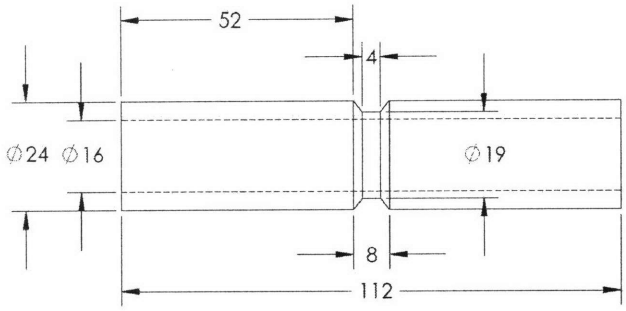

Fig. 7-19: Dimension of torsional tubing specimens.

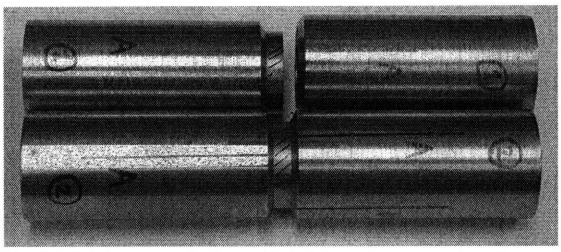

Fig. 7-20: Two torsional tubing specimens after fracture.

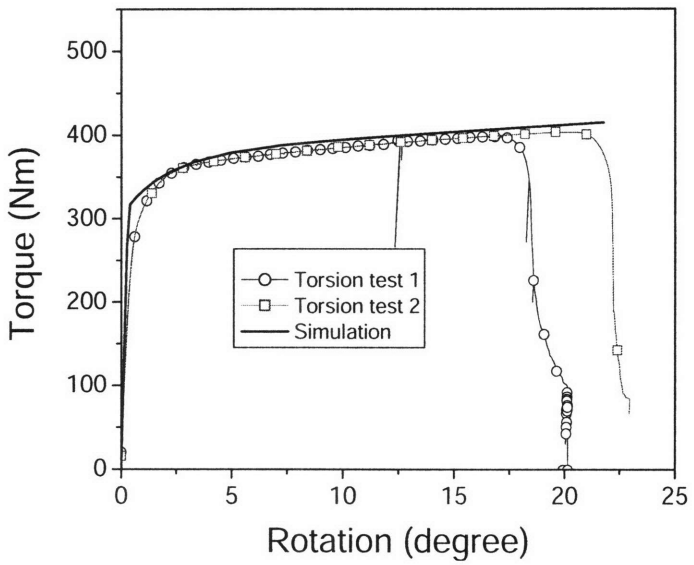

Fig. 7-21: Comparison of torque-rotation curves of tubes under torsional loading.

A finite element model was built using 43040 solid elements (C3D8R) to simulate the torsional test. The mesh of the FE model is shown in Fig. 7-22. A comparison of the force-displacement curves between experiments and numerical simulation is shown in Fig. 7-21. One can see that the simulation result agree with the experimental results very well. From the simulation, the stress state parameters and the equivalent strain to fracture at the fracture initiation site were obtained, which are listed in Table 7.4.

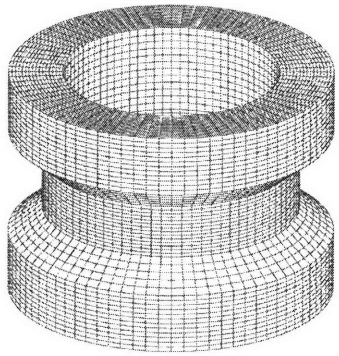

Fig. 7-22: Finite element model with 43040 solid elements of the tubing specimen.

The tubular specimens will be used to study the fracture initiation under torsion-tension loading conditions, so the pure tension as the pure torsion test is an important reference test. In order to apply tensile loading, two holes were made on the specimen shoulder, see Fig. 7-23. The specimen was loaded using two pins in the MTS machine. The loading velocity is $0.2mm/min$. For a thin-walled tube, its loading condition is very close to plane strain tension, so a shear dominant fracture was observed after fracture in the form of a 45° fracture surface, see Fig. 7-23. This point also explains why a cup-cone fracture mode occurs at the uniaxial tension test of round bars of ductile materials. The measured force-displacement curve is shown in Fig. 7-24. The corresponding gauge length is $12.7mm$.

Similarly, a finite element model was developed to simulate the tensile test. Axisymmetric elements (CAX4R) were used to build the model. Figure 7-24 shows the comparison of force-displacement curves between numerical simulation and experiment. It is found that there is some errors in the simulation. The material hardening curves used in the simulation were calibrated from the compression tests, and there is some asymmetry in the material hardening properties between compression and tension (Cazacu and Barlat, 2004; Bai and Wierzbicki, 2007a). This asymmetry is believed to be the main reason of the error. The simulation result could be improved if a more complicated plasticity model is used.

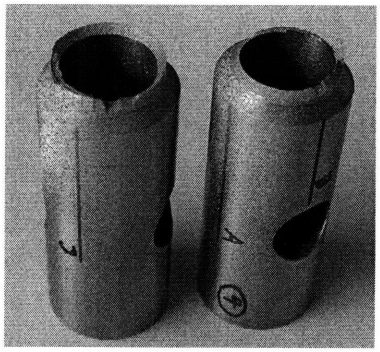

Fig. 7-23: A tubing specimen subject to tensile loading (after fracture).

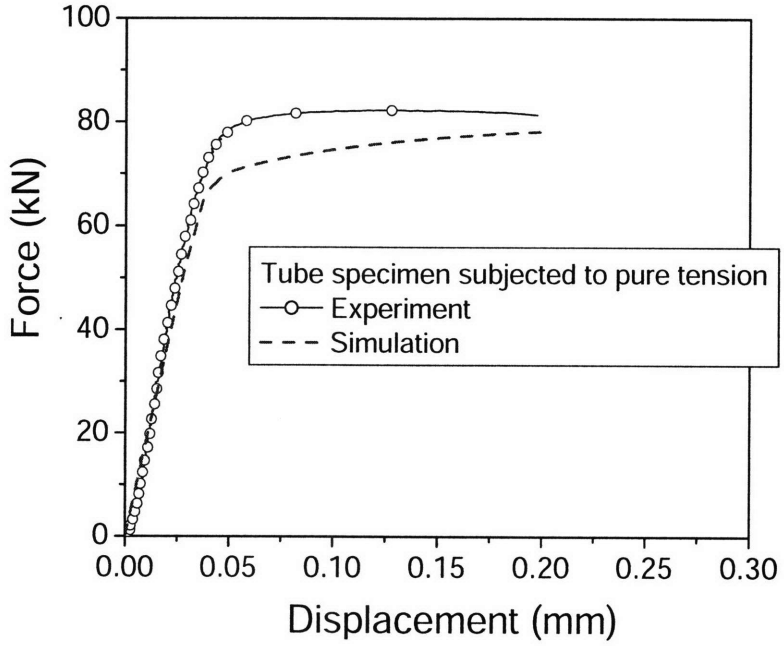

Fig. 7-24: Comparison of force-displacement curves of a tube under pure tensile loading. The gauge length equals to $12.7mm$.

7.4.4 Upsetting tests

The three types of tests discussed above (round bars in tension, flat grooved specimens in tension, and tubular specimen in torsion or tension) are either under the loading condition of axial symmetry tension ($\bar{\theta} = 1$) or plane strain tension ($\bar{\theta} = 0$, or called generalized shear).

According to the asymmetric 3D fracture locus proposed by the present authors (Bai and Wierzbicki, 2007a), information on fracture under axial symmetric compression ($\bar{\theta} = -1$) is missing. The cylindrical specimens upsetting tests will be able to fill this gap.

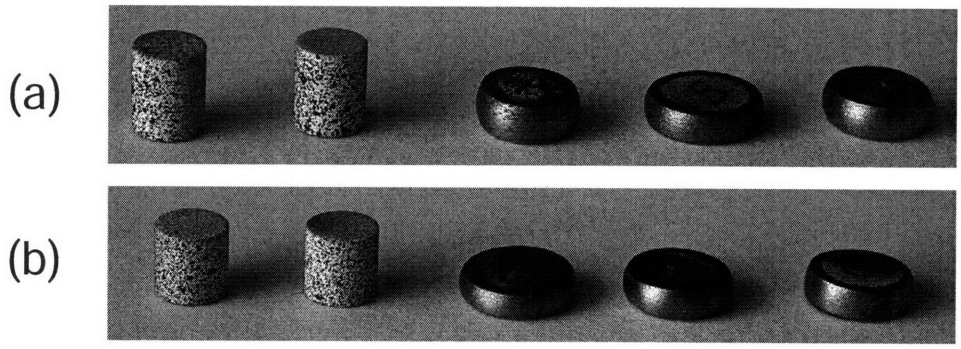

Fig. 7-25: Cylindrical specimens for upsetting tests. (a) the ratio of cylinder diameter to height equals to 0.8, (b) ratio of cylinder diameter to height equals to 1.0.

Two groups of cylindrical specimens (with different ratios of cylinder diameter to height, $d/h = 0.8$ and $d/h = 1.0$) were machined. The diameters of the specimens are equal to $5mm$, and two heights are specified, $5mm$ and $6.25mm$. The specimens were tested in the MTS machine. An optical measurement system was used to measure the displacements between two compressive platens. Specimens before test and after test are shown in Fig. 7-25. Unfortunately, there was no crack observed in the present upsetting tests. The 1045 steel shows strong pressure dependence on the fracture strain. The fracture strain is small in tensile tests, but it increases to a large value in compressive tests. From the measured height reduction, one can estimate that the fracture strain at upsetting test will be greater than 1.0. In order to protect the testing machine, the upsetting tests were stopped at the points without observing fracture. The measured force-displacement curves for the case of $d/h = 0.8$ are shown in Fig. 7-26. In the test B, two teflon layers were placed on the compressive platens to reduce the friction effect. Although the teflon layers reduced some barreling effect on the cylinder, there was no obvious effect on the force-displacement curve, see Fig. 7-26.

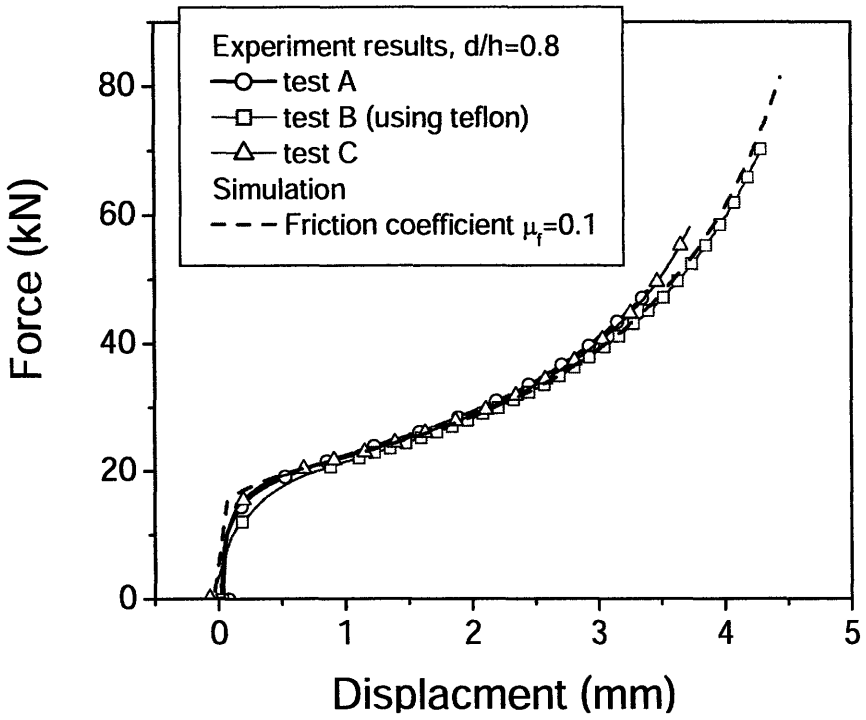

Fig. 7-26: Comparison of force-displacement curves of a upsetting test (ratio of cylinder diameter to height equals to 0.8).

Although there was no observed crack in the present upsetting tests, a finite element simulation using axisymmetric elements was still conducted to further validate the plasticity model. Assigning the value of a constant friction coefficient to $\mu_f = 0.1$, the simulation was shown to agree well with the experimental results, see Fig. 7-26.

7.4.5 3D fracture locus of 1045 steel calibrated from classical specimens

A summary of the data points for the tests discussed in this section is listed in Table 7.4, which includes both direct measurement results of experiments and numerical simulation results. If more than one tests were done for one type of specimen, then the given value is the average value. Each set of data includes the stress triaxiality, the Lode angle parameter and the equivalent strain to fracture.

Table 7.4: A summary of test results on 1045 steel using classical specimens

Results from analytical solution using **experimental measurements**				
No.	Specimen description	$\eta_{initial}$	$\bar{\theta}_{initial}$	$\bar{\epsilon}_f$,test
1	Smooth round bar,tension	0.33	1.0	0.43
2	Notched round bar,tension	0.55	1.0	0.26
3	Flat grooved ($R = 12.7mm$),tension	0.61	0.0	0.13
4	Flat grooved ($R = 3.97mm$),tension	0.68	0.0	0.11
5	Flat grooved ($R = 1.59mm$),tension	0.84	0.0	0.072
6	Tubular specimen, tension	–	0.0	–
7	Tubular specimen, torsion	0.0	0.0	0.48
Results from **numerical simulations**				
No.	Specimen description	η_{av}	$\bar{\theta}_{av}$	$\bar{\epsilon}_f$,simulation
1	Smooth round bar,tension	0.4338	1.0000	0.3411
2	Notched round bar,tension	0.7446	0.9990	0.2013
3	Flat grooved ($R = 12.7mm$),tension	0.6429	0.0513	0.1804
4	Flat grooved ($R = 3.97mm$),tension	0.7321	0.0836	0.1106
5	Flat grooved ($R = 1.59mm$),tension	0.9855	0.1130	0.0850
6	Tubular specimen, tension	0.7479	0.0681	0.0998
7	Tubular specimen, torsion	-0.0003	0.0007	0.5241

The fracture tests discussed in this section are either under the loading condition of axial symmetry tension ($\bar{\theta} = 1$) or plane strain tension ($\bar{\theta} = 0$, or called generalized shear). All the data points from direct experimental measurements are plot in the plane of stress triaxiality and equivalent strain to fracture, see Fig. 7-27. Each group of data points are fitted using Rice-Tracy's exponential function (Rice and Tracey, 1969). It is found that the fracture locus of 1045 steel is strongly dependent on the Lode angle parameter $\bar{\theta}$.

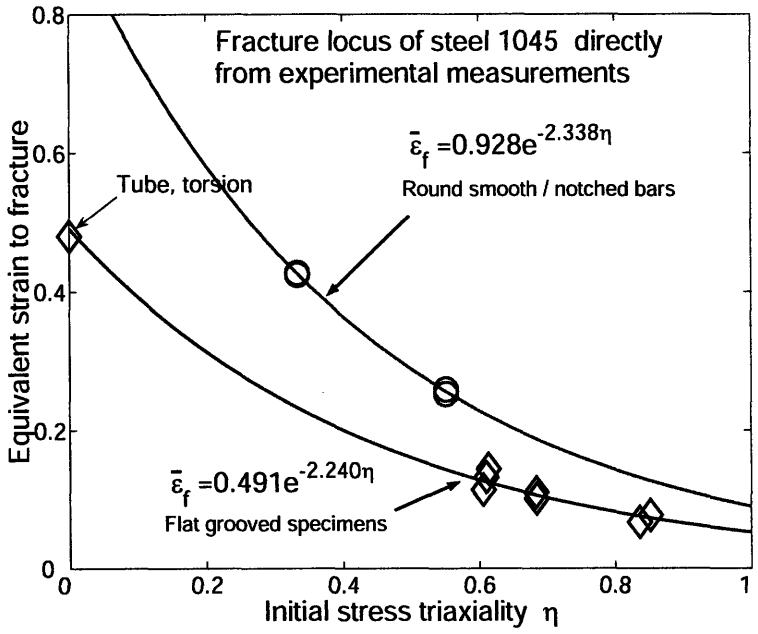

Fig. 7-27: Comparison of the fracture loci of 1045 steel measured from two groups of classical specimen in the plane of equivalent strain to fracture and stress triaxiality, which clearly shows the effect of Lode angle of ductile fracture locus.

The data points from the numerical simulations will be used to construct the 3D fracture locus. Since there is no data points available under the loading condition of axial symmetric compression ($\bar{\theta} = -1$), the 3D fracture locus is assumed to be symmetric, $\hat{\varepsilon}_f^{(+)} = \hat{\varepsilon}_f^{(-)}$ or $D_1 = D_5$ and $D_2 = D_6$. The calibrated parameters of the fracture locus (Eq. (7.32)) is listed in Table 7.5. A comparison of the three bound limits of the 3D fracture locus is shown in Fig. 7-28. A 3D geometrical representation of the fracture locus is illustrated in Fig. 7-29. The error of every data point is also marked in Fig. 7-29. It is shown that the 3D fracture locus agrees well with all the data points. Since all the data points were obtained under monotonic loadings, this fracture locus will be used as a reference for the correction of loading history effect under complex loading conditions.

Table 7.5: Calibrated parameters of the fracture locus of 1045 steel using classical specimens

D_1	D_2	D_3	D_4	D_5	D_6
0.7121	1.6968	0.5187	1.9454	0.7121	1.6968

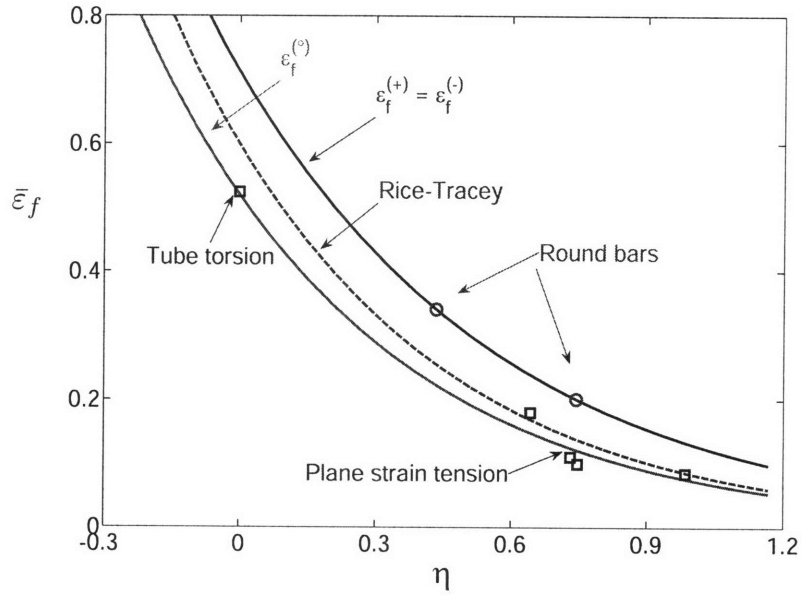

Fig. 7-28: Projection of the fracture locus of 1045 steel from classical specimens into the plane of equivalent strain to fracture and stress triaxiality.

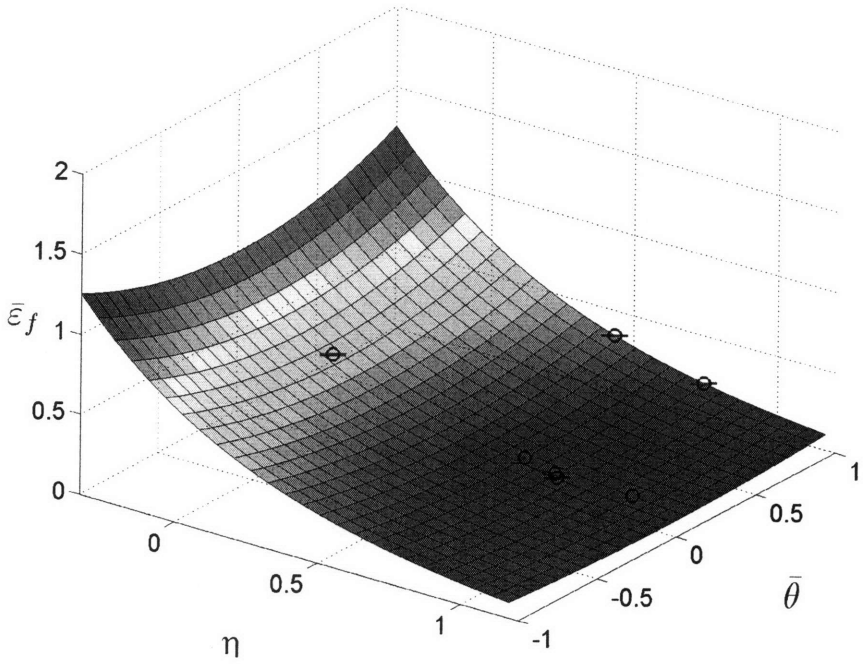

Fig. 7-29: Calibrated 3D fracture locus of 1045 steel from classical specimens.

7.5 Fracture locus calibration using butterfly specimens under biaxial loading

7.5.1 Fracture tests on butterfly specimens of 1045 steel

The fracture locus described in Section 7.4 was calibrated using "classical" specimens. A novel butterfly shape specimen with double curvature gauge section has been designed to calibrate the fracture locus in the space of stress triaxiality and equivalent fracture strain (Bao et al., 2004; Wierzbicki et al., 2005a). The butterfly specimen was mounted into a custom made universal biaxial testing device (UBTD) (Mohr and Doyoyo, 2004; Mohr and Henn, 2004, 2007), and then tested in the MTS uniaxial testing machine. The results for the butterfly specimens have recently been used to constructed the 3D fracture locus (Bai and Wierzbicki, 2007a).

In the present study, 16 butterfly specimens were machined. The specimens were tested in a newly designed INSTRON biaxial testing machine (Mohr and Oswald, 2007), see Fig. 7-31. Detail dimensions about the specimen can be found in Bao et al. (2004); Wierzbicki et al. (2005a). A set of specimens is shown in Fig. 7-30. There are two parts of test procedures on the butterfly specimens. Nine specimens were tested under monotonic loading conditions to calibrate the fracture locus. Seven specimens were tested under complex loading conditions to study the loading history effect on fracture. This section will deal with the part of tests under monotonic loading conditions, and the other part of tests with complex loading conditions will be presented in Section 7.7.

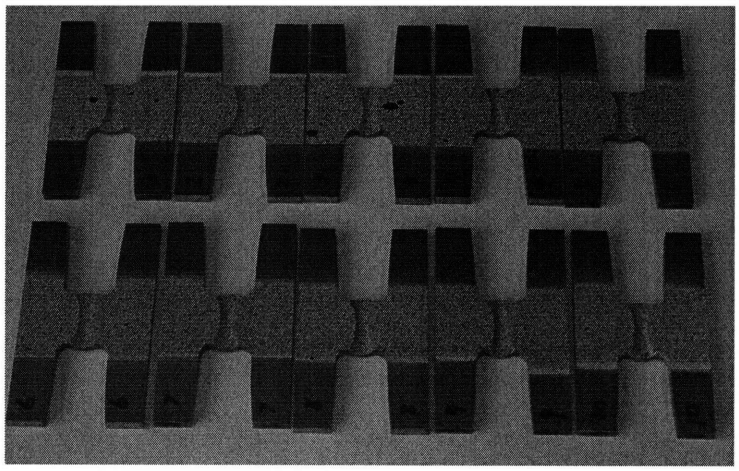

Fig. 7-30: Butterfly specimens tested under monotonic loading conditions.

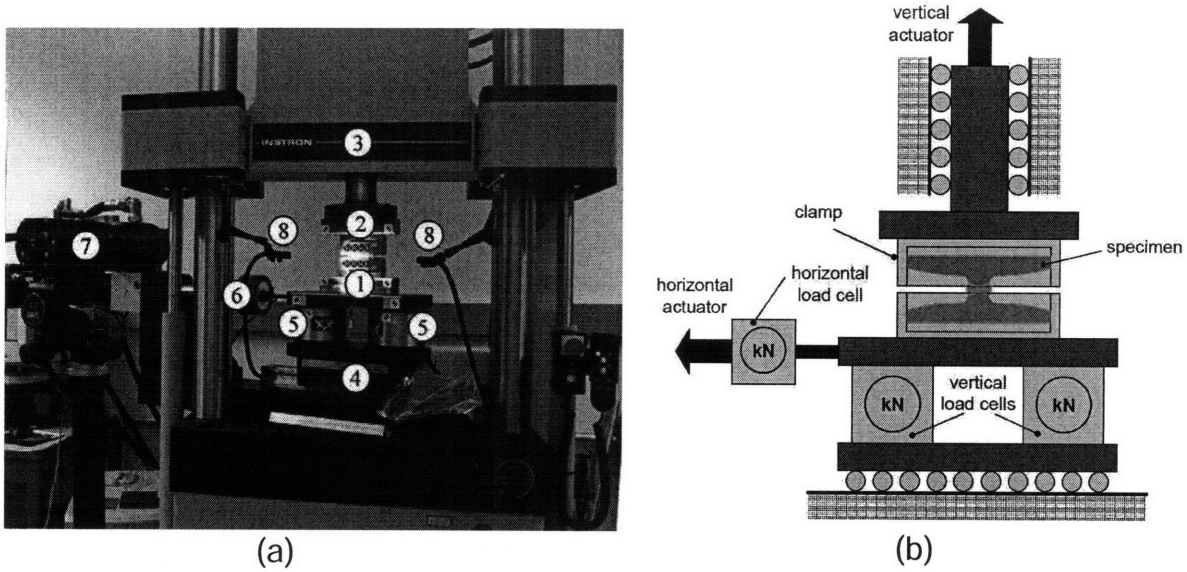

Fig. 7-31: (a) INSTRON dual actuator loading system: 1-lower system grip, 2-upper grip, 3-upper cross-head, 4-sliding table, 5-vertical load cells, 6-horizontal load cell and actuator, 7-digital camera. (b)Schematic of the mechanical system. (photo modified after Mohr and Oswald (2007)).

The butterfly specimen was fixed on one part, and the other part was subjected to different loading combinations of tension, shear, and compression. As shown in Fig. 7-32, if the specimen is subjected to simple shear, the loading condition is called $+0°$ or $-0°$ loading; pure tension is called $+90°$ loading; combination of shear and tension is named as $+\Theta°$; and combination of shear and compression is denoted by $-\Theta°$ loading. Eight different loading conditions were chosen to conduct the tests: $+90°$, $+30°$, $+22°$, $+10°$, $+5°$, $+0°$, $-5°$ and $-10°$. Due to limited number of specimens, one test was done for each case except for $+0°$, which was done twice.

The INSTRON biaxial testing machine has two independent actuators, vertical actuator and horizontal actuator (see Fig. 7-31). Both actuators have both displacement control and force control mode. In the simple shear loading case ($+0°$), the force control mode was used for the vertical actuator to keep a total zero vertical force, and the displacement control mode was used for the horizontal actuator to apply constant loading velocity. For all other loading conditions, displacement control modes were used for both actuators to apply a constant loading velocity with a fix loading angle. The combined loading velocities were $0.05mm/min$ for the loading case of $+90°$, $0.1mm/min$ for $+30°$, $0.2mm/min$ for $+22°$, and

$0.3mm/min$ for all the remaining cases.

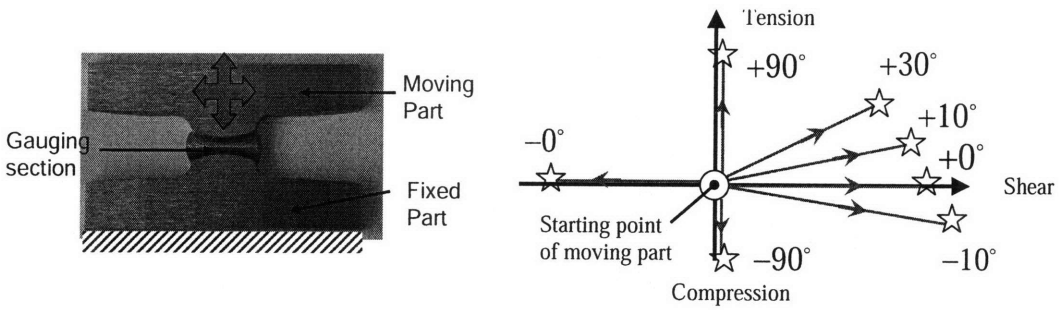

Fig. 7-32: Definition of different loading angles for butterfly specimens.

The specimens were painted with random dots before tests (see Fig. 7-30), and an optical measurement system was used to accurately capture the local displacement field of the specimen's gauge section. The measured curves of horizontal force v.s. horizontal displacement and vertical force v.s. vertical displacement are shown in Fig. 7-33 - 7-40. The optical gauge length used in the curves is $5.6mm$. For fracture tests, it is important to detect the location of the fracture initiation. According to previous work on butterfly specimens (Wierzbicki et al., 2005a; Bai et al., 2006c), a summary of the locations of fracture initiation is listed in Table 7.6. From the measurement force-displacement curves, the corresponding displacements to fracture are found for all cases, which is also included in Table 7.6.

Table 7.6: List of locations of fracture initiation of butterfly specimens

No.	Loading condition	Displacement to fracture (mm) *	Location in the main plane	Location in the thickness direction
1	+90°	$v_f = 0.1017$	Center	Middle of thickness
2	+30°	$u_f = 0.2193$	Center	Middle of thickness
3	+22°	$u_f = 0.2870$	Center	Middle of thickness
4	+10°	$u_f = 0.4216$	Center	Middle of thickness
5	+5°	$u_f = 0.4569$	Center	Middle of thickness
6	+0°	$u_f = 1.030$	Center	Surface
7	−5°	$u_f = 1.712$	Center	Surface
8	−10°	$u_f = 2.524$	Center	Surface

* *The horizontal displacement to fracture is denoted by u_f, and the vertical one is denoted by v_f*

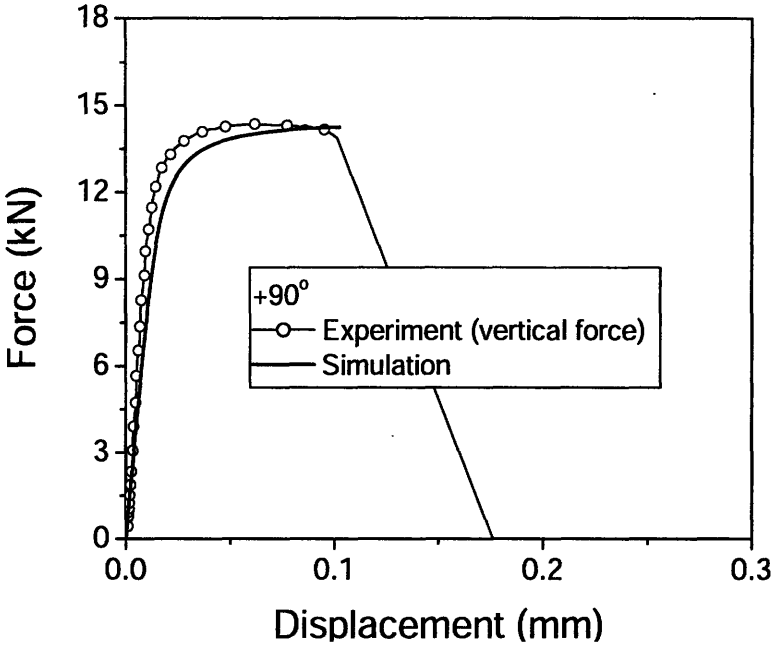

Fig. 7-33: Comparison of force-displacement curves under pure tension (+90°).

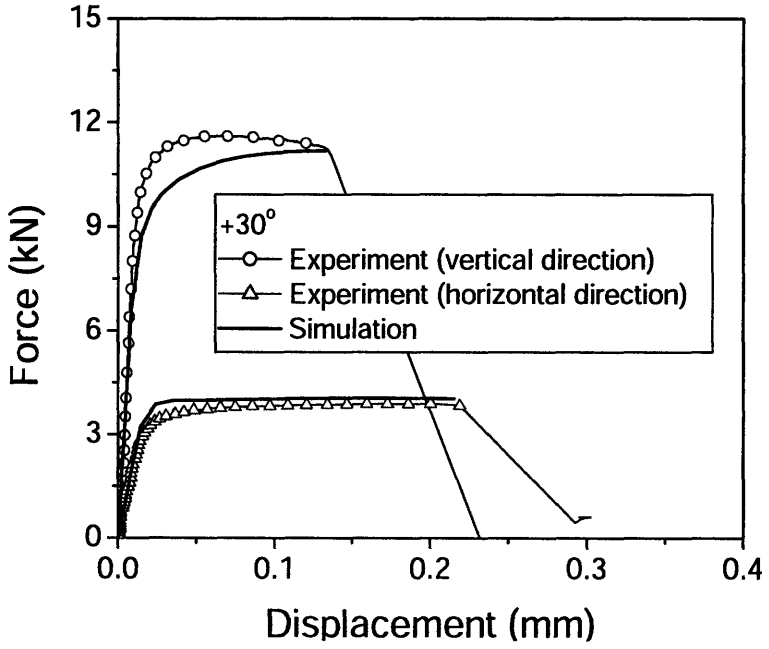

Fig. 7-34: Comparison of force-displacement curves under biaxial loading (+30°).

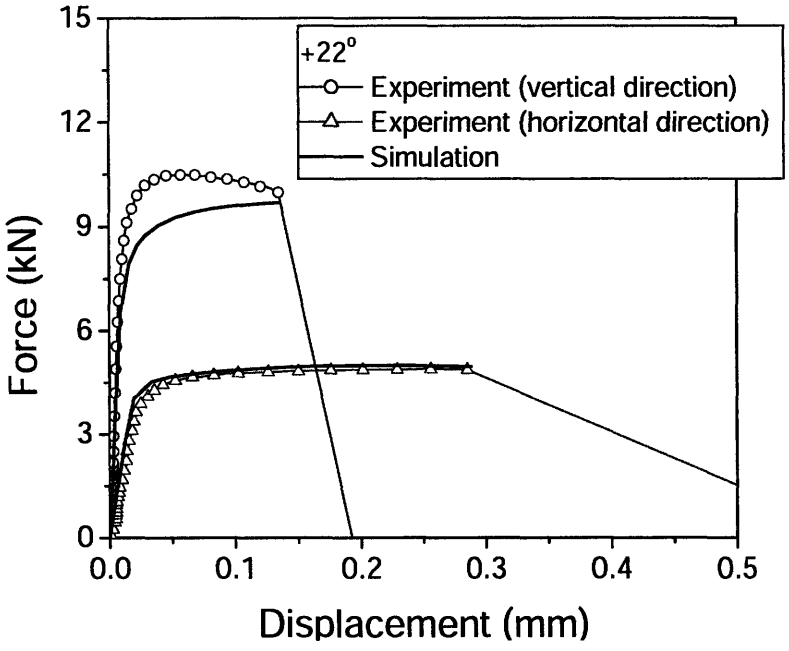

Fig. 7-35: Comparison of force-displacement curves under biaxial loading (+22°).

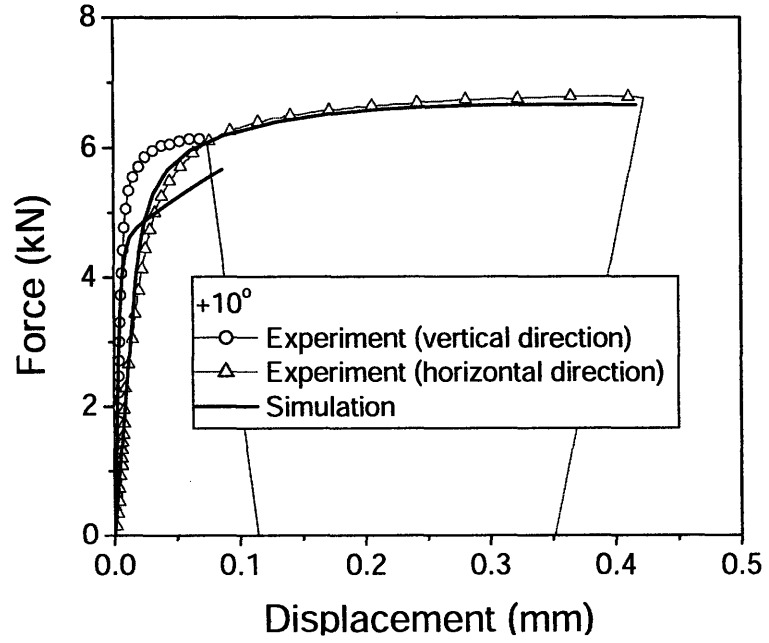

Fig. 7-36: Comparison of force-displacement curves under biaxial loading (+10°).

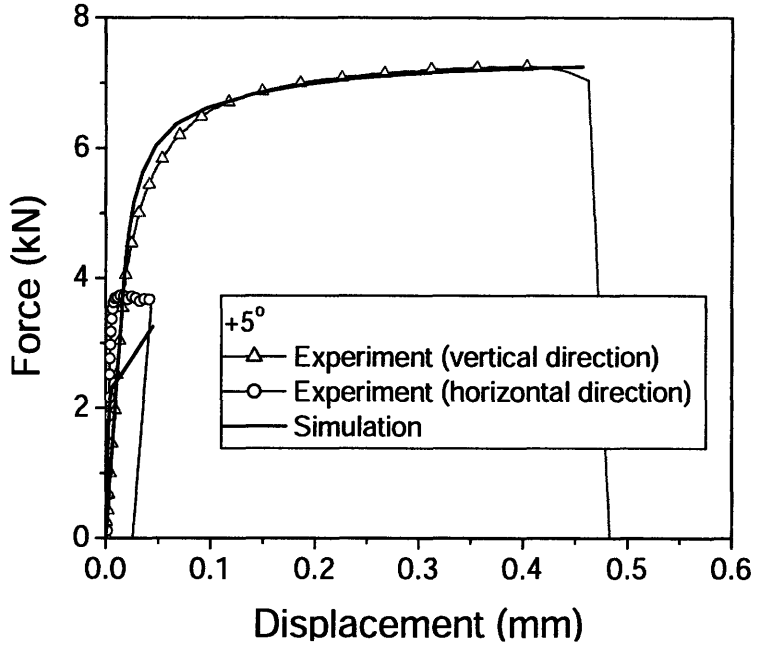

Fig. 7-37: Comparison of force-displacement curves under biaxial loading (+5°).

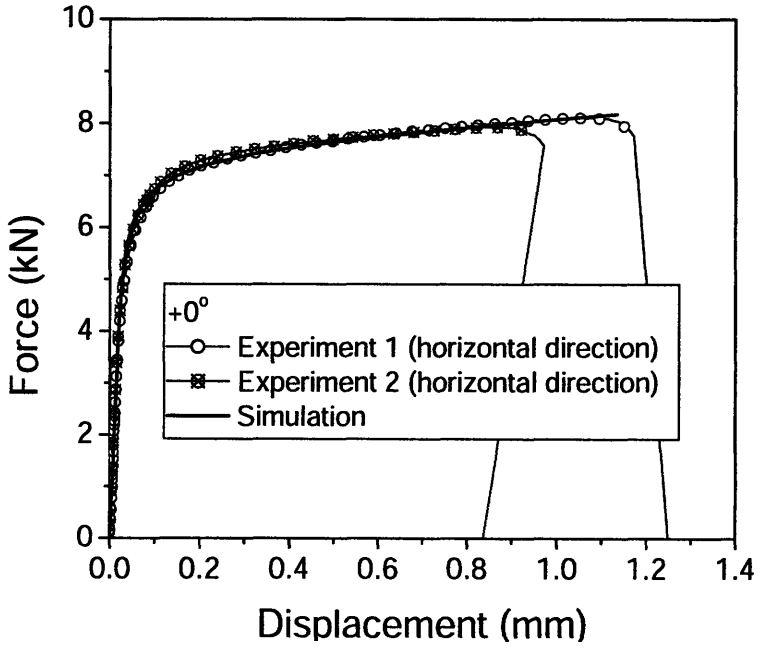

Fig. 7-38: Comparison of force-displacement curves under simple shear (+0°).

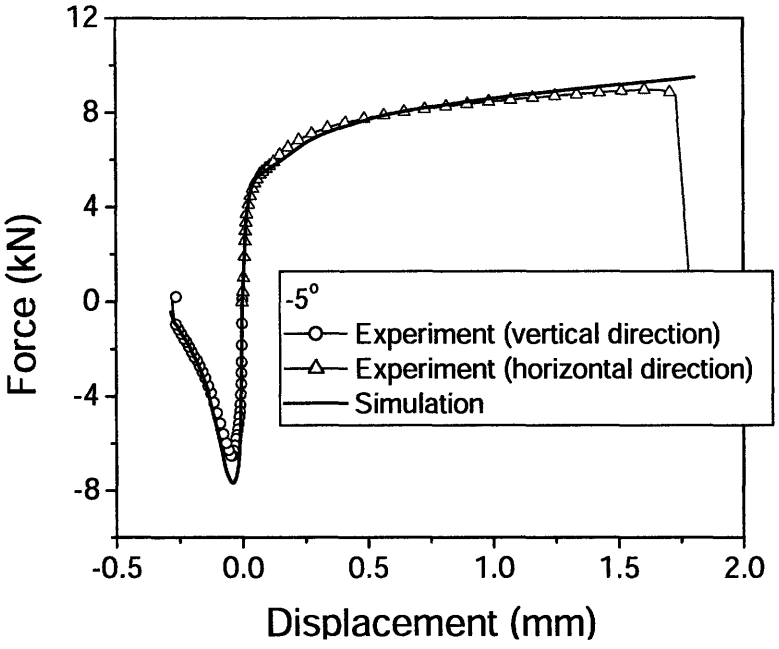

Fig. 7-39: Comparison of force-displacement curves under biaxial loading ($-5°$).

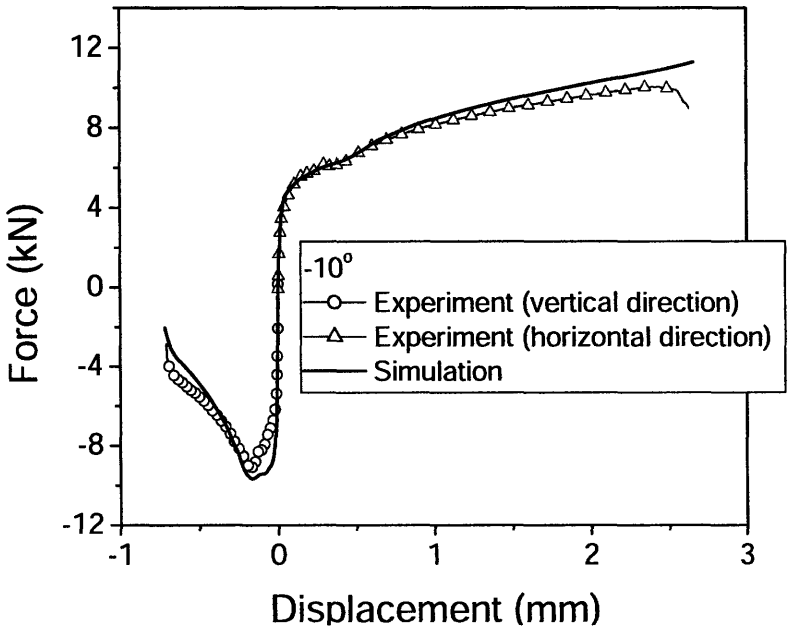

Fig. 7-40: Comparison of force-displacement curves under biaxial loading ($-10°$).

Since stress state parameters and the equivalent strains to fracture can not be directly measured from the butterfly specimens, numerical simulations are necessary for this study. Finite element simulations were performed for all eight loading cases. The butterfly specimen was modeled using 28120 solid elements (C3D8R), see Fig. 7-41. In the simulations, the lower shoulder of the butterfly specimen was fixed, and the upper shoulder was subjected to prescribed displacements. Because the rigidity of the testing machine is limited, in the loading angles ($-5°$ and $-10°$) at which the total forces were larger than other cases, the real loading angle applied on the specimen was not exactly the same as what the machine specified during the test. Therefore, the real curves of loading angle measured from the optical system were used in the numerical simulations of $-5°$ and $-10°$. Comparisons of the force-displacement responses are shown in Fig. 7-33 - 7-40. One can see the numerical simulations are in accord with the experimental results, especially for the horizontal force-displacement curves.

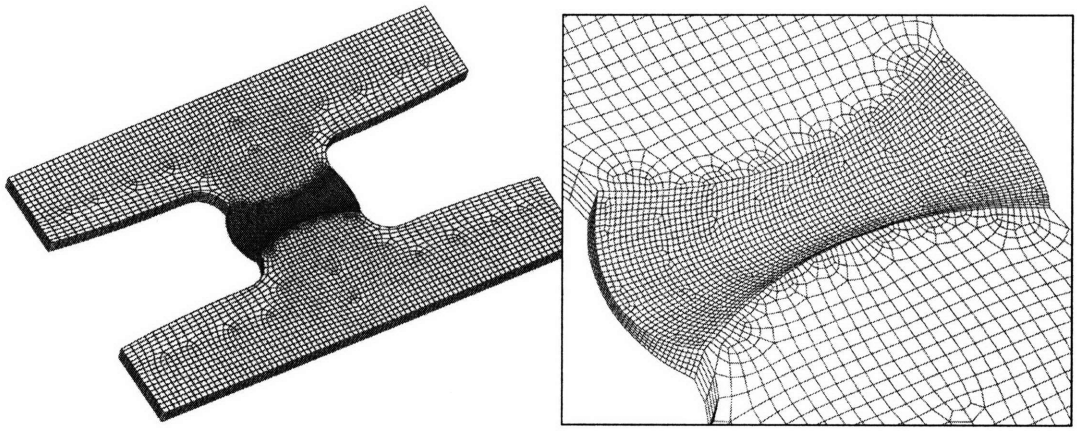

Fig. 7-41: Finite element model with 28120 solid elements of the butterfly specimen.

7.5.2 3D fracture locus of 1045 steel calibrated from butterfly specimens

Using the measured horizontal or vertical displacements to fracture (u_f or v_f) and the detected fracture initiation positions (see Table 7.6), the corresponding stress state parameters (η and $\bar{\theta}$) and the equivalent strain to fracture $\bar{\varepsilon}_f$ were calculated. A summary of the fracture data points for all eight loading cases is listed in Table 7.7. The butterfly specimen has been well designed and optimized without unwanted edge fracture, so a wide range of stress

state can be achieved under different loading angles. The stress state parameters may vary during the loading process for each monotonic loading condition (Wierzbicki et al., 2005a), especially for ductile materials with large deformation. In order to capture this variation, average values of stress state parameters are used.

Table 7.7: A summary of test results on 1045 steel using butterfly specimens

No.	Loading condition	η_{av}	$\bar{\theta}_{av}$	$\bar{\epsilon}_f$
1	+90°, tension	0.8192	0.0955	0.1566
2	+30°, tension and shear	0.6892	0.6563	0.2359
3	+22°, tension and shear	0.6202	0.8482	0.2766
4	+10°, tension and shear	0.3750	0.5176	0.3553
5	+5°, tension and shear	0.2051	0.2442	0.4026
6	+0°, shear	-0.0214	-0.0206	0.8601
7	−5°, compression and shear	-0.1693	-0.3831	0.9655
8	−10°, compression and shear	-0.2547	-0.6081	1.1826

An optimization procedure was run to best fit the data points in Table 7.7) to get a 3D fracture locus. The details about this procedure can be found in Bai and Wierzbicki (2007a). Finally, the calibrated parameters of the 3D fracture locus (Eq. (7.32)) from butterfly specimens is listed in Table 7.8. A comparison between the three bound limits of the 3D fracture locus and the data points is shown in Fig. 7-42. A 3D geometrical representation of the fracture locus is illustrated in Fig. 7-43. The error of every data point is also marked in Fig. 7-43. One can see that the 3D fracture locus well fit all the data points. The average error of all eight cases is only 5.0%. This fracture locus will be used as a reference for the study of loading history effect under complex loading conditions of other butterfly specimens.

Table 7.8: Calibrated parameters of the fracture locus of 1045 steel using butterfly specimens

D_1	D_2	D_3	D_4	D_5	D_6
0.8057	1.5501	0.6664	1.7329	0.9918	1.2880

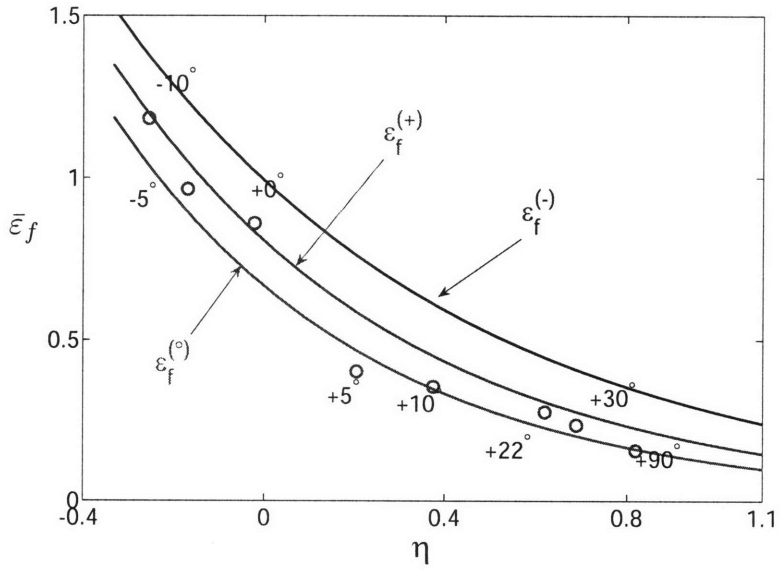

Fig. 7-42: Projection of the fracture locus of 1045 steel from butterfly specimens into the plane of equivalent strain to fracture and stress triaxiality.

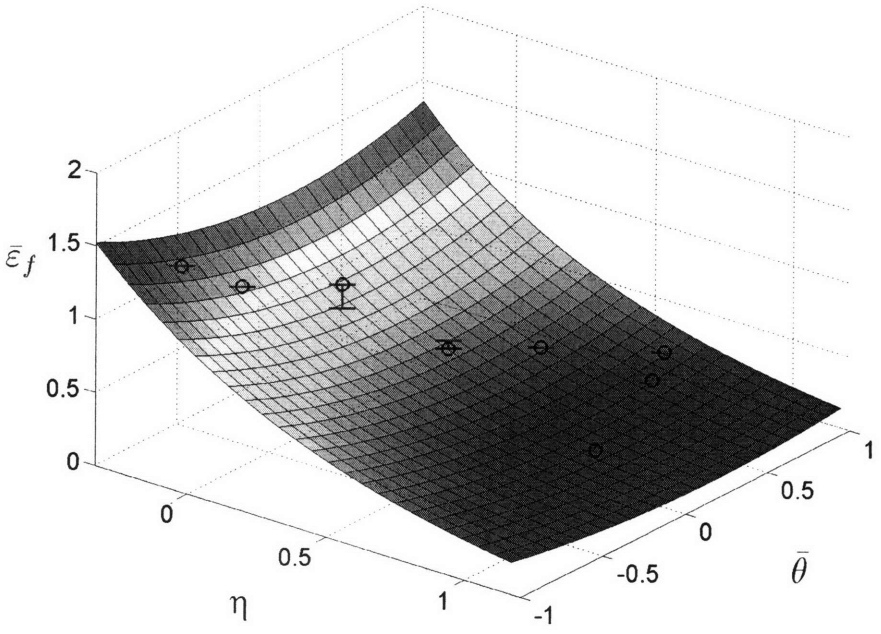

Fig. 7-43: Calibrated 3D fracture locus of 1045 steel from butterfly specimens.

7.5.3 Comparison of two 3D fracture loci of 1045 steel

Section 7.4 describes the calibration of the fracture locus of 1045 steel using "classical" specimens. Meanwhile, Section 7.5 gives another fracture locus of 1045 steel using butterfly specimens. These two fracture loci should be identical since all the specimens were cut from the same material block. However, it is found that the fracture locus calibrated from butterfly specimens is higher than the one from "classical" specimens. A comparison of the three bound limits ($\hat{\varepsilon}_f^{(+)}$, $\hat{\varepsilon}_f^{(o)}$ and $\hat{\varepsilon}_f^{(-)}$) of these two fracture loci is shown in Fig. 7-44.

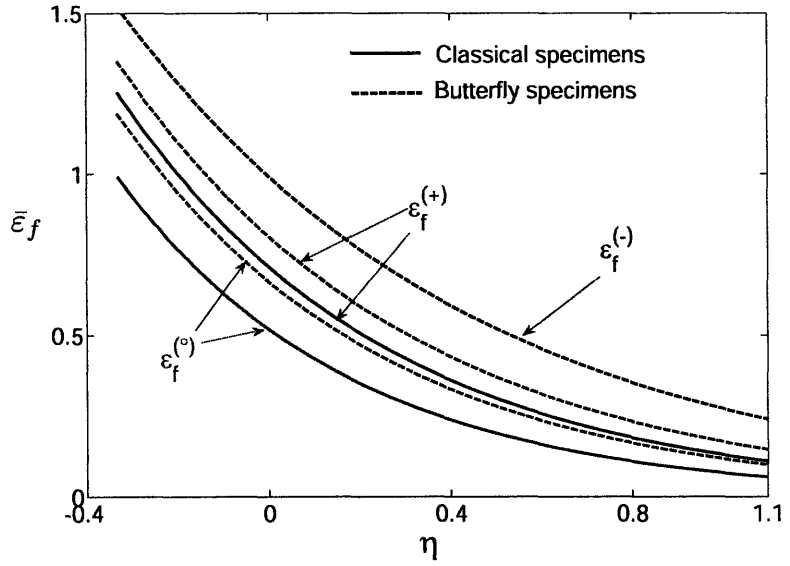

Fig. 7-44: Comparison of two fracture loci of 1045 steel calibrated from classical specimens and butterfly specimens in the plane of equivalent strain to fracture and stress triaxiality.

In Fig. 7-44, solid curves denote bound limits from "classical" specimens, and dashed curves denote those from butterfly specimens. One can see that these two groups of bound limits are highly similar, and their main difference is an offset of a scale. The 3D representation of two fracture loci (Fig. 7-29 and Fig. 7-43) confirms this similarity. One reason for the difference in the two calibrated fracture loci may be due to *mesh size effect* (more generally including mesh type and mesh shape effect). It is shown by many authors that the calculated equivalent strain to fracture will increase when the mesh size decreases (for example, Lee (2005); Wierzbicki et al.), especially for ductile material with large deformation. The mesh size of the butterfly specimen is $0.14mm$, and the average mesh size of the

"classical" specimens is $0.25mm$. It is noted that the simulation of butterfly specimens uses only one mesh, so the mesh size effect is partially removed in the relative point of view.

Since this paper is focused on the loading history effect, the fracture locus calibrated under monotonic or proportional loading conditions is a very important reference point. Therefore, the fracture locus calibrated from the either kind of specimen will be used as the reference point for the study of loading history effect on the corresponding kind of specimen.

7.6 Calibration of the loading history effect on fracture on 1045 steel

In this section, three types of tests with complex loading conditions will be used to calibrate and validate the proposed correction for the loading history effect, Eq. (7.26) or Eq. (7.31). Totally, there are five material parameters, c_g, c_h β_1, β_2, and k, to be calibrated. Those tests include two stages tension with changing notches, reversal loading of compression-tension, and the torsion followed by tension.

7.6.1 Two-stage-tension tests

This group of test is to confirm Tai's finding (Tai, 1990), see Section 7.3.2. Four smooth round bars were machined and subjected to pre-tension, and the tests were stopped at two different amounts of deformation. Then, notches with a radius of $7.5mm$ were introduced carefully to the pre-pulled specimens. The new diameter of specimens at the neck is $5.0mm$. Special attention was paid to the re-machining to make sure that no damage was introduced. A collection of the specimens at both two stages loading is shown in Fig. 7-45. The measured force-displacement curves for both two stage loading are shown in Fig. 7-46 and Fig. 7-47. The difference between the results in these two figures is different amount of pre-tension. These tests are denoted respectively as group A and group B based on two different amounts of pre-tension.

Two smooth round bars and two notched round specimens with the same ratio of neck diameter to notch radius ($d/R = 5.0/7.5 = 2/3$) were already tested under pure tension to get the reference value for these two stages tension, which is described in Section 7.4.2.

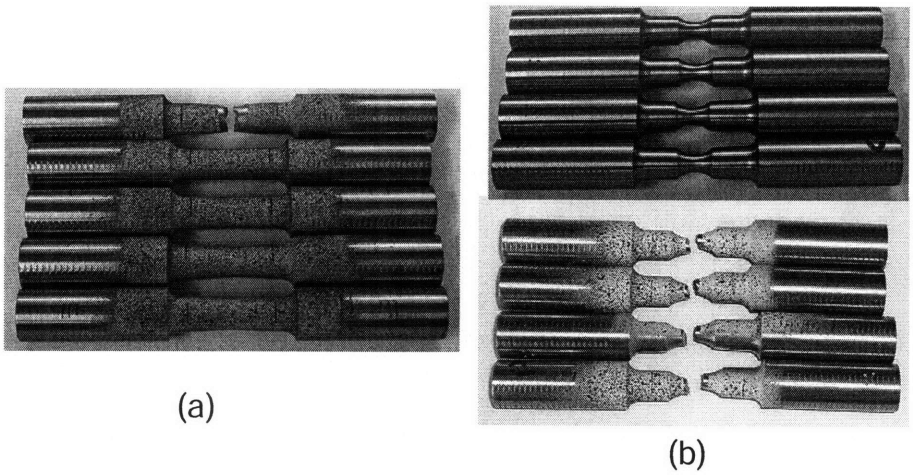

Fig. 7-45: Specimens of two-stage-tension test on 1045 steel. (a) specimens after first stage tension, (b)second stage specimens with re-machining introduced notches.

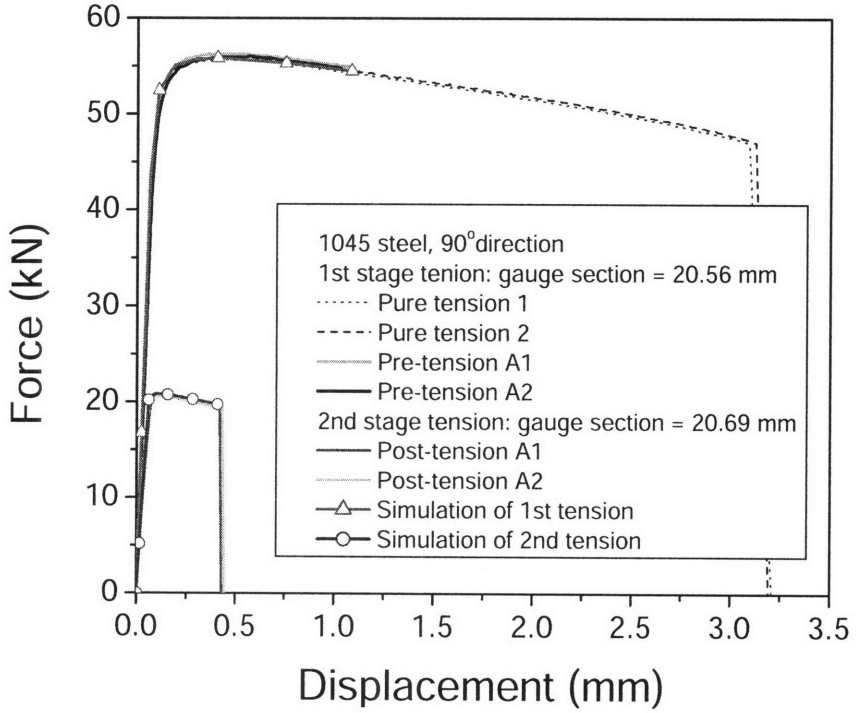

Fig. 7-46: Comparison of force-displacement curves for a group of two-stage-tension tests (group A).

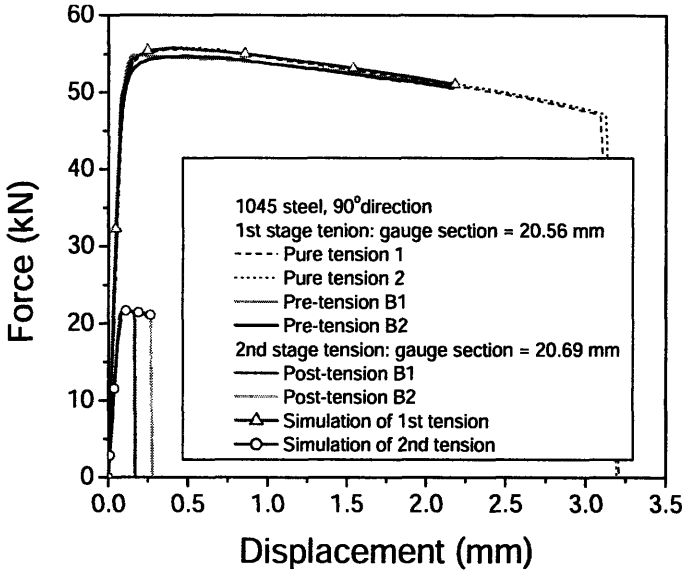

Fig. 7-47: Comparison of force-displacement curves for a group of two-stage-tension tests (group B).

Finite element simulations were performed using axisymmetric elements (CAX4R). As described in Section 7.4.2, there is some error in the simulation of tensile tests of smooth round bars using combined isotropic/kinematic hardening plasticity model calibrated from compression-tension tests. If a combined hardening model is used, then the material should become anisotropic (due to existence of non-zero initial back stress components) after the first stage tension . Before the second stage tension, some materials were cut out during re-machining, and it is difficult to simulate the process of re-machining. Therefore, the classical J2 plasticity model with isotropic hardening is used in the simulation instead of the combined kinematic/isotropic hardening model discussed earlier. The stress-strain curve of the material (Fig. 7-48) was calibrated from the tensile test of smooth round bars following standard procedures. It is found that this plasticity model predicts the force-displacement curves of pure tension on smooth/notched round bars with excellent accuracy, as shown in Fig. 7-49.

After the pre-tension, the material is still assumed to isotropic, but the stress-strain curves used in the second stage tension are shifted relative to the amount of plastic strain introduced in the pre-tensions. The stress-strain curves used in the second stage tension are also shown in Fig. 7-48. Comparisons of force-displacement curves of the two-stage-tension tests between experiments and numerical simulations are shown in Fig. 7-46, and 7-47. One

can see that very good correlations are achieved for both two stages of tension.

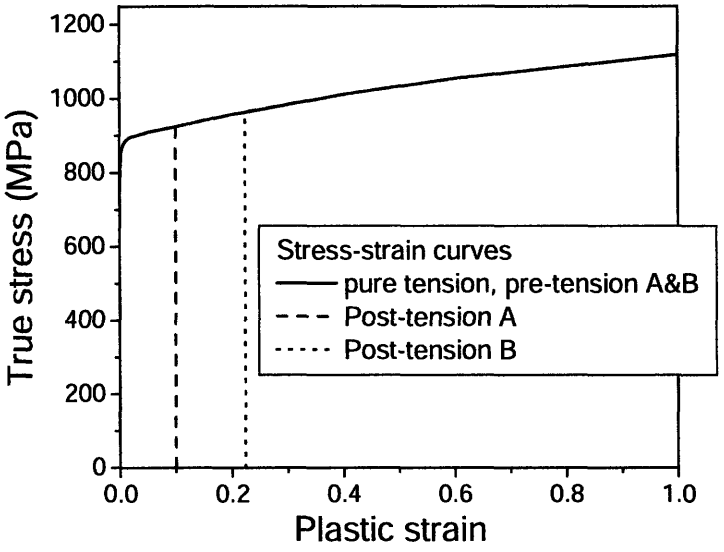

Fig. 7-48: Stress-strain curves used to simulate the two-stage-tension tests.

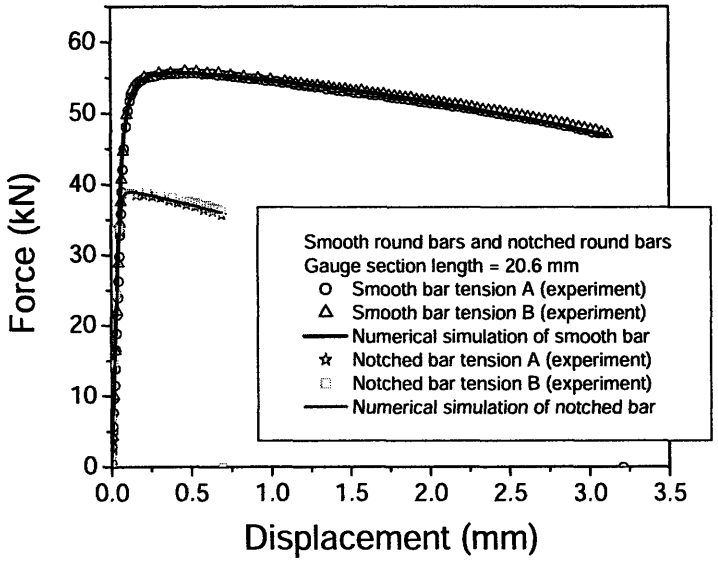

Fig. 7-49: Another simulation of smooth/notched round bars subjected to pure tension. This figure shows the comparison of force-displacement curves.

Here, the results of new simulations on pure tension of smooth/notched round bars are

used to obtained the baseline fracture locus, see Eq. (7.43).

$$\hat{\varepsilon}_f^{(+)} = 1.665e^{-2.429\eta} \tag{7.43}$$

Since all the tests in the two-stage-tension are under axial symmetry tension ($\bar{\theta} = 1$), it is sufficient to consider only one bound limit, $\hat{\varepsilon}_f^{(+)}$. In this type of test, the direction of the current stress tensor σ is accord with the direction of the back stress tensor S_{back}, so the parameter χ equals zero, and the parameter $\mu = 0$. Therefore, this type of test can be used to calibrate the parameter c_g.

From the numerical simulations, all the strain and stress components at the fracture initiation site (the center of the round specimens) were obtained. As a starting point, both terms in the history effect correction are switched off, $g(\lambda) = 1$ and $h(D, \mu) = 1$, then the accumulated damages of both stages loading are calculated based on the baseline fracture locus (Eq. (7.43)). A bar plot of the results is shown in Fig. 7-50. It is found that the total damages at fracture is very close to unity except for case 4, clearly which exhibited a pre-matured fracture (It is found from Fig. 7-47 that the test of post-tension B1 was an pre-matured fracture). The reason is probably due to the damage introduced by re-machining of notch.

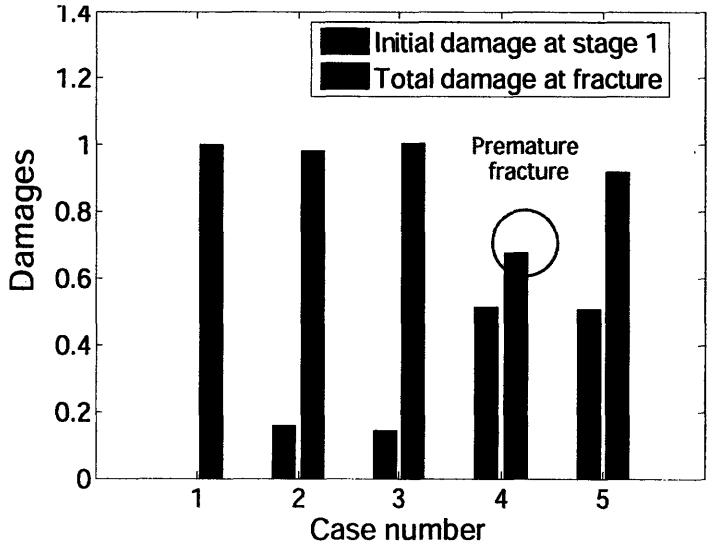

Fig. 7-50: Comparison of damage accumulation for the two-stage-tension tests (case 1: for pure tension, case 2&3: group A, case 4&5: group B).

The two-stage-tension tests imply that there is no need to introduce the weighting function $g(\lambda)$ if there is no change in loading directions. Hence, the parameter c_g is equal to zero. This result is consistent with Tai's conclusion (Tai, 1990).

7.6.2 Compression followed by tension tests on notched round bars

The compression-tension tests can be used not only to calibrate the material plasticity model, but also to study the loading history effect on fracture. In order to avoid buckling during compression, the notched round bars were mounted on the MTS machine in a special method. The experimental setup is shown in Fig. 7-51. Two specimens were subjected to pure tension, and three specimens were subjected to different amounts of pre-compression followed by tension till fracture. Three different amounts of pre-compression were applied: $\varepsilon_{o1} = 0.053$, $\varepsilon_{o2} = 0.14$, and $\varepsilon_{o3} = 0.21$. The specimens show a cup-cone fracture mode. The measured force-displacement curves are shown in Fig. 7-15. The gauge length is equal to $20.64mm$. Numerical simulations of the tests were also conducted. A comparison of the force-displacement curves was already shown in Fig. 7-15. Very good correlation is achieved using the calibrated combined hardening model.

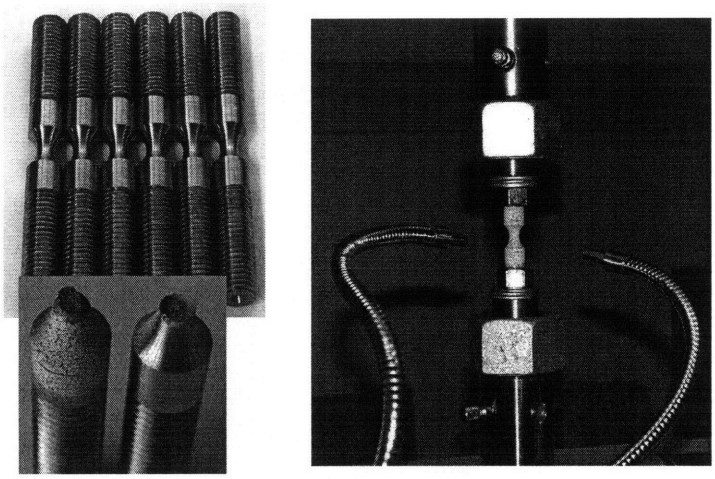

Fig. 7-51: Specimens and experimental setup for compression-tension test on 1045 steel.

The fracture initiation site of this type of test is the center of the specimens. If the weighting function $h(D, \mu)$ in Eq. (7.26) is set to $h(D, \mu) = 1$ (without loading history

correction), the calculated total damage at fracture of different pre-compression strain is shown in Fig. 7-52. In the calculation, the fracture locus parameters listed in Table 7.5 are used. It is interesting to find that the pre-compression increases the ductility of 1045 steel, which is totally different from the tests results of 2024-T351 aluminum reported by Bao and Treitler (2004). The results of 2024-T351 aluminum is also shown in Fig. 7-52 for comparison. Actually, from Fig. 7-15, one can see that the pre-compression on 1045 steel increases the displacement of the tensile stage to fracture. Both these types of loading history effect are included in the model using the parameter k. For 2024-T351 aluminum, the parameter $k = 1$, and for 1045 steel, $k = -1$.

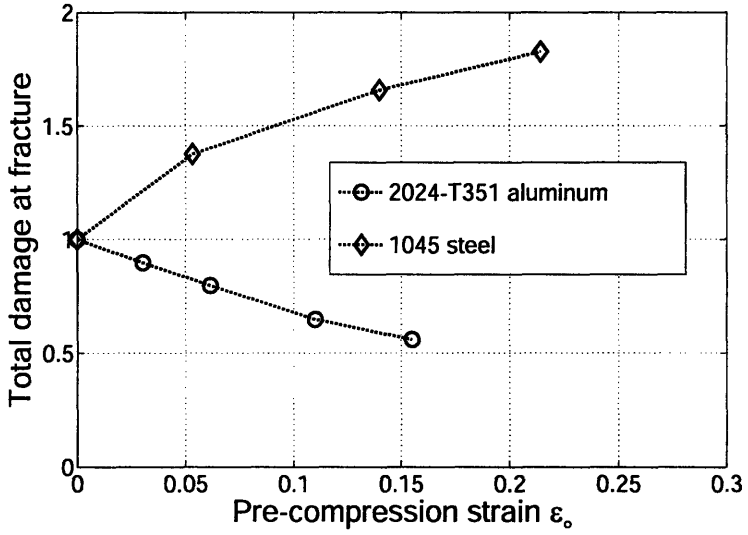

Fig. 7-52: Comparison of two types of loading history effect on fracture under reverse loading (without any correction of loading history effect).

7.6.3 Torsion followed by tension tests on tubular specimens

In addition to the pure torsion and pure tension tests of tubing specimens (see Section 7.4.3), a group of tests on pre-torsion followed by tension were performed. The fractured specimens after two stages loading are shown in Fig. 7-53. Three different amounts of pre-torsion were applied: $\Delta\phi_1 = 7.3°$, $\Delta\phi_2 = 12.6°$, and $\Delta\phi_3 = 16.9°$. The measured torque-rotation curves for the pre-torsion and the force-displacement curves with a gauge length $12.7mm$ are shown in Fig. 7-54 and 7-55 respectively. The fracture mode of the first two specimens is shear dominate slant fracture, and the third one is flat fracture due to larger initial damage

in pre-torsion. The fracture initiation sites are on the outer surface of tube close to the shoulder.

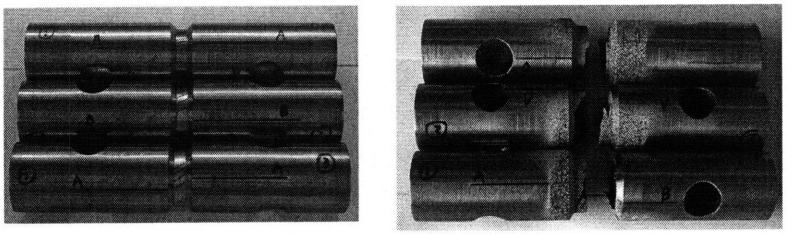

Fig. 7-53: Specimens subjected to torsion followed by tension. (a)specimens after initial torsion, (b) specimens after tension of the second stage loading.

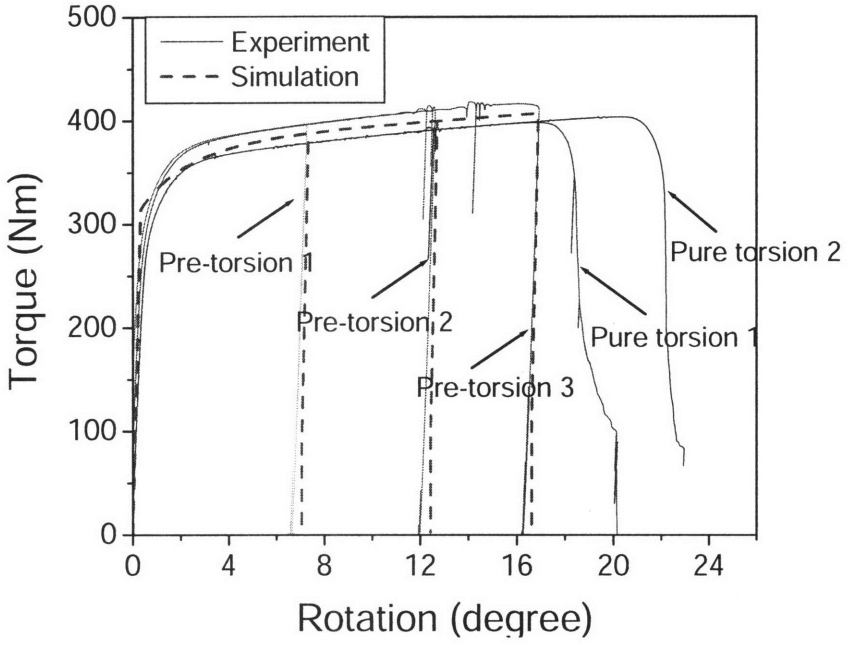

Fig. 7-54: Comparison of torque-rotation curves for the pre-torsion part of the loading cycle.

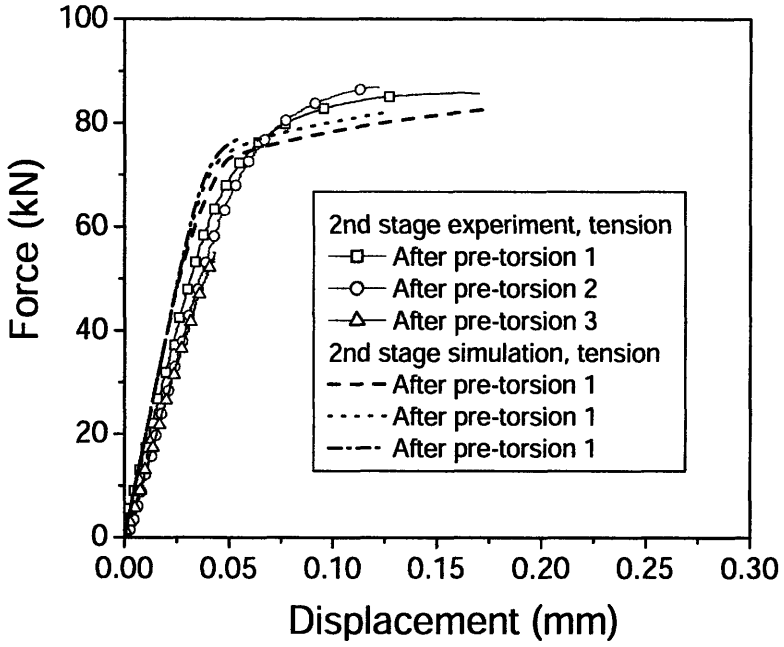

Fig. 7-55: Comparison of force-displacement curves for tension of the second stage loading on tubes.

Finite element simulations were conducted using solid elements (C3D8R), see Fig. 7-22. Three loading steps were used in each simulation: pre-torsion, unloading to zero force/torque, followed by pure tension. A comparison of the the torque-rotation curves for the pre-torsion loading is shown in Fig. 7-54. A comparison of the the force-displacement curves for the tensile loading is shown in Fig. 7-55. One can see that the numerical simulations agree with the experimental results.

If no loading history effect term is used, using the fracture locus calibrated from "classical" specimens (see the Table 7.5), the total damages at fracture for crack initiation sites in all five cases are shown in Fig. 7-56. The results of OFHC copper reported by Johnson and Cook (1985) are also plot in Fig. 7-56 for comparison. It is found that changes in the loading direction/condition increase the ductility of 1045 steel, which is different from that of OFHC copper. Referring to the result in section 7.6.2, it is concluded that change in the loading direction (or the parameter χ) increases the ductility of 1045 steel. This loading history effect is relatively smaller in torsion-tension loading than in reversal loading due to smaller values of the parameter χ and μ in the second stage loading. A comparison of the evolution of the parameter μ in these two types of tests in shown in Fig. 7-57. These two group of

tests will be used to calibrate the parameters in the weighting function $h(D, \mu)$.

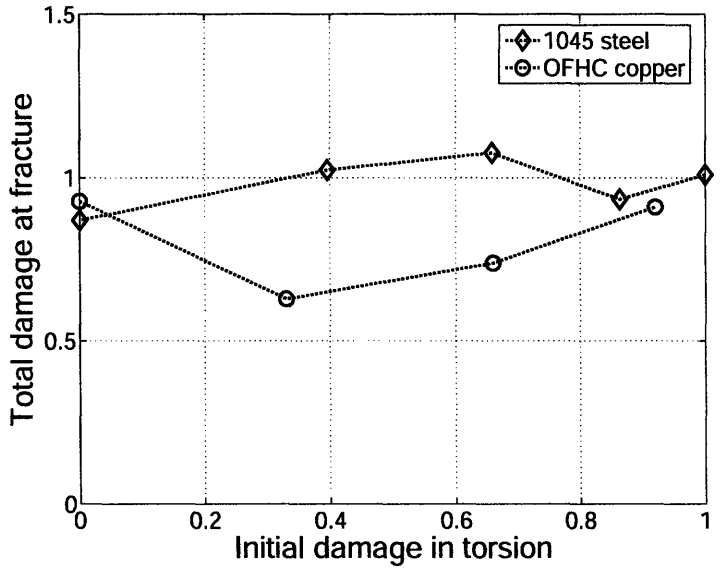

Fig. 7-56: Comparison of two types of loading history effect on fracture under torsion-tension loading.

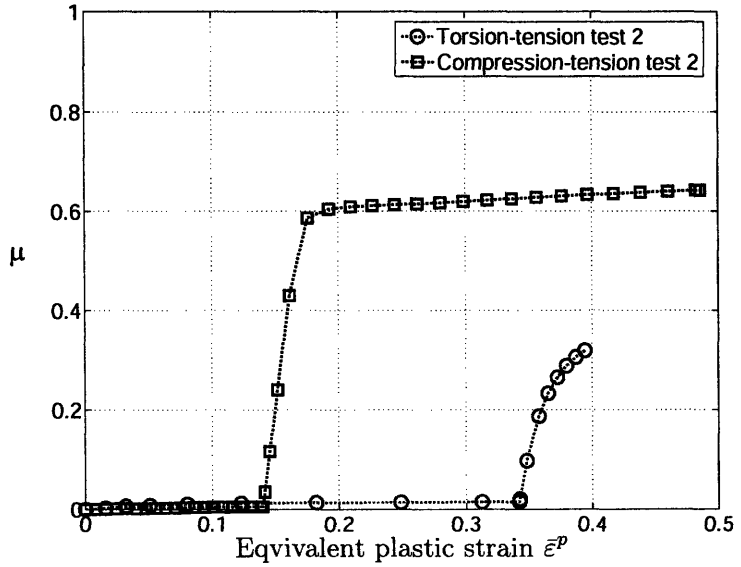

Fig. 7-57: Comparison of the evolution of the parameter μ between the torsion-tension loading and the compression-tension loading.

7.6.4 Parameter calibration

From the above three groups of tests, it is found that any change in loading directions (or the parameter μ) increases the ductility of 1045 steel, so the parameter $k = -1$ is chosen. It is found in Section 7.6.1 that the weighting function $g(\lambda) = 1$, so the parameter c_g is set as $c_g = 0.0001$. A very small value is used in order to avoid mathematical singularity. All the histories of the parameters ($\bar{\varepsilon}^p$, η, $\bar{\theta}$, and μ) at the fracture initiation sits were obtained from the numerical simulations. A Matlab code was written to calculate the damages and optimize the remaining three parameters: c_h, β_1, and β_2. The differential form of damage model, Eq. (7.31), and the fracture locus calibrated from "classical" specimens are used. The objective in the optimization is the make all the values of damage accumulation at fracture D_c as close to unity as possible. Finally, a combination of these three parameters is achieved. The calibrated parameters of loading history effect is listed in Table 7.9.

Table 7.9: Calibrated parameters of the loading history effect on fracture of 1045 steel

c_g	c_h	β_1	β_2	k
0.0001	5.5	2.0	2.0	-1

Comparisons of the total damages at fracture between without and with correction of loading history effect are shown in Fig. 7-58 and 7-59. Now, the total damages at fracture are much closer to unity for all cases. If the damage is assumed to occur at $D_c = 1$ (as is proposed by the model), then the predicted displacements to fracture will be very close to the fracture displacement in tests. Therefore, one can see that the proposed loading history functions works well for both the compression-tension loading and the torsion-tension loading. So far, the calibration of the proposed ductile fracture model is completed. In next section, the model will be used to predict fracture of butterfly specimens under complex loading histories.

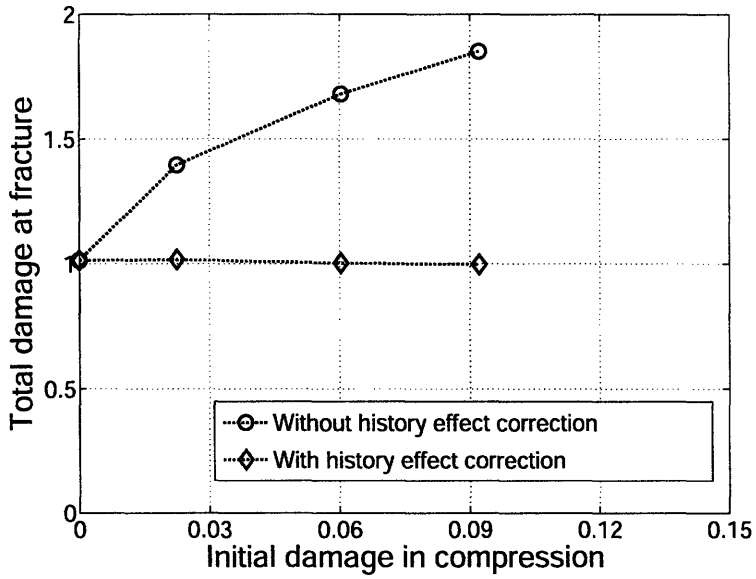

Fig. 7-58: Correction of the loading history effect on fracture, notched round bars of 1045 steel subjected to compression followed by tension.

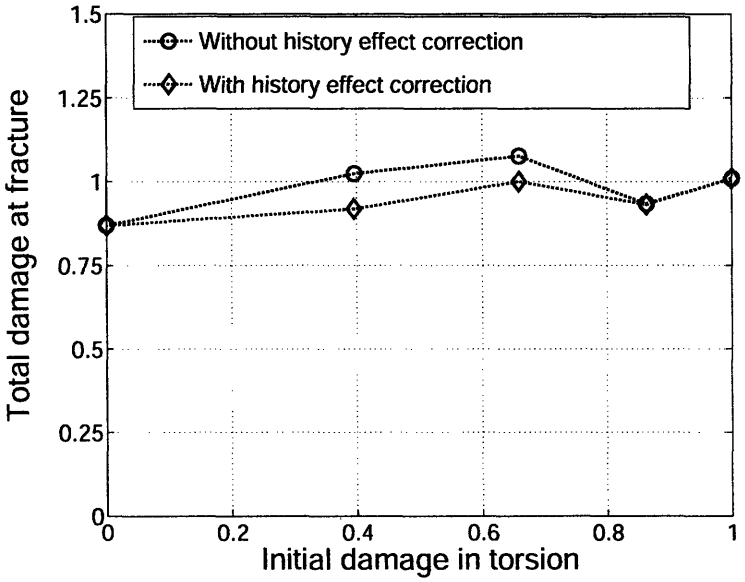

Fig. 7-59: Correction of the loading history effect on fracture, tubing specimens of 1045 steel subjected to torsion followed by tension.

7.7 Fracture validation tests on butterfly specimens with complicated loading histories

In Section 7.5, the butterfly specimens were used to calibrate the fracture locus under monotonic loading conditions. In this section, three types of the tests with complex loading conditions are conducted, which can be denoted by $+0° \rightarrow +30°$, $-90° \rightarrow +90°$, and $-0° \rightarrow +0°$. The calibrated fracture locus (parameters listed in Table 7.8) and the calibrated loading history effect functions (parameters listed in Table 7.9) will be used to predict fractures of butterfly specimens under complex loading conditions.

7.7.1 Tests on butterfly specimens: complex loading of $+0° \rightarrow +30°$

Three tests of butterfly specimens under complex loading of $+0° \rightarrow +30°$ were performed. In the first stage loading, $+0°$, the total vertical force was kept to be zero, and in the second stage loading, $+30°$, displacement control mode was used to both horizontal and vertical actuators. The specimens after fracture are shown in Fig. 7-60. The measured force-displacement curves for both two stage loading are shown in Fig. 7-61, 7-62, and 7-63. Note that the vertical force curve of test 1 in the second stage loading was not saved due to a computer error. The displacements to fracture were obtained through the optical measurement system.

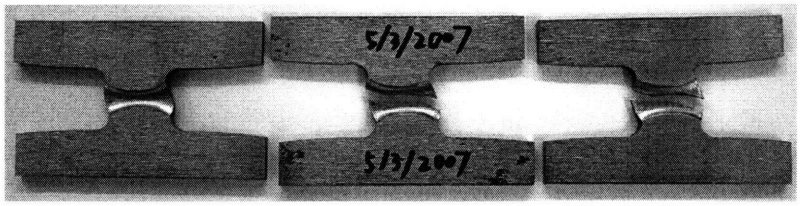

Fig. 7-60: Butterfly specimens subject to the complex loading of $+0° \rightarrow +30°$.

Finite element simulations were performed. Comparisons of the force-displacement responses are also shown in Fig. 7-61, 7-62, and 7-63. Very good correlations are obtained using the calibrated plasticity model with combined hardening. The fracture initiation sites are on the surface point in the center of the specimen. The loading condition of $+0° \rightarrow +30°$ is similar to that of torsion followed by tension. The calculated total damage at fracture of the fracture initiation points is illustrated in Fig. 7-64. The results under monotonic loading

of +0° and +30° are also plotted for comparison. One can see that the proposed model well predicts the fractures under this type of complex loading.

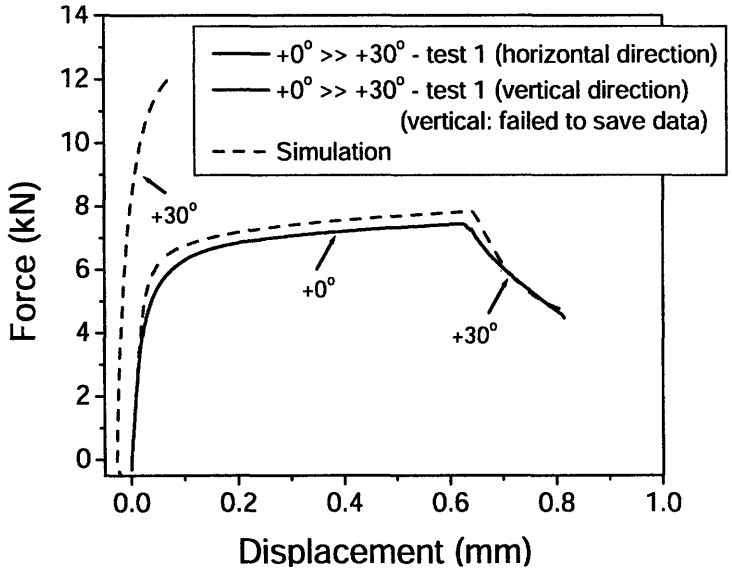

Fig. 7-61: Comparison of force-displacement curves under two-stage loading of (+0° → +30°, test 1).

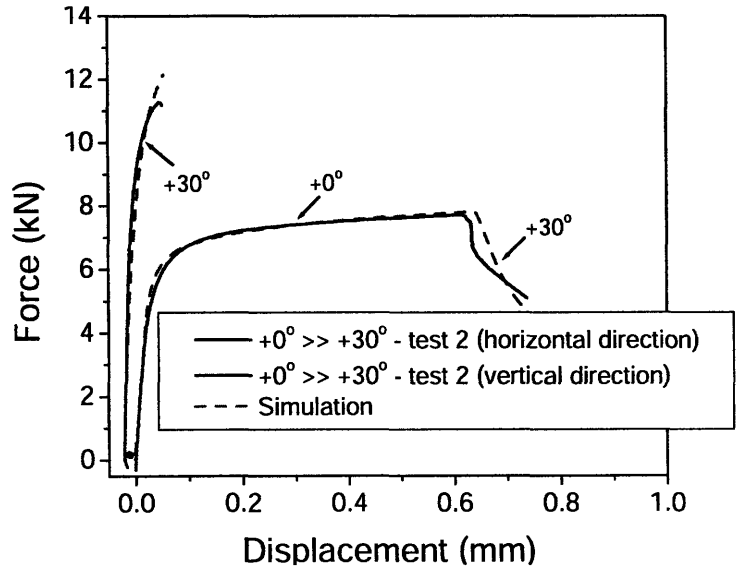

Fig. 7-62: Comparison of force-displacement curves under two-stage loading of (+0° → +30°, test 2).

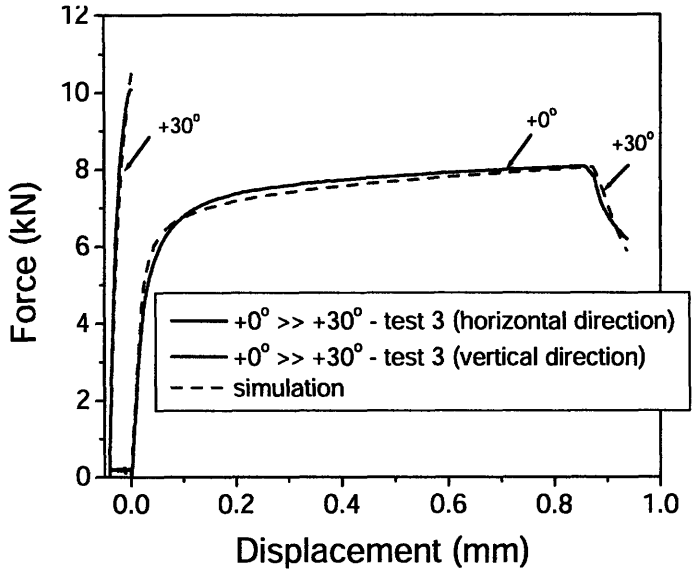

Fig. 7-63: Comparison of force-displacement curves under two-stage loading of (+0° → +30°, test 3).

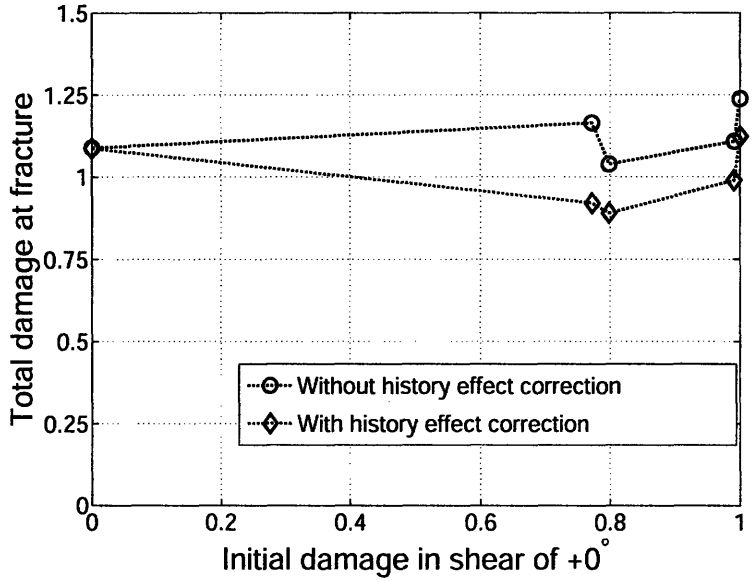

Fig. 7-64: Correction of the loading history effect on fracture, butterfly specimens of 1045 steel subjected to complex loading of +0° → +30°.

7.7.2 Tests on butterfly specimens: reverse loading of $-90° \rightarrow +90°$

Two tests of butterfly specimens under the reverse loading of $-90° \rightarrow +90°$ were conducted. During the tests, the horizontal actuator was fixed, and displacement control mode was used to the vertical actuator. The two specimens after fracture is shown in Fig. 7-65. The measured force-displacement curves are shown in Fig. 7-66. Finite element simulations were also performed. A comparison of the force-displacement responses is also shown in Fig. 7-66. It is found that the simulation follows the experiments closely. The fracture initiation sites are in the center of the specimen. This loading condition of $-90° \rightarrow +90°$ is a reversal loading under plane strain condition.

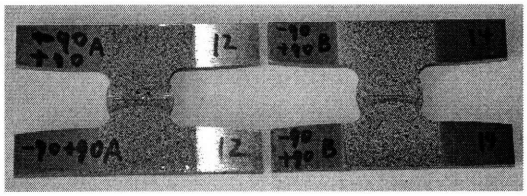

Fig. 7-65: Butterfly specimens subject to the reverse loading of $-90° \rightarrow +90°$.

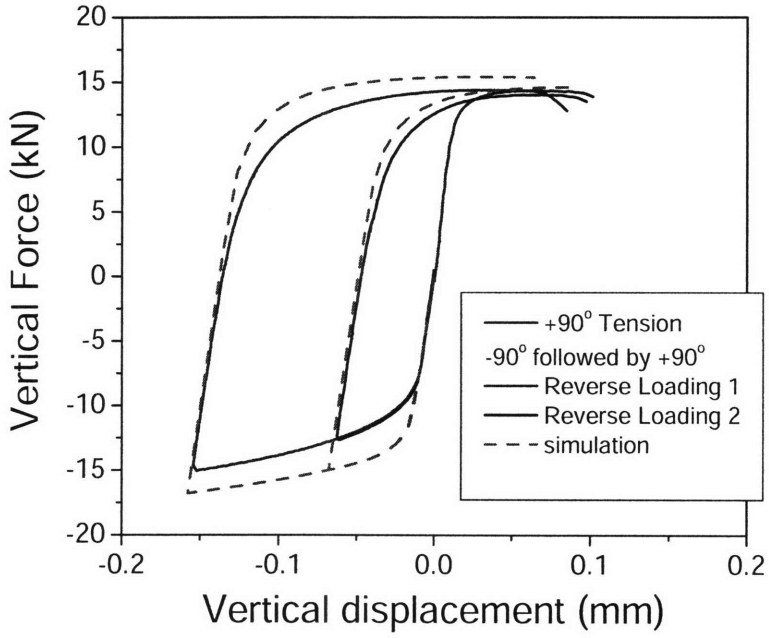

Fig. 7-66: Comparison of force-displacement curves under reverse loading of $(-90° \rightarrow +90°)$.

The calculated total damage at fracture of the fracture initiation points is illustrated in Fig. 7-67. The result under the monotonic loading of $+90°$ is also plotted for comparison. It is shown that the proposed model predicts the fractures under this type of reverse loading very well.

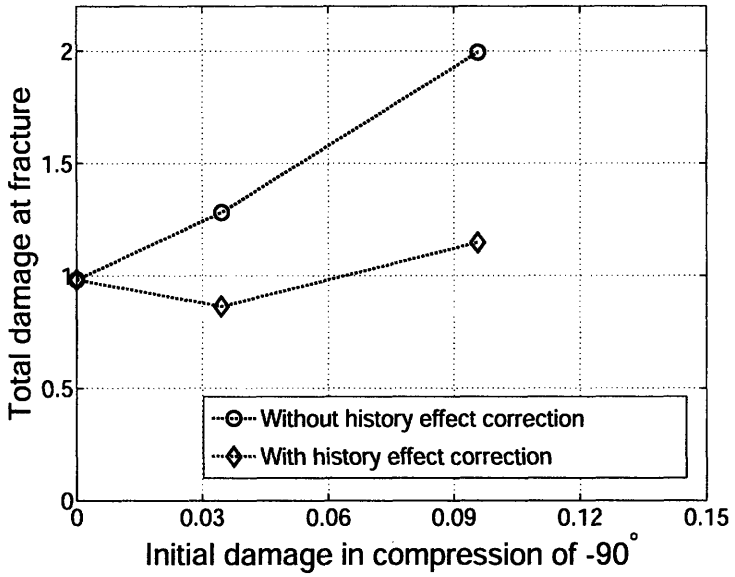

Fig. 7-67: Correction of the loading history effect on fracture, butterfly specimens of 1045 steel subjected to reverse loading of $-90° \rightarrow +90°$.

7.7.3 Tests on butterfly specimens: reverse loading of $-0° \rightarrow +0°$

Two tests of butterfly specimens under the reverse loading of $-0° \rightarrow +0°$ were conducted. During the tests, the total vertical force was kept at zero, and displacement control mode was used to the horizontal actuator. The two specimens after fracture is shown in Fig. 7-68. The measured horizontal force-displacement curves are shown in Fig. 7-69. A comparison of the force-displacement responses between simulations and experiments is also shown in Fig. 7-69. One can see the simulations agree well with the experimental results. This loading condition of $-0° \rightarrow +0°$ is a reversal shear loading. The fracture initiation sites are on the surface point in the center of the specimen.

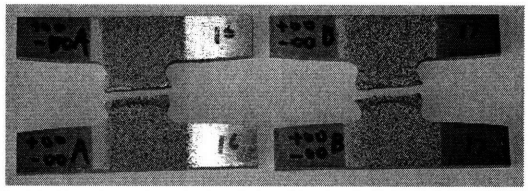

Fig. 7-68: Butterfly specimens subject to the reverse loading of $-0° \rightarrow +0°$.

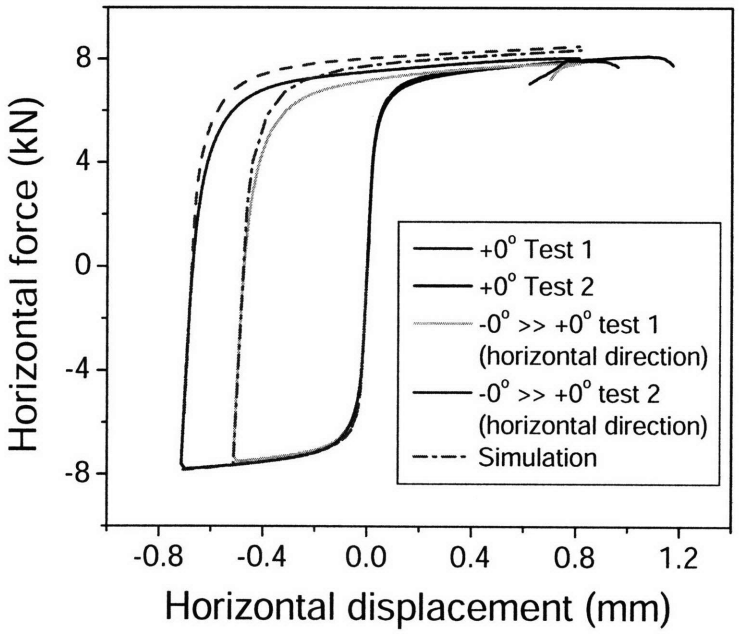

Fig. 7-69: Comparison of force-displacement curves under reverse loading of $(-00° \rightarrow +00°)$.

The calculated total damage at fracture of the fracture initiation points is illustrated in Fig. 7-70. The result under the monotonic loading of simple shear $(+0°)$ is also plotted for comparison. It is shown again that the proposed model with loading history correction well predicts the fractures under this type of reverse loading.

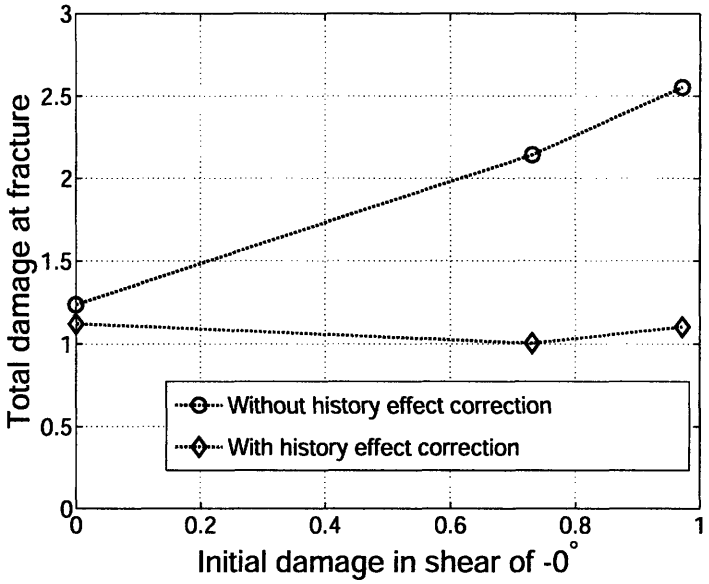

Fig. 7-70: Correction of the loading history effect on fracture, butterfly specimens of 1045 steel subjected to reverse loading of $-0° \rightarrow +0°$.

7.8 Discussion and conclusion

In the paper, a new form of ductile fracture model accounting for the loading history effect was proposed. As an extension to the conventional linear damage evolution assumption, two weighting functions were introduced to the calculation of damage indicator (D). One function, $g(\lambda)$, considers the non-linear damage evolution under proportional loading, the other function, $h(D, \mu)$, accounts for the effect of change in the loading directions. Test results with complicated (non-proportional) loading paths from the literatures were reviewed using the newly proposed ductile fracture model. These tests includes two-stage-tension test, compression-tension test and torsion-tension test.

A round of comprehensive fracture tests on 1045 steel was conducted to validate the proposed fracture model. Firstly, the plasticity model of the material was calibrated using compression-tension tests. Following the procedure proposed by Khan and Jackson (1999), the parameters of the kinematic hardening and isotropic hardening of the material were determined directly from the experiments. Together with iterative run in numerical simulations, the plasticity model with combined kinematic/isotropic hardening was calibrated. Secondly, the 3D fracture locus of 1045 steel was calibrated by two methods. One method

made use of the "classical" specimens, including smooth/notched round bars, flat grooved specimens, and tubular specimens. In the other method, the butterfly specimens tested in a biaxial testing machine were used. It is found that the fracture locus calibrated from butterfly specimen is higher than from "classical" specimens due to the mesh size effect. The shape of the two fracture loci are similar. Each fracture locus was to be used for the studying of loading history effect using the corresponding method. Thirdly, the proposed correction of loading history effect is studied and calibrated by three groups of tests: two-stage-tension test, compression-tension test and torsion-tension test. Two opposite trends of loading history effect on ductile fracture were observed. Changes in loading direction can either decrease the material ductile (for example, 2024-T351 aluminum and OFHC copper) or increase the material ductility (for example 1045 steel). Using the calibrated fracture locus and the loading history correction, the proposed model predicts very well the fractures of butterfly specimens under complex loading conditions.

A more comprehensive study on the 3D fracture locus and the loading history effect on ductile fracture are needed to further confirm the present findings. More work should be done in the future on the following issue.

- *Mesh size effect.* It is hard to get a convergent result on equivalent strain at the fracture initiation site if larger deformations are involved. Larger mesh size effect is observed for materials with less strain hardening.

- *Weighting function* $g(\lambda)$. Although the weighting function $g(\lambda)$ is found to be very important to predict necking under complex loading paths (Bai and Wierzbicki, 2007c), it has almost no effect on the fracture prediction under complex loading conditions for materials tested so far. For the consistency of theory, this term is retained in the present model. More two-stage-tension tests on other materials should be done in the future.

- *Plasticity model.* An significant asymmetry between the tensile tests and compression tests for 1045 steel was observed for initial yield and subsequent hardening, which is not accounted for the present method. A more complicated plasticity model with strain dependent coefficients should be explored in the future.

- *Anisotropic plasticity and fracture.* The present model was built for isotropic materials. For anisotropic materials, both and plasticity and fracture model should be modified.

Chapter 8

Application Example: Fracture of Prismatic Aluminum Tubes under Reverse Straining

In this chapter, the newly developed fracture theory was applied to predict initiation of fracture in prismatic square aluminum tubes subjected to crush loading. Compression tests were performed on small columns with the width to thickness ratio covering the range 10-30. First fracture was observed at different locations depending on the thickness of the tube. Analytical solution shows that there exists strain reversal in the bucking process of a prismatic square tube. The numerically predicted sites of fracture initiation and the displacement corresponding to formation of crack agreed very well with test results. It is concluded that the effect of loading history must be included in the application to the failure analysis of structural components, where large pre-compression is expected.

8.1 Introduction

In an axially compressed prismatic tube, the strain rate ratio changes sign from negative to positive. Wierzbicki and Huang (1992) proved through a simple analytical model that the strain in the transverse direction (perpendicular to the axis of the tube) changes from compression to tension. A thorough numerical study on the strain path in several critical points of a square aluminum tube was performed by Wierzbicki and Thomas (1993); Dyrli (1999). Dyrli showed that for example in a $3mm$ extruded aluminum tube, the minor principal logarithmic strain (in the transverse direction) reached -0.2 and then changes into

a positive value of +0.04. He found that the most strained point in the tube is along the corner line. The isotropic plasticity theory was used in his simulation and no attempts were made to predict fracture.

The objective of this chapter is to revisit the problem of axial compression of tubes and predict the location of the fracture site and the amount of crosshead displacement corresponding to first fracture. This is achieved through a comprehensive experimental, analytical, and numerical approach. Small size square tubes were manufactured by the machining process from a block of 2024-T351 aluminum alloy. This was the same type of material which was extensively calibrated for plasticity and fracture by the same team, see for example Bao (2003); Bao and Wierzbicki (2004a); Bao and Treitler (2004); Bao and Wierzbicki (2004b, 2005). The reported test results are used to calibrate the fracture model proposed in the present thesis. Because of high manufacturing costs, only four specimens with same width and length were made, each with a different thickness. Compression tests were run up to the point of crack formation and the load-displacement response as well as the displacement to fracture was recorded. A simple analytical model was also developed to demonstrate qualitatively the existence of strain reversal in the transverse direction.

A detailed numerical model was constructed to determine histories of components and invariants of the stress and strain tensor during the loading process. The effects of the mesh size and the number of integration points on the convergence of the solution were thoroughly investigated, which is reported in Bai et al. (2006a). A material user subroutine of the present model was built into Abaqus/Explicit for shell elements, and it was used to the simulations of fracture initiation. It was found that the location of fracture initiation and the corresponding tube shortening were predicted with great accuracy as compared to test results. The history effect was more evident in thin rather than thick tubes.

8.2 Experimental program

The material chosen for this investigation is the 2024-T351 aluminum alloy studied by Bao (2003). Four aluminum tubes were machined from the block of Al 2024-T351. This particular material was chosen because its fracture and plastic properties were determined in previous research of the present investigating team (Bao, 2003; Bao and Wierzbicki, 2004a; Bao and Treitler, 2004; Bao and Wierzbicki, 2004b, 2005). The tubes were prismatic with a square cross section, $b \times b = 30 \times 30mm$ and four different thickness. Only one tube was machined for each thickness because of high manufacturing cost. The geometrical parameters of the

virgin tubes are gathered in Table 8.1. Moderate thickness variations were detected in tube samples. It was too difficult to map those change in the FE model. Instead, nominal thickness was used which is given in Table 8.1. Thickness variability is a rather random process over the length and circumference of tubes. It is believed that this effect cancels out as far as the mean crushing force is concerned. Of course, the local strain may be affected more strongly. To give the reader an idea about the degree of thickness uniformity, Table 8.1 provides the values of the measured thicknesses for each flange separately at both ends of the tube.

Table 8.1: Initial geometry of the tubes and thickness variation)

Label	L(mm)	$b \times b$ (mm)	t ** (mm)	τ_1 ** (mm)	τ_2 (mm)	τ_3 (mm)	τ_4 (mm)
Tube A	120	30 × 30	1.0	0.96/0.83*	0.96/1.0	1.06/1.06	0.9/0.9
Tube B	120	30 × 30	1.5	1.43/1.50	1.54/1.55	1.58/1.46	1.45/1.49
Tube C	120	30 × 30	2.0	1.95/2.0	1.97/2.10	1.99/2.05	1.96/2.06
Tube D	120	30 × 30	3.0	3.0/3.02	2.96/3.04	3.0/3.04	3.02/3.05

* *0.96/0.83 means the two thicknesses measured at both ends of a tube flange.*

** *t denotes the nominal thickness. τ_1, τ_2, τ_3, and τ_4 denote the actual thickness of sidewalls*

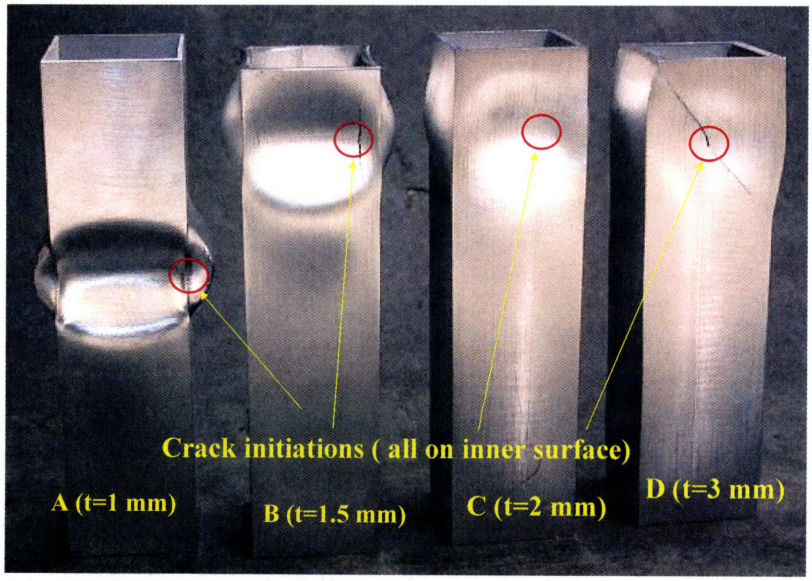

Fig. 8-1: Photographs of the partially crushed tubes at the stage of formation of first cracks.

The tubes were placed between loading platens of the MTS universal 200kN screw driven testing machine. The loading was applied quasi-statically at the cross head relative velocity of 1.2 mm/min. The lower and upper ends of the tubes were unconstrained except of friction. Recorded in the test was the force-displacement response. The tube was compressed until first cracks were detected by the visual inspection and the test was interrupted in this stage. The crack formation was also associated with a sudden drop of the tube resistance in all four cases. However, the location of the fracture initiation site was different between the tubes with different thicknesses. Photographs of the crushed specimens are shown in Fig. 8-1, where the fracture initiation sites are indicated. Crack can easily be seen for tubes B and D on the outer surface. In fact, fracture initiated on the inner surface in all four cases. A close up view of internal cracks in tubes A and C are shown in Fig. 8-2.

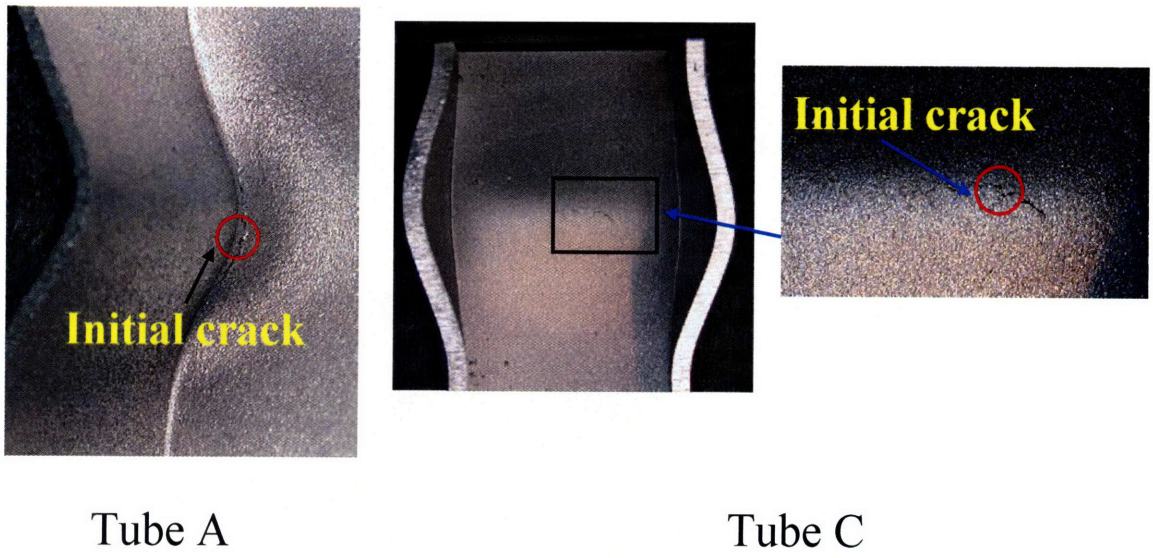

Fig. 8-2: A close up view of cracks on the inner surface in tubes A and C.

The load-displacement response of four tubes is plotted in Fig. 8-3. The experimentally found instants of fracture are indicated by circles in Fig. 8-3. Note that tube C cracked earlier than expected contrary to the trend of the remaining tubes. This was probably due to some imperfection introduced during machining process or even there were some flaws in the bulk material.

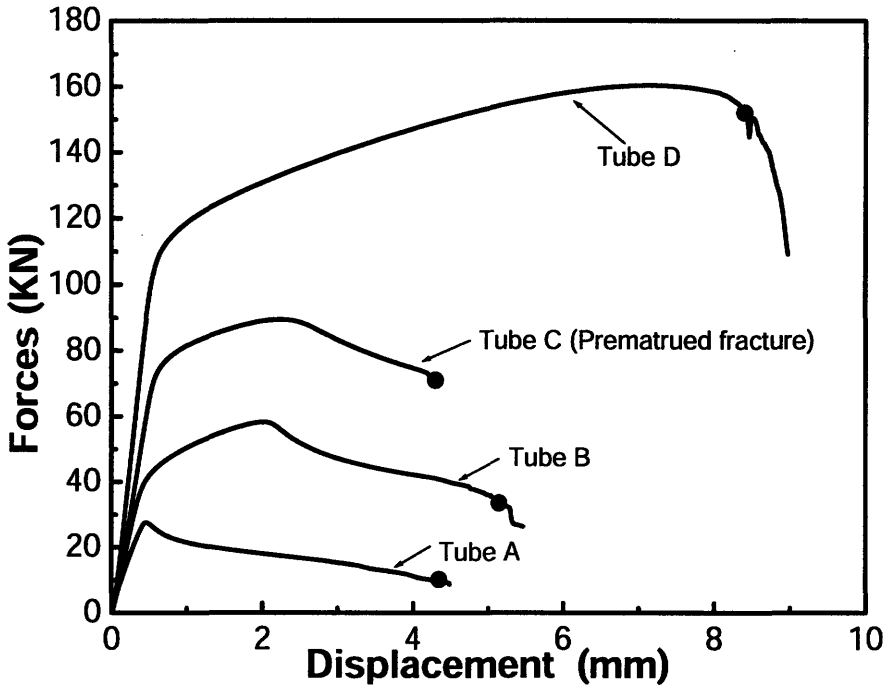

Fig. 8-3: Force-displacement responses in experiment. The observed displacements to fracture initiation are marked with circles.

In order to check the accuracy of numerical simulation of the folding process, three parameters characterizing the shape of the deformed tube were measured in all four cases, see Table 8.2. Upon compression, the initial square shape is converted into a rectangular shape in the symmetry plane of the center of the fold. The longer (outside) width is denoted by H while the shorter (inner) width is denoted by B, see Fig. 8-4. The wavelength of the fold is denoted by W.

Table 8.2: Parameters characterizing partially crushed tubes (refer to Fig. 8-4)

Label	t(mm)	b/t	W (mm)	H (mm)	B (mm)
Tube A	1.0	30	21.5	41.5	16.5
Tube B	1.5	20	22	38	17.4
Tube C	2.0	15	24	37.7	19
Tube D	3.0	10	28/23*	38	20

* *The deformation of tube D is asymmetric.*

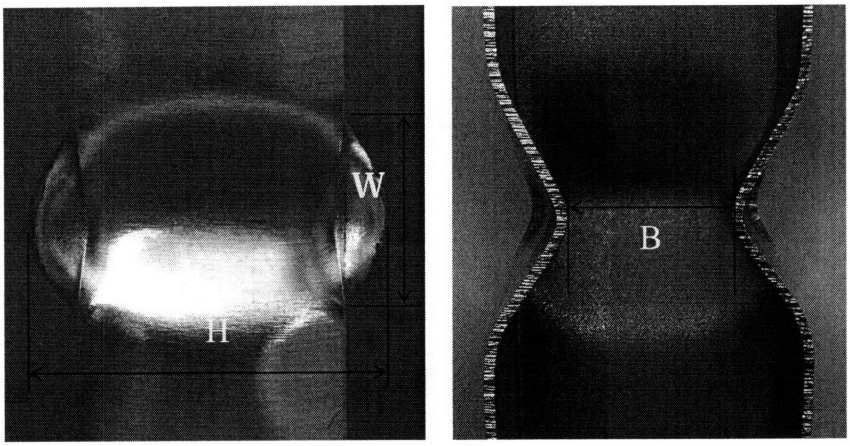

Fig. 8-4: Definition of parameters W, H and B.

It was difficult to determine experimentally the point of fracture in tube D. The experiment was stopped as soon as a crack appeared on the external surface. The fracture process was very fast and the slant crack has already traveled a long way from the center to the edges before the test was interrupted. The post-test examination of the specimen revealed that the crack is even wider in the inner surface. Clearly, fracture must have started much earlier, presumably, soon after the point of maximum load. It can be concluded that it is not possible to pin-point initiation of fracture in the present type of tests without putting a video camera inside the tube. However, the large difference in the force magnitude corresponds to only small difference (0.5 mm) in the crosshead displacement. In numerical simulation, it is the displacement to fracture that is predicted, so that the error in locating precisely the experimental point of fracture initiation will be of an order of less than 5%.

8.3 Analytical solution

Let us consider a simple computational model consisting of a system of stationary hinge lines and rigidly rotating elements (Wierzbicki and Huang, 1992), see Fig. 8-5. The distance from the tip of the diagonal hinge line to the initial corner line is denoted by ξ , which is treated as a parameter of the process. In the order to visualize the amount of the transverse stretching in the side flange near the corner line, a cut is made along the corner line. Because all triangular, rectangular, and trapezoidal elements are assumed to be rigid, a gap is created upon compression of the tube, Fig. 8-5b.

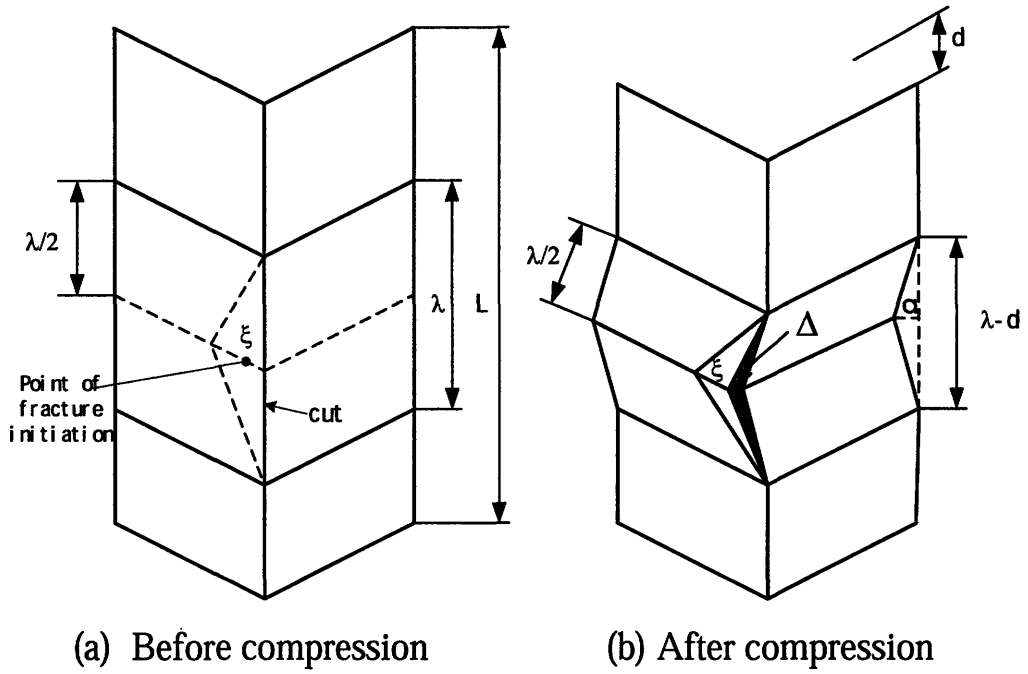

Fig. 8-5: A simple folding model with stationary plastic hinges and rotating planar elements. The shaded area represents the amount of relative transverse in plane displacement in the area adjacent to the corner line.

The average transverse strain ε_{av} can be calculated from a simple geometrical construction, and is given by

$$\varepsilon_{av} = \frac{\Delta}{\lambda/2} = \pm\frac{a}{\lambda/2}\sqrt{2 - \frac{4\frac{\xi}{\lambda/2}\frac{a}{\lambda/2}}{\left(\frac{\xi}{\lambda/2}\right)^2 + \left(\frac{a}{\lambda/2}\right)^2}}, \tag{8.1}$$

where, $\frac{a}{\lambda/2} = \sqrt{1-\left(1-\frac{d}{\lambda}\right)^2}$. Here, Δ is the maximum amplitude of the gap, a is the amplitude of the transverse displacement, and d is the shortening of the tube. The sign of the strain depends on the interplay of the geometrical parameters.

If $a < \xi$, then ε_{av} is negative (compressive average strain). If $a = \xi$, then ε_{av} is zero (zero average strain). If $a > \xi$, then ε_{av} is positive, (tensile average strain). Because the transverse deflection a is the function of the crush distance d, there will be a change from compression to tension.

In the case of tube A, the experimentally measured location of diagonal hinge $\frac{\xi}{\lambda/2}$. The

plot of the average strain vs. the crosshead displacement is shown in Fig. 8-6 by a solid line. The dash lines in the same figure are the numerically obtained history of the local strain at the location fracture initiation (Bai et al., 2006a). It is seen that the magnitude of strain predicted by the simple model (0.18) is close to the more exact numerical value (0.17). Clearly, the whole history diagram is shifted between the analysis and simulation because in the former case an average strain is calculated while in the latter plot is the local principal strain.

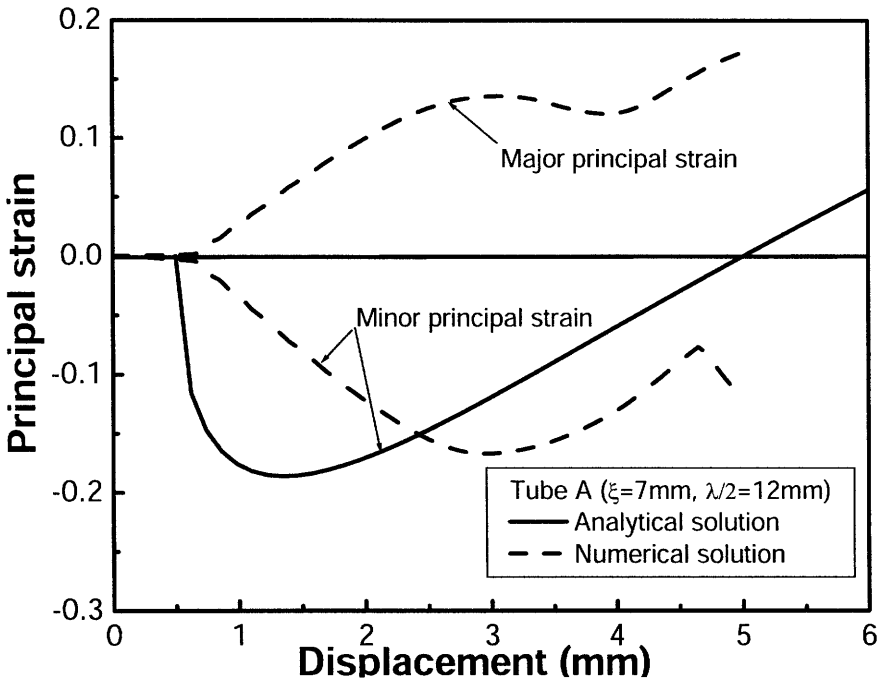

Fig. 8-6: Evolution of strain obtained from numerical and analytical analysis.

In conclusion, a simple analytical model gives fairly good idea about the magnitude of stresses, strains, and forces in the initial phase of tube crushing. The model proves conclusively the existence of the strain reversal in crushed tubes.

8.4 Material model of plasticity and fracture

The plasticity model of 2024-T351 aluminum alloy with combined kinematic/isotropic hardening was calibrated by Bao (2003); Bao and Treitler (2004). It has also been shown that

there are no pressure dependence and Lode angle dependence on plasticity of this material. Therefore, a list of the parameters of the proposed plasticity model is shown in Table 8.3.

The fracture tests reported by Bao (2003) on the 2024-T351 aluminum alloy were reviewed by the present author using the proposed six parameter empirical fracture locus, see Section 3.6.1. The calibrated fracture locus is shown in Fig. 3-15. Compression-tension tests were also reported by Bao and Treitler (2004). It was found that the pre-compression decrease the material ductility, which is different from that of 1045 steel, see the Fig. 7-52 in Section 7.6.2. The test results of compression-tension on notched round bars reported by Bao and Treitler (2004) are revisited using the proposed fracture model with loading history effect correction. The calibrated parameters of the fracture model is listed in Table 8.4. It is also assumed that there is a cut-off region in the stress state plane, see Section 5.6.7. A value of $c_{1-cutoff} = 0.57$ is assumed and used in the simulation. The calibrated material model of plasticity and fracture will be used to the finite element simulations in next section.

Table 8.3: Calibrated parameters of the plasticity model of 2024-T351 aluminum alloy

E	ν	σ_o	σ_{st}	b	C	Γ
7.463e+4MPa	0.3	300 MPa	220 MPa	14	750 MPa	10
c_η	η_o	c_θ^s	c_θ^t	c_θ^c	m	
0.0	0.333	1.0	1.0	1.0	6	

Table 8.4: Calibrated parameters of the fracture model of 2024-T351 aluminum alloy

D_1	D_2	D_3	D_4	D_5	D_6
0.5862	1.3576	0.2170	0.0400	0.4859	0.700
c_g	c_h	β_1	β_2	k	$c_{1-cutoff}$
0.0001	1.3	2.0	2.0	1	0.57

8.5 Finite element simulation

Finite element simulations were performed for all four tubes using ABAQUS/Explicit with the built material user subroutine. Four-node shell elements with reduced integration were

used. In numerical simulations the bottom edge was fixed in all directions, and the top side was also fixed except for the free translation in the vertical direction. A constant prescribed compression velocity was applied at the top edge. Study on some numerical aspects, such as mesh type, mesh size and number of integration points through thickness, can be found in Bai et al. (2006a) where the program LS-DYNA was used. A comparison of force-displacement curves between experiment and numerical simulation in shown in Fig. 8-7, in which one can see that the force-displacement curves are well simulated in the models. It is also found that the predicted displacements to fracture initiation agree well with the experimental ones. Without the correction of loading history effect, large errors are expected, which is summarized in Table 6 of Bai et al. (2006a). A comparison of deformations and fracture initiations of three tubes (A, B and D) are shown in Figs. 8-8, 8-9 and 8-10. (Tube C is included because of pre-matured fracture.) The contour plots in these three figures show the distribution of damage indicate D at the final stages of experiments (the experimentally controlled fracture initiation stages). The fractured elements were deleted and marked with circles.

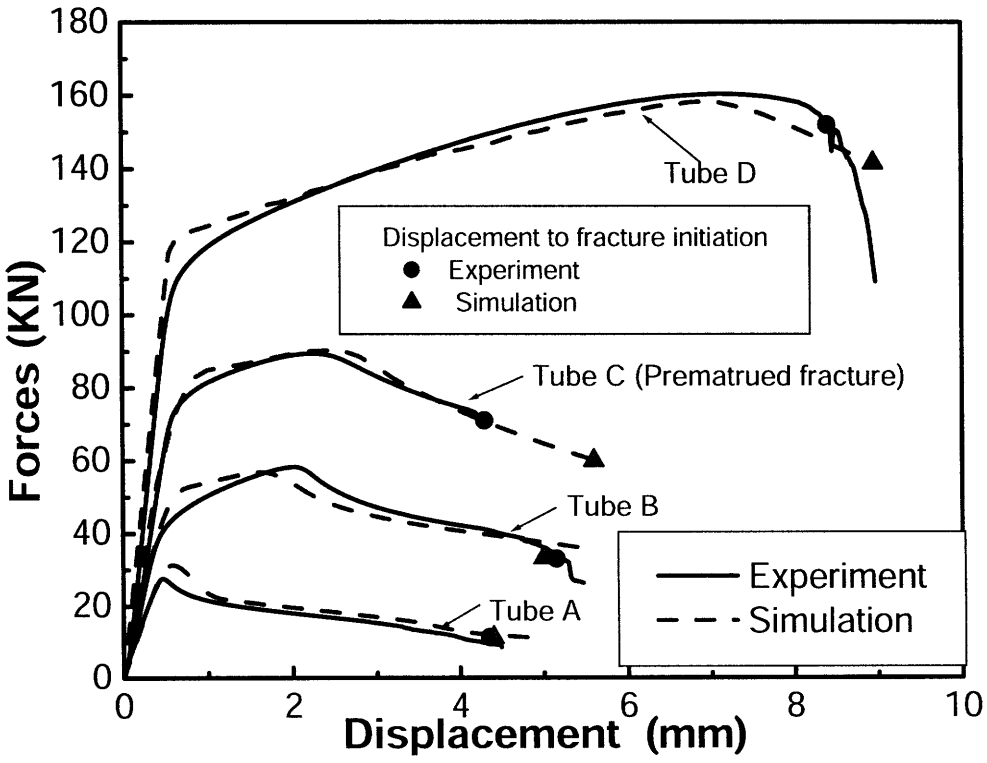

Fig. 8-7: Comparison of force-displacement responses for all four tubes.

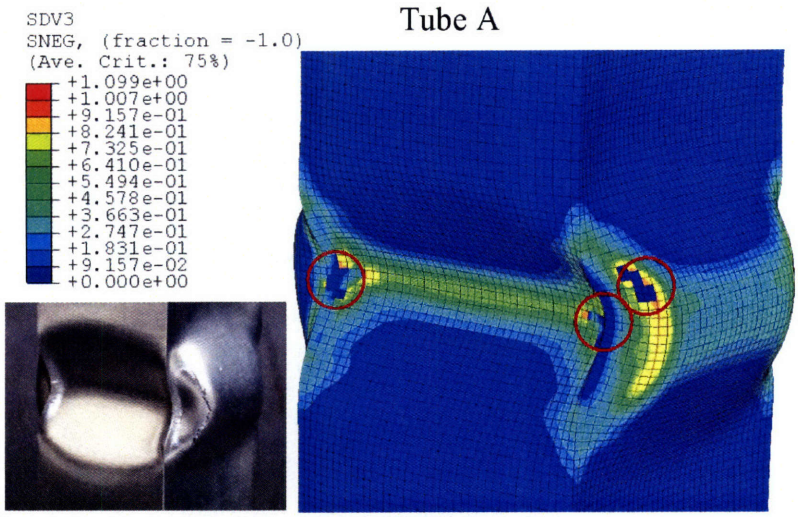

Fig. 8-8: Comparison of predicted deformation and fracture initiation for Tube A. The contour plot shows the distribution of the damage indicator D.

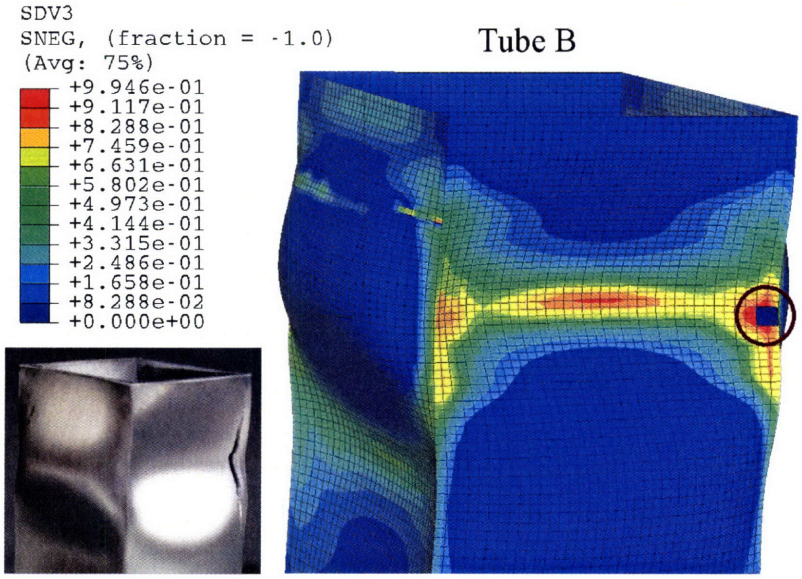

Fig. 8-9: Comparison of predicted deformation and fracture initiation for Tube B. The contour plot shows the distribution of the damage indicator D.

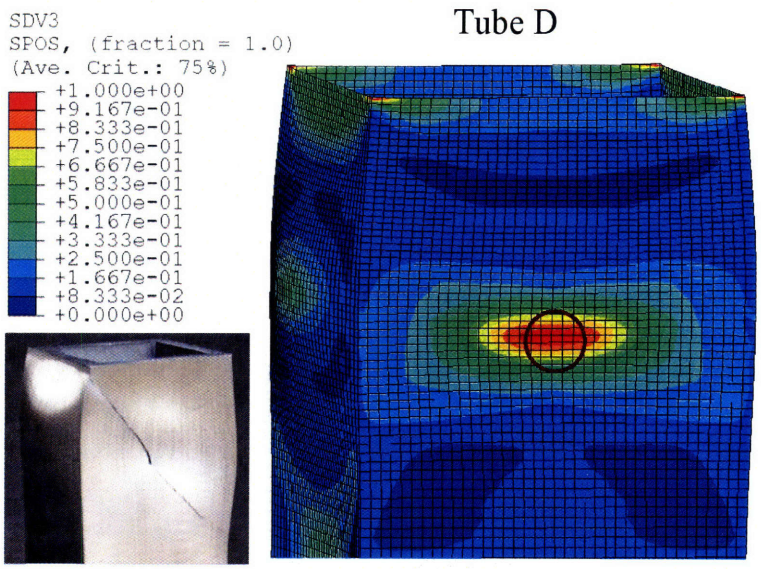

Fig. 8-10: Comparison of predicted deformation and fracture initiation for Tube D. The contour plot shows the distribution of the damage indicator D.

Compared with the pictures taken at the experiments, one can see that good correlations were obtained on the experimentally observed sites and numerically predicted sites of fracture initiation. The point of fracture initiation was found to be strongly dependent on the width to thickness of the column. It is located at the center of the flange only in the thickest column. For thin tubes, it is moving towards the corner lines of the tubes. The theory also predicts that fracture starts on the inner surface mainly because the membrane and bending induced strains are acting in the same direction.

8.6 Discussion and conclusion

In this chapter, the newly developed fracture theory was successfully applied to predict initiation of fracture in prismatic square aluminum tubes subjected to crush loading. Both analytical solution and numerical simulation show that there exists strain reversal in the compressed prismatic tubes. Complete experiments were conducted to study the fractures on small tubes with the width to thickness ratio covering the range 10-30. First fractures were observed at different locations depending on the thickness of the tubes. The calibrated ductile fracture model with loading history effect correction is shown to correctly predict

both the displacements to fracture and the fracture initiation sites in the crushed tubes.

It is found that the effect of loading history on fracture of structural components, such as crushed box columns is weaker than the calibration test (compression-tension test) would suggest. It is seen that the effect of loading history is different for different tube thickness. The amount of strain reversal not only depends on the tube thickness but also on the location of fracture (edges vs. center). Therefore, it is difficult a priori to tell where this effect is stronger. A unified approach was used for all tubes, but it is found that a strong history effect shows up only for one tube (Tube A), in which there is a large amount of pre-compression followed by tension. The effect of loading history appears not to be so important for thick tubes, for which the amount of pre-compression is much smaller so that the effect of loading history is negligible. However, there are many other practical applications where there is considerable strain reversal during loading process. An extreme example of such situation is the high velocity impact fracture of thick plates. The material point in the vicinity of the projectile/target interface undergoes large compressive stresses followed by shear and finally leading to tension. The developed fracture model will be used to predict such complex fractures in the future.

THIS PAGE INTENTIONALLY LEFT BLANK

Chapter 9

Conclusion and future studies

9.1 Summary of main results

Study on the Lode angle effect on plasticity and fracture: The stress distribution inside the neck of a flat-grooved plane strain specimen was analyzed. A Bridgman-like stress triaxiality formula was derived for the flat-grooved plane strain specimen. This formula was further corroborated using finite element simulations. In addition to the smooth and notched round bars, the flat-grooved specimens were used to study the Lode angle (or the third deviatoric stress invariant) effect on both plasticity and fracture. Experimental results on 2024-T351 aluminum alloy, 1045 steel and DH36 steel provided sufficient data for the validation. It is interesting to note that the Lode angle effect on plasticity and fracture are complementary each other, which means that if there is a stronger Lode angle dependence on plasticity, then there will be less dependence on fracture, and *visa versa.*

Asymmetric plasticity and fracture model: A generalized asymmetric plasticity model for isotropic materials with both pressure and Lode angle dependence was proposed. Calibration method of the plasticity model was discussed in detail. Test results on 2024-T351 aluminum alloy confirmed the proposed plasticity model. Similarly, a generalized asymmetric 3D empirical fracture locus with *six free parameters* was proposed. The proposed fracture locus, which depends on both the stress triaxiality (or pressure) and the Lode angle parameter, was calibrated using two types of methods: classical specimens under uniaxial testing, and butterfly specimens under biaxial testing. Experimental results on 2024-T351 aluminum alloy and A710 steel validated the proposed 3D fracture locus.

Design of butterfly specimen for fracture testing: A new type of specimen with a butterfly shape was designed and optimized. A wide range of stress state (stress triaxiality

and Lode angle parameter) can be generated through different combination of tension, shear and compression. Another important advantage of the butterfly specimen is that fracture always initiates in the center of the specimen, rather than at the edges. The butterfly specimens were mounted into a customer-made universal biaxial testing device (UBTD, see Mohr (2003); Mohr and Doyoyo (2004)), then loaded in the MTS uniaxial testing machine. The specimen was also tested under the newly installed INSTRON biaxial testing machine. This type of specimen has been successfully applied to calibrate five types of material for fracture: A710 steel, 1045 steel, cast aluminum (Mae et al., 2007), tungsten alloy (Bai et al., 2006c), and a hot form martensitic steel from Volkswagen.

Application of Mohr-Coulomb criterion to ductile fracture: The Mohr-Coulomb (M-C) criterion was shown to be applicable to ductile fracture, even though the M-C criterion was originally developed for studying failure of brittle materials. Using the proposed generalized plasticity model, the M-C criterion was transformed from the stress space (τ^f, σ_n) to the mixed space of strain and stress invariants $(\bar{\varepsilon}_f, \eta, \bar{\theta})$ under the assumption of proportional loading. It was found that the transformed M-C criterion exhibits both stress triaxiality and Lode angle dependence on equivalent strain to fracture. Parametric study revealed the relationship between plasticity and fracture, which confirmed that the M-C criterion is physically correct for ductile fracture prediction. The fracture tests reported by Bao (2003) and Bao and Wierzbicki (2004a) on 2024-T351 aluminum alloy were used to check the model. Calibrated using just two tests, the model predicted the remaining nine tests with good accuracy. Since there are only *two free parameters* in the phenomenological M-C model, it has a great potential to be used as an engineering tool for predicting ductile fracture.

Loading history effect on forming limit diagram (FLD): A new concept of forming severity was introduced to study the loading history effect on necking. The FLD was transformed to the space of equivalent strain to neck and the Lode angle parameter $(\bar{\varepsilon}_n, \bar{\theta})$, which defines the *necking locus* of a material under proportional loading conditions. Similar to the idea of cumulative damage model (CDM) in ductile fracture mechanics, the prediction of necking was modeled in an incremental form with a non-linear accumulation rule of forming severity. Experimental data from literatures were used to check the proposed concept of necking prediction. Calibrated from only one test with non-proportional loading condition, the model is able to predict the remaining tests of complex loading paths with good accuracy.

Loading history effect on ductile fracture: The loading history on ductile fracture was extensively explored. First, the combined kinematic/isotropic hardening plasticity model

was calibrated from the compression-tension tests on notched round bar. Secondly, the ductile fracture locus was calibrated using either "classical" specimens or the butterfly specimens in the INSTRON biaxial testing machine. Then, several types of tests with complex loading histories were designed and performed to study the loading history effect on ductile fracture. Those tests included two-stage-tension, compression-tension, torsion-tension tests and the tests on butterfly specimens with programmed complex loading histories. A new parameter, which accounts for the accumulated direction difference between back stress tensor and current stress tensor, was introduced to described the non-proportionality of a loading path. A new form of ductile fracture model considering the loading history effect was proposed. Extensive experimental studies confirmed the proposed model.

Study on fractures in crushed prismatic tubes: Fracture of prismatic aluminum tubes under reverse straining was investigated. Crushed tests were performed for four tubes made of the same material but with different sidewall thicknesses. First fractures were observed at different locations depending on the thickness of the tubes. Analytical solution on the crushed prismatic tubes showed that there is strain reversal at the fracture initiation sites. Finite element models were built to simulate the crushing and buckling of tubes. Using the calibrated material ductile fracture model with loading history effect corrections, the proposed model was shown to be able to well predict the locations of the fracture initiation sites in crushed prismatic tubes and also the load and displacement to fracture.

9.2 Suggestions for future studies

Although comprehensive studies have been performed in the present thesis on the 3D fracture locus and the loading history effect on necking and ductile fracture, the following topics are suggested for future studies.

- *Mesh size effect.* It is difficult to get a convergent result on equivalent strain at the fracture initiation site if large deformations and deformation gradients are involved. Larger mesh size effect is observed for materials with less strain hardening, which develop local instability in a form of a neck.

- *Plasticity model.* A significant asymmetry between the tensile tests and compression tests for 1045 steel was observed for both initial yield and subsequent hardening (see Chapter 7), which is not accounted for by the present method. A more complicated plasticity model with strain dependent coefficients should be explored to consider the strength asymmetry introduced during strain hardening.

- *Anisotropic plasticity and fracture.* In the present studies, material isotropy is assumed. For anisotropic materials such as sheets, both and plasticity and fracture models should be extended or modified.

- *Element post failure behavior and fracture propagation.* It is commonly assumed that a fracture propagation consists of a series of fracture initiation. The current finite element codes use either element deletion or element split along the element edges for simulation of the fracture propagation. However, neither of them correctly simulate the boundary conditions after fracture initiation. It would be much more accurate to use element split along the crack plane inside a given element, which is called element post failure behavior. The energy release of fractured surfaces would also be considered here. This technology will significantly improve accuracy of the simulation of fracture propagation, and will partially remove the mesh size effect.

- *Specification for sheet materials.* The fracture theory and experimental methods developed in the present thesis is based on a general 3D stress state. For sheet material, which is widely used in industries, the present theory, especially the experimental methods, should be specified under plane stress condition.

Appendix A

Derivation of stress distribution inside the neck of a plane strain specimen

A.1 Transverse plane strain specimens

Following the derivation method of Bridgman (1952) on the round notched bars, the flat specimens with different grooves are analyzed. A flat grooved plane strain specimen with the free body diagram (FBD) of an arbitrary surface point P is shown in Fig. A-1. For real specimens, see Fig. 2-12.

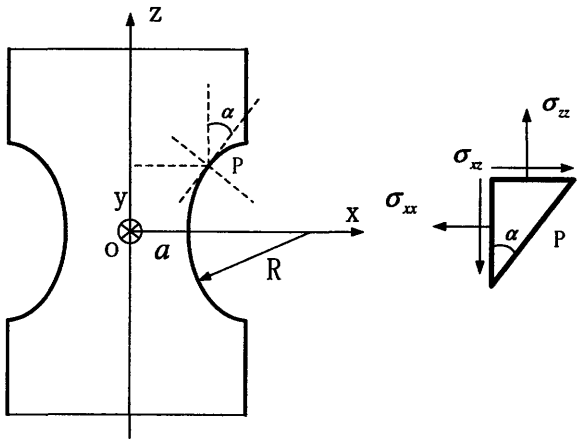

Fig. A-1: The cross-section of a flat grooved plane strain specimen and the free body diagram of its surface point on the notch

Firstly, the material is assumed to be rigid-perfect plastic. In the Cartesian coordinate system, the equations of equilibrium are

$$\sigma_{ij,j} = 0. \tag{A.1}$$

In plane strain condition (y direction), we have the following additional conditions.

$$\sigma_{xy} = \sigma_{yz} = 0, \ \frac{\partial}{\partial y}() = 0, \ and \ \epsilon_{yy} = 0. \tag{A.2}$$

Referring to Fig. A-1, the surface points on the notch is free from stress, from the force equilibrium in x direction and y direction we get that

$$\sigma_{xx} \cos\alpha = \sigma_{xz} \sin\alpha$$

$$\sigma_{xz} \cos\alpha = \sigma_{zz} \sin\alpha.$$

These two equations can be rewritten as

$$\sigma_{xx} = \sigma_{zz} \tan^2\alpha, \quad \sigma_{xz} = \sigma_{zz} \tan\alpha. \tag{A.3}$$

At the neck cross-section ($z = 0$), $\alpha = 0$ yields that

$$\sigma_{xx}\,|_{x=a} = 0, \quad \sigma_{xz}\,|_{z=0} = 0, \quad and \quad \frac{\partial \sigma_{zz}}{\partial z}\,|_{z=0} = 0, \tag{A.4}$$

where a denotes the half thickness of the specimen. From the plane strain condition ($\dot{\epsilon}_{yy} = 0$), one gets that

$$\sigma_{yy} = \frac{1}{2}(\sigma_{xx} + \sigma_{zz}), \tag{A.5}$$

Furthermore, we assume that all the material in the necking cross-section is in the plastic regime, and the von Mises yield condition is used.

$$\bar{\sigma} = \sqrt{\frac{1}{2}\left[(\sigma_{xx} - \sigma_{yy})^2 + (\sigma_{yy} - \sigma_{zz})^2 + (\sigma_{zz} - \sigma_{xx})^2\right]} \tag{A.6}$$

Here, the stress components are in the principal directions, and $\bar{\sigma}$ denotes the equivalent stress.

The problem is to find a stress system which meets the various requirements so far imposed. Inspection shows that we can have a simple solution which satisfies a certain

conditions. If we set that

$$\sigma_{zz} = \sigma_{xx} + \sigma_{zz}\,|_{x=a} = \sigma_{xx} + F, \tag{A.7}$$

where $F = \sigma_{zz}\,|_{x=a}$ denotes the stress in z direction of the surface point, then the von Mises plasticity condition (equ(A.6)) is satisfied. This is a simply stress system, in which the longitudinal tension is uniform for all the cross-section.

There is no direct method to solve all the above equations, but it is possible to find a solution valid in the immediate neighborhood of the necking cross-section by assuming the shape contour of the neck region. Fig. A-2 represents the state of affairs in a neighborhood close enough to the necking cross-section.

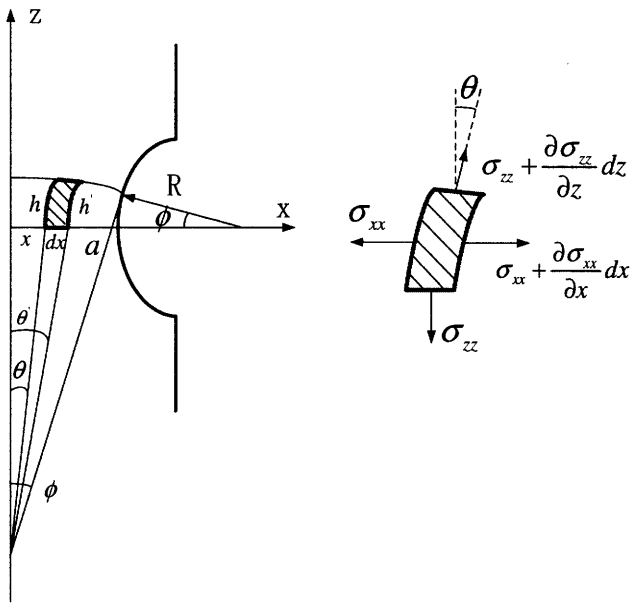

Fig. A-2: Diagram of the approximate stress analysis in the neighborhood of the neck of a plane strain specimen

From Eq. (A.3), one of the lines of principal stresses is normal to the notch surface. Also, on the central axis, the lines are normal to the axis. Therefore, it is reasonable to approximate the lines of principal stress by circles with centers on the axis, as shown in Fig. A-2. Through the point x perpendicular to the ox axis, there passes another family of lines of principal stress. It is assumed that this line is also a circle, and the notch circle of the specimen is also one of these lines. Taking a very small angle ϕ, the radius of the notch is R, and the radius of the circle is $R' = a/\phi$. From the geometry, it is noted that angle

$\angle OAB = \angle OCB = \phi$. Now, a small element, with unit width in y direction, bounded by x and $x + dx$, which are corresponding to axial plane angle θ and θ', is considered. From the geometry, one can get that

$$\begin{aligned} \theta &= \tfrac{x\phi}{a} \\ \theta' &= \tfrac{(x+dx)\phi}{a} = \tfrac{x\phi}{a} + \tfrac{dx\phi}{a}. \end{aligned} \tag{A.8}$$

The free body diagram of the shaded element is also shown in Fig. A-2. From the force equilibrium in x direction, we get that

$$\left(\sigma_{zz} + \frac{\partial \sigma_{zz}}{\partial z} dz\right) \sin\theta \cdot dx - \sigma_{xx} h + \left(\sigma_{xx} + \frac{\partial \sigma_{xx}}{\partial x} dx\right) h' = 0. \tag{A.9}$$

From the geometry, we have the following relation.

$$\begin{aligned} h &= R\phi + R'(\cos\theta - \cos\phi) \\ h' &= R\phi + R'\left(\cos\theta' - \cos\phi\right) \end{aligned} \tag{A.10}$$

Substitute Eq. (A.8) into Eq. (A.10). Since ϕ is very small, use the formula $\cos x = 1 - \frac{x^2}{2}$ to expand *cos* terms. Neglect all the high order terms, we can attain that

$$\begin{aligned} h &= \phi\left(R + \tfrac{a^2 - x^2}{2a}\right) \\ h' &= \phi\left(R + \tfrac{a^2 - x^2}{2a} - \tfrac{x}{a} dx\right). \end{aligned} \tag{A.11}$$

Substitute Eq. (A.11) into Eq. (A.9), use the formula $\sin x = x$ to expand *sin* term. Also, keep only the lowest terms, then we get the following equation.

$$\frac{d\sigma_{xx}}{dx} = -\frac{Fx}{a\left(R + \frac{a^2 - x^2}{2a}\right)} \tag{A.12}$$

Integrating Eq. (A.12), with the boundary condition in Eq. (A.4), we finally get the approximate solution for the stress component σ_{xx}.

$$\sigma_{xx} = F \ln\left(\frac{a^2 + 2aR - x^2}{2aR}\right) \tag{A.13}$$

Pluging Eq. (A.13) into Eq. (A.7) and Eq. (A.5), and using the boundary conditions, the

solution for the other two stress components is obtained.

$$\sigma_{zz} = F\left[1 + \ln\left(\frac{a^2 + 2aR - x^2}{2aR}\right)\right] \tag{A.14}$$

$$\sigma_{yy} = F\left[\frac{1}{2} + \ln\left(\frac{a^2 + 2aR - x^2}{2aR}\right)\right] \tag{A.15}$$

All the other shear stress components at the necking cross-section are zero, so the three formulas of normal stress components are also the principal stresses. We now consider the surface point on the notch ($x = a$, $z = 0$) at the neck. The stress state of this point is $\sigma_{xx} = 0$, $\sigma_{zz} = F$, and $\sigma_{yy} = F/2$. Use the von Mises yield condition in Eq. (A.6), then we can link F and the equivalent stress (von Mises stress) $\bar{\sigma}$.

$$F = \frac{2}{\sqrt{3}}\bar{\sigma}. \tag{A.16}$$

A.2 Summary of three types of specimens: axisymmetry, plane strain and plane stress

The stress analysis for the flat-grooved plane strain specimen (Section A.1) can also be extended to the case of plane stress specimens with two cutouts. Fig. A-3 shows three types of specimens with neck: notched round bars, flat-grooved plane strain specimens, and plane stress specimens with two cutouts. Listed in Table A.1 is a summary of stress components and stress state parameters in the center of these three types of specimens. The definitions of coordinate system for these three types of specimens are shown in Fig. A-3.

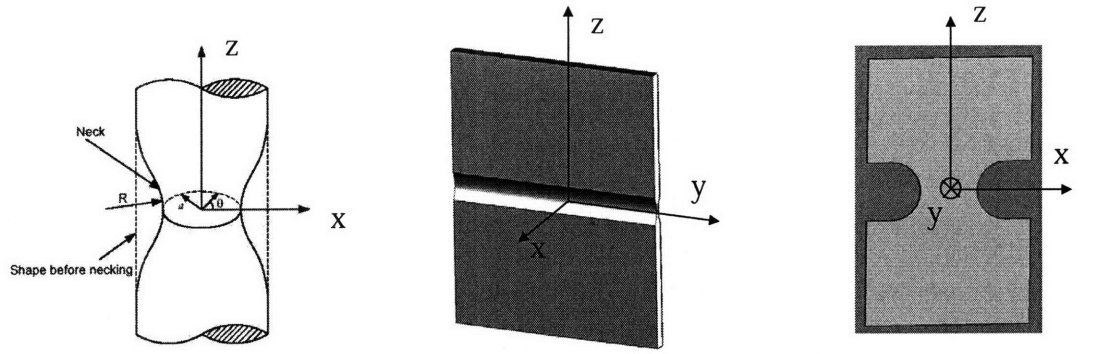

(a) Round notched bars (axial symmetry) (b) Flat-grooved specimens (plane strain) (c) Flat specimens with cutouts (plane stress)

Fig. A-3: Three types of specimens with necks

Table A.1: Stress distribution inside a neck of three types of specimens

	Axial symmetry	Plane strain	Plane stress
σ_{xx}	$\bar{\sigma}\ln\left(\frac{a^2+2aR-x^2}{2aR}\right)$	$\frac{2}{\sqrt{3}}\bar{\sigma}\ln\left(\frac{a^2+2aR-x^2}{2aR}\right)$	$F\ln\left(\frac{a^2+2aR-x^2}{2aR}\right)$
σ_{zz}	$\bar{\sigma}\left[1+\ln\left(\frac{a^2+2aR-x^2}{2aR}\right)\right]$	$\frac{2}{\sqrt{3}}\bar{\sigma}\left[1+\ln\left(\frac{a^2+2aR-x^2}{2aR}\right)\right]$	$F\left[1+\ln\left(\frac{a^2+2aR-x^2}{2aR}\right)\right]$
σ_{yy}	$\bar{\sigma}\ln\left(\frac{a^2+2aR-x^2}{2aR}\right)$	$\frac{2}{\sqrt{3}}\bar{\sigma}\left[\frac{1}{2}+\ln\left(\frac{a^2+2aR-x^2}{2aR}\right)\right]$	0
$\eta(x=0)$*	$1/3+\Lambda$	$\sqrt{3}/3\,[1+2\Lambda]$	$\frac{1+2\Lambda}{3\sqrt{\Lambda^2+\Lambda+1}}$
$\xi(x=0)$*	1	0	$\frac{(\Lambda-1)(-2\Lambda-1)(\Lambda+2)}{2(\Lambda^2+\Lambda+1)^{3/2}}$
$\bar{\epsilon}_f$	$2\ln(a_0/a_f)$	$\frac{2}{\sqrt{3}}\ln(t_0/t_f)$	optical measurement

* Where $\Lambda=\ln[1+a/(2R)]$. Relationship between ξ and $\bar{\theta}$ can be found in Eq. (2.8).

Bibliography

ABAQUS User's Manual, Version 6.5, Hilbbit, Karlsson and Sorensen Inc., 2005.

P. M. A. Areias and T. Belytschko. Analysis of three-dimensional crack initiation and propagation using the extended finite element method. *International Journal for Numerical Methods in Engineering*, 63:760–788, 2005.

P. Armstrong and C. Frederick. A mathematical representation of the multiaxial bauschinger effect, g.e.g.b. report rd/b/n 731. 1966.

A. G. Atkins and Y. W. Mai. Elastic and plastic fracture. *Chichester:Ellis Horwood*, 1985.

Y. Bai and T. Wierzbicki. A new model of metal plasticity and fracture with pressure and lode dependence. *International Journal of Plasticity*, Accepted, 2007a.

Y. Bai and T. Wierzbicki. Application of mohr-coulomb criterion to ductile fracture. *Submitted for publication*, 2007b.

Y. Bai and T. Wierzbicki. Forming severity concept for predicting sheet necking under complex loading histories. *To be submitted for publication*, 2007c.

Y. Bai, Y. Bao, and T. Wierzbicki. Fracture of prismatic aluminum tubes under reverse straining. *International Journal of Impact Engineering*, 32(5):671–701, May 2006a. URL `http://www.sciencedirect.com/science/article/B6V3K-4GPW3G9-1/2/bdc524839023abe1b0c23adb1e1b5ba3`.

Y. Bai, X. Teng, and T. Wierzbicki. Study on the effect of the third stress invariant on ductile fracture, report 151. Technical report, Impact and Crashworthiness Laboratory, Massachusetts Institute of Technology, Cambridge, MA, 2006b.

Y. Bai, C. Walters, and T. Wierzbicki. Fracture of tungsten alloy under combined loading, report 156. Technical report, Impact and Crashworthiness Laboratory, Massachusetts Institute of Technology, Cambridge, MA, 2006c.

Y. Bai, X. Teng, and T. Wierzbicki. Derivation and application of stress triaxiality formula for plane strain fracture testing. *Presented at ASME conference of Applied Mechanics of Materials, Austin, TX*, June 3-7, 2007.

Y. Bao. *Prediction of ductile crack formation in uncracked bodies.* PhD thesis, Massachusetts Institute of Technology, 2003.

Y. Bao and R. Treitler. Ductile crack formation on notched al2024-t351 bars under compression-tension loading. *Materials Science and Engineering A*, 384(1-2):385–394, Oct. 2004. URL http://www.sciencedirect.com/science/article/B6TXD-4D4VHHJ-8/2/56c0b400039774e5f859d3acfa0e5906.

Y. Bao and T. Wierzbicki. On fracture locus in the equivalent strain and stress triaxiality space. *International Journal of Mechanical Sciences*, 46(1):81–98, Jan. 2004a. URL http://www.sciencedirect.com/science/article/B6V49-4BYR2P8-1/2/2c3ad89a1f17ea9e18fd57c7117c1cb1.

Y. Bao and T. Wierzbicki. A comparive study on various ductile crack formation criteria. *Journal of Engineering Materials and Technology*, 126:314–324, 2004b.

Y. Bao and T. Wierzbicki. On the cut-off value of negative triaxiality for fracture. *Engineering Fracture Mechanics*, 72(7):1049–1069, May 2005. URL http://www.sciencedirect.com/science/article/B6V2R-4DS6RB2-3/2/13abd4e661a040fd1f99880377331529.

Y. Bao, Y. Bai, and T. Wierzbicki. Calibration of a710 steel for fracture, report 135. Technical report, Impact and Crashworthiness Laboratory, Massachusetts Institute of Technology, Cambridge, MA, 2004.

J. Bardet. Lode dependences for isotropic pressure-sensitive elastoplastic materials. *Journal of Applied Mechanics, Transactions ASME*, 57(3):498–506, 1990. ISSN 0021-8936.

F. Barlat, R. C. Becker, Y. Hayashida, Y. Maeda, M. Yanagawa, K. Chung, J. C. Brem, D. J. Lege, K. Matsui, S. J. Murtha, and S. Hattori. Yielding description for solution strengthened aluminum alloys. *International Journal of Plasticity*, 13(4):385–401, 1997. URL http://www.sciencedirect.com/science/article/B6TWX-3SP7T58-5/2/e7b2047d417bee7db1170cc3fcdbc28c.

F. Barlat, H. Aretz, J. Yoon, M. Karabin, J. Brem, and R. Dick. Linear transfomation-based anisotropic yield functions. *International Journal of Plasticity*, 21(5):1009–1039, May 2005. URL http://www.sciencedirect.com/science/article/B6TWX-4D9D7KY-1/2/8adeeb70a296d70fe61f8c9b7cd514fa.

I. Barsoum. *Ductile failure and rupture mechanisms in combined tension and shear.* PhD thesis, Royal Institute of Technology (KTH), Stockholm, Sweden, 2006.

I. Barsoum and J. Faleskog. Rupture mechanisms in combined tension and shear–experiments. *International Journal of Solids and Structures*, 44(6):1768–1786, Mar. 2007. URL http://www.sciencedirect.com/science/article/B6VJS-4M15CVW-1/2/6f6e5700fb22b5cf41bf053a6ca1217d.

D. Bigoni and A. Piccolroza. A new yield function for geomaterials. in c. viggiani, editor. *Constitutive Modeling and Analysis of Boundary Value Problems in Geotechnical Engineering*, pages 266–281, 2003.

N. Bonora. A nonlinear cdm model for ductile failure. *Engineering Fracture Mechanics*, 58(1-2):11–28, Sept. 1997. URL http://www.sciencedirect.com/science/article/B6V2R-3SN6KB0-G/2/99bb1acf554fc5f6bea815647d9d7219.

T. Borvik, O. S. Hopperstad, and T. Berstad. On the influence of stress triaxiality and strain rate on the behaviour of a structural steel. part ii. numerical study. *European Journal of Mechanics - A/Solids*, 22(1):15–32, 2003. URL http://www.sciencedirect.com/science/article/B6VKW-47HC7X0-1/2/dbf3e91a93c8b88fd36ff6c81b166083.

P. W. Bridgman. *Studies in large plastic flow and fracture.* McGraw-Hill, New York, 1952.

A. Brownrigg, W. A. Spitzig, O. Richmond, D. Teirlinck, and J. D. Embury. The influence of hydrostatic pressure on the flow stress and ductility of a spherodized 1045 steel. *Acta Metallurgica*, 31(8):1141–1150, Aug. 1983. URL http://www.sciencedirect.com/science/article/B7598-48H2XD8-5C/2/e4f5b249ed564def5076714fb37f61a9.

J. Cao, H. Yao, A. Karafillis, and M. C. Boyce. Prediction of localized thinning in sheet metal using a general anisotropic yield criterion. *International Journal of Plasticity*, 16(9):1105–1129, Aug. 2000. URL http://www.sciencedirect.com/science/article/B6TWX-40S0CP7-4/2/dd57795c5737d015f225d4f13e5274ee.

O. Cazacu and F. Barlat. A criterion for description of anisotropy and yield differential effects in pressure-insensitive metals. *International Journal of Plasticity*, 20(11):2027–2045, Nov. 2004. URL http://www.sciencedirect.com/science/article/B6TWX-4C5HPM5-1/2/b798ea1404016dd7f229a8b5d5545364.

J. Chaboche. Viscoplastic constitutive equations for the description of cyclic and anisotropic behavior of metals. *Bulletin de l'Academie Poloanise des Sciences. Serie des Sciences Techniques*, 25:33, 1977.

C. L. Chow, L. G. Yu, W. H. Tai, and M. Y. Demeri. Prediction of forming limit diagrams for al6111-t4 under non-proportional loading. *International Journal of Mechanical Sciences*, 43(2):471–486, Feb. 2001. URL http://www.sciencedirect.com/science/article/B6V49-4177NW7-C/2/3d4a086972bb12c2229f4a7df96a330f.

F. Cirak, M. Ortiz, and A. Pandolfi. A cohesive approach to thin-shell fracture and fragmentation. *Computer Methods in Applied Mechanics and Engineering*, 194(21-24):2604–2618, June 2005. URL http://www.sciencedirect.com/science/article/B6V29-4FBW600-4/2/06c015e841d7fba329790dd872c4986e.

D. P. Clausing. Effect of plastic strain state on ductility and toughness. *International Journal of Fracture Mechanics*, 6:71–85, 1970.

M. G. Cockcroft and D. J. Latham. Ductility and the workability of metals. *Journal of the Institute of Metals*, 96:33–39, 1968.

C. Coulomb. Essai sur une application des regles des maximis et minimis a quelues problemes de statique relatifs a larchitecture. *Mem Acad Roy des Sci*, 1776.

D. Drucker and W. Prager. Soil mechanics and plastic analysis or limit design. *Quarterly of Applied Mathematics*, 10:157–165, July 1952.

H. Dyrli. Strain analysis and fracture of crushed aluminum tubes. report 30. Technical report, Impact and Crashworthiness Laboratory, MIT, Camrbidge, MA., 1999.

E. El-Magd, H. Gese, R. Tham, H. Hooputra, and H. Werner. Fracture criteria for automobile crashworthiness simulation of wrought aluminium alloy components. *Mat.-wiss. u. Werkstofftech*, 32:712–724, 2001.

A. Fossum and R. Brannon. The sandia geomodel: theory and user's guide. Technical report, Sandia National Laboratories, Albuquerque, NM and Livermore, CA, 2005.

A. Fossum and R. Brannon. On a viscoplastic model for rocks with mechanism-dependent characteristic times. *Acta Geotechnica*, 1:89–106, 2006.

H. P. Ganser, A. G. Atkins, O. Kolednik, F. D. Fischer, and O. Richard. Upsetting of cylinders: A comparison of two different damage indicators. *Journal of Engineering Materials and Technology*, 123:94–99, 2001.

X. Gao and J. Kim. Modeling of ductile fracture: Significance of void coalescence. *International Journal of Solids and Structures*, 43:6277–6293, 2006. URL `http://www.sciencedirect.com/science/article/B6VJS-4H74M97-2/2/3b24a669759db40d6453387bf6ce394a`.

G. Goodwin. Application of strain analysis to sheet metal forming in the press shop. In *SAE paper 680093*, 1968.

A. Graf and W. Hosford. The influence of strain-path changes on forming limit diagrams of a1 6111 t4. *International Journal of Mechanical Sciences*, 36(10):897–910, Oct. 1994. URL `http://www.sciencedirect.com/science/article/B6V49-47YSCWR-T4/2/1209d97d3698b146728e999496d9b9c5`.

A. L. Gurson. *Plastic flow and fracture behavior of ductile materials incorporating void nucleation, growth and interaction.* PhD thesis, Brown University, 1975.

D. J. Han and W. F. Chen. A nonuniform hardening plasticity model for concrete materials. *Mechanics of Materials*, 4(3-4):283–302, Dec. 1985. URL `http://www.sciencedirect.com/science/article/B6TX6-47XSWXC-33/2/ab2b8e3db49edd51d1ceb433ed598047`.

J. W. Hancock and D. K. Brown. On the role of strain and stress state in ductile failure. *Journal of the Mechanics and Physics of Solids*, 31(1):1–24, 1983. URL `http://www.sciencedirect.com/science/article/B6TXB-46G2K1M-87/2/e6fcd075c309501a080e5fa7c8839559`.

J. W. Hancock and A. C. Mackenzie. On the mechanisms of ductile failure in high-strength steels subjected to multi-axial stress-states. *Journal of the Mechanics and Physics of Solids*, 24(2-3):147–160, June 1976. URL `http://www.sciencedirect.com/science/article/B6TXB-46G4XY9-15/2/659b0a9ca9dafdb5156b08e40c774f51`.

C. Hari Manoj Simha, J. Gholipour, A. Bardelcik, and M. J. Worswick. Prediction of necking in tubular hydroforming using an extended stress-based forming limit curve. *Journal of Engineering Materials and Technology*, 129:36–47, 2007.

R. Hill. On discontinuous plastic states, with special reference to localized necking in thin sheets. *Journal of the Mechanics and Physics of Solids*, 1(1):19–30, Oct. 1952. URL http://www.sciencedirect.com/science/article/B6TXB-46PYMRP-4R/2/499e9a0d308978574bc8504d7797669f.

H. Hooputra, H. Gese, H. Dell, and H. Werner. A comprehensive failure model for crashworthiness simulation of aluminium extrusions. *International Journal of Crashworthiness*, 9:449–464, 2004.

H. Hooputra, H. Gese, H. Dell, H. Werner, and A. Heath. A new comprehensive failure model for crashworthiness simulation - validation for aluminum extrusions. In *13th European Conference on Digital Simulation for Virtual Prototyping, Virtual Manufacturing and Virtual Environment, Mainz, Germany*, Oct. 2003.

O. S. Hopperstad, T. Borvik, M. Langseth, K. Labibes, and C. Albertini. On the influence of stress triaxiality and strain rate on the behaviour of a structural steel. part i. experiments. *European Journal of Mechanics - A/Solids*, 22(1):1–13, 2003. URL http://www.sciencedirect.com/science/article/B6VKW-47GYM1N-1/2/7c3a54ab75a4b6b90a44ce3f72eed052.

W. Hosford. A generalized isotropic yield criterion. *Journal of Applied Mechanics*, 39:607, 1972.

G. R. Johnson and W. H. Cook. Fracture characteristics of three metals subjected to various strains, strain rates, temperatures and pressures. *Engineering Fracture Mechanics*, 21(1):31–48, 1985. URL http://www.sciencedirect.com/science/article/B6V2R-481DR3X-37/2/b7243b477f475eb0d2855ef21ac1e538.

A. Kamoulakos, P. Culiere, and T. Araki. Prediction of ductile metal rupture with the e-w model in pam-crash. In *IBEC 2003 Chiba, Japan*, 2003.

A. P. Karafillis and M. C. Boyce. A general anisotropic yield criterion using bounds and a transformation weighting tensor. *Journal of the Mechanics and Physics of Solids*, 41(12):1859–1886, Dec. 1993. URL http://www.sciencedirect.com/science/article/B6TXB-46PYMNM-46/2/e113a20f7b4e2ea2e216e93bb01dab74.

D. G. Karr, F. P. Law, M. H. Fatt, and G. F. N. Cox. Asymptotic and quadratic failure criteria for anisotropic materials. *International Journal of Plasticity*, 5(4):303–336, 1989. URL http://www.sciencedirect.com/science/article/B6TWX-481DS9M-M/2/a743a7608406bdeec4b093c1a542788d.

S. Keeler and W. Backhofen. Plastic instability and fracture in sheet stretched over rigid punches. In *ASM Trans. Quart. 56, 25-48*, 1964.

A. S. Khan and K. M. Jackson. On the evolution of isotropic and kinematic hardening with finite plastic deformation part i: compression/tension loading of ofhc copper cylinders. *International Journal of Plasticity*, 15(12):1265–1275, 1999. URL http://www.sciencedirect.com/science/article/B6TWX-3Y1CDNX-1/2/580ee9657c1102a0811de1c6fcfc2a1f.

H. Kudo and K. Aoi. Effect of compression test conditions upon fracturing of medium carbon steel. *Journal of Japanese Society of Technology and Plasticity*, 18:17–27, 1967.

H. A. Kuhn and G. E. Dieter. Workability in bulk forming processes. *In "Fracture" ICF4, Waterloo, canada.*, 1977.

D. Lee and J. F. Zavenl. A generalized strain rate dependent constitutive equation for anisotropic metals. *Acta Metallurgica*, 29:1771, 1978.

Y.-W. Lee. *Fracture prediction in metal sheets.* PhD thesis, Massachusetts Institute of Technology, 2005.

J. Lemaitre. *A course on damage mechanics.* Springer, Berlin, Germany, 1996.

U. Lindholm, A. Nagy, G. Johnson, and J. Hoegfeldt. Large strain, high strain rate testing of copper. *Journal of Engineering Materials and Technology, Transactions of the ASME*, 102:376–381, 1980.

A. Lund and C. Schuh. The mohr-coulomb criterion from unit shear processes in metallic glass. *Intermetallics*, 12(10-11):1159–1165, 2004. URL `http://www.sciencedirect.com/science/article/B6TX8-4D34M87-2/2/4cdeddb3b8707a57dc37ee1a6c9e369c`.

A. C. Mackenzie, J. W. Hancock, and D. K. Brown. On the influence of state of stress on ductile failure initiation in high strength steels. *Engineering Fracture Mechanics*, 9(1):167–168, 1977. URL `http://www.sciencedirect.com/science/article/B6V2R-481DRSD-F4/2/47dd660061eb08c2380cb4353d0c53b8`.

H. Mae, X. Teng, Y. Bai, and T. Wierzbicki. Calibration of ductile fracture properties of a cast aluminum alloy. *Materials Science and Engineering: A*, 459(1-2):156–166, June 2007. URL `http://www.sciencedirect.com/science/article/B6TXD-4MVN123-8/2/e75f43f09a31a15fae3a9efecb1080c1`.

L. E. Malvern. *Introduction to the mechanics of a continuous medium.* Prentice-Hall, Inc., 1969.

Z. Marciniak and K. Kuczynski. Limit strains in the processes of stretch-forming sheet metal. *International Journal of Mechanical Sciences*, 9(9):609–612, Sept. 1967. URL `http://www.sciencedirect.com/science/article/B6V49-480TBRN-42/2/6609754d29dbf235aa4ffa1602d750cf`.

F. A. McClintock. A criterion of ductile fracture by the growth of holes. *Journal of Applied Mechanics*, 35:363–371, 1968.

P. Menetrey and K. Willam. Triaxial failure criterion for concrete and its generalization. *ACI Structural Journal*, 92:311–318, 1995.

M. S. Mirza, D. C. Barton, and P. Church. The effect of stress triaxiality and strain-rate on the fracture characteristics of ductile metals. *Journal of Materials Science*, 31, 1996.

R. v. Mises. Gottinger nachrichten. *Math.Phys.Klasse*, page 582, 1913.

D. Mohr. *Experimental investigation and constitutive modeling of metallic honeycombs in sandwich structures.* PhD thesis, Massachusetts Institute of Technology, 2003.

D. Mohr and M. Doyoyo. Experimental investigation on the plasticity of hexagonal aluminum honeycomb under multiaxial loading. *Journal of Applied Mechanics, Transactions ASME*, 71(3):375–385, 2004. URL http://www.sciencedirect.com/science/article/B6WPV-4FGYXV6-414/2/d573eab7cade2b0dea239b5d78bf187a.

D. Mohr and S. Henn. A new method for calibrating phenomenological crack formation criteria, report 113. *Technical report, Impact and Crashworthiness Laboratory, Massachusetts Institute of Technology, Cambridge, MA.*, 2004.

D. Mohr and S. Henn. Calibration of stress-triaxiality dependent crack formation criteria: A new hybrid experimental-numerical method. *Experimental Mechanics*, in press, 2007.

D. Mohr and S. Oswald. A new experimental technique for the multi-axial testing of advanced high strength steel sheets. *Experimental Mechanics*, In press, 2007.

O. Mohr. *Abhandlungen aus dem Gebiete der Technischen Mechanik (2nd ed).* Ernst, Berlin, 1914.

W. Muschenborn and H. Sonne. Influence of the strain path on the forming limits of sheet metal. *Arch. Eisenhuttenwes*, 46:597–602, 1975.

K. Nahshon and J. Hutchinson. Modification of the gurson model for shear failure. *In press*, 2007.

A. Needleman and V. Tvergaard. An analysis of ductile rupture in notched bars. *Journal of the Mechanics and Physics of Solids*, 32(6):461–490, 1984. URL http://www.sciencedirect.com/science/article/B6TXB-46G2K9M-91/2/8745c3f1a46fb597913967f26e65753f.

M. Oyane, T. Sato, K. Okimoto, and S. Shima. Criteria for ductile fracture and their applications. *Journal of Mechanical Working Technology*, 4(1):65–81, Apr. 1980. URL http://www.sciencedirect.com/science/article/B756R-481MX44-8W/2/4c541035d2fadeee9ad756d83536309a.

V. Palchik. Application of mohr-coulomb failure theory to very porous sandy shales. *International Journal of Rock Mechanics and Mining Sciences*, 43(7):1153–1162, Oct. 2006. URL http://www.sciencedirect.com/science/article/B6V4W-4K12CJM-1/2/f92cab23fa1b59640a75649a64f01ef3.

M. Pfestorf. The application of multiphase steel in the body-in white. In *Great designs in 2005 steel seminar presentations*, 2005.

J. R. Rice and D. M. Tracey. On the ductile enlargement of voids in triaxial stress fields. *Journal of the Mechanics and Physics of Solids*, 17:201–217, 1969.

O. Richmond and W. A. Spitzig. Pressure dependence and dilatancy of plastic flow. In *Theoretical and Applied Mechanics, Proceedings of the 15th International Congress of Theoretical and Applied Mechanics.*, pages 377–386, Toronto, Ont, Can, 1980. North-Holland Publ Co, Amsterdam, Neth.

L. M. Smith, R. C. Averill, J. P. Lucas, T. B. Stoughton, and P. H. Matin. Influence of transverse normal stress on sheet metal formability. *International Journal of Plasticity*, 19(10):1567–1583, Oct. 2003. URL http://www.sciencedirect.com/science/article/B6TWX-46YXJ7T-4/2/551b3812abdfcda516bb97170d3aa6ae.

W. A. Spitzig and O. Richmond. The effect of pressure on the flow stress of metals. *Acta Metallurgica*, 32(3):457–463, Mar. 1984. URL http://www.sciencedirect.com/science/article/B7598-48JJKNR-BK/2/e7e1ca14f30434f53bc8aa4f5de7ce6c.

S. Storen and J. R. Rice. Localized necking in thin sheets. *Journal of the Mechanics and Physics of Solids*, 23(6):421–441, Dec. 1975. URL http://www.sciencedirect.com/science/article/B6TXB-46G50H8-K5/2/ce9783773d9351b54ed477ce4e9047e6.

T. B. Stoughton. A general forming limit criterion for sheet metal forming. *International Journal of Mechanical Sciences*, 42(1):1–27, Jan. 2000. URL http://www.sciencedirect.com/science/article/B6V49-3X6JVSK-1/2/8109d22d0b6d66942d9b6eb46fd1b7dc.

T. B. Stoughton. A non-associated flow rule for sheet metal forming. *International Journal of Plasticity*, 18(5-6):687–714, Oct. 2002. URL http://www.sciencedirect.com/science/article/B6TWX-45FGBF6-7/2/d40b70efbaec08187a21108dec818508.

T. B. Stoughton. Private communication.

T. B. Stoughton and X. Zhu. Review of theoretical models of the strain-based fld and their relevance to the stress-based fld. *International Journal of Plasticity*, 20(8-9):1463–1486, 2004. URL http://www.sciencedirect.com/science/article/B6TWX-4B8B8JX-3/2/35ad2aec88757af8839a9890e10d2926.

W. H. Tai. Plastic damage and ductile fracture in mild steels. *Engineering Fracture Mechanics*, 37(4):853–880, 1990. URL http://www.sciencedirect.com/science/article/B6V2R-481G0KR-34/2/442237f2bd1dc487777fc805925be09f.

X. Teng. *High Velocity Impact Fracture*. PhD thesis, Massachusetts Institute of Technology, 2004.

X. Teng and T. Wierzbicki. Evaluation of six fracture models in high velocity perforation. *Engineering Fracture Mechanics*, 73(12):1653–1678, Aug. 2006. URL http://www.sciencedirect.com/science/article/B6V2R-4JCBPDF-1/2/089b90721a40a1aae6f84883b5baf8b3.

P. F. Thomason. The use of pure aluminium as an analogue for the history of plastic flow, in studies of ductile fracture criteria in steel compression specimens. *International Journal of Mechanical Sciences*, 10(6):501–518, June 1968. URL http://www.sciencedirect.com/science/article/B6V49-480TBGR-1H/2/59860a3cfa24da2dceb8df9ac907b95a.

P. F. Thomason. Tensile plastic instability and ductile fracture criteria in uniaxial compression tests. *International Journal of Mechanical Sciences*, 11(2):187–194, Feb. 1969. URL http://www.sciencedirect.com/science/article/B6V49-480TBD4-C/2/a933add90a81bc04298873e687ac063d.

H. Tresca. *Comptes Rendus Acad. Sci.*, 59:754, 1864.

V. Tvergaard and A. Needleman. Analysis of the cup-cone fracture in a round tensile bar. *Acta Materialia*, 32:157–169, 1984.

H. Vegter and A. van den Boogaard. A plane stress yield function for anisotropic sheet material by interpolation of biaxial stress states. *International Journal of Plasticity*, 22(3):557–580, Mar. 2006. URL http://www.sciencedirect.com/science/article/B6TWX-4GRH71M-2/2/5ee587eeaca035a7853d51a00b01e861.

M. S. Walp, A. Wurm, J. F. I. Siekirk, and A. K. Desai. Shear fracture in advanced high strength steels. *SAE technical papers 2006-01-1433*, 2006.

C. Walters. Recitation material of the course of structrual mechanics, mit. 2006.

H. Werner, H. Hooputra, H. Dell, and H. Gese. A phenomenological failure model for sheet metals and extrusions. In *Annual review meeting and workshop of Impact and Crashworthiness Lab at MIT, Cambridge, MA*, Oct. 2004.

C. S. White, C. A. Bronkhorst, and L. Anand. An improved isotropic–kinematic hardening model for moderate deformation metal plasticity. *Mechanics of Materials*, 10(1-2):127–147, Nov. 1990. URL http://www.sciencedirect.com/science/article/B6TX6-47XSWRY-19/2/4142fae8329d88d5dbd9dfd7033debc3.

T. Wierzbicki and Y. Bao. Bridgman revisited: on the history effect on ductile fracture. impact and crashworthiness laboratory, massachusetts institute of technology, cambridge, ma.

T. Wierzbicki and J. Huang. Initiation of plastic folding mechanism in crushed box columns. *Thin-Walled Structures*, 13(1-2):115–143, 1992. URL http://www.sciencedirect.com/science/article/B6V59-481MVGF-17/2/f1b852eb5cb57de049037c5bf73b8939.

T. Wierzbicki and P. Thomas. Closed-form solution for wedge cutting force through thin metal sheets. *International Journal of Mechanical Sciences*, 35(3-4):209–229, 1993. URL http://www.sciencedirect.com/science/article/B6V49-47YSD2B-V7/2/8d38a35f9f141df321a480be97a1a919.

T. Wierzbicki and L. Xue. On the effect of the third invariant of the stress deviator on ductile fracture. Technical report, Impact and Crashworthiness Laboratory, Massachusetts Institute of Technology, Cambridge, MA, 2005.

T. Wierzbicki, M. A. Beese, and Y. Bai. A comparative study of three methods of measuring fracture strain in metals. In *To be prsented at the International Plasticity Symposium, Hawaii, January, 2008.*

T. Wierzbicki, Y. Bao, and H. Werner. Ductile fracture, theory, calibration and applications. *In "EuroPAM 2002" Antibes Juan les Pins, France*, 2002.

T. Wierzbicki, Y. Bao, and Y. Bai. A new experimental technique for constructing a fracture envelope of metals under multi-axial loading. *Proceedings of the 2005 SEM Annual Conference and Exposition on Experimental and Applied Mechanics*, pages 1295 – 1303, 2005a.

T. Wierzbicki, Y. Bao, Y.-W. Lee, and Y. Bai. Calibration and evaluation of seven fracture models. *International Journal of Mechanical Sciences*, 47(4-5):719–743, 2005b. URL http://www.sciencedirect.com/science/article/B6V49-4G0M3XX-1/2/6ebd431547d5c5b1bdac30c7428bcffb.

M. L. Wilkins, R. D. Streit, and J. E. Reaugh. Cumulative -strain-damage model of ductile fracture: simulation and prediction of engineering fracture tests, ucrl-53058. Technical report, Lawrence Livermore Laboratory, Livermore, California, 1980.

C. D. Wilson. A critical reexamination of classical metal plasticity. *Journal of Applied Mechanics, Transactions ASME*, 69(1):63–68, 2002. ISSN 0021-8936.

B. Xu and X. Liu. *Applied mechanics: elasticity and plasticity.* Tsinghua University Press, Beijing, China, 1995.

L. Xue. *Ductile Fracture Modeling Theory, Experimental Investigation and Numerical Verification.* PhD thesis, Massachusetts Institute of Technology, 2007a.

L. Xue. Damage accumulation and fracture initiation in uncracked ductile solids subject to triaxial loading. *International Journal of Solids and Structures*, 44(16):5163–5181, Aug. 2007b. URL http://www.sciencedirect.com/science/article/B6VJS-4MP56BV-1/2/30d3c7da24a040dc0faf92c5aad4b026.

K. S. Zhang, J. B. Bai, and D. Francois. Numerical analysis of the influence of the lode parameter on void growth. *International Journal of Solids and Structures*, 38(32-33):5847–5856, Aug. 2001. URL http://www.sciencedirect.com/science/article/B6VJS-4372YCH-S/2/36bc3739d1cabab0b97215ebc7aee851.

J. Zhao. Applicability of mohr-coulomb and hoek-brown strength criteria to the dynamic strength of brittle rock. *International Journal of Rock Mechanics and Mining Sciences*, 37(7):1115–1121, Oct. 2000. URL http://www.sciencedirect.com/science/article/B6V4W-41DHXGR-9/2/226b1e4e698bdce5e290541aea714186.

L. Zhao, R. Sowerby, and M. P. Sklad. A theoretical and experimental investigation of limit strains in sheet metal forming. *International Journal of Mechanical Sciences*, 38(12):1307–1317, Dec. 1996. URL http://www.sciencedirect.com/science/article/B6V49-3VTT6SY-4/2/d78e5f8ad0b96af8c6c3eae510c1fdb0.